A practical perspective on post-lithium-ion organic batteries

zur Erlangung des akademischen Grades eines

Doktors der Naturwissenschaften

(Dr. rer. nat.)

von der KIT-Fakultät für Chemie und Biowissenschaften
des Karlsruher Instituts für Technologie (KIT)

genehmigte

Dissertation

von

Alessandro Innocenti

Referent:	Prof. Dr. Stefano Passerini
Korreferent:	Prof. Dr. Armin Grunwald
Tag der mündlichen Prüfung:	18.07.2023

Kurzfassung

Die steigende Nachfrage nach Lithium-Ionen-Batterien und den damit verbundenen kritischen Mineralien hat Bedenken hinsichtlich der Verfügbarkeit von Ressourcen und der nachhaltigen Kostenentwicklung aufkommen lassen. Als Folge haben alternative Lösungen wie organische und Natrium-Ionen-Batterien im Bereich der elektrochemischen Energiespeicherung erhebliche Aufmerksamkeit erlangt. Unsere Forschung behandelt die Bedeutung einer kritischen Erkundung dieser Alternativen bereits auf Laborebene und schlägt eine Methodik vor, um ihre praktische Umsetzbarkeit in kommerziellen Batteriesystemen zu bewerten, unter Verwendung einer Kombination aus experimentellen Ergebnissen und Modellierung.

Wir betonen zunächst die Notwendigkeit einer Kosten- und Leistungsanalyse als grundlegenden Schritt in der Erforschung neuer Batteriematerialien. Es wird betont, wie wichtig es ist, diese Analyse bereits in der Entdeckungsphase der Materialien anzuwenden, um die Forschungsbemühungen auf praktische Lösungen auszurichten. Anhand einer Fallstudie zu Natrium-Ionen-Batterien zeigen wir, wie detaillierte Simulationen der Energiedichte und der Kosten die vielversprechendsten Kathodenmaterialien für reale Anwendungen effektiv identifizieren können.

Im Kontext von organischen Batterien konzentrieren wir uns dann auf n-Typ organische Materialien und bewerten ihre Eigenschaften auf Systemebene der Batterie. Eine umfassende Überprüfung relevanter Kathodenmaterialien wird durchgeführt, gefolgt von einer detaillierten Kosten- und Leistungsanalyse. Die Analyse berücksichtigt wichtige Designentscheidungen der Elektroden und hebt das Potenzial von n-Typ organischen Materialien als kostengünstige und nachhaltige Lösungen für die Energiespeicherung hervor, insbesondere im Fall von lithiumbereicherten, luftstabilen Materialien. Allerdings sind weitere Fortschritte notwendig, um diese Materialien zu optimieren und die Leistungslücke zu anorganischen Kathoden zu schließen.

P-Typ-Materialien für Batterien, die sowohl Kationen als auch Anionen in den Redoxreaktionen umfassen, werden ebenfalls untersucht, jedoch erfordert ihre Bewertung ein detailliertes Verständnis ihres Arbeitsprinzips, da es sich signifikant von Lithium-Ionen- und n-Typ organischen Batterien unterscheidet aufgrund des Verbrauchs des Elektrolytsalzes während des Ladevorgangs. Eine modifizierte Version des Doyle-Fuller-Newman-Modells wird vorgeschlagen, um die Variation der durchschnittlichen Salzkonzentration im Elektrolyten während des Lade- und Entladevorgangs zu simulieren. Das Modell berücksichtigt erfolgreich die einzigartigen Herausforderungen, die mit der Beteiligung von Anionen verbunden sind, und ermöglicht das Design praktischer P-Typ-Batterien (und allgemein von Dual-Ionen-Batterien) mit maximierter Kapazität und Energiedichte.

Abschließend demonstrieren wir die Anwendung dieser umfassenden Methodik anhand von experimentellen Ergebnissen zu Poly(2,2,6,6-tetramethyl-1-piperidinyloxy methacrylat) (PTMA), einem vielversprechenden p-Typ-organischen Kathodenmaterial. Die laborbasierte Studie zeigt die Machbarkeit von Kathoden mit hoher aktiver Massebeladung und bemerkenswerter theoretischer Flächenkapazität für organische Batterien. Die detaillierten physikalischen Simulationen und die Kosten-Leistungsanalyse beleuchten die kritische Rolle des Elektrolyten und den Einfluss der Anionenbeteiligung am Redoxprozess von PTMA, um solche Batterien mit hoher Massebeladung in einem realistischen Szenario zu ermöglichen.

Zusammenfassend verdeutlichen unsere Ergebnisse die Notwendigkeit einer ganzheitlichen Herangehensweise, die über die Grenzen von Laborbatterien hinausgeht. Wir betonen die Herausforderungen, die mit der effektiven Umsetzung erfolgreicher experimenteller Ergebnisse in realen Konfigurationen einhergehen. Indem wir diese Herausforderungen erkennen, ebnen wir den Weg für die Entwicklung praktischer und wirtschaftlich machbarer post-Lithium-Ionen-Batterietechnologien. Unsere Studie stellt eine Methodik vor, die in zukünftigen Untersuchungen angepasst und eingesetzt werden kann und bietet einen vielversprechenden Weg zur Realisierung kostengünstiger und tragfähiger Batterielösungen für die Zukunft.

Abstract

The increasing demand for lithium-ion batteries and the associated critical minerals has raised concerns about resource availability and cost sustainability. As a result, alternative solutions, such as organic and sodium-ion batteries, have gained significant attention in the field of electrochemical energy storage. Our research addresses the importance of critically exploring these alternatives already at the laboratory-scale level, and we propose a methodology to assess their feasibility for practical implementation in commercial-scale battery systems, using a combination of experimental results and modelling.

We initially highlight the need for cost and performance analysis as a fundamental step in the research for new battery materials. It emphasizes the importance of applying this analysis at the material discovery stage to guide research efforts towards practical solutions. Through a case study on sodium-ion batteries, we demonstrate how detailed simulations of energy density and cost can effectively identify the most promising cathode materials for real-world applications.

In the context of organic batteries, we focus then on n-type organic materials and assesses their properties at the full battery system level. A comprehensive review of relevant cathode materials is provided, followed by a detailed cost and performance analysis. The analysis considers key electrode design choices and highlights the potential of n-type organic materials as low-cost and sustainable solutions for energy storage, especially in the case of lithium-sufficient, air-stable materials. However, further advancements are necessary to optimize these materials and bridge the performance gap with inorganic cathodes.

P-type materials batteries, which involve both cations and anions in the redox reactions, are also explored, but their evaluation requires a detailed understanding of their working principle, since it differs significantly from lithium-ion and n-type organic batteries due to the depletion of the electrolyte salt during the charge process. A modified version of the Doyle-Fuller-Newman model is proposed to simulate the variation of average salt concentration in the electrolyte during charge and discharge. The model successfully accounts for the unique challenges associated with the involvement of anions, enabling the design of practical p-type batteries (and in general of dual-ion batteries) with maximized capacity and energy density.

Finally, we demonstrate an application of this comprehensive methodology using experimental results on poly(2,2,6,6-tetramethyl-1-piperidinyloxy methacrylate) (PTMA), a promising p-type organic cathode material. The laboratory-scale study demonstrates the viability of high active mass loading cathodes with remarkable theoretical areal capacities for organic batteries. The detailed physical simulations and cost-performance analysis shed light on the critical role of the electrolyte and the impact of the anion involvement in the redox process of PTMA to enable such high mass loading batteries in a realistic scenario.

In summary, our findings highlight the necessity of embracing a holistic approach that extends beyond the confines of laboratory-scale batteries. We emphasize the challenges inherent in effectively implementing successful experimental results in real-world configurations. By recognizing these challenges, we pave the way for the development of practical and economically feasible post-lithium-ion battery technologies. Our study introduces a methodology that can be adapted and employed in future investigations, providing a promising path towards the realization of cost-effective and viable battery solutions for the future.

Contents

Kurzfassung i

Abstract iii

Contents v

1. Motivation 1

2. Introduction 5

- 2.1. Basic electrochemistry for batteries 5
- 2.2. Lithium-ion batteries 10
  - 2.2.1. Cathodes 11
  - 2.2.2. Anodes 13
  - 2.2.3. Electrolytes and separators 15
  - 2.2.4. Alternatives to lithium-ion batteries 16
- 2.3. Sodium-ion batteries 18
- 2.4. Organic batteries 19
  - 2.4.1. N-type materials 20
  - 2.4.2. P-type materials 29

3. Aim of the dissertation 33

4. Theory overview 35

- 4.1. Chronopotentiometric techniques 35
- 4.2. Electrochemical impedance spectroscopy (EIS) 37
- 4.3. Scanning Electron Microscopy (SEM) 39
- 4.4. Thermogravimetric analysis (TGA) 40
- 4.5. Gas pycnometry 41
- 4.6. Macroscale battery physical model 42

4.6.1. Microscale equations for the cathode 42
4.6.2. Boundary conditions of the microscale equations for the cathode 46
4.6.3. Macroscopic model for the porous cathode 48
4.6.4. Boundary conditions of the macroscopic model 52
4.6.5. Other definitions 53

5. Materials and methods 55

5.1. Experimental techniques 55
5.1.1. Physicochemical characterization 55
5.1.2. Electrochemical characterization 55
5.2. Materials preparation 57
5.2.1. Polymer synthesis 57
5.2.2. Electrode preparation 59
5.3. Modeling tools 59
5.3.1. Macroscale physical model of the battery 59
5.3.2. Cost and performance analysis model 60

6. Results and discussion 61

6.1. Cost and energy density analysis as valuable tool for battery material research 62
6.1.1. Impact of raw material price increases on LIBs and SIBs 63
6.1.2. Link between voltage profile and performance in sodium-ion battery packs 68
6.2. Assessing N-Type Organic Materials for Lithium-Batteries 79
6.2.1. Analysis of lithium-deficient organic materials 84
6.2.2. Analysis of lithium-sufficient organic materials 86
6.2.3. Influence of the carbon content 88
6.2.4. Influence of the active material content 90
6.2.5. Influence of the electrode density 92
6.2.6. Conclusion 94
6.3. A modified Doyle-Fuller-Newman model for the simulation of dual-ion batteries 95
6.3.1. Physical model 98

6.3.2. Comparison of model results and experimental data 102
6.3.3 Application of the model for the design of dual-ion batteries 106
6.3.4 Conclusions 107
6.4. Practical cell design for PTMA-based organic batteries 108
6.4.1 Experimental results 108
6.4.2 Design of a PTMA battery: physical simulations 117
6.4.3 Design of a PTMA battery: cost and energy density analysis 122
6.4.4 Conclusions 125
7. Summary and conclusions 126
Appendix 1: Supporting information for Section 6.1 128
Appendix 2: Supporting information for Section 6.2 145
Appendix 3: Supporting information for Section 6.3 147
Appendix 4: Supporting information for Section 6.4 150
List of Abbreviations 166
List of Tables 169
List of Figures 171
References 181
List of publications 215
Journal articles 215
Conference contributions 217
Ringraziamenti 221
Acknowledgments 223

1. Motivation

Reducing greenhouse gas (GHG) emissions to mitigate climate change is a critical global issue that requires urgent attention. The rising concentrations of CO_2, methane and other GHGs in the atmosphere due to human activities have already caused an average increase of the global temperature of 1.1°C in the 2010-2020 decade compared to the 1850-1900 period.[1] It is almost certain that any temperature increase beyond 1.5-2°C will result in significant disruptions across environmental, societal, political, economic, and health domains of the human society. To avoid overshooting the 2°C target, the annual emissions must peak within the next few years, with the goal of achieving a zero-carbon economy by 2050 (**Figure 1.1.a**). Hence, this shift must occur within a relatively short timeframe.[1]

To address climate change and limit temperature increases to safe levels, a coordinated effort is needed across all major sectors of the economy. Being the energy sector the major contributor (40% of the 2022 overall global emissions, **Figure 1.1.b**), a shift towards a decarbonized energy mix is essential to achieve a significant reduction in greenhouse gas emissions.[2] The technologies needed to make the transition to a low-carbon energy sector are already available, including solar photovoltaic, wind, hydro, biomass, and nuclear power generation, with the first two that saw a phenomenal growth of installed capacity and generated energy in the last ten years, and an even faster adoption will be required in the next future to be on track with the climate goals. Nevertheless, the inherent intermittency and lack of programmability of solar and wind energy requires energy storage systems that can act as an interface with the electric grid, to provide flexibility in the production-demand matching which is the key to maintain a stable and reliable power supply.

Another large share of the GHGs emission is caused by the transport sector with 23% of the 2022 GHG emissions,[2] predominantly due to the use of internal combustion engines, for land vehicles and ships, and gas turbines, for aviation. Several countries around the world have already planned the phase-out of internal combustion engines and/or the allowance of only zero-emission vehicles for sale within a 10-30 year timeframe.[3] The widespread adoption of electric vehicles is seen as a promising solution to mitigate the environmental impact of transportation. Electric vehicles produce zero tailpipe emissions, reducing harmful pollutants and greenhouse gas emissions that contribute to climate change.[4] However, electric vehicles require an energy storage system that can ensure high gravimetric and volumetric energy and power density, high efficiency, excellent safety, large low cost and good cycle life.

The development and deployment of lithium-ion batteries in the last thirty years made possible to address the aforementioned challenges.[5–7] This technology currently dominates the commercial market for both stationary energy storage and electric vehicles, since they offer a good balance of energy density, power density, and cycle life, making them suitable for a wide range of applications.

Grid energy storage systems based on lithium-ion batteries have been and are being successfully implemented in various regions around the world, with almost 6.5 GW of storage capacity installed only in 2021, an increase of 85% compared to the previous year.[8] These systems store excess electricity produced by renewable power plants during periods of low demand and release it during peak demand, helping to stabilize the grid and avoid the need for additional fossil fuel-based power plants. The scalability and modularity of battery-based grid storage solutions make them the most favorable option for a storage duration in the order of the hours, while other existing or emerging systems such as pumped hydroelectric, compressed air storage, hydrogen or reactive metals are more suited to cover days-long and seasonal storage.[9,10]

The growing adoption of electric vehicles (EVs) has significantly contributed to the increasing demand for lithium-ion battery technology, too. In 2022, the share of electric car sales in the total number of cars sold reached 14%, marking a significant rise from 9% in 2021 and 5% in 2020.[11]

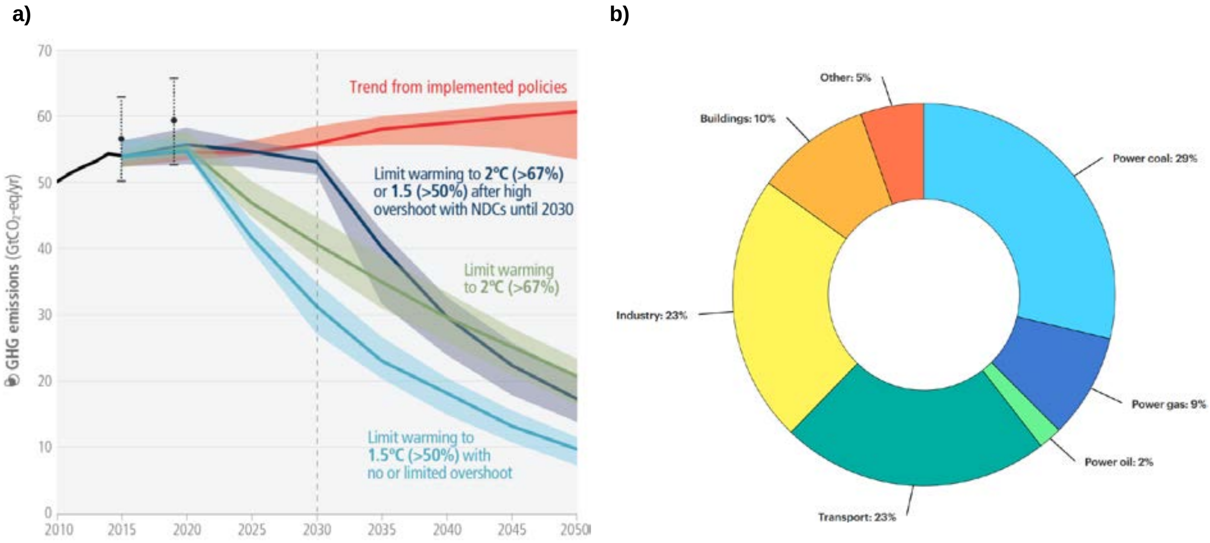

***Figure 1.1** – a) Forecasted yearly GHG emission trends from possible pathways, according to the policies implemented by statesm Copyright © 2022, IPCC [1] b) Breakdown by sector of the global GHG emissions in 2022. CC BY 4.0, 2023 IEA [2]*

This growth has been primarily driven by the Chinese, European, and US markets. In the first quarter of 2023, the best-selling car in the world was for the first time a fully-electric vehicle, highlighting the accelerating transition towards electric mobility.[12]

However, as the demand for batteries continues to increase, projections indicate a need for a substantial number of batteries to meet future requirements.[13–15] The demand may exceed the production of necessary raw materials, especially critical ones like lithium and cobalt (**Figure 1.2**). Consequently, the sustainability of the entire industry becomes a pressing concern. The production of a modern lithium-ion battery not only depletes several critical natural resources but also emits greenhouse gases. To gain a comprehensive understanding of battery sustainability, it is imperative to thoroughly evaluate the scale of these environmental impacts and consider the implementation of more sustainable technologies. [16,17]

To address this staggering demand and these pressing challenges, there is the need to explore new chemistries and complementary solutions. While lithium-ion batteries remain the frontrunners, researchers and industry experts are actively investigating alternative battery chemistries that can offer even higher energy and power densities, improved safety, reduced costs, and better sustainability.[18–20]

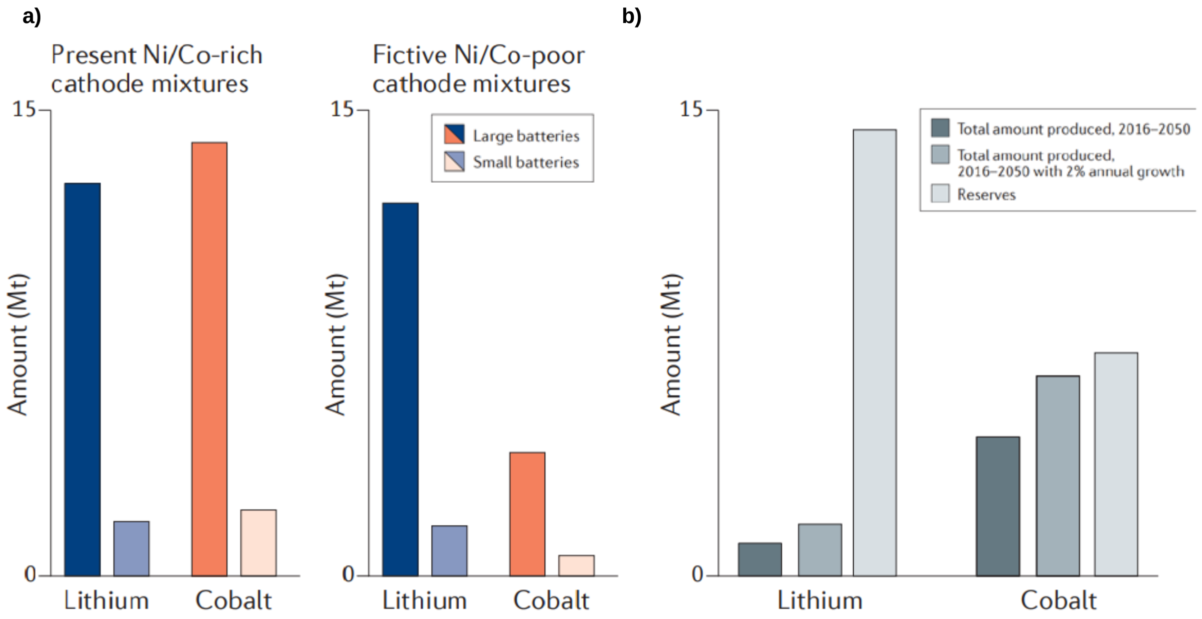

Figure 1.2 *– a) Predicted demand of lithium and cobalt for the battery industry between 2016 and 2050; b) Total amount of produced lithium and cobalt with current production rates and with a 2% yearly increase of production between 2016 and 2050. Adapted with permission from Vaalma et al.*[13]*, Copyright © 2018, Springer Nature*

2. Introduction

2.1. Basic electrochemistry for batteries

Electrochemical energy storage devices exploit oxidation and reduction electrochemical reactions to reversibly convert chemical energy into electric energy, hence they can store (charge) and release (discharge) electric energy according to the needs of the user and the capabilities of the devices.[21]

The basic components of an energy storage device are:

- the electrodes, electronically conductive elements based on metals and/or carbon which make available electrons at their surface for the electrochemical reactions. The electrode where the oxidation reaction happens is called anode, while the one where the reduction reaction takes place is named cathode. During discharge, in the electrical circuit the anode has the negative polarity and the cathode the positive one, and vice versa during charge.

$$\text{Cathode: } M^{x+} + ne^- \underset{discharge}{\overset{charge}{\rightleftarrows}} M^{(x-n)+} \tag{2.1}$$

$$\text{Anode: } A^{y-} \underset{discharge}{\overset{charge}{\rightleftarrows}} A^{(y-n)-} + ne^- \tag{2.2}$$

$$\text{Overall reaction: } M^{x+} + A^{y-} \underset{discharge}{\overset{charge}{\rightleftarrows}} M^{(x-n)+} + A^{(y-n)-} \tag{2.3}$$

- the electrolyte, an ionically conductive layer that separates the electrodes and supplies ions for the electrochemical reactions to ensure electroneutrality. The electrolyte does not allow the passage of electrons, as this would short the energy storage device. The electrolyte is typically a liquid in which a salt is dissolved, but solid- or gel-state electrolytes are also common. When the electrolyte is liquid, an additional non-electronically conductive membrane, the separator, is usually added to have a better isolation between the electrode and to enhance the mechanical stability of the whole structure.

- the external electric circuit that connects the electrodes, allowing the flow of electrons in and out the energy storage device. The circuit also connects the device to a load, when the device is discharged, or to an energy source, when the device is charged.

The sequence of two electrodes divided by the electrolyte and connected through an external circuit forms an electrochemical cell. When the cell is designed as an open system where the reactants flow in when and the products flow out, it is named fuel cell, and the energy and power characteristics are decoupled, since the reactants can be stored externally from the cell. Instead, a closed system where the reactants and products are stored in the cell is called battery, and the energy and power density are in this case strongly correlated. Batteries are further divided in primary batteries, which can only transform chemical energy into electric energy in a non-reversible way and act as energy sources, and secondary batteries, where the reverse conversion of electric energy into chemical energy is also possible and can then serve as energy storage devices, too. In this work, the focus is on secondary batteries, and following the convention in battery terminology, the discharge is used as reference for naming the electrodes. Hence, the positive electrode will be always called cathode, and the negative one anode (**Figure 2.1**).

The energy J that can be stored in and released by a battery, usually measured in Wh, can be defined as

$$J = \int \Delta E \cdot I \, dt \tag{2.4}$$

where ΔE is the battery voltage, i.e., the electric potential difference between the two electrodes, and I is the current applied on the battery during charge or discharge. The current I is normally set as a working parameter based on characteristics of the load or the energy source, and on the capabilities of the battery. Instead, the battery voltage ΔE strictly depends on the nature of the electrodes and of the electrochemical reactions taking place in the battery (**Figure 2.2**). In fact, we can correlate ΔE to the electrode reaction Gibbs free energy ΔG at constant pressure and temperature with the Faraday equation

$$\Delta G = -nF\Delta E \tag{2.5}$$

where n is the number of electrons exchanged in the reaction and F is the Faraday constant, approximately equal to 96485.33 C·mol^{-1}. The product on the right-hand side of the equation is the electrical work done by the system on its surroundings and this corresponds to a negative change in free energy in the system equal to ΔG, i.e., a spontaneous process.

The potential of a single electrode E can be obtained through the Nernst equation

$$E = E^{\circ} + \frac{RT}{nF} \ln\left(\frac{a_{Ox}}{a_{Red}}\right) \tag{2.6}$$

where E° is the standard electrode potential of the reaction, R is the universal gas constant (≈ 8.3145 J·K^{-1}·mol^{-1}), T is the temperature of the reaction, and a_{Ox} and a_{Red} are the activity coefficients of

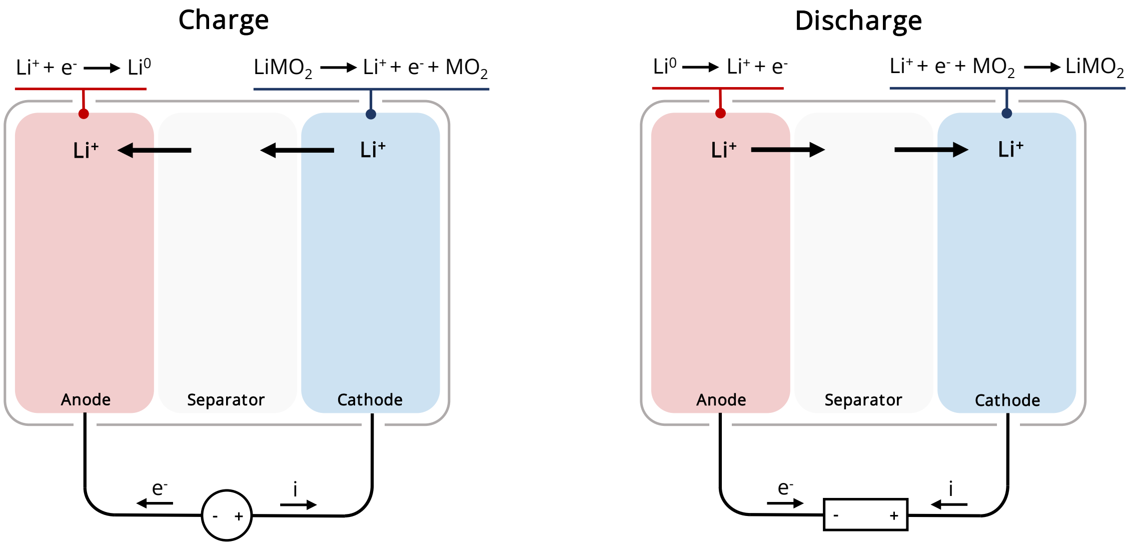

***Figure 2.1** – Scheme of the charge and discharge process of a battery (the reactions refer to a lithium-ion battery)*

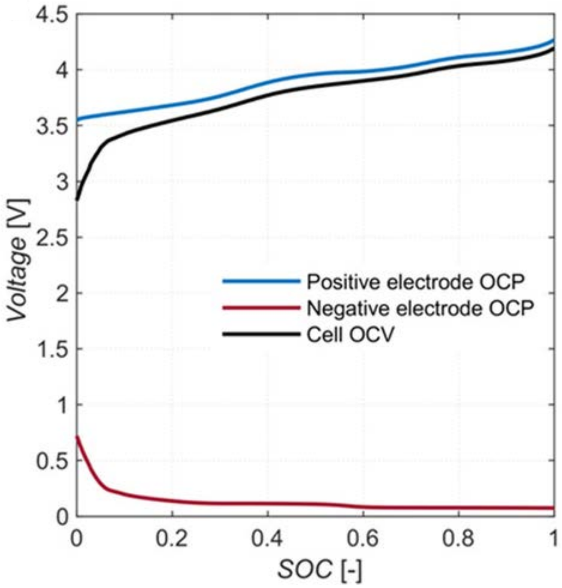

***Figure 2.2** – Example of the potential of the electrodes and the resulting cell voltage of a battery vs. the state of charge (SOC). Reproduced with permission from Rabissi et al., Copyright © 2021 Wiley*[22]

the oxidized species and the reduced species, respectively. The standard electrode potential E° is calculated in standard conditions and it is referred to the Standard Hydrogen Electrode (SHE). Other reference potentials that will be employed in this work are the lithium electrode potential (-3.04 V vs. SHE) and the sodium electrode potential (-2.71 V vs. SHE). In equilibrium conditions, i.e., when the current flowing in the battery is equal to zero or anyway negligible, the potential difference ΔE of a battery is called open circuit voltage (OCV), and the potential of an electrode E is called open circuit potential (OCP).

The change in Gibbs free energy is related to the electrochemical potential of the species that partake in the reaction $\overline{\mu}$

$$\overline{\mu} = \mu + zF\phi \tag{2.7}$$

where the chemical potential μ is corrected by the contribution of the electrostatic interaction with z equal to the charge of the species and ϕ equal to the electric potential felt by the species. The chemical potential μ is defined as the change of free energy caused by the introduction of a quantity of species equal to m at constant temperature and pressure, and we can write

$$\mu = \left.\frac{\partial G}{\partial m}\right|_{T,P=const.} \tag{2.8}$$

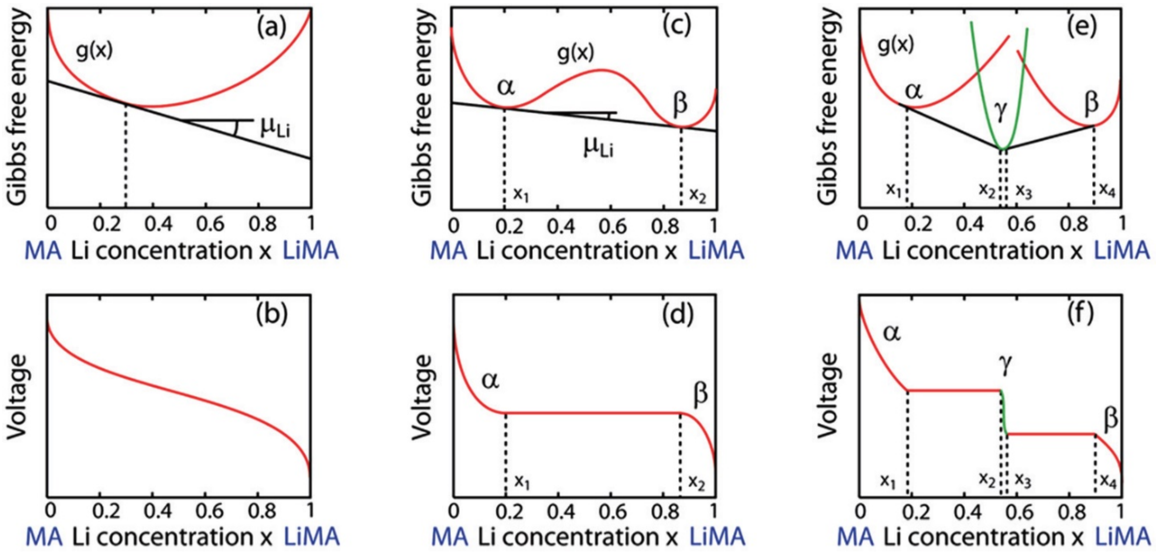

__Figure 2.3__ - Relationship between Gibbs free energy, chemical potential and open circuit potential in a battery. (a) and (b): single phase solid solution, (c) and (d): two phase solid solution, (e) and (f): two phase solid solution with intermediate phase. Reproduced with permission from Gao et a., Copyright © 2015, IOP Publishing [23]

From equations (2.5) and (2.8) we can infer the shape of the open circuit potential according to the trend of the chemical potential of the reacting species in the electrodes (**Figure 2.3**). If a single-phase reaction takes place, a solid solution behavior is observed, resulting in a sloping potential curve (**Figure 2.3.a** and **Figure 2.3.b**). Instead, when two phases are involved in the reaction the OCP is characterized by a constant value, since during an isothermobaric phase transition the chemical potential of the two phases is equal and constant (**Figure 2.3.c** and **Figure 2.3.d**). Reactions that involve multiple phase transitions separated by show a step-like potential characteristic ((**Figure 2.3.e** and **Figure 2.3.f**).

The difference between the open circuit potential and the actual measured voltage during operation is called overpotential. The total overpotential η can be due to different resistance phenomena in the battery which are triggered by applying a current to the device:

- Voltage loss resulting from internal resistances within the cell gives rise to ohmic overpotential η_{ohm}, which lead to an immediate drop or rise in voltage upon initiation of discharge or charge, following Ohm's law. Consequently, the ohmic overpotential is directly proportional to the applied current.

- When electrochemical reactions are initiated in an electrode, a charge transfer overpotential η_{kin} occurs as charges, such as electrons and ions, are exchanged between different phases. According to the Butler-Volmer theory, this charge transfer reaction has a specific rate and requires the surpassing of an energy barrier known as activation energy. Hence, a part of the energy is spent to overcome this barrier, causing a kinetic-related overpotential.

- The diffusion overpotential η_{pol} becomes dominant at high current rates when the reacting species undergo diffusion processes within the electrolyte and electrodes. When the rate at which the reactants are supplied at the surface where the electrochemical reaction happen is lower than the reaction rate, this reaction becomes limited by the mass transfer and concentration polarization is observed.

The total overpotential η is equal to the sum of the three single contributions

$$\eta = \eta_{ohm} + \eta_{kin} + \eta_{pol} \tag{2.9}$$

2.2. Lithium-ion batteries

Lithium-ion batteries (LIBs) are the technology are currently enabling the electrification of transportation and a better integration of intermittent renewable energy sources in the grid, as well as the ubiquitous presence of consumer electronics.[5–7] Based on redox reactions where the electrodes exchange reversibly lithium ions, they were developed between the 70s and the early 90s and first commercialized by Sony in 1991, in a collective effort that was recognized with the 2019 Nobel Prize in Chemistry for Stanley Whittingham, John B. Goodenough, and Akira Yoshino.[24]

Being lithium both the lightest metal and the one with the lowest redox potential (-3.04 V vs. SHE), the energy density of lithium-ion batteries easily surpassed the performance of established chemistries such as lead-acid, nickel cadmium, and nickel-hydride batteries.[21] According to the type of anode and cathode, the size, and the purpose, commercial LIBs are characterized by a gravimetric energy density in the 100-250 Wh·kg^{-1} range, a volumetric energy density of 200-700 Wh·l^{-1} (**Figure 2.4.b**), and a cycle life in the order of 10^2-10^3 number of cycles.[25] The cost of LIBs, which was initially one of the main factors hindering their widespread application, decreased tremendously since their market introduction (-97% since 1992 considering the increase of performance in the years, see **Figure 2.4.a**),[25] and their current average price is around 150 \$·kWh^{-1} (compare with ≈1000 \$·kWh^{-1} in 2008).[26]

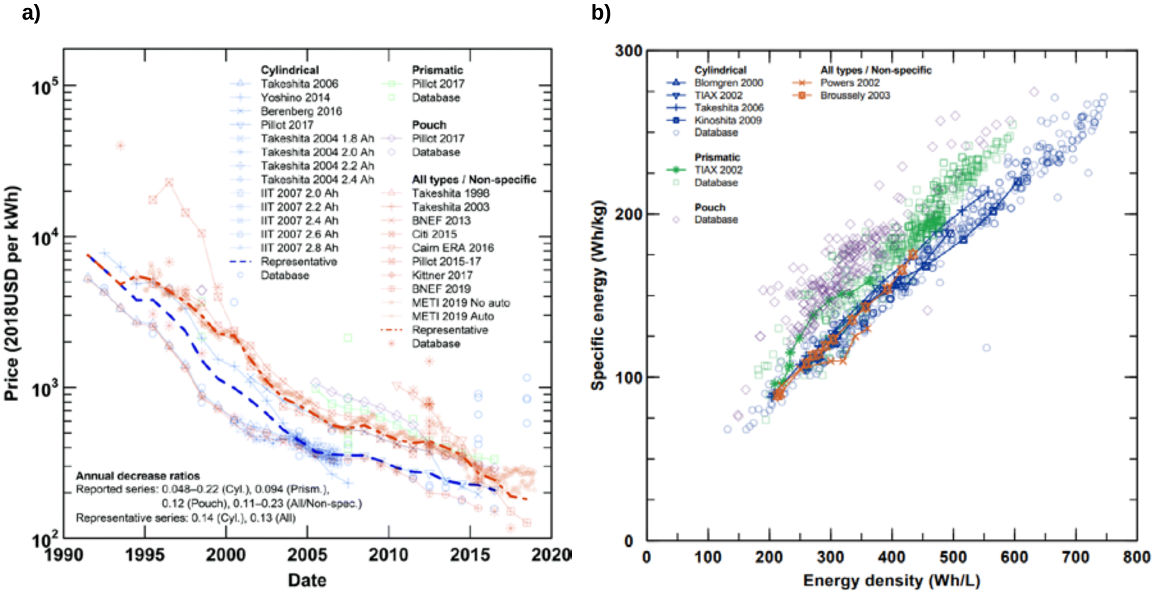

__Figure 2.4__ – a) Trend of the price per kWh of commercial lithium-ion batteries in the last thirty years, b) Gravimetric vs. Volumetric energy density of commercial lithium-ion batteries. Reproduced with permission from Ziegler and Trancik. CC BY-BC 3.0 2021, RSC Publishing[25]

2.2.1. Cathodes

Modern lithium-ion batteries are based on lithiated transition metal compounds as cathodes, in order to provide lithium to the anode during the first charge. In fact, lithiated cathodes are normally air-stable and can be safely handled in a <-50°C dew point dry room without harmful consequences for the stability of the battery [27] (except high-nickel layered oxides, which show particularly high moisture sensitivity[28]). Instead, lithiated anodes are extremely reactive towards air, even in a dry room environment, and they also react strongly with commonly used organic electrolytes when the cells are filled with it,[29] hence their discharged form is preferred during the manufacturing phase. After the first charge, the delithiated cathode and lithiated anode are formed in the closed, protected environment inside the cell case, hence protecting the reactive compounds from the contact with moisture and oxygen.

Layered metal oxides ($LiMO_2$) are one of the most successful classes of cathodes for lithium-ion batteries. They are characterized by a crystal structure with slightly distorted oxygen octahedrons, with a two-dimensional channel for the transportation of lithium that ensures good rate capability (**Figure 2.5.a**). The thermal and chemical stability is rather poor, due to the relatively loose bonding of the oxygen. The M transition metal is in high valence state at the end of the charge, when the material is delithiated, hence it can be easily reduced, releasing oxygen and heat. The first cathode material commercialized in lithium-ion batteries, $LiCoO_2$, belongs to this class.[30] Its success stemmed from his high average voltage (between 3.8 and 4.3 V vs. Li/Li+), long cycle life, good thermal stability, and easy manufacturing, but only 50-60% of its maximum capacity (270 $mAh \cdot g^{-1}$) is used to avoid irreversible structural changes.[21] Moreover, the toxicity and cost of cobalt have prompted the search for alternatives. In nickel-manganese-cobalt (NMC) family, both nickel and cobalt serve as redox centers, while manganese provides a stable scaffold and enhances the redox activity of nickel.[21] The cobalt content is much lower than $LiCoO_2$, while maintaining good capacity, stability, and average voltage. $LiNi_{0.5}Mn_{0.3}Co_{0.2}O_2$ (NMC 532), $LiNi_{0.6}Mn_{0.2}Co_{0.2}O_2$ (NMC 622), and $LiNi_{0.8}Mn_{0.1}Co_{0.1}O_2$ (NMC 811) are nowadays the most widely used high-voltage cathode materials.

Spinels (LiM_2O_4) possess a crystal structure where lithium and manganese occupy the tetrahedral and octahedral sites of the oxygen array, respectively, forming a three-dimensional conduction pathway for the lithium ions (**Figure 2.5.b**). The capacity is halved when compared to $LiMO_2$: while the latter exploit the $M^{3+/4+}$ (or even $M^{2+/4+}$, in case of nickel), spinels are based on the $M^{3.5+/4+}$ couple, since the $M^{3+/3.5+}$ redox process is situated at a potential too low to be effectively exploited and brings to unfavorable structural changes from the stability point of view. The only commercially available material belonging to this class is $LiMn_2O_4$, which found success thanks to his high average voltage (≈4 V vs Li/Li+), its high thermal stability, and its low cost due to the absence of expensive transition metals in the structure. The main problem of $LiMn_2O_4$ lies in the manganese dissolution because of the disproportionation of Mn^{+3}, which causes not only capacity fading of the cathode, but also poisoning of the anode following manganese deposition.[31] $LiMn_2O_4$ is often mixed with materials belonging to the NMC class to obtain cathodes with balanced properties.[32] $LiNi_{0.5}Mn_{1.5}O_2$, a material still in the research phase, possess also a spinel structure and, being a 5V-class material, attracted much interest as a cobalt-free sustainable material for lithium-ion batteries.[33,34]

Olivines ($LiMM'O_4$) contain divalent M and quintvalent M', with the latter forming a $M'O_4^{3-}$ polyanion, obtaining a distorted hexagonal oxygen arrangement and increasing the redox potential of the $M^{2+/3+}$ couple. Lithium and the transition metal (**Figure 2.5.c**). M occupy the octahedral sites, and M' the tetrahedral sites, forming one-dimensional conduction channels for the ions. $LiFePO_4$ (LFP) is the most prominent compound of this class: despite having moderate specific capacity (170 mAh mAh·g^{-1}) and voltage (3.4 V vs. Li/Li+), and a lower density than other metal oxides (3.45 g·cm^{-3} vs. >4.5 g·cm^{-3}), the low cost and excellent thermal stability enabled its effective and widespread adoption not only in grid storage batteries, but also in electric vehicles.[35,36]

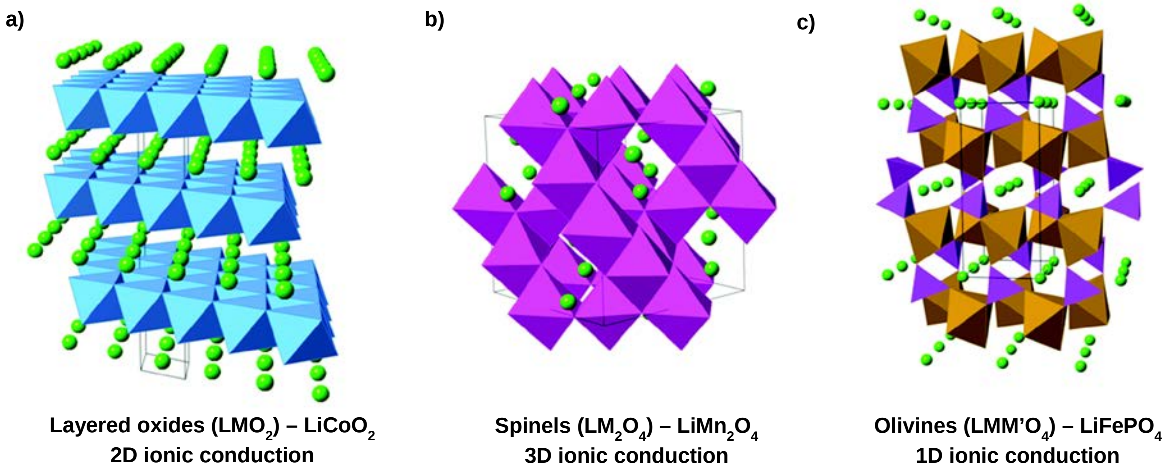

Figure 2.5 *– Examples of crystal structures of cathode materials for lithium-ion batteries: (a) Layered oxide: $LiCoO_2$, (b) Spinel: $LiMn_2O_4$, (c) Olivine: $LiFePO_4$. Lithium ions are represented as green spheres, CoO_6 octahedra in blue; MnO_6 octahedra in fuchsia, Fe–O polyhedra in ochre, PO_4 tetrahedra in violet. Reproduced with permission from Islam and Fisher, CC BY 3.0 2014, RSC Publishing*[37]

2.2.2. Anodes

Utilizing lithium metal as an anode material appears to be the most apparent choice due to the high gravimetric capacity (3860 mAh/g) and the lowest possible potential (-3.04 V vs. SHE, i.e., 0 V vs. Li/Li+). Despite the low density (0.534 g·cm^{-3}), it also maintains a significant volumetric capacity (3.22 mAh/cm^3).[38] However, the deposition of lithium on the surface of the lithium metal anode tends to occur in an irregular manner, with the continuous formation of an extensive solid electrolyte interphase (SEI) from the decomposition of the electrolyte, due to the high reactivity of the surface. This progressively reduces the availability of lithium in the cell, and the capacity of a cell with a lithium metal anode consequently decreases rapidly. Additionally, the deposited lithium forms needle-shaped structures called dendrites, which pose significant safety concerns due to the possibility of putting in contact anode and cathode, i.e., a short circuit.[39]

Carbon-based materials have emerged as the preferred choice for lithium-ion anode materials. In particular, graphite offers advantageous characteristics such as a decent theoretical gravimetric capacity (372 mAh·g^{-1}), low lithium insertion potential (0.05-0.8 V vs. Li/Li$^+$), and excellent reversibility of the intercalation reaction, leading to high efficiency of the battery.[40] Moreover, the volume expansion caused by the lithium insertion is small (≈10% along the c-axis), and graphite is a relatively cheap material, with both natural and artificial origins.[41]

The phenomenon of intercalation of lithium in graphite is extensively studied in lithium-ion batteries and results in a complex open-circuit voltage (OCV) curve due to a process known as staging.[40,42,43] Initially, lithium ions occupy interlayers that are widely separated due to repulsion effects before gradually occupying neighboring interlayers. This mechanism gives rise to distinct solid phases of Li-C, with substantial two-phase transition regions occurring in specific voltage regions (**Figure 2.6**).

Since graphite has relatively poor rate capability and specific capacity, there is a considerable drive to (partially) substitute this material with more energy and power dense ones. Anodes based on conversion or alloying reactions with lithium are currently in the research and development phase, since such reactions have the potential of achieving specific capacities >1000 mAh·g^{-1}.[44,45] The most prominent example of this class is silicon, with theoretical gravimetric and volumetric specific capacities of 4200 mAh·g^{-1} and 2386 mAh·cm^{-3} at a rather low redox potential of 0.4 V vs. Li/Li$^+$. However, the full lithiation of silicon causes a volume expansion up to 400%, and the capacity retention of silicon anodes is then rather poor, due to the constant cracking of the anode particles and the loss of electric contact.

To address this issue, various strategies such as nanostructuring and composite materials have been employed to mitigate the volume expansion effect.[21]

Since the problems with the pure material still have to be successfully addresses, currently the most popular strategy is to mix a small percentage of silicon (or silicon oxide, which also shows redox activity with lithium) with graphite, to enhance the latter's specific capacity without harming excessively the cyclability of the battery.[40]

Another type of commercial anode for lithium-ion batteries is lithium titanate ($Li_4Ti_5O_{12}$), which, due to its unique crystal structure and high working potential (1.55 V vs. Li/Li^+), exhibits excellent rate performance and cycling stability. While its lower capacity (175 $mAh \cdot g^{-1}$) compared to graphite or silicon severely limits its energy density, lithium titanate is suitable for applications that prioritize safety and durability over space or weight of the battery.[21,46]

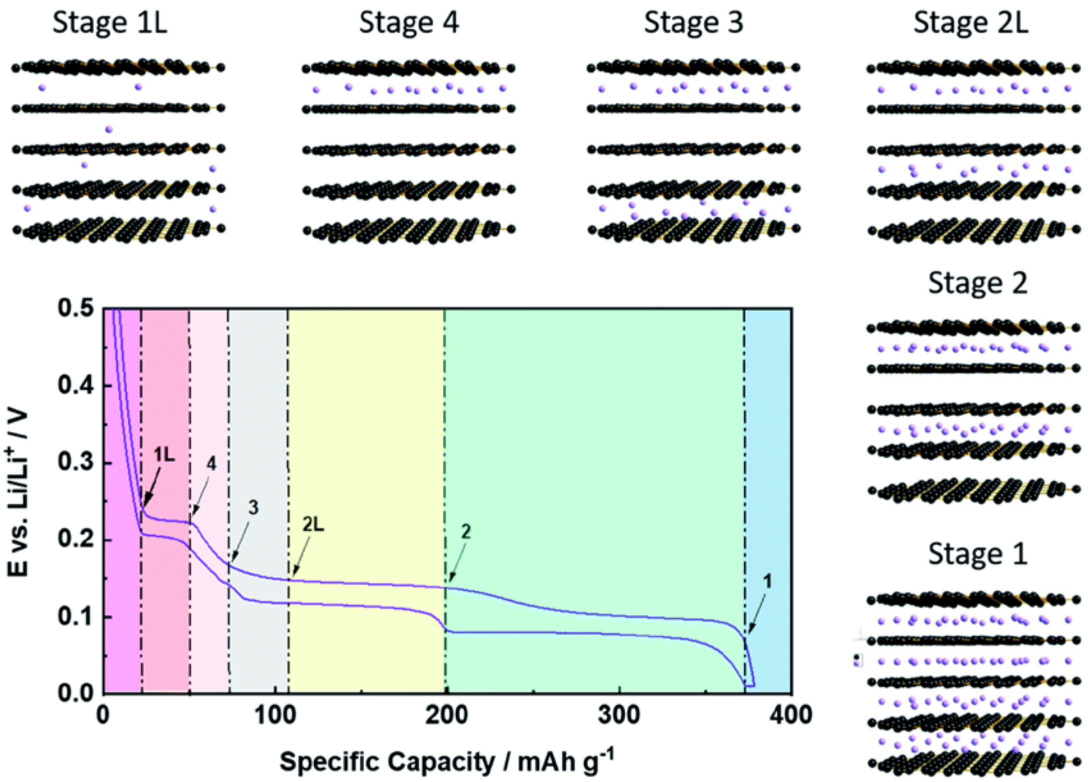

Figure 2.6 *– Depiction of lithium intercalation (staging) into graphite, with the related potential curves during charge and discharge of a graphite anode vs. lithium metal. Reproduced with permission from Asenbauer et al., CC BY 3.0 2020, RSC Publishing* [40]

2.2.3. Electrolytes and separators

Electrolytes play a crucial role in the operation of lithium-ion batteries by allowing the movement of lithium ions between the electrodes. To enable the flow of lithium ions, these electrolytes consist of a combination of non-aqueous organic solvents and a soluble salt based on lithium. The electrolyte should be characterized by a high ionic conductivity in the operative temperature range of the battery (>1 $mS\cdot cm^{-1}$), and it must exhibit chemical stability and inertness towards all components of the battery, including the electrodes, separator, and housing materials. Additionally, the electrolyte should possess a wide electrochemical stability window (ESW) that encompasses the potentials of both the anode and cathode, preventing electrolyte decomposition.[47]

State-of-the-art electrolytes consist of solutions containing around 1M lithium hexafluorophospate ($LiPF_6$) dissolved in organic carbonates like ethylene carbonate (EC) and dimethyl carbonate (DMC).[48,49] Polar organic carbonates such as EC are capable of dissolving substantial amounts of lithium salt, making them suitable solvents, while linear carbonates as DMC decrease the viscosity of the solution and ensure ionic conductivities >10 $mS\cdot cm^{-1}$ at room temperature. In practice, such electrolytes are thermodynamically unstable on graphitic anodes, since the lithium insertion potential is lower than the bottom limit of their ESW. However, the formed solid electrolyte interphase (SEI), product of the electrolyte decomposition on the surface of the graphite, kinetically hinders further decomposition and still ensures good lithium ionic conductivity and no electronic conductivity, hence enabling the use of these unstable molecules as electrolyte.[24]

With liquid electrolyte, a polymeric separator is sandwiched between the anode and cathode to prevent their direct contact and avoid short circuits. These membranes are usually very thin (< 20 µm) and with a high porosity (>35%) to ensure the flow of lithium ions without increasing excessively the battery resistance.[50,51] Polymers as polypropylene (PP) and polyethylene (PE) can be used as separator materials since they can be well wetted with the electrolyte solution, and thin ceramic coatings are then made on the surface to increase the mechanical stability, creating a multilayered structure.[52]

To enable lithium metal anodes and prevent the formation of dendrites on its surface, much efforts are being devoted to the development of ionically conductive and stable solid-state electrolytes which can act as a mechanical barrier to the dendrites and ensure the homogeneous deposition and stripping of lithium on the anode surface.[53] Such solid-state electrolytes can be made of polymers, ceramics, sulfides, halides, or a composite material that combines two or more of these classes.[54,55]

2.2.4. Alternatives to lithium-ion batteries

Forecasts regarding the capacity requirements of lithium-ion batteries for achieving full electrification in the transportation sector and supporting solar and wind power plants indicate a demand in the tens of terawatt-hours (TWh) over the next three decades [7,13,14]. The increasing strain on battery supply chains resulting from this growing demand has become apparent, as evidenced by the consistent price hikes observed in numerous raw materials over the past two years (**Figure 2.7**)[56]. Consequently, significant efforts are now being devoted to exploring alternative or complementary solutions to lithium-ion batteries. These solutions aim to utilize raw materials that are more affordable and evenly distributed, while still delivering comparable performance levels [20,57].

Among the various proposals being put forth, sodium-ion batteries [58,59], lithium-sulfur batteries[60,61], multivalent cation batteries[62,63], dual-ion batteries[64], halogen batteries[65], and organic batteries[66–68] have emerged for instance as potential alternatives. Each class of materials has its own advantages and disadvantages, but sodium-ion batteries are presently the only new chemistry near the commercialization stage, with both startups and established companies producing practical cells on the Ah scale[69,70].

In the quest for finding viable solutions, and with the plethora of new materials proposed as cathodes and anodes, exaggerated claims about electrochemical performances and projected costs all too often occur[71–74]. This leads frequently to baseless assertions and sensational headlines, in a moment when battery energy storage is in the spotlight thanks to the exponential growth of its market. If reiterated, this situation has the potential to undermine the credibility not only of the research area but also of the entire industry.

The implementation of cost and performance analysis in research works could be hence a way to put in the right perspective the results obtained in a laboratory setting. But to obtain sound outcomes, such an analysis requires usually a comprehensive understanding of battery manufacturing processes: setting a cell format (pouch, cylindrical, prismatic) and designing accordingly the full battery pack, considering the electrical cables and the thermal management system, modeling the investment and operating cost of a production plant, etc. Nowadays, peer-reviewed, open-source tools that enable this level of analysis such as BatPac and CellEst are available, allowing a very detailed simulation of the price and size commercial-scale battery packs starting from the definition of the electrochemical and physical properties of the cathode and anode materials[75,76]. Such software can empower every researcher in the field to model the potential performance of their newly synthesized materials in an upscaled system using the experimental data as input and to compare it with already commercial chemistries or with other innovative solutions.

In this dissertation, the focus will be on organic batteries as potential alternatives to lithium-ion batteries. Organic batteries are a 2-4 TRL technology, without proven upscaled cells. To introduce the methodology based on the cost and performance analysis, we will also use sodium-ion batteries, a much more developed post-lithium-ion technology (TRL 6-8), as subject of case studies of the application of cost and energy density analysis both in a high- and a low-level approach.[36]

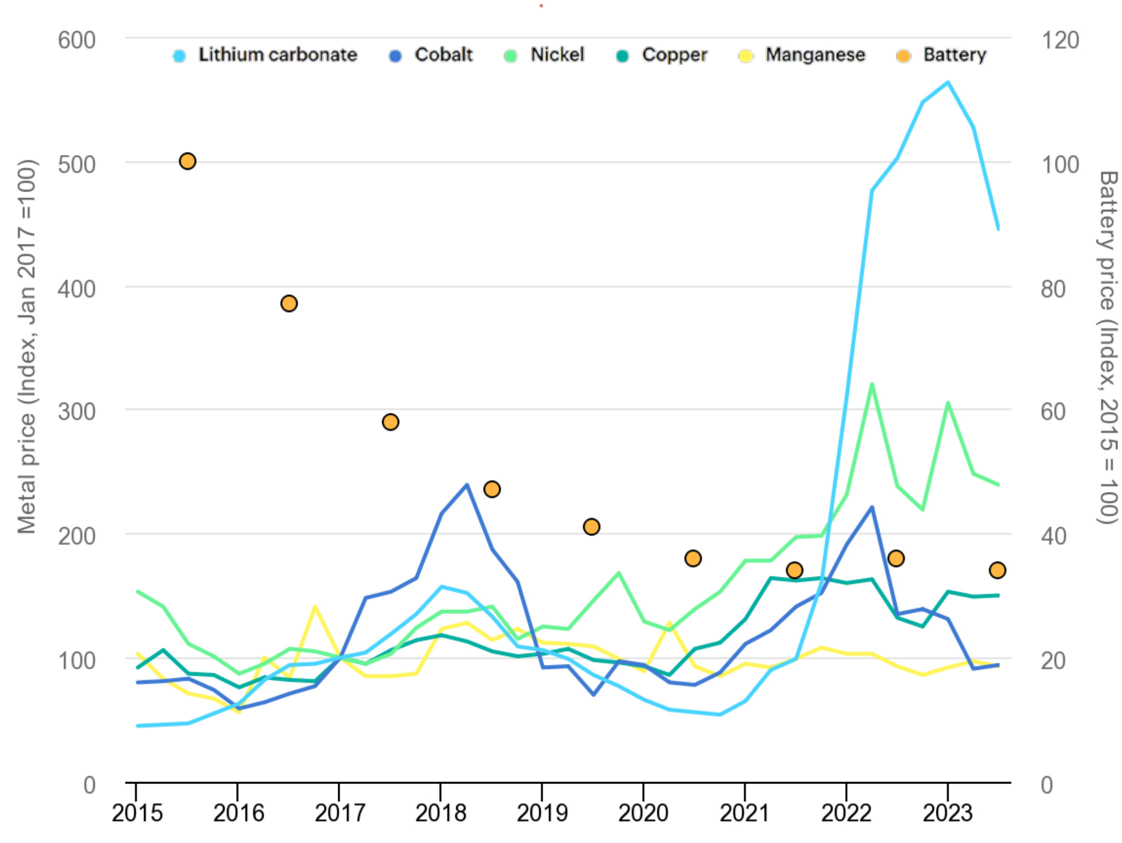

Figure 2.7 *– Price of selected battery raw materials and lithium-ion batteries, 2015-2023. Reproduced with permission, CC BY 4.0, 2023 IEA*[11]

2.3. Sodium-ion batteries

This section is partially reproduced from the article "*Layered Oxide Cathodes for Sodium-Ion Batteries: Storage Mechanism, Electrochemistry, and Techno-economics*" (see **Section 6.1**).

Among all the proposed post-lithium-ion concepts, sodium-ion batteries (SIBs) have the great advantage of being essentially a "drop-in" technology.[20,58,77,78] SIBs and LIBs share the same architecture, similar working mechanisms and components, and identical cell fabrication steps, which implies that SIBs maintain the core of the roll-to-roll system optimized for LIB manufacturing during the last 30 years. The primary advantage of SIBs is the abundance and lower cost of sodium compared to lithium. Sodium and the main transition metals for SIB cathodes are more readily available in the earth's crust, making them a cost-effective alternative.[56] However, the lower specific capacities and average voltages than the commercial lithium-based solution would result in energy densities of maximum 150 $\text{Wh}\cdot\text{kg}^{-1}$ at the cell level, similar to what is achievable with low-end LFP batteries.[78]

After a decade of development, SIBs are at a critical moment of commercialization. Several companies such as HiNa and CATL in China, Faradion in the United Kingdom, Tiamat in France, and NATRON ENERGY in the USA, are close to achieving the commercialization of SIBs, with the aim of employing sodium layered transition metal oxides, Prussian blue analogues, or vanadium-based polyanion compounds as cathode materials.[69,70,79–81] Similarly to lithium-ion batteries, carbonate-based solvents with $NaFP_6$ and $NaClO_4$ as Na salts are the most widely used liquid electrolytes for SIBs.[82,83]

Sodium ions are not able to reversibly de-/intercalate in graphite, as lithium ions do, since the formation energy of the NaC_6 compound is positive.[84] Some degree of intercalation is possible with ether-based electrolytes, but rather limited specific capacities are then achieved.[85] Instead, hard carbons, i.e., non-graphitizable carbons, are the materials of choice for SIB anodes. They are characterized by a highly micro-/nanoporous structure with randomly oriented graphitic domains with a larger interlayer distance than graphite. Such a disordered structure is able to accommodate well sodium-ions, and capacities between 250 and 400 $\text{mAh}\cdot\text{g}^{-1}$ are reported, with an average of about 300 $\text{mAh}\cdot\text{g}^{-1}$.[59] The voltage profile is characterized by a sloping region (between 0.1 and 1.5 V vs Na/Na^+) and a plateau region (below 0.1 V vs Na/Na^+). Hard carbons, due to the porous structure, are less dense than graphite ($<1.6\ \text{g}\cdot\text{cm}^{-3}$ vs. 2.26 $\text{g}\cdot\text{cm}^{-}$3), which is disadvantageous for the energy density of the batteries. Moreover, hard carbons have lower ICE than graphite due to the higher surface area that leads to increased SEI formation, decreasing the quantity of available sodium in a full cell if compared to the lithium counterpart.[86,87]

2.4. Organic batteries

This section is partially reproduced from the articles "*Assessing N-Type Organic Materials for Lithium Batteries: A Techno-Economic Review*" and "*Practical cell design for PTMA-based organic batteries: an experimental and modeling study*" (see **Sections 6.2** and **6.4**).

Due to the ubiquitous presence of organic elements (i.e., carbon, oxygen, hydrogen, nitrogen), research interest in organic materials for batteries has peaked over the past 20 years, being regarded as potentially more widely available, affordable, and sustainable than the commercial LIB materials.[66–68,88,89]

Conjugated conductive polymers were already intensively studied in the 80s' as cathodes for lithium metal batteries, an effort that culminated in a commercialization attempt of batteries with poly(aniline) and poly(pyrrole) as active materials.[90,91] Nevertheless, the overall superior performance of their inorganic counterparts made this tentative effort short-lived, and now metal-based cathodes with graphite as anode remain the state-of-the art.[88]

Since the early 2000s, interest in organic electrode materials has reemerged,[92–94] and in laboratory settings, various monomers and polymers capable of redox reactions have been synthesized and studied. Materials that react with cations are labelled as n-type, while those that react with anions are referred to as p-type (**Figure 2.8**). Some bipolar compounds show redox activity with both cations and anions, although at very different potentials.[95] N-type materials generally have lower average voltage, slower kinetics, and higher specific capacity compared to p-type materials, and their redox mechanism is analogue to the one of commercial lithium-ion anodes and cathodes. Instead, in p-type materials, the electrochemical reaction generally occurs at a relatively high potential (3.5-4.5 V) due to their interaction with anions, which makes them suitable for coupling with alkali metal anodes or carbonaceous anode materials with low intercalation potential, resulting in high-voltage cells.[96] Such batteries operate in a dual-ion configuration, where the anode and cathode interact with cations and anions, respectively.[64] As a result, batteries based on p-type materials differ from typical lithium-ion batteries because the electrolyte plays a crucial role as a source of anions in the redox reaction.[97]

The main advantages of organic materials can be found in their high tailorability and versatility, due to the richness of organic chemistry, and in their potential low cost and high sustainability, since they could be obtained by bio-derived sources and be biodegradable. As drawbacks, organic materials usually present very poor electronic conductivity, requiring high amounts of conductive carbon (>30% in weight) to be added in the electrode formulation. and a strong tendency to dissolve in the electrolytes commonly used for batteries, causing severe capacity fading during cycling. Moreover, their low density, when compared to inorganic materials, limits the energy density achievable with organic batteries.[98]

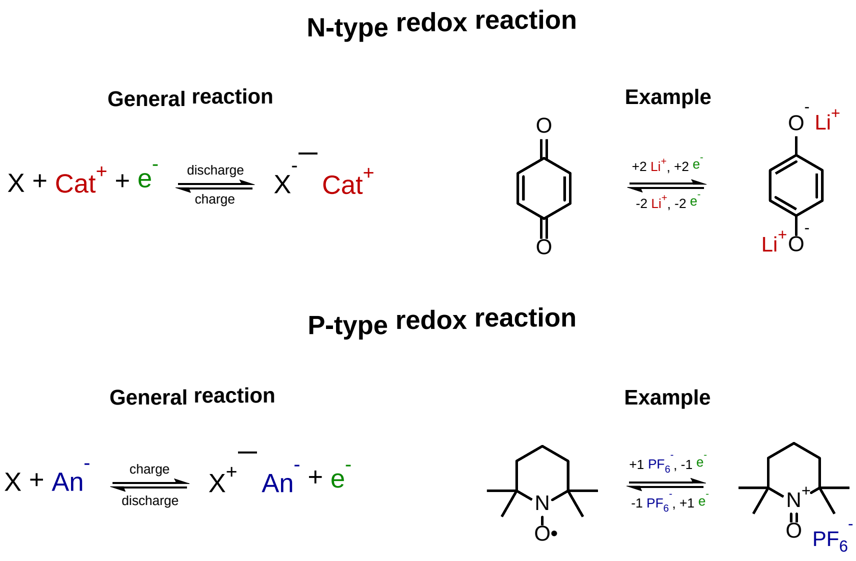

Figure 2.8 – General electrochemical reactions for n-type (top left) and p-type (bottom left) organic materials and relative examples of reactions with 1,4-benzoquinone and (2,2,6,6-tetramethylpiperidin-1-yl)oxyl (TEMPO).

2.4.1. N-type materials

The majority of the n-type materials investigated in literature involve the reversible reduction of the oxygen atom in a carbonyl group,[99–101] but a rich chemistry of nitrogen-containing molecules is also present, involving azo, imine, sulfonamide, and nitrile redox centers.[102–104] Materials belonging to the organosulfide class are mainly characterized by the reversible breaking and reformation of a disulfide bond, the same type of reaction present in lithium-sulfur batteries;[105,106] notably, a few examples exploiting thiocarbonyl groups are also present.[107,108] Some p-type materials can also undergo n-type reactions (hence correctly classified as bipolar materials), such as molecules and polymers based on the (2,2,6,6-tetramethylpiperidin-1-yl)oxyl (TEMPO) moiety or other conjugated polymers.[109–111]

N-type materials can be reversibly reduced from their neutral state to a negatively charged molecule, which then interacts with a lithium cation to store energy. In lithium-deficient cathodes, the materials are synthesized in this neutral form, and they must extract the necessary lithium from the anode; the first cycle of the corresponding battery starts with a discharge. Even though some materials described in this Section may contain lithium, the content is not sufficient to exploit the full capacity of the organic cathode and its complete removal may hinder the capacity retention of the battery.[112]

Small molecules have garnered attention as n-type cathodes, being materials that can potentially combine several redox centers with a low molecular weight. In a comprehensive study by Liang et al., it was shown how a variety of such molecules can easily achieve more than 250 $mAh\cdot g^{-1}$ as specific capacity, with a redox potential between 2.0 and 3.0 V vs. Li/Li^+ (**Figure 2.9.a**).[113] Among the materials investigated in the aforementioned work, anthraquinone (AQ) is distinct as it is an economical chemical used in the paper and dye industry with a good theoretical specific capacity (257 $mAh\cdot g^{-1}$),[114,115] and it has become the foundation for a range of small molecules and polymers used as organic electrode materials. Pyrene-4,5,9,10-tetraone (PTO) also attracted much interest due to a remarkably high theoretical specific capacity (409 $mAh\cdot g^{-1}$), owing to its four-electron redox mechanism with the four active carbonyl groups (**Figure 2.9.a**).[116]

However, such ketone-based materials are prone to dissolution in the conventional organic electrolytes employed in lithium batteries, i.e., mixtures of ethylene carbonate and carbonate esters with 1M salts such as lithium hexafluorophosphate, limiting the useful life of the battery to few cycles.[117] Another promising n-type material such as dilithium rhodizonate (DLR) displays a theoretical specific capacity of 589 $mAh\cdot g^{-1}$ with the lithiation of the four available ketone groups,[118] but its cyclability is extremely limited in the extended voltage range that transitions the material from $Li_2C_6O_6$ to $Li_6C_6O_6$. Interestingly, when cycled in a smaller voltage window, between $Li_4C_6O_6$ and $Li_6C_6O_6$, the cyclability improved, at the expense of the energy density.[93] Proposed reasons are the suppression of the delamination of the material by avoiding a deep charging of the cathode and the presence of intermolecular Li-O interactions that hinders the dissolution in the electrolyte.[119] In general, the presence of a high degree of intermolecular forces through hydrogen bonds and interactions with lithium ions have been found to be beneficial for the cycling stability of ketone-based molecules.[120,121] An example of the implementation of this strategy is demonstrated in the recent work of Li et al., where 2,3,7,8-tetraaminophenazine-1,4,6,9-tetraone (TAPT) was synthesized and tested in a battery.[122] This molecule, derived from the condensation of two tetraaminobenzoquinones, shows a six-electron redox mechanism where both the ketone oxygens and the phenazine and amine nitrogens are involved, and in the 3.5-1.5 V vs Li/Li^+ voltage range, reaches a capacity of ~300 $mAh\cdot g^{-1}$ with good cycling stability (**Figure 2.9.b**).

Increasing the molecular weight of the monomer together with the number of redox-active sites has been regarded as an effective strategy to suppress the molecules dissolution, since larger molecules are in principle, harder to solvate. This idea has led to the investigation of macrocyclic molecules such as calix[4]quinone (C4Q) and pillar[5]quinone (P5Q), derivations of calixarenes, a host-guest chemistry molecules class.[123] C4Q and P5Q, formed by several benzoquinones bounded by methylene groups, possess respectively 8 and 10 ketone oxygens, resulting in a specific capacity for both molecules of 446 mAh·g^{-1}. Nevertheless, their cyclability in organic electrolytes is still poor, and relatively stable cycling of these molecules has been achieved only in quasi-solid-state batteries or with ionic liquids (**Figure 2.9.c**).[124–127] Instead, a successful approach with the same principle of increasing the mass of the molecule was proposed by Luo et al., where 2,3,5,6-tetraphthalimido-1,4-benzoquinone (TPB) presents four rigid phthalimide groups around a benzoquinone center.[128] The increase of molecular weight is related to the aromatic functionality with the possibility of stacking, which has been shown to enhance the cyclability.[129] Each phthalimide group carries two carbonyl oxygens, for a total of 10 redox active sites, including the ones on the benzoquinone. This material, characterized by an initial specific capacity of 225 mAh·g^{-1} and two plateaus at 3.1 and 2.1 V vs. Li/Li^{+}, was able to cycle for 100 cycles at 0.2 C.

Molecules belonging to the anhydride and imide classes are also characterized by four carbonyl groups as PTO, but only two of these are redox-active due to the unfavourable electronic configuration of the completely reduced structure.[113] Materials such as the organic dye perylenetetracarboxylic dianhydride (PTCDA) or the supramolecular chemistry compound 1,4,5,8-naphthalenediimide (NDI) show respectively 137 mAh·g^{-1} at 2.4 V vs. Li/Li^{+} and 202 mAh·g^{-1} at 2.3 V vs. Li/Li^{+} as theoretical capacity values.[130,131] Nevertheless, such molecules have generally higher stability in conventional organic electrolytes compared to ketone-based ones, due to the extended aromatic structure that provides strong intermolecular π–π stacking forces and the stabilization of intermediate radical species formed during the redox reaction (**Figure 2.9.d**).[131] For instance, the stable crystal structure of PTCDA allows a high degree of reversibility of the de/intercalation of lithium and other monovalent and divalent metal cations.[132,133]

Other organic dyes have been proposed as energy storage materials, owing to their natural occurrence and/or high availability as widely used chemicals.[134–138] Among these, indigo carmine (IC) has received the most attention, being already employed as food colorant, pH indicator, and diagnostic dye. In a work from Deunf et al., where the design of indigo carmine electrodes was optimized, this material managed to achieve more than 100 mAh·g^{-1} between 3.0 and 1.5 V vs Li/Li^{+} with only 10% of conductive carbon, with a remarkably stable cycling even at low current rate influenced by the polar sulfonate groups that hindered the dissolution in the electrolyte.[139]

In addition to the reliance on intermolecular forces and molecule size to improve the capacity retention of n-type batteries, the polymerization of small organic molecules into macromolecules has also been extensively studied.[140] Well-designed polymers can suppress the loss of capacity due to the solvation of the electrode molecules, and achieving a high molecular weight[141–143] and employing crosslinking agents[144–147] are regarded as effective strategies in this direction.

Ketones that are unstable as molecules in lithium batteries managed to achieve good cycling stability when polymerized, at the cost of some specific capacity and a slightly lower redox potential. Polybenzoquinonyl sulphide (PBQS)[141,148–150] and polyanthraquinonyl sulphide (PAQS)[151–153], i.e., linear polymers of benzoquinone and anthraquinone, respectively, with sulfur-based linkages, are two n-type polymers which are representative examples of this method. PAQS showed a practical specific capacity of 199 $mAh\cdot g^{-1}$ at 2.2 V vs. Li/Li^+, with a sloping voltage profile, while an example of AQ-based battery achieved 250 $mAh\cdot g^{-1}$ with a potential plateau at 2.26 V vs. Li/Li^+. Nevertheless, this decrease in energy density of the polymeric cathode when compared to the molecule-based one comes with an increase of the useful cycle life, which improves from few cycles to more than 100.[148] Whereas, PBQS achieved a specific capacity of 274 $mAh\cdot g^{-1}$ at an average potential of 2.7 V vs. Li/Li^+, with hundreds of stable cycles. Benzoquinone was able to cycle with 430 $mAh\cdot g^{-1}$ at ~2.8 V vs. Li/Li^+ in the first cycle, although the performances quickly decayed due to the dissolution of the small molecule in the electrolyte.[152]

The same polymerization approach was also extensively applied to imide molecule, and polyimides represent a widely studied class of n-type organic cathode materials.[154] A representative example belonging to this class is poly(3,4,9,10-perylenetetracarboxylic dianhydride ethylene diamine) (PDI), deriving from the condensation reaction of PTCDA with ethylenediamine.[155] This material exhibited a remarkably higher stability than PTCDA in the same electrolyte, with 127 $mAh\cdot g^{-1}$ in a two-step reaction with two plateaus at 2.75 V and 2.25 V vs. Li/Li^+, in contrast to the PTCDA that displays a single plateau at 2.45 V vs. Li/Li^+ during charge and discharge.

The main focus of a recent work by Li et al. on n-type redox polymers was the cost of the final active material.[156] The expensiveness of the molecules, of the eventual catalysts, and the final yield of the synthesis reaction is rarely the focus of research works in this field, as demonstrated by Li et al. Poly(piperazine-altbenzoquinone) (PPA), a product of the condensation reaction between vanillin and piperazine (**Figure 2.9.e**) resulted in a ketone-based lithium-deficient active material with a theoretical production cost of 0.48 $\$\cdot g^{-1}$, which would correspond to 480 $\$\cdot kg^{-1}$, and a practical specific capacity of 232 mAh·g^{-1}. The cost was reported as one of the lowest among the organic materials present in the literature.

Sulfur-based polymers, exploiting a type of redox reaction analogous to the one of lithium-sulfur batteries, were also designed to achieve very high specific capacity with organic materials and contemporarily alleviate some typical issues that plague pure sulfur cathodes, such as polysulfide shuttling and poor reversibility.[105] Sulfurized polyacrylonitrile (SPAN) was recently employed by Liu et al. with an ionic liquid-based electrolyte and lithium metal as anode, obtaining 580 mAh·g^{-1} at an average voltage of 1.8 V vs. Li/Li$^+$, with stable cycling for more than 200 cycles with both thick and thin lithium metal anode foils (**Figure 2.9.f**).[157]

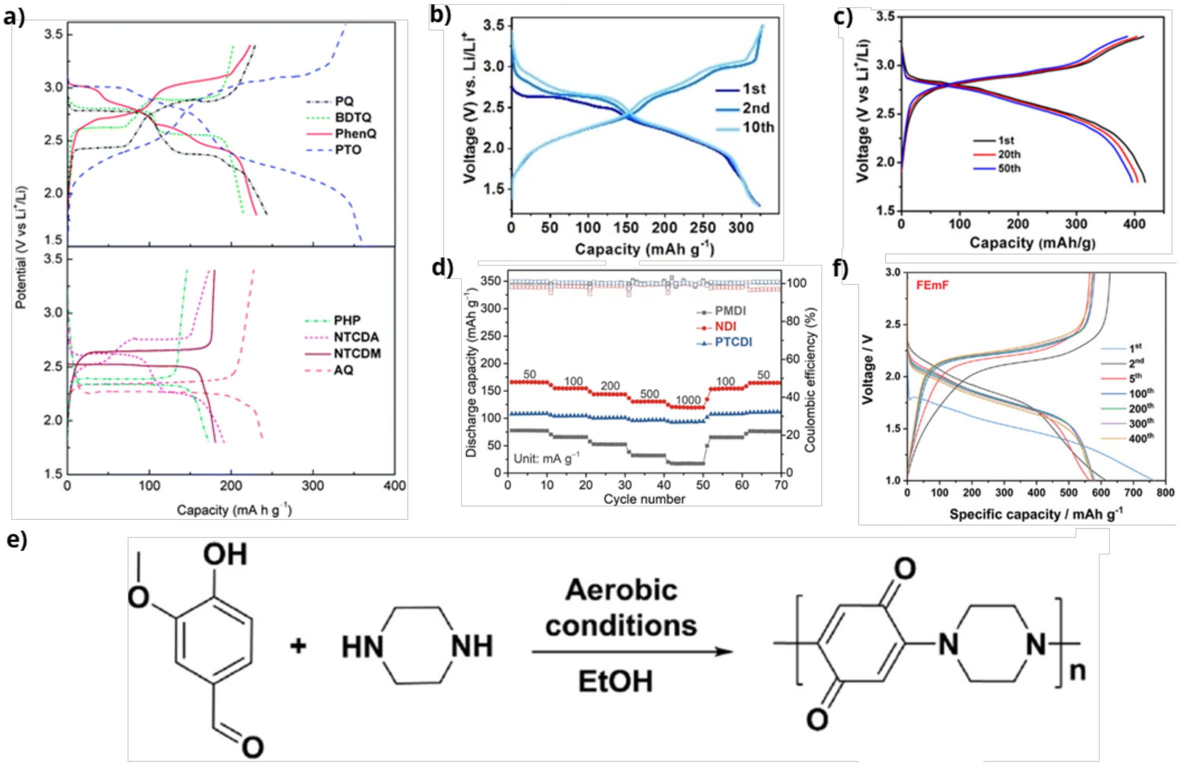

Figure 2.9 – a) Voltage/specific capacity curves of several n-type small molecule organic cathodes, among which AQ and PTO [113]*, b) Voltage/specific capacity curve of the 1st, 2nd and 10th cycle of a TAPT/Li metal cell in 1M LiTFSI in DOL/DME* [122]*, c) Voltage/specific capacity curve of the 1st, 20th and 50th cycle of a P5Q/Li metal cell in a poly(methacrylate)/poly(ethylene glycol)-based gel polymer electrolyte* [125]*, d) Specific capacity vs. cycle number for three small imide molecules as cathodes for lithium metal batteries, including NDI* [131]*, e) Reaction scheme for the synthesis of PPA from vanillin and piperazine* [156]*, f) Voltage/specific capacity curve of a SPAN/Li metal cell in an ionic liquid-based electrolyte. All the images are reproduced from permission from the respective publishers.*

In contrast with the lithium-deficient materials presented above, lithium-sufficient n-type cathodes contain enough lithium to fully lithiate the anode in a full-cell configuration, similar to commercial lithium-ion batteries. A major challenge to the development of lithium-sufficient materials is their stability towards the oxygen present in the atmosphere.[158] The air stability threshold is ~2.9 V vs. Li/Li^+, depending on the water content in the atmosphere, but many lithium-containing materials studied in the literature tend to have redox potentials below this threshold, due to the presence of numerous electron-donating OLi groups.[159–163] The air-instability has the effect of strongly decreasing the lithium content upon oxygen exposure, decomposing the OLi groups to OH groups, hence hindering the effective use of the cathode material in a battery. Moreover, the lithiation of lithium-containing n-type materials, transpiring in liquid media through the exchanging of H by Li, requires degassed and anhydrous solvents like tetrahydrofuran or dimethylformamide, and prohibitively expensive lithium salts such as lithium hydride or methoxide in case of air-unstable cathodes.[164] Instead, the lithiation reaction can efficiently proceed in aqueous media and with lithium carbonate or hydroxide for air-stable materials, hence enabling a cost-effective and scalable synthesis. Due to the impractical production, handling, and storage conditions required for air-unstable lithium-sufficient materials, only the air-stable materials are discussed in this section.

Air-stable lithium-containing n-type cathodes have been the major focus of several works of Vlad et al. where a high redox potential is achieved in small organic molecules and coordination polymers with the use of electron-withdrawing sulphonamide groups and exploiting nitrogen as redox center.[164–168] Two relevant materials belonging to this class are tetralithium benzene-1,2,4,5-tetra-methylsulfonamide (Li_4-PTtSA) and dilithium 2,5-dichloro-1,4-phenylene-bis-methylsulfonylamide (Li_2-DC-PDSA).[164] Both materials present a flat voltage plateau upon discharge, respectively at 2.7 V vs. Li/Li^+ and 3.3 V vs. Li/Li^+, and the specific capacity reaches 111 $mAh\cdot g^{-1}$ for Li_4-PTtSA and 155 $mAh\cdot g^{-1}$ for Li_2-DC-PDSA (**Figure 2.10.a**, **Figure 2.10.b**, and **Figure 2.10.c**). As evidenced in **Figure 2.10.c**, the voltage profile of Li_2-DC-PDSA resembles the one of LFP, both in terms of capacity and potential. Nevertheless, the resistance towards dissolution of these molecules in conventional organic electrolytes is low, and stable cycling was achieved with only 5M LiTFSI in DOL/DME.

Another class of molecules studied by the same group are oximates, where the electron-withdrawing $N\text{-}O^-$ group is exploited as redox center increasing the redox potential, allowing the air-stability of the lithiated oximate molecules.[169,170] An example is represented by dilithium benzoquinone dioximate (Li_2-BQDO), a small molecule resembling lithiated benzoquinone where the ketone oxygens have been substituted with oximate groups.[169] This material managed to achieve 335 mAh·g^{-1}, and the cycling stability was remarkable for such a low molecular weight compound, supposedly due to the reversible formation of a polymerized form of the material upon charge (**Figure 2.10.d**).

Deng et al. found that the tetracyanoquinodimethane anion can also form an air-stable lithiated compound, i.e., lithium tetracyanoquinodimethane (Li-TCQM).[171] This compound, containing a single lithium cation in the discharged form, was able to obtain 126 mAh·g^{-1} with a voltage plateau at 3.15 V vs. Li/Li$^+$ during discharge (**Figure 2.10.e** and **Figure 2.10.f**). A good capacity retention was reached with the coating of the Celgard separator with a 5:5 weight ratio mixture of Nafion and Super P, which according to the authors hindered the dissolution of the Li-TCQM.

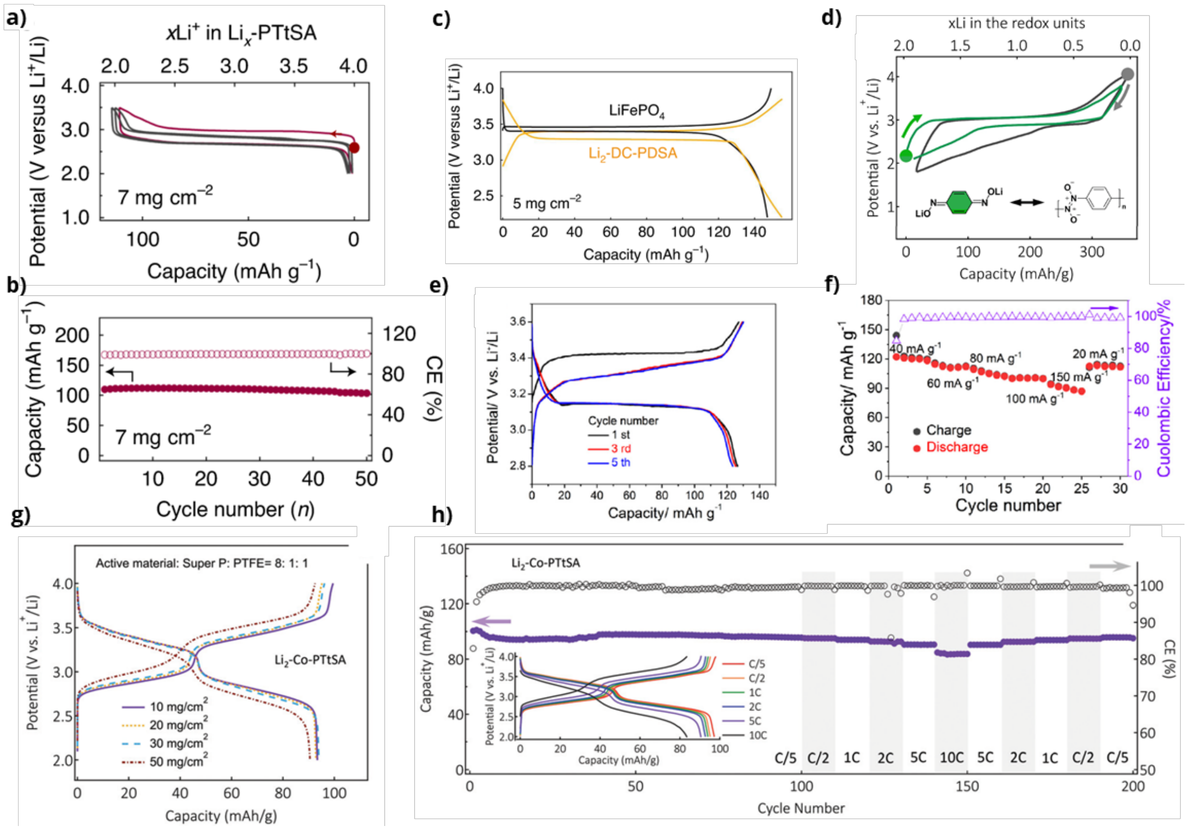

Figure 2.10 – *a) Voltage/specific capacity curve for the first cycles of Li$_4$-PTtSA and b) the related specific capacity vs. cycle number chart* [164], *c) Comparison between the voltage and specific capacity of LFP and Li$_2$-DC-PDSA* [164], *d) First two cycles of Li$_2$-BQDO, with a depiction of the charged and discharged forms of the molecule* [169], *e) Voltage/specific capacity curve for the first cycles of Li-TCQM and f) the related specific capacity vs. cycle number chart at different current rates* [171], *g) Voltage/specific capacity curve at different active material mass loadings of Li$_2$-Co-PTtSA and h) the related specific capacity vs. cycle number chart at different current rates* [166] *All the images are reproduced from permission from the respective publishers.*

So far, the only example of air-stable lithium-containing n-type redox polymer is represented by a class of coordination polymers studied by the Vlad group, which combine the structure of the Li_4-PTtSA molecule with divalent transition metal coordination centers, obtaining materials which are both electronically conductive and more stable towards dissolution.[166] Dilithium cobalt benzene-1,2,4,5-tetra-methylsulfonamide (Li_2-Co-PTtSA) is a representative of this group of organic cathodes, with which 93 $mAh \cdot g^{-1}$ and a voltage between 3.5 and 2.7 V vs. Li/Li^+ are achieved (**Figure 2.10.g**). This material was able to cycle for almost 1000 cycles at 5C, and at least 200 cycles at lower rates in a common LP30 (1M $LiPF_6$ in EC:DMC 1:1) electrolyte, owing to the stability afforded by the polymeric structure, and full cells with graphite as anode reached 80% of the initial discharge capacity after around 200 cycles (**Figure 2.10.h**).

Looking instead at the field of n-type organic anode materials, we can see how it has received ever-increasing attention in the last years, thanks to the plethora of possible redox-active compounds at low potential versus lithium offered by organic chemistry.[172,173] After the landmark paper of Armand et al. in 2009 on the redox activity of lithiated terephthalic acid, many researchers became interested in organic anodes, leading to a surge in research on the topic.[94] Nevertheless, some pitfalls in evaluating organic anode materials make it difficult to determine whether their performance are sufficient for practical applications.

In the majority of works in this area, the proposed materials are cycled down to almost 0 V vs. Li/Li^+, far below the potential at which the redox reaction between lithium and the redox active groups in the molecule or polymer would occur. The great amount of conductive carbon additive when preparing electrodes for the electrochemical tests of organic anodes (usually between 20% and 60%) can then contribute to the specific capacity. For instance, Liang et al. measured the specific capacity of Super P electrodes as blank electrode measurements, and the conductive additive can reversibly cycle between 200 and 300 $mAh \cdot g^{-1}$ in the 0.01-3 V voltage window, depending on the current rate (**Figure 2.11.a**).[174] Other conductive additives commonly employed, such as graphene or carbon nanotubes, usually display even higher capacities in the same voltage range.[175,176] Since blank electrode measurements are seldom reported in literature, it becomes difficult to evaluate the true specific capacity that can be assigned only to the organic molecule, especially if that molecule tends to dissolve in the electrolyte.

Moreover, at such low potentials, organic anodes tend to show a “superlithiation” behaviour, i.e., the bonding of lithium with almost all the carbon atoms present in the molecule.[177–179] This extreme lithiation state provides a very high specific capacity, but the reversibility is poor after the first cycle, requiring high overpotentials for the delithiation of the anode. With this phenomenon, impressive specific capacities can be reported (>1000 mAh·g^{-1}) but the organic anode has to provide capacity at voltages up to 3 V with a sloping profile, making the final voltage of a hypothetical full cell too low to be of practical utility (**Figure 2.11.b**).[180–182]

For this reason, in the analysis presented in **Section 6.2** we included only two anode materials belonging to this class, whose electrochemical performances can be safely attributed to the electrochemical reaction of the organic molecule. The first one is 3,4,9,10-perylene-tetracarboxylic-dianhydride ($PTCLi_4$), which was proposed for the first time as anode material for lithium batteries by Iordache et al.,[183] demonstrating great stability upon cycling, and viable batteries with only 0.5% of multiwalled carbon nanotubes as conductive additive were assembled. In the same work, $PTCLi_4$ managed to achieve 108 mAh·g^{-1}, a relatively low value due to the high molecular mass, with a flat potential at ~1.20 V vs. Li/Li$^+$ during charging (**Figure 2.11.c** and **2.11.d**). The second one is dilithium terephthalate (LiTPT), the lithium salt of terephthalic acid, introduced by Armand et al. as the first "modern" organic anode.[94] The molecule shows an initial specific capacity of 276 mAh·g^{-1}, higher than $PTCLi_4$ due to a lower molar mass, and a voltage plateau with an average value of 0.96 V (**Figure 2.11.e** and **2.11.f**). LiTPT is less stable than $PTCLi_4$, however, it has the advantage of being synthesized from the widely available terephthalic acid, the building block of polyethylene terephthalate (PET).

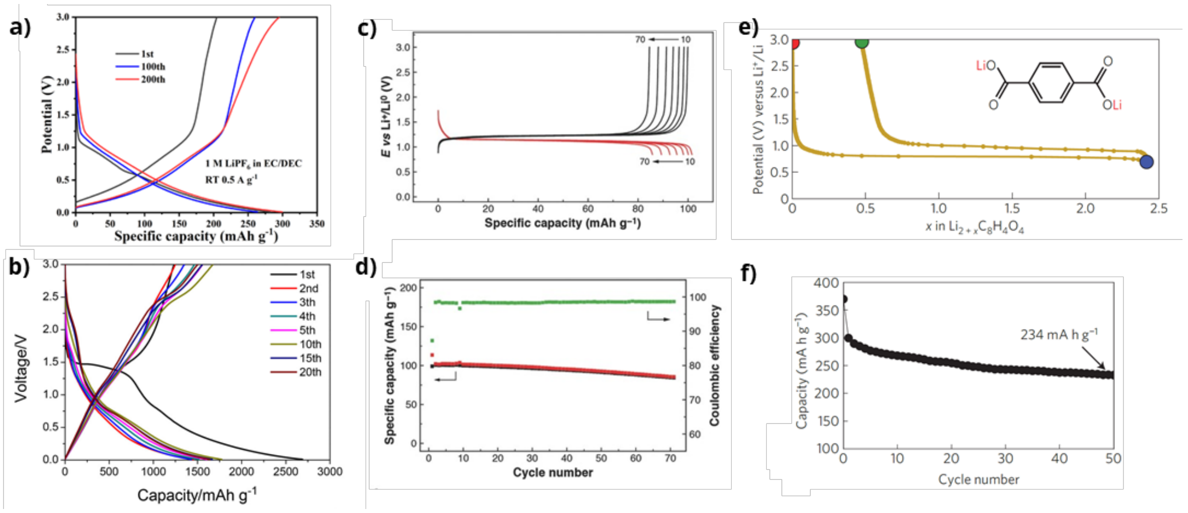

Figure 2.11 – *a) Voltage/specific capacity curve of a Super P blank electrode in 1M $LiPF_6$ in EC/DEC*[174]*, b) Voltage/specific capacity curve of selected cycles of a maleic acid-based organic anode*[181]*, c) Voltage/specific capacity and d) cycling stability of a 12.0 mg·cm^{-2} $PTCLi_4$ electrode in 1M $LiPF_6$ in a 1:1:1 volume mixture of EC, DMC and EMC*[183]*, e) Voltage/specific capacity curve and f) cycling stability of a LiTPT electrode in 1M $LiPF_6$ in EC/DMC*[94]*. All the images are reproduced from permission from the respective publishers.*

2.4.2. P-type materials

As already remarked, p-type materials undergo oxidation and form a positive charge that is balanced by a counter anion from the electrolyte.[96] Since in this redox process electrons are removed from the highest occupied molecular orbital (HOMO), the potential at which the reaction takes place is relatively high, usually >3.5 V vs. Li/Li^+. However, p-type materials electrochemical reactions are often characterized by single electron redox processes and by bulky monomers/polymers, hence achieving only limited specific capacity.

Conjugated polymers, belonging to the p-type class, were one of the early proposals for the commercialization of lithium-based rechargeable batteries, as already mentioned in the introduction of this section. Conjugated polymers are able to conduct electricity as metals or semiconductiors, thanks to the combination of delocalized p_z orbitals from the hybridized sp^2 carbon orbitals in the backbone. When the polymer is doped, i.e., it is oxidized to remove electrons from these delocalized orbitals, the electronic conductivity of the polymer can increase of several orders of magnitudes. Conjugated polymers were hence proposed as battery cathode materials thanks to the high potential of their redox reaction and their high electronic conductivity, which removes the need to add high amounts of conductive carbon in the electrode. For instance, a polyacetylene-lithium metal battery could achieve 200 $mAh·g^{-1}$ at an average voltage of 3.28 V vs Li/Li^+,[184] while a polyaniline cathode in the same configuration was able to cycle at an average of 3.5 V vs Li/Li^+ and 170 $mAh·g^{-1}$, which a much higher cycling stability than the polyacetylene-based battery (**Figure 2.12.a**).[185] However, the use of the doping mechanism as redox reaction for the storage of energy is also the main drawback of conjugated polymers, since the electronic conductivity decreases sharply as soon as the polymer is de-doped, during the discharge of the battery. Hence, the voltage profiles of such batteries are sloping, and they have to be cycled in very large voltage ranges to exploit fully the available capacity.

Phenylamine-based polymers have also found application as p-type materials.[96] Thanks to the multiple phenyl rings bonded to a central nitrogen atom, the radical nitrogen formed during oxidation can be stabilized, and the charge is balance by an anion from the electrolyte. A microporous poly(triphenylamine) polymer exhibited a specific surface area of 1557 $m^2·g^{-1}$ and a specific capacity of 105 $mAh·g^{-1}$. A high surface area is beneficial to have good rate performance, and in fact this p-type polymer retained 90% of the initial capacity at 20C (**Figure 2.12.b**).[186]

Dibenzo-annulated heterocyclic compounds show p-type redox activity too, with the advantage of the possibility of multi-electron reactions, which are beneficial to increase the specific capacity obtainable from the materials.[96] The two heteroatoms of the central ring can be nitrogen, sulfur and oxygen, and the redox potential of the electrochemical reaction can be tuned according to the number and type of heteroatoms. Notable examples of this class are poly(3-vinyl-N-methylphenothiazine) and N,N-diphenyl-5,10-phenazine. The former achieved only 50% of the theoretical capacity, because of the partial irreversibility of the redox reaction.[187] Nevertheless, the polymer was able to cycle stably for 10,000 cycles at 10C, thanks to the strong π–π interaction between the pendants groups which prevented dissolution in the electrolyte (**Figure 2.12.d**). The latter presents a repeating unit formed by a phenazine molecule bonded to a benzene ring, and with this structure it was possible to realize a multistep two-electron redox reaction at 4.1 and 3.3 V vs. Li/Li$^+$, for an overall specific capacity of ≈135 mAh·g^{-1} at 1C (**Figure 2.12.e**).[188]

Not only polymers, but also small molecules with strong intermolecular interaction can serve as p-type materials. One notable example is coronene, which was employed as cathode in a lithium metal battery, with a specific capacity of ≈40 mAh·g^{-1} at around 4.0 V vs. Li/Li$^+$.[189] This material, which can mimic the ensemble of graphene nanosheets being a seven-ring polycyclic aromatic hydrocarbon, was able to reversibly intercalate PF_6^- anions, with much higher stability than graphite as anion host. A charge-transfer complex between dibenzo-1,4-dioxine and TCNQ molecules was also proposed as p-type cathode material, with the benefit of improved electronic conductivity thanks to the intermolecular π–π interactions.[190] With a remarkable 90% of active material weight fraction in the cathode, the material was able to achieve 90 mAh·g^{-1} at low current rate between 3.5 and 2.5 V vs. Li/Li$^+$ (**Figure 2.12.c**).

Nitroxide radical compounds are probably the most prominent p-type materials, with poly(2,2,6,6-tetramethyl-1-piperidinyloxy methacrylate) (PTMA) as one of the most investigated polymer active materials for batteries.[191,192] Being the polymerized form of the stable radical 4-methacryloyloxy-2,2,6,6-tetramethylpiperidin-1-oxyl (TEMPO-methacrylate), it shows excellent rate capabilities and a stable, plateau-like redox potential at around 3.6 V vs. Li/Li$^+$.[192,193] First reported in 2002 by Nishide et al.,[92] in the last twenty years it was the subject of plenty of studies that focused on its mechanistic behavior,[194–197] on its electrochemical properties,[198–201] and on the development of PTMA-based organic batteries.[202–205]

Several strategies to stabilize this polymer against the dissolution in the electrolyte and to improve its very poor electronic conductivity have been proposed and implemented, and good results have been achieved in the development of electrodes with relevant active material mass loadings.[142,206–208] For instance, Iwasa et al. managed to obtain a 4.69 mg·cm^{-2} active mass loading PTMA electrode, using 30% in weight of vapor grown carbon fibers (VGCF) as conductive additive in the electrode.[209] With a LiFSI-based electrolyte, PTMA-lithiated graphite batteries retained more than 70 mAh·g^{-1} at 100C in discharge, using a procedure with a slow CC-CV charging step (**Figure 2.12.f)**. Hatakeyama-Sato et al. were able to fabricate electrodes up to 16 mg·cm^{-2} of active material loading with poly(2,2,6,6-tetramethylpiperidinyloxy-4-yl acrylamide) (PTAm) as cathode material, a polymer analogue to PTMA but with a hydrophilic amide group in the pendant group, and 5% in weight of single-walled carbon nanotubes as conductive additive.[208] These electrodes were used with a 3M NaCl aqueous electrolyte and tested with cross-linked poly(anthraquinone-substituted ethyleneimine), an n-type material, as anode in a beaker cell. The metal-free batteries achieved 80 mAh·g^{-1} at 10C at an average output voltage of 1 V, and were able to withstand at least 1000 cycles at 5C with 67% of capacity retention.

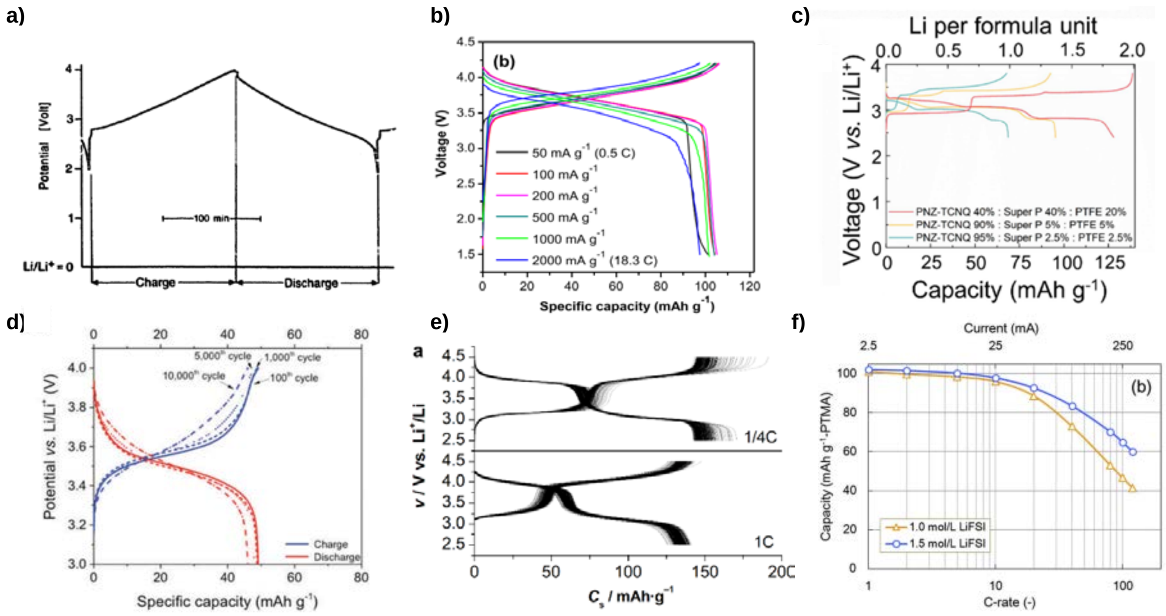

Figure 2.12 *– a) Charge/discharge curve of a polyacetylene-lithium metal battery*[185]*, b) Voltage vs. specific capacity for a triphenylamine-based microporous polymer battery vs. lithium metal at different current rates*[186]*, c) Voltage vs. specific capacity curves of a dibenzo-1,4-dioxine-TCNQ charge-transfer complex cathode vs. lithium metal at different weight ratios of active material in the positive electrode*[190]*, d) Voltage vs. specific capacity curves at the 100th, 1000th, 5000th, and 10000th cycle at 10C of a poly(3-vinyl-N-methylphenothiazine)-based battery vs. lithium metal* [187]*, e) Voltage vs. specific capacity curves at 1C and 1/4C for a N,N-diphenyl-5,10-phenazine-based battery vs. lithium metal*[188]*, f) Capacity vs. current rate plot for a PTMA-based battery vs. lithiated graphite, using 1M and 1.5M LiFSI in EC:DMC 4:6*[209]*. All the images are reproduced from permission from the respective publishers.*

3. Aim of the dissertation

From the analysis of the existing literature on organic batteries, and in general on post-lithium-ion solutions, it is evident that there is a lack of focus on the requirements that new battery materials should possess to be well-suited for proper implementation in cells, modules, and packs, as well as to compete with the current commercial technology. Our dissertation aims to offer a practical perspective on laboratory-scale experimental results in battery material research. We identify a methodology to assess these results and we implement it on a promising organic electrode material. If applied effectively, such a perspective can guide research efforts in prioritizing the exploration of the most promising alternatives.

Firstly, we present the potential of cost and performance analysis in battery research by studying a more established post-lithium chemistry, namely sodium-ion batteries. We present two case studies: one focuses on the relative impact of raw material price increases on lithium-ion and sodium-ion batteries, while the other examines the relationship between the shape of the sodium-ion cathodes' potential curves and their performance in battery packs.

Next, we provide an overview of n-type organic materials for batteries and compare them with the current commercial technology in terms of cost and energy density. This analysis sheds light on their potential performance in real-world scenarios, helping to understand the advantages and drawbacks of utilizing n-type organic materials in battery applications. Additionally, we introduce, for the first time, a fundamental distinction between lithium-deficient and lithium-sufficient n-type battery materials.

P-type organic materials, which store charge through anions, exhibit a distinct working mechanism compared to n-type organic batteries and lithium-ion batteries. To effectively design batteries using p-type organic materials and make meaningful comparisons with other technologies, a deeper understanding of their operation is necessary, particularly due to changes in electrolyte concentration during charge and discharge. As part of our research, we develop a physical model to simulate such behavior in batteries based on p-type organic materials (as well as dual-ion batteries in general).

Finally, we propose an integrated methodology that combines lab-scale experimental results on PTMA-based organic batteries, physical simulations, and cost and energy density analysis. This comprehensive approach aims to provide insights into the practical design of batteries using PTMA as an electrode material and offers a critical evaluation of the results obtained in typical laboratory battery setups

4. Theory overview

4.1. Chronopotentiometric techniques

Chronopotetiometric techniques involve applying a current pulse I to an electrode (working electrode) and measuring its potential E against a reference (reference electrode).[210] The potential of the working electrode is recorded, measuring its variation in time caused by the current, up to (or down to) a potential limit. According to the different overpotentials that develop due to the magnitude and the duration of the current pulse and to the nature of the electrochemical reaction, a certain potential vs. time or charge curve will characterize the investigated electrode.

The duration, direction and variation of the current pulse, chronopotentiometric techniques can be divided in different classes (**Figure 4.1**). The most used technique in the realm of batteries is galvanostatic cycling, where a constant current is applied and switched repeatedly when the potential reaches an upper or lower boundary (**Figure 4.1.d**).

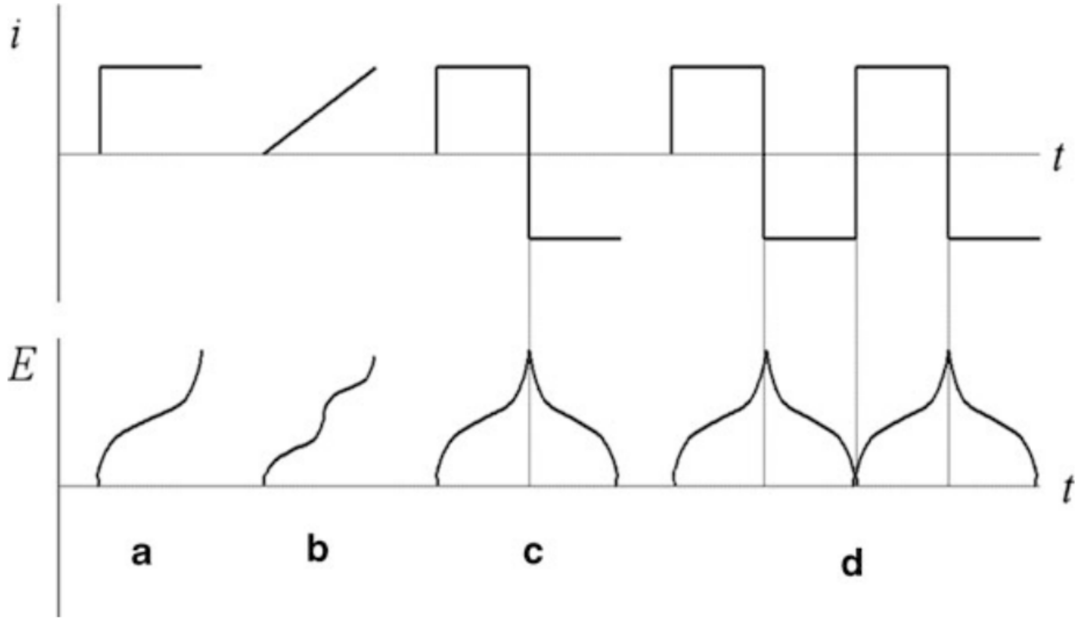

Figure 4.1 *– Different types of chronopotentiometric techniques, according to the value and the direction of the current pulse: a) Constant current chronopotentiometry, b) Chronopotentiometry with linearly rising current, c) Current reversal chronopotentiometry, d) Cyclic chronopotentiometry (galvanostatic cycling). Reproduced with permission from Pyun et al., Copyright © 2012 Springer Nature*[210]

The most important quantities investigated during galvanostatic cycling are briefly presented. The amount of exchanged charge Q, also called capacity, is written as

$$Q = \int I\, dt \tag{4.1}$$

and its typical unit of measure is Ah, or mAh.

The exchanged capacity Q can be compared with the theoretical capacity of a cathode or anode material Q_{th}, to understand the extent of the charge or discharge by comparing with the maximum exchangeable capacity. Q_{th} is written as

$$Q_{th} = m \cdot \frac{nF}{M} \tag{4.2}$$

where m is the active material mass of the electrode, and M is the molecular weight of the active material. When the capacity (or the theoretical capacity) are divided by the mass of the active material in the electrode that is involved in the electrochemical reaction, it is named specific capacity, and measured typically in mAh·g^{-1}.

By measuring the charged and discharged capacity, it is possible to define two types of efficiency that characterize a battery. The first one is the coulombic efficiency η_c, that represents the ratio between the capacity obtained in discharge in a certain cycle Q_{dis} and the capacity that was charged in the previous cycle Q_{ch}, and it is then defined as

$$\eta_c = \frac{Q_{dis}}{Q_{ch}} \tag{4.3}$$

When referring to the coulombic efficiency of the first cycle, the term “initial coulombic efficiency” (ICE) is commonly used.

The second type of efficiency is the energy efficiency η_e, which considers the energy exchanged during charge and discharge, and it is written as

$$\eta_e = \frac{\int_{dis} \Delta E \cdot I\, dt}{\int_{ch} \Delta E \cdot I\, dt} \tag{4.4}$$

The capacity retention of the battery at the cycle n+x is defined as the ratio between the remaining capacity at the cycle n+x and the one of cycle n. A common criterion to define the end of the useful life of a battery is the reaching of 80% capacity retention, with the capacity of the first cycle as reference.

4.2. Electrochemical impedance spectroscopy (EIS)

Electrochemical impedance spectroscopy (EIS) is a powerful non-destructive method to understand how batteries work and degrade over time, based on the application of an alternate current or potential signal with varying frequency to the studied electrochemical system.[211] In the realm of batteries, researchers have use EIS, for instance, to study battery degradation, to measure ionic conductivity of electrolytes, or to understand the interfacial resistance between electrode and electrolyte.[212–215]

EIS can be galvanostatic or potentiostatic, when the alternate signal is a current or a potential applied to the system, respectively. The EIS fundamental hypotheses of linearity, stationarity, and causality require the potential perturbation to be reasonably small (10 mV of signal amplitude is commonly used as an indication[213]), and it requires the system to be at a steady state, i.e., the potential should be stable before starting the measurement.

The alternate signal frequency f determines the measured impedance Z as

$$Z = \frac{E \cdot \exp\{i\theta_1(f)\}}{I \cdot \exp\{i\theta_2(f)\}} = Z_0(\cos\theta(f) + i\sin\theta(f)) \tag{4.5}$$

where Z_0 is impedance module, measured in Ω or $\Omega\cdot\mathrm{m}^2$ and calculated as the ratio between the modules of the alternate potential and current, and θ is the phase shift angle between the alternate potential and current, i.e., the difference between the phase of the potential θ_1 and the phase of the current θ_2. Hence, the impedance will be composed by a real and an imaginary part.

Each frequency range highlights a specific set of phenomena occurring during battery operation, such as ohmic resistance, charge transfer resistance, and resistance caused by the diffusion of ions in the electrode and electrolyte, according to corresponding characteristic time, enabling an effective separation of the different resistance sources (**Figure 4.2**).

Usually, the interpretation of EIS results heavily relies on equivalent circuit models (ECM), which simulate the battery's behavior using a network of circuit elements.[216] These models are widely used due to their simplicity and computational efficiency. However, it's important to note that they offer only partial understanding of the battery's physical behavior. This limitation arises from the purely phenomenological resemblance between the electrical elements in the circuit and the electrochemical processes happening within the battery.

More interesting approaches from this point of view aim to interpret the impedance spectra as the results of simulations coming from physical models, analytical or numerical, which simulate the battery behavior through a set of differential equations.[22,217,218] The different features of spectra can be then connected to actual physical parameters, often measurable or estimable, that characterize the electrodes, the electrolyte and the separator.

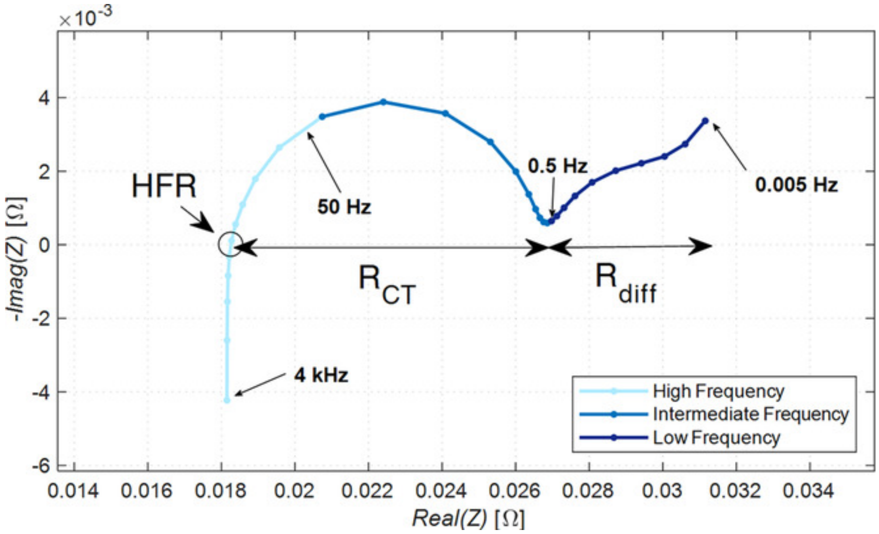

Figure 4.2 *– Example of an impedance spectra obtained by physical simulations of a commercial lithium-ion battery, with highlighted the frequency ranges and the associated different resistance sources (HFR=high frequency resistance,* R_{CT}*: charge transfer resistance,* R_{diff}*: diffusion resistance). Reproduced with permission from Rabissi et al., Copyright © 2021 Wiley* [22]

4.3. Scanning Electron Microscopy (SEM)

The scanning electron microscopy (SEM) is a characterization technique that allows to investigate the morphology of the surface of a sample by obtaining images, also called micrographs, through the detection of secondary or backscattered electrons emitted by the material after being excited with a focused beam of electrons.[219] An acceleration voltage (0.5-20 kV) is applied to the electron source (cathode), which accelerates the electrons towards the anode. The electron beam, after being focused by condenser lenses, scans the sample surface and produces different detectable signals (**Figure 4.3**).

Backscattered electrons result from the elastic scattering of emitted electrons by the electric field of the sample's atoms. The number of backscattered electrons increases with the nuclear charge of the atoms, making heavier elements appear brighter in micrographs. These electrons are useful for analyzing the composition of the material's surface. On the other hand, secondary electrons are ejected from the sample due to inelastic scattering of the electron beam. They are valence electrons weakly bound to the atoms, providing a surface-sensitive signal that helps understand the sample's morphology. When an electron originating from an external shell occupies an electron vacancy in an internal shell, the energy difference is released as a distinctive X-ray specific to each atom. An energy-dispersive X-ray (EDX) detector can identify these X-rays, enabling elemental mapping of the specimen's surface[220]. Various parameters such as the electron beam aperture, acceleration voltage, detector type, and sample conductivity influence the characteristics and quality of the resulting micrographs.

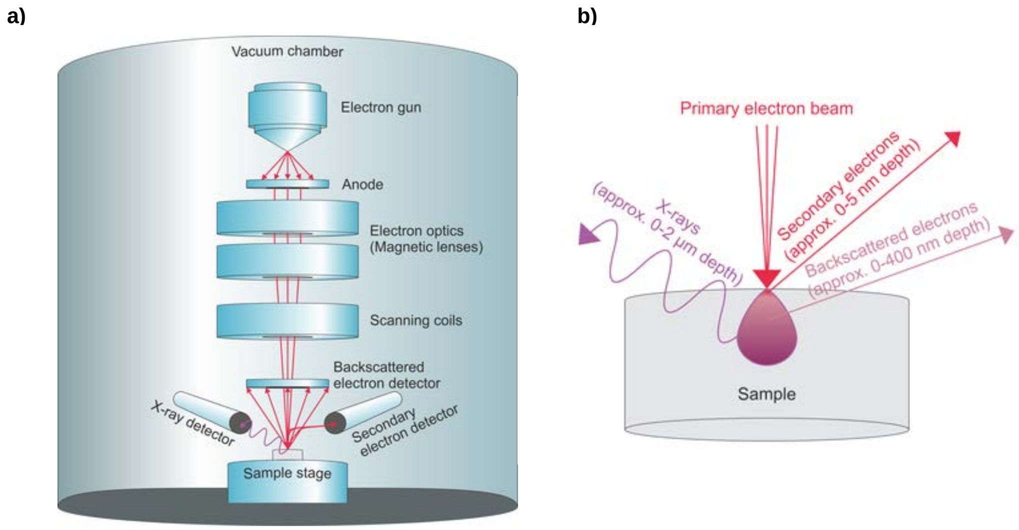

Figure 4.3 *– a) Scheme of a scanning electron microscope; b) Different signals generated during SEM measurements and their penetration depth. Reproduced with permission from T. Schmid*[221]

4.4. Thermogravimetric analysis (TGA)

Thermogravimetric analysis (TGA) is a characterization method in which a weight change is measured as a function of the temperature.[222] Such a technique provides insights on physicochemical phenomena such as decomposition, dehydration, sublimation, ab/ad/desorption and solid-gas reactions.[223]

An instrument for TGA is basically made of a precision balance, a furnace that can be programmed to adjust the temperature of the environment in which the sample is inserted, and a gas inlet which controls the nature and the flow rate of the gas in the furnace (**Figure 4.4.a**). The sample is loaded on a crucible, which can be made of different materials (aluminum, alumina, platinum, sapphire, etc.) and have different shapes and volumes according to the nature of the investigated materials and the objective of the measurement. The measured quantity is the mass loss compared to the initial sample weight (thermogravimetric curve, TG), which can be expressed both in absolute units or as a percentage of the initial weight. The derivative of the mass loss (differential thermogravimetric curve, DTG) can be obtained by calculating the slope of the TG curve, and it can help in identifying features that are not evident from the TG curve alone, such as multiple mass loss peaks in one mass loss step.[222]

The TGA can be used to determine decomposition temperatures and investigate the stability at high temperatures of materials with different gases (e.g., O_2, N_2, Ar, He and mixtures). The values of mass loss and decomposition temperature are heavily dependent on the loaded sample weight, on the flow rate of the gas, the type of gas, and the heating rate (**Figure 4.4.b**).[224]

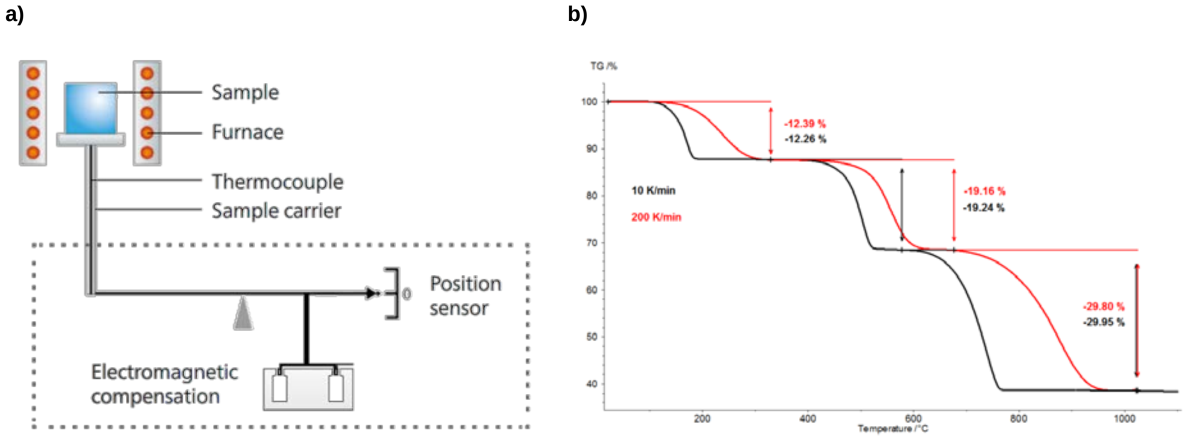

Figure 4.4 *– a) Depiction of the main parts of a TGA instrument; b) Mass loss vs. temperature in a TGA measurement on calcium oxalate monohydrate, at 10 and 200 K·min*$^{-1}$*. Reproduced with permission from NETZSCH GmbH*[224]

4.5. Gas pycnometry

Gas pycnometry is a technique that utilizes the principles of fluid displacement and gas expansion to measure the true (or skeletal) density of solids, usually in form of powder. The true density is defined as the weight of the material divided by the occupied volume, without considering the volume of the open pores and the interparticle volume (**Figure 4.5.a**). Hence, the true density is always higher than the bulk (or tap) density, which instead takes into account also the volume between the particles.[225,226] For crystalline compounds, the true density approaches the crystallographic density that can be obtained from single-crystal x-ray diffraction (XRD) measurements, but since closed pores are included in the true density determination, in presence of closed porosity the former will be lower than the latter.[227]

By employing an inert gas, such as helium or nitrogen, the pycnometer ensures thorough penetration of the sample's pores. The process involves pressurizing a sealed sample chamber to a predetermined level with the chosen gas, recording the stabilized pressure. Subsequently, the gas expands into a reference chamber, whose volume is known, and the second stabilized pressure is recorded (**Figure 4.5.b**). By comparing the pressure drop ratio to that of a known volume standard undergoing the same procedure, the measurement is performed without the need for pressure transducer calibration. In fact, a standard with volume similar to the investigated sample is always measured together with the sample.[228]

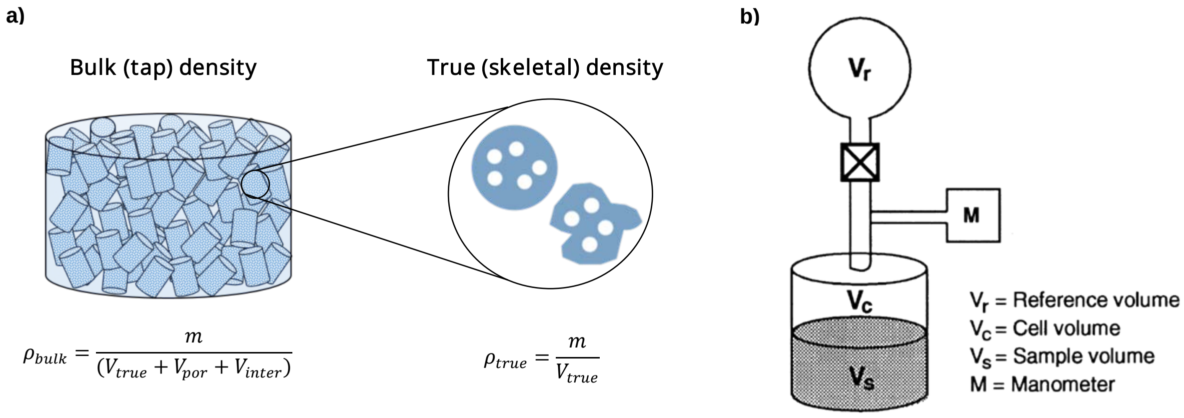

Figure 4.5 – *a) Difference between bulk density and true density. Adapted from 3P Instruments* [229] *b) Scheme of the main components and volumes of a gas pycnometer. Reproduced with permission from Pharmacopeia*[230]

4.6. Macroscale battery physical model

The domain of the model is shown in Section 6.3.1 in **Figure 6.14**. Firstly, the microscale PDEs will be derived, and then the volume-averaged macroscale PDEs will be obtained from the microscale ones, with the necessary boundary conditions. Both the standard model for lithium-ion batteries and the novel one for dual-ion batteries will be derived and presented, in order to highlight the main differences between the two.

4.6.1. Microscale equations for the cathode

For **the conservation of the charge in the solid electrode**, there are no relevant changes with respect to the standard DFN model, since the electrode reaction is not considered in this PDE. Assuming negligible magnetic effects, a continuous charge density, a non-time-varying volume, and that the movement of electrons is much faster than any other process, we can write

$$\nabla \cdot \mathbf{i_s} = \nabla \cdot (-\sigma \nabla \phi_s) = 0 \tag{4.6}$$

where $\mathbf{i}_s$ is the current density vector in the solid electrode, σ is the electronic conductivity of the solid electrode, and ϕ_s is the potential in the solid electrode.

In the **conservation of the mass in the liquid electrolyte** PDE, there are also no changes with respect to the DFN model for lithium-ion batteries, for the same reason of the previous equation. Assuming a binary electrolyte solution where electroneutrality holds and employing the Maxwell-Stephan theory for multicomponent diffusion, we obtain

$$\begin{cases} \mathbf{N}_+ = -\nu_+ D_e \nabla c_e + \dfrac{\mathbf{i_e} t_+^0}{z_+ F} + c_+ \mathbf{v}_0 \\ \mathbf{N}_- = -\nu_- D_e \nabla c_e + \dfrac{\mathbf{i_e} t_-^0}{z_- F} + c_- \mathbf{v}_0 \end{cases} \tag{4.7}$$

where $\mathbf{N}_+$ and $\mathbf{N}_-$ are respectively the molar flux vectors of cations and anions, c_+ and c_- are respectively the concentrations of cations and anions in the liquid electrolyte, c_e is the salt concentration in the liquid electrolyte, D_e is the salt diffusion in the liquid electrolyte, $\mathbf{i_e}$ is the current density vector in the liquid electrolyte, t_+^0 and t_-^0 are respectively the transference number of cations and anions in the liquid electrolyte, ν_+ and ν_- are respectively the stoichiometric coefficient of cations and anions in the electrolyte salt, z_+ and z_- are the charge of cations and anions, F is the Faraday constant, and $\mathbf{v_0}$ is the velocity vector of the electrolyte solvent.

Considering that

$$c_e = \frac{c_+}{\nu_+} = \frac{c_-}{\nu_-} \tag{4.8}$$

$$\frac{\partial c_+}{\partial t} = -\nabla \cdot \mathbf{N}_+ \tag{4.9}$$

$$\nabla \cdot \mathbf{i_e} = 0 \tag{4.10}$$

we obtain the final expression for the mass conservation in the liquid electrolyte, which is

$$\frac{\partial c_e}{\partial t} = \nabla \cdot (D_e \nabla c_e) - \frac{\mathbf{i_e} \cdot \nabla t_+^0}{\nu_+ z_+ F} + \nabla \cdot (c_e \mathbf{v_0}) \tag{4.11}$$

Since the model deals with anion-insertion reactions, it could be tempting to write equation (4.11) with the anion-related quantities, i.e., t_-^0, ν_-, and z_-. The new conservation equation would be

$$\frac{\partial c_e}{\partial t} = \nabla \cdot (D_e \nabla c_e) - \frac{\mathbf{i_e} \cdot \nabla t_-^0}{\nu_- z_- F} + \nabla \cdot (c_e \mathbf{v_0}) \tag{4.12}$$

Nevertheless, since we have

$$\nu_+ z_+ = -\nu_- z_- \tag{4.13}$$

$$\nabla t_+^0 = -\nabla t_-^0 \tag{4.14}$$

the equations (4.11) and (4.12) are actually equal.

For the **conservation of the charge in the liquid electrolyte**, the general PDE can be written as

$$\mathbf{i_e} = -\kappa \nabla \phi_e - \frac{\nu \kappa R T}{F} \left(\frac{s_+}{n \nu_+} - \frac{s_0 c_e}{n c_0} + \frac{t_+^0}{\nu_+ z_+} \right) \left(1 + \frac{\partial f_\pm}{\partial \ln c_e} \right) \nabla \ln c_e \tag{4.15}$$

where κ is the ionic conductivity of the electrolyte, ϕ_e is the potential in the electrolyte, ν is the sum of the stoichiometric coefficients of the ions in the electrolyte salt, R is the universal gas constant, T is the temperature, c_0 is the concentration of the solvent in the electrolyte, and $\left(1 + \frac{\partial f_\pm}{\partial \ln c_e}\right)$ is the activity coefficient. The parameters s_+, s_-, and s_0 are respectively the stoichiometric coefficient in the reaction respectively of the cation, the anion and the solvent in the electrode reaction

$$s_- M_-^{Z_-} + s_+ M_+^{Z_+} + s_0 M_0 \rightleftharpoons n e^-$$

where M_-, M_+, and M_0 are respectively the anionic, cathodic and solvent species, and n is the number of electrons involved in the reaction.

In the lithium-ion battery model, the electrochemical reactions of the two electrodes both result with the same values of stoichiometric coefficients ($s_+ = -1$, $s_- = s_0 = 0$),[231] while in the dual-ion battery model the positive electrode reaction ($s_- = 1$, $s_+ = s_0 = 0$) has different stoichiometric coefficients than the negative electrode one. Nevertheless, the chosen electrode reaction should be the one of the reference electrode against which the potential of the electrode is measured.[232] The lithium reference electrode is then chosen, being the anode of the simulated battery, and hence equation (4.15) becomes

$$\mathbf{i_e} = -\kappa \nabla \phi_e - \frac{2\kappa RT}{F}(t_+^0 - 1)\left(1 + \frac{\partial f_\pm}{\partial \ln c_e}\right) \nabla \ln c_e \tag{4.16}$$

reminding that we have $\nu_+ = -1$, $\nu = 2$ and $z_+ = 1$ for our case of a binary monovalent electrolyte solution.

The **conservation of the mass in the solid electrode** is unvaried compared to the standard DFN battery model. Assuming Fickian diffusion, a continuous solid density, and a non-time-varying volume, we can write

$$\frac{\partial c_s}{\partial t} = \nabla \cdot (D_s \nabla c_s) \tag{4.17}$$

where c_s is the ion concentration in the solid electrode and D_s is the diffusion coefficient of the ion in the solid electrode.

Finally, the **kinetics of the electrochemical reaction** can be modelled with the Butler-Volmer equation, hence obtaining

$$i = i_0 \left(\exp\left\{ \frac{(1-\alpha) n F \eta}{RT} \right\} - \exp\left\{ -\frac{\alpha n F \eta}{RT} \right\} \right) \tag{4.18}$$

where i is the applied current density on the battery, i_0 is the exchange current density, α is the charge transfer coefficient, and η is the overpotential in the non-equilibrium conditions. In a lithium-ion battery electrode, the relationship between the current density and the ionic molar flux j is

$$i = jF \tag{4.19}$$

since j is defined as positive when going from the electrode to the electrolyte. For this reason, in the cathode of the dual-ion battery, the current density and the ionic molar flux are related by the equation

$$i = -jF \tag{4.20}$$

because when charging the battery ($i > 0$), the flux of anions goes from the electrolyte to the electrode ($j < 0$), and vice versa when discharging.

From the Butler-Volmer theory, the exchange current density i_0 can be written as

$$i_0 = nFk_0 \left(\prod c_{ox}\right)^{1-\alpha} \left(\prod c_{red}\right)^{\alpha} \tag{4.21}$$

where k_0 is the reaction rate of the electrochemical reaction, c_{ox} are the concentrations of the oxidizing species, and c_{red} are the concentrations of the reducing species. For the lithium-ion battery model, both electrodes have a reaction in the form

$$\Theta + Li^{+} + e^{-} \rightleftharpoons \Theta - Li$$

where Θ is a vacancy in the lattice of the host material or a species reacting with lithium ions, and $\Theta - Li$ is the occupied vacancy or the species reacted with lithium. We can express the concentration of $\Theta - Li$ as $c_{s,r}$, i.e., the concentration of ions on the surface of the electrode particles, and the concentration of Θ as $(c_{s,max} - c_{s,r})$, i.e., the concentration of available sites for insertion/reaction, obtained by subtracting the actual concentration of ions on the surface $c_{s,r}$ from the maximum possible concentration of ions $c_{s,max}$. The concentration of free lithium ions in the electrolyte is c_e, as already remarked. With this notation, the expression of the exchange current density from equation (4.21) is then

$$i_0 = nFk_0 {c_e}^{1-\alpha} (c_{s,max} - c_{s,r})^{1-\alpha} {c_{s,r}}^{\alpha} \tag{4.22}$$

In the dual-ion battery case, the positive electrode reaction is instead

$$\Theta - A + e^{-} \rightleftharpoons \Theta + A^{-}$$

where Θ is a vacancy in the lattice of the host material or a species reacting with anions A^{-}, and $\Theta - A$ is the occupied vacancy or the species reacted with anions. Hence, if we keep the same notation of the lithium-ion case for the different species concentration, we have that the exchange current density is expressed as

$$i_0 = nFk_0 {c_e}^{\alpha} (c_{s,max} - c_{s,r})^{\alpha} {c_{s,r}}^{1-\alpha} \tag{4.23}$$

Hence, the exponents for the concentrations in equations (4.22) and (4.23) are not the same because of the different electrode reactions. Nevertheless, the charge transfer coefficient α is commonly set to 0.5 for the simulations, and with this value the aforementioned equations are then equal.

4.6.2. Boundary conditions of the microscale equations for the cathode

The boundary condition for the **charge conservation in the solid electrode** changes according to the electrode reaction. From the Butler-Volmer equation, we have that the flux of ions is positive when the current is positive (eq. (4.19)) in a lithium-ion battery. Hence, this boundary condition in this case is

$$\mathbf{n}_{\mathrm{s}} \cdot \nabla\phi_s = -\frac{\mathbf{i}_{\mathrm{s}} \cdot \mathbf{n}_{\mathrm{s}}}{\sigma} = -\frac{jF}{\sigma} \tag{4.24}$$

where $\mathbf{n}_{\mathrm{s}}$ is the normal vector on the surface of the solid electrolyte that goes in the direction of the electrolyte, which points in the same direction of the positive molar flux j.

Instead, for the dual-ion cathode case, the flux of ions is positive when the current is negative (eq. (4.20)) and the boundary condition for the charge conservation in the solid electrode is

$$\mathbf{n}_{\mathrm{s}} \cdot \nabla\phi_s = -\frac{\mathbf{i}_{\mathrm{s}} \cdot \mathbf{n}_{\mathrm{s}}}{\sigma} = \frac{jF}{\sigma} \tag{4.25}$$

The boundary condition for the **mass conservation in the liquid electrolyte** also depends on the type of electrode reaction. In fact, for lithium-ion batteries we have that

$$\begin{cases} \mathbf{N}_{+} \cdot \mathbf{n}_{\mathrm{e}} = -j \\ \mathbf{N}_{-} \cdot \mathbf{n}_{\mathrm{e}} = 0 \\ \mathbf{N}_{\mathbf{0}} \cdot \mathbf{n}_{\mathrm{e}} = 0 \end{cases} \tag{4.26}$$

where $\mathbf{N}_{\mathbf{0}}$ is the molar flux vector of solvent molecules between the electrolyte and the electrode, and $\mathbf{n}_{\mathrm{e}}$ is the normal vector that points from the electrolyte to the electrode surface, the opposite direction of a positive molar flux j.

Evaluating these expressions considering equation *(4.7)*, we can write

$$\begin{cases} -j = -D_e \nabla c_e \cdot \mathbf{n}_{\mathrm{e}} + \dfrac{\mathbf{i}_{\mathrm{e}} \cdot \mathbf{n}_{\mathrm{e}} t_{+}^{0}}{F} \\ 0 = -D_e \nabla c_e \cdot \mathbf{n}_{\mathrm{e}} - \dfrac{\mathbf{i}_{\mathrm{e}} \cdot \mathbf{n}_{\mathrm{e}} t_{-}^{0}}{F} \end{cases} \tag{4.27}$$

Adding t_{+}^{0}/t_{-}^{0} times the second equation to the first to eliminate $\mathbf{i}_{\mathrm{e}}$ and rearranging, the boundary condition for the concentration gradient for the lithium-ion battery can be written as

$$\nabla c_e \cdot \mathbf{n}_{\mathrm{e}} = \frac{1 - t_{+}^{0}}{D_e} j = \frac{t_{-}^{0}}{D_e} j \tag{4.28}$$

The dual-ion battery cathode has different ion fluxes, because the anions are involved in the positive electrode redox reaction. In fact, maintaining the same notation we have

$$\begin{cases} \mathbf{N}_{+} \cdot \mathbf{n}_{\mathrm{e}} = 0 \\ \mathbf{N}_{-} \cdot \mathbf{n}_{\mathrm{e}} = -j \\ \mathbf{N}_{0} \cdot \mathbf{n}_{\mathrm{e}} = 0 \end{cases} \tag{4.29}$$

By putting these values in the equation (*4.7),* we can write

$$\begin{cases} 0 = -D_e \nabla c_e \cdot \mathbf{n}_{\mathrm{e}} + \dfrac{\mathbf{i}_{\mathrm{e}} \cdot \mathbf{n}_{\mathrm{e}} t_{+}^{0}}{F} \\ -j = -D_e \nabla c_e \cdot \mathbf{n}_{\mathrm{e}} - \dfrac{\mathbf{i}_{\mathrm{e}} \cdot \mathbf{n}_{\mathrm{e}} t_{-}^{0}}{F} \end{cases} \tag{4.30}$$

Again, adding t_{+}^{0}/t_{-}^{0} times the second equation to the first and rearranging, we obtain the boundary condition for the concentration gradient in the dual-ion battery cathode

$$\nabla c_e \cdot \mathbf{n}_{\mathrm{e}} = \frac{t_{+}^{0}}{D_e} j = \frac{1 - t_{-}^{0}}{D_e} j \tag{4.31}$$

The boundary condition for the **charge conservation in the liquid electrolyte** also changes with the electrode reaction, because it is derived from the boundary condition on the mass conservation in the liquid electrolyte.

For the lithium-ion battery case, inserting the result of equation (4.27) in the equation (4.26) we get

$$\begin{cases} -j = -D_e \dfrac{(1 - t_{+}^{0}) j}{D_e} + \dfrac{\mathbf{i}_{\mathrm{e}} \cdot \mathbf{n}_{\mathrm{e}} t_{+}^{0}}{F} \\ 0 = -D_e \dfrac{t_{-}^{0} j}{D_e} - \dfrac{\mathbf{i}_{\mathrm{e}} \cdot \mathbf{n}_{\mathrm{e}} t_{-}^{0}}{F} \end{cases} \tag{4.32}$$

Both equations give as result

$$\mathbf{i}_{\mathrm{e}} \cdot \mathbf{n}_{\mathrm{e}} = -jF \tag{4.33}$$

Instead, the dual-ion battery cathode case requires using the result of equation (4.30) in the equation (4.29), obtaining

$$\begin{cases} 0 = -D_e \dfrac{t_{+}^{0} j}{D_e} + \dfrac{\mathbf{i}_{\mathrm{e}} \cdot \mathbf{n}_{\mathrm{e}} t_{+}^{0}}{F} \\ -j = -D_e \dfrac{(1 - t_{-}^{0}) j}{D_e} - \dfrac{\mathbf{i}_{\mathrm{e}} \cdot \mathbf{n}_{\mathrm{e}} t_{-}^{0}}{F} \end{cases} \tag{4.34}$$

From each of the two equations we can write

$$\mathbf{i}_\mathrm{e} \cdot \mathbf{n}_\mathrm{e} = jF \tag{4.35}$$

Finally, the boundary equation for the **mass conservation in the solid electrode** is written as

$$\mathbf{n}_s \cdot \nabla c_s = -\frac{\mathbf{N}_\mathbf{s} \cdot \mathbf{n}_\mathrm{s}}{D_s} = -\frac{j}{D_s} \tag{4.36}$$

where $\mathbf{N}_\mathbf{s}$ is the molar flux vector of ions at the interface between the electrode and the electrolyte, pointing in the same direction of the molar flux j.

4.6.3. Macroscopic model for the porous cathode

The microscale equations have to be integrated to a volume that considers both the solid electrode and the liquid electrolyte, in order to get equations that can describe the behavior of a porous electrode where both phases coexist. The overbarred variables will indicate the volume-average quantities.

The three volume-averaging theorems used for the derivation of the macroscopic model are[231]

$$\varepsilon_\alpha \overline{\nabla \psi_\alpha} = \varepsilon_\alpha \nabla \overline{\psi_a} + \frac{1}{V} \oiint_{A_{\alpha\beta}} \psi_a \mathbf{n}_{\boldsymbol{\alpha}} \, dA \tag{4.37}$$

$$\varepsilon_\alpha \overline{\nabla \cdot \boldsymbol{\Psi}_\mathbf{a}} = \varepsilon_\alpha \nabla \cdot \overline{\boldsymbol{\Psi}_\mathbf{a}} + \frac{1}{V} \oiint_{A_{\alpha\beta}} \boldsymbol{\Psi}_\mathbf{a} \cdot \mathbf{n}_{\boldsymbol{\alpha}} \, dA \tag{4.38}$$

$$\varepsilon_\alpha \overline{\left[\frac{\partial \psi_\alpha}{\partial t}\right]} = \varepsilon_\alpha \frac{\partial \overline{\psi_\alpha}}{\partial t} - \frac{1}{V} \oiint_{A_{\alpha\beta}} \psi_\alpha \mathbf{v}_{\boldsymbol{\alpha\beta}} \cdot \mathbf{n}_{\boldsymbol{\alpha}} \, dA \tag{4.39}$$

where α and β are two different phases, ψ_α is a scalar field associated to the phase α, $\boldsymbol{\Psi}_\mathbf{a}$ is a vector field associated to the phase α, $A_{\alpha\beta}$ is the interface between the two phases, $\mathbf{v}_{\boldsymbol{\alpha\beta}}$ is the vector of the displacement velocity of the interface between the two phases, $\mathbf{n}_{\boldsymbol{\alpha}}$ is the vector normal to the interface between the two phases pointing from α to β, and ε_α is the volume fraction of phase α.

For the **charge conservation in the solid electrode**, the volume-averaging of equation gives

$$\varepsilon_s \overline{\nabla \cdot (-\sigma \nabla \phi_s)} = \varepsilon_s \nabla \cdot \overline{(-\sigma \nabla \phi_s)} + \frac{1}{V} \oiint_{A_{se}} (-\sigma \nabla \phi_s) \cdot \mathbf{n}_{\boldsymbol{s}} \, dA = 0 \tag{4.40}$$

where ε_s is the solid volume fraction of the porous electrode, A_{se} is the area of the porous electrode, V is the volume of the porous electrode.

To solve the integral of the right-hand side of equation (4.40), we have to differentiate according to the type of battery. For lithium-ion batteries, reminding the boundary condition from equation (4.24) and assuming that the molar flux j is homogeneous and can be modelled with volume-averaged parameters, we can write

$$\frac{1}{V}\oiint_{A_{se}}(-\sigma\nabla\phi_s)\cdot\mathbf{n}_{\boldsymbol{\alpha}}\,dA=\frac{1}{V}\oiint_{A_{se}}jF\,dA\approx\frac{A_{se}}{V}\bar{j}\,F=a_s\bar{j}F \tag{4.41}$$

where a_s is the specific surface area of the electrode, defined as the ratio between the electrode area and the electrode volume. The other term of the right-hand side of equation (4.40) can instead be approximated as

$$\varepsilon_s\nabla\cdot\overline{(-\sigma\nabla\phi_s)}\approx\nabla\cdot\left(-\sigma_{eff}\nabla\overline{\phi_s}\right) \tag{4.42}$$

where σ_{eff} is the effective electronic conductivity of the porous positive electrode. Its value can be approximated according to the Bruggeman theory of transport in porous media, as

$$\sigma_{eff}=\sigma\,\varepsilon_s^{bg} \tag{4.43}$$

where ^{bg} is the exponent given to the electrode solid fraction to get the effective conductivity. The final equation for the conservation of charge in the solid electrode for the lithium-ion case is then

$$\nabla\cdot\left(-\sigma_{eff}\nabla\overline{\phi_s}\right)=-a_s\bar{j}F \tag{4.44}$$

In the dual-ion battery case, the boundary condition to consider is the one of equation (4.25), and we will then obtain

$$\frac{1}{V}\oiint_{A_{se}}(-\sigma\nabla\phi_s)\cdot\mathbf{n}_{\boldsymbol{\alpha}}\,dA=\frac{1}{V}\oiint_{A_{se}}-jF\,dA\approx-\frac{A_{se}}{V}\bar{j}\,F=-a_s\bar{j}F \tag{4.45}$$

Therefore, the macroscopic equation for the charge conservation in the solid electrode for a dual-ion battery cathode is

$$\nabla\cdot\left(-\sigma_{eff}\nabla\overline{\phi_s}\right)=a_s\bar{j}F \tag{4.46}$$

The **mass conservation in the liquid electrolyte** is derived from equation(4.11), which is also simplified by assuming that the velocity of the solvent v_0 is null, i.e., absence of convection, and that the gradient of the transference number ∇t_+^0 is negligible.

Assuming no displacement of the boundary between the electrode and the electrolyte, the averaging of the left-hand side of equation (4.11) results in

$$\varepsilon_e \overline{\left[\frac{\partial c_e}{\partial t}\right]} = \varepsilon_e \frac{\partial \overline{c_e}}{\partial t} \tag{4.47}$$

where ε_e is the electrolyte volume fraction, i.e., the porosity of the electrode. Instead, for the right-hand side of the same equation we obtain

$$\varepsilon_e \overline{\nabla \cdot (D_e \nabla c_e)} = \varepsilon_e \nabla \cdot \left(\overline{D_e \nabla c_e}\right) + \frac{1}{V} \oiint_{A_{se}} D_e \nabla c_e \cdot \mathbf{n}_\mathrm{e} dA \tag{4.48}$$

With the same approach of equation (4.42), we can approximate the first part of the right-hand side of the previous equation as

$$\varepsilon_e \nabla \cdot \left(\overline{D_e \nabla c_e}\right) \approx \nabla \cdot \left(D_{e,eff} \nabla \overline{c_e}\right) \tag{4.49}$$

The effective salt diffusion coefficient in the electrolyte is defined as

$$D_{e,eff} = D_e \varepsilon_e^{bg} \tag{4.50}$$

according to the Bruggeman theory of transport in porous media, as already explained for the equation (4.43).

Depending on the type of battery, the boundary condition used to solve the integral of equation (4.48) changes. For the lithium-ion battery case, the boundary condition comes from equation (4.28), which is inserted in the integral of equation (4.48) to give

$$\frac{1}{V} \oiint_{A_{se}} D_e \nabla c_e \cdot \mathbf{n}_\mathrm{e} dA = \frac{1}{V} \oiint_{A_{se}} (1 - t_+^0) j \, dA \approx \frac{A_{se}}{V} (1 - t_+^0) \bar{j} = a_s (1 - t_+^0) \bar{j} \tag{4.51}$$

Overall, the equation for the mass conservation in the liquid electrolyte for lithium-ion batteries is

$$\varepsilon_e \frac{\partial \overline{c_e}}{\partial t} = \nabla \cdot \left(D_{e,eff} \nabla \overline{c_e}\right) + a_s (1 - t_+^0) \bar{j} \tag{4.52}$$

The dual-ion battery cathode case, instead, uses equation (4.31) as boundary condition, and the integral of equation *(4.48)* becomes

$$\frac{1}{V} \oiint_{A_{se}} D_e \nabla c_e \cdot \mathbf{n}_\mathrm{e} dA = \frac{1}{V} \oiint_{A_{se}} t_+^0 \, j \, dA \approx \frac{A_{se}}{V} t_+^0 \, \bar{j} = a_s \, t_+^0 \, \bar{j} \tag{4.53}$$

Hence, the equation for the mass conservation in the liquid electrolyte for dual-ion battery cathode is written as

$$\varepsilon_e \frac{\partial \overline{c_e}}{\partial t} = \nabla \cdot \left(D_{e,eff} \nabla \overline{c_e}\right) + a_s\, t_+^0\, \bar{j} \tag{4.54}$$

Regarding the **conservation of charge in the liquid electrolyte**, we apply the volume averaging to the combination of equations (4.10) and (4.16), obtaining

$$\varepsilon_e \overline{\nabla \cdot \mathbf{i_e}} = \nabla \cdot (\varepsilon_e \overline{\mathbf{i_e}}) + \frac{1}{V} \oiint_{A_{se}} \mathbf{i_e} \cdot \mathbf{n}_\mathrm{e} dA \tag{4.55}$$

where the first term of the right-hand side of the equation is

$$\nabla \cdot (\varepsilon_e \overline{\mathbf{i_e}}) = \nabla \cdot \left(-\overline{\varepsilon_e \kappa \nabla \phi_e} - \overline{\frac{2\varepsilon_e \kappa RT}{F} (t_+^0 - 1) \left(1 + \frac{\partial f_\pm}{\partial \mathrm{ln} c_e}\right) \nabla \mathrm{ln} c_e} \right) \tag{4.56}$$

These terms can be rewritten as effective quantities in a porous medium, as already done for the electronic conductivity and the salt diffusion coefficient. Hence, we can write

$$-\overline{\varepsilon_e \kappa \nabla \phi_e} \approx -\kappa_{eff} \nabla \overline{\phi_e} \tag{4.57}$$

$$-\overline{\frac{2\varepsilon_e \kappa RT}{F} (t_+^0 - 1) \left(1 + \frac{\partial f_\pm}{\partial \mathrm{ln} c_e}\right) \nabla \mathrm{ln} c_e} \approx -\frac{2\kappa_{eff} RT}{F} (t_+^0 - 1) \left(1 + \frac{\partial f_\pm}{\partial \mathrm{ln} c_e}\right) \nabla \mathrm{ln} \overline{c_e} \tag{4.58}$$

where κ_{eff} is the effective ionic conductivity in the liquid electrolyte, defined as

$$\kappa_{eff} = \kappa\, \varepsilon_e^{bg} \tag{4.59}$$

The resolution of the integral, again, depends on the type of battery we are analyzing. For the lithium-ion battery case, the correct boundary condition is equation (4.33), which is inserted in the integral of equation (4.55) to give

$$\frac{1}{V} \oiint_{A_{se}} \mathbf{i_e} \cdot \mathbf{n}_\mathrm{e} dA = \frac{1}{V} \oiint_{A_{se}} -jF\, dA \approx -\frac{A_{se}}{V} \bar{j} F = -a_s \bar{j} F \tag{4.60}$$

Putting together the results, we obtain for the charge conservation in the liquid electrolyte for lithium-ion batteries

$$\nabla \cdot \left(-\kappa_{eff} \nabla \overline{\phi_e} - \frac{2\kappa_{eff} RT}{F} (t_+^0 - 1) \left(1 + \frac{\partial f_\pm}{\partial \mathrm{ln} c_e}\right) \nabla \mathrm{ln} \overline{c_e} \right) = a_s \bar{j} F \tag{4.61}$$

In the case of a dual-ion battery cathode, equation (4.35) as boundary condition is used to solve the integral of equation (4.55), and we can write

$$\frac{1}{V} \oiint_{A_{se}} \mathbf{i_e} \cdot \mathbf{n}_\mathrm{e} dA = \frac{1}{V} \oiint_{A_{se}} jF\, dA \approx \frac{A_{se}}{V} \bar{j} F = a_s \bar{j} F \tag{4.62}$$

Altogether, the charge conservation in the liquid electrolyte equation for dual-ion battery cathodes is

$$\nabla\cdot\left(-\kappa_{eff}\nabla\overline{\phi_e}-\frac{2\kappa_{eff}RT}{F}(t_+^0-1)\left(1+\frac{\partial f_\pm}{\partial \ln c_e}\right)\nabla\ln\overline{c_e}\right)=-a_s\bar{j}F \tag{4.63}$$

Finally, the **mass conservation in the solid electrode**, defined in equation (4.17), is written in spherical coordinates as

$$\frac{\partial c_s}{\partial t}=\frac{1}{r^2}\frac{\partial}{\partial r}\left(D_s r^2\frac{\partial c_s}{\partial r}\right) \tag{4.64}$$

since we assume spherical particles for the electrode active material.

4.6.4. Boundary conditions of the macroscopic model

For the **charge conservation in the solid electrode**, the boundary conditions are

$$\begin{cases}\nabla\overline{\phi_s}\big|_{x=L_{sep}+L_{pos}}=-\dfrac{i}{\sigma_{eff}}\\ \nabla\overline{\phi_s}\big|_{x=L_{sep}}=0\\ \overline{\phi_s}\big|_{x=0}=0\end{cases} \tag{4.65}$$

The first condition states that all the current in the cell is flowing through the electrode at the cathode current collector, the second one that no current is flowing through the electrode at the cathode/separator interface, and the third one that the potential is set to zero at the lithium metal interface.

The **mass conservation in the electrolyte** has as boundary conditions

$$\begin{cases}\nabla\overline{c_e}|_{x=L_{sep}+L_{pos}}=0\\ D_{e,eff}\nabla\overline{c_e}|_{x=0}=(1-t_+^0)\,\bar{j}\end{cases} \tag{4.66}$$

Where the first condition refers to the absence of electrolyte flux at the cathode current collector, while the second one considers the flux of lithium from the lithium metal anode upon charge and discharge.

Regarding the **charge conservation in the electrolyte**, we can write as boundary conditions

$$\begin{cases}-\kappa_{eff}\nabla\overline{\phi_e}-\dfrac{2\kappa_{eff}RT}{F}(t_+^0-1)\left(1+\dfrac{\partial f_\pm}{\partial \ln c_e}\right)\nabla\ln\overline{c_e}\bigg|_{x=L_{sep}+L_{pos}}=0\\ -\kappa_{eff}\nabla\overline{\phi_e}-\dfrac{2\kappa_{eff}RT}{F}(t_+^0-1)\left(1+\dfrac{\partial f_\pm}{\partial \ln c_e}\right)\nabla\ln\overline{c_e}\bigg|_{x=0}=i\end{cases} \tag{4.67}$$

where the first condition refers to the absence of current in the electrolyte at the cathode current collector, and the second one states that all the current is flowing through the electrolyte at the lithium anode/separator interface.

Lastly, the boundary condition for the **mass conservation in the solid electrode** particles are

$$\begin{cases} \nabla\overline{c_s}|_{r=0} = 0 \\ \nabla\overline{c_s}|_{r=R_p} = -\,\overline{j} \end{cases} \tag{4.68}$$

where we have the no-flux condition at the center of the particle ($r = 0$), and the correspondence between the averaged molar flux and the concentration gradient at the particle outer surface ($r = R_p$, where R_p is the radius of the cathode particles).

4.6.5. Other definitions

The cell voltage is calculated as the difference between the solid potential of the cathode current collector and the lithium metal anode. Since the potential of the anode is set to zero, we will have

$$V = \overline{\phi_s}\big|_{x=L_{sep}+L_{pos}} - \overline{\phi_s}\big|_{x=0} + R_{ext}\, i \tag{4.69}$$

The overpotential η is calculated as

$$\eta = \overline{\phi_s} - \overline{\phi_e} - E_{ocp} \tag{4.70}$$

where E_{ocp} is the open circuit potential of the electrode.

The initial anion concentration in the cathode $c_{s,pos,0}$ is calculated as

$$c_{s,0,pos} = c_{s,max,pos}\left[SOC\left(SOC_{max,pos} - SOC_{min,pos}\right) + SOC_{min,pos}\right] \tag{4.71}$$

where SOC is the state of charge of the cell, $c_{s,max,pos}$ is the maximum anion concentration in the cathode, and $SOC_{max,pos}$ and $SOC_{min,pos}$ are respectively the maximum and minimum state of charge limits of the positive electrode.

The capacity of the cell Q can be written as

$$Q = A\, \varepsilon_{s,pos}\, L_{pos}\, c_{max,pos}\, F\, (SOC_{max,pos} - SOC_{min,pos}) \tag{4.72}$$

where A is the surface area of the cell.

Since the only source of anions in the battery is the electrolyte, the salt concentration of the electrolyte will vary according to the state of charge of the cell. The salt concentration will be at the maximum when the battery is fully discharged, and at the minimum when the battery is fully charged. Hence, we can write the initial salt concentration in the electrolyte $c_{e,0}$ as a function of SOC as

$$c_{e,0} = c_{e,ref}\left(1 - \frac{SOC\ \frac{Q}{F}}{c_{l,ref}\ A\ \left(\varepsilon_{e,sep}\ L_{sep} + \varepsilon_{e,pos}\ L_{pos}\right)}\right) \tag{4.73}$$

where $c_{e,ref}$ is the reference salt concentration, i.e., the salt concentration when the state of charge is equal to zero. The fraction of equation (4.73) represent the ratio between the number of anions required by the cathode and the number of available anions that are present in the electrolyte.

The empirical equations that correlate the temperature and salt concentration in the electrolyte with the ionic conductivity κ, the salt diffusion coefficient D_e, the activity coefficient $\left(1 + \frac{\partial f_{\pm}}{\partial \ln c_e}\right)$ and the cation transference number t_{+}^{0} are respectively[233]

$$\kappa = 0.1 \cdot 0.798\left(1 + (T - 228)\right) c_e \cdot \frac{1 - 1.22\sqrt{c_e} + 0.509\left(1 - 0.004\, e^{\frac{1000}{T}}\right) c_e}{1 + c_e^{4}\left(0.00379\, e^{\frac{1000}{T}}\right)} \tag{4.74}$$

$$D_e = 1 \cdot 10^{-10} \cdot 1470\, e^{1.33\, c_e} \cdot e^{-\frac{1690}{T}} \cdot e^{-\frac{563}{T} c_e} \tag{4.75}$$

$$\begin{aligned}\left(1 + \frac{\partial f_{\pm}}{\partial \ln c_e}\right) = {} & -5.58 + 7.17\, c_e + 0.038\, T + 1.91\, c_e^{2} - 0.0665\, c_e T - 5.08 \\ & \cdot 10^{-5}\, T^{2} + 0.11\, c_e^{3} - 0.0061\, c_e^{2} T + 1.51 \cdot 10^{-4}\, c_e T^{2}\end{aligned} \tag{4.76}$$

5. Materials and methods

5.1. Experimental techniques

5.1.1. Physicochemical characterization

The **thermogravimetric analysis (TGA)** was performed with a TG 209 F1 Libra (NETZSCH GmbH) to analyze the PTMA powder samples and the related conductive carbon additives. All the tests were performed with a heating rate of 5 $K \cdot min^{-1}$ with a total gas flow of 40 $ml \cdot min^{-1}$. 65 µl alumina open crucibles were used, filled with 10 ± 0.010 mg of sample. The conductive carbon additives were analyzed too, and the crucibles were filled with the amount of carbon additive that should be present in 10 mg of the respective polymer-carbon mixture. The first part of the test (pyrolysis) used only nitrogen gas, heating up to 800°C. After cooling down back to 30°C, the gas was switched to a mixture of 5% oxygen and 95% nitrogen (volume fraction) and the temperature was kept constant for 30 min. Then, in the second part of the test (oxidation) the sample was heated up to 800°C, for the samples with multi-walled carbon nanotubes, or 1000°C, for the samples with graphene nanoplatelets and carbon black.

The true density of the PMTA powder samples was measured through **gas pycnometry** with a helium pycnometer (Ultrapyc 1200e, Quantachrome Instruments) at room temperature. The large volume cell was used to obtain the density values, and the measurement was repeated for a maximum of 12 times until a standard deviation lower than 0.01 $g \cdot cm^{-3}$ was obtained.

The **scanning electron microscopy (SEM)** micrographs of the PTMA powders and electrodes were taken with a ZEISS Crossbeam XB340 field-emission electron microscope at a working voltage of 5 kV.

5.1.2. Electrochemical characterization

The **electronic conductivity** of the PTMA powder samples was measured with the two-contact probe method. The powder samples were mixed with polytetrafluoroethylene (PTFE) binder, in weight ratio 9:1 in dispersion of isopropanol. Mixtures were subjected to ball milling on a Retsch PM100 for 30 minutes (300 rpm). Black gum-like slurries were then rolled between parchment paper and glass plate, and left to dry in vacuum overnight. For each sample, three pellets were prepared, containing 50, 100, 200 mg, and/or 400 mg of active material, and they were pressed with 4 ton for 1 minute. The diameter of all of the pellets was 10 mm. After drying in vacuum oven, conductive adhesive silver paste was applied on both sides of the pellet and the pellet was dried once more in vacuum oven overnight at 80 °C. The thickness of all of the samples was measured after drying with a beak scale. For the impedance measurement, the pellets were put between two copper foils which were connected to the cycler. All of the impedance measurements were conducted on VMP Bio-Logic in the frequency range from 1 MHz to 10 mHz at 25 °C. The resistance found at the crossing of the real axis was used as the resistance value for the sample. Three pellets for each sample with different thicknesses were measured, and the slope of the resistance-thickness chart was obtained through linear regression. This slope k was used in the formula

$$\sigma = \frac{1}{k} \cdot \frac{1}{A} \tag{5.1}$$

where A is the area of the pellet, to calculate the electronic conductivity σ.

The **galvanostatic charge/discharge tests** were performed in a two-electrode coin cell setup, using a 12 mm diameter PTMA-based cathode, a 16 mm diameter glass fiber separator (Whatman GF/A) normally soaked with 70 µl of 1M $LiPF_6$ or 1M lithium bis(fluorosulfonyl)imide (LiFSI) in ethyl carbonate (EC)/dimethyl carbonate (DMC) 1:1 (battery grade, UBE), and a 14 mm diameter lithium metal anode (500 µm, battery grade, Honjo). For the tests with commercial separators, 10 µm thick polyolefin Hipore SV718 (Asahi Kasei) with 16 mm diameter were employed, which were left overnight in a vial with the abovementioned electrolyte and then used after removing the excess electrolyte on the surface, with an additional drop of electrolyte added on the cathode. For the tests with sodium metal (99.8 %, Acros Organics) a 14 mm anode was used, and the electrolyte was 1M $NaPF_6$ (battery grade, Fluorochem) dissolved in EC (battery grade, UBE)/PC (battery grade, UBE) 3:7. The cells were tested in a Maccor Series 4000 battery cycler in climatic chambers (Binder) at 20°C, between 3 and 4 V (2.8 and 3.8 V for the tests with sodium metal). The specific capacity used to calculate the current was 111 $mAh \cdot g^{-1}$, and the active material mass of the electrodes was calculated using the theoretical weight fraction of PTMA in the electrode. The error in the reported specific capacities is estimated to be ~2.5% based on the difference between the theoretical and actual weight fraction of PTMA in the polymer-carbon mixtures, weighing errors of the balances used for the synthesis and the slurry preparation (±0.001 g) and for the weighing of the electrodes (±0.00001 g). The cells performed 3 cycles at 0.1C, 5 cycles at 0.2C, 0.5C, 1C, 2C, 5C, 10C and 25C, and then they cycled at 1C till the stop of the test.

The **electrochemical impedance spectroscopy (EIS)** tests were conducted using a three-electrode ECC-PAT-Core cell (EL-CELL GmbH) setup. The cathode consisted of an 18 mm diameter PTMA-based electrode. The separator was made of glass fiber (Whatman GF/A) with a diameter of 21 mm, soaked in 200 µl of the electrolyte solution. An 18 mm diameter lithium metal disk (500 µm, battery grade, Honjo) served as the anode, and a lithium-coated nickel ring (EL-CELL GmbH) acted as the reference electrode, positioned between the cathode and the separator. The EIS measurements were carried out at a temperature of 20°C in climatic chambers (Binder) using a Biologic VMP battery cycler equipped with a frequency response analyzer. The EIS tests were executed in the potentiostatic mode, covering a frequency range of 100 kHz to 100 mHz, with 10 points for each decade. The voltage amplitude for EIS measurements was set at 10 mV. Galvanostatic charge/discharge tests were also performed with the same setup, instrument, and conditions, together with the EIS measurements. The cells performed 3 cycles at 0.1, then 3 cycles at 0.2C, 0.5C, 1C, 2C, and 5C, followed by 20 cycles at 1C. This whole procedure was repeated two times, with the impedance measurements made each time before the 0.2C cycles, measuring 10 impedance spectra at different state of charge (SOC) points along the 0.1C discharge that preceded the 0.2C cycles.

5.2. Materials preparation

5.2.1. Polymer synthesis

To synthesize the mixture of poly(2,2,6,6-tetramethyl-1-piperidinyloxy methacrylate) (PTMA) and conductive carbon additives, a procedure based on the melt polymerization method described in Vlad et al. was employed.[206] The amount of carbon additive added during the synthesis x (in grams) is equal to its weight fraction in the mixture multiplied by 20.

In a typical synthesis, $(20\text{-}x)$ g of 2,2,6,6-tetramethyl-4-piperidyl methacrylate (TMPM 98%, TCI) and $6.765\cdot(20\text{-}x)$ mg of asobisisobutyronitrile (AIBN, recrystallized in ethanol, TCI) were dissolved in acetone (VWR, technical grade). Subsequently, $30.59\cdot(20\text{-}x)$ µl of ethylene glycol dimethacrylate (EGDME 98%, Acros Organics) as a crosslinking agent were added to the solution. The solvent was removed by evaporating it first in a rotary evaporator and then in a Schlenk line connected to a vacuum pump equipped with a nitrogen trap.

The resulting dried precursor mixture was placed in a ball mill apparatus (Type S1, Retsch GmbH) containing three agate balls with a diameter of 3 cm. Additionally, x g of conductive carbon additive were added to the mixture. The precursor mixture was ball-milled for 1 hour at 80% of the maximum speed. Subsequently, the milled mixture was transferred to a 1000 ml cylindrical glass reactor, which underwent three purges with argon gas. The reactor was then immersed in a stirred oil bath and kept at 80°C overnight to facilitate the polymerization reaction.

After cooling to room temperature, the product, poly(2,2,6,6-tetramethyl-1-piperidyl methacrylate) (PTMPT) mixed with the carbon additive, was extracted by the reactor. Swelling it with dichloromethane (DCM, technical grade, VWR) allowed for the removal of the product, which was subsequently washed with the same solvent. The polymer-carbon mixture was dried using a rotary evaporator and a vacuum pump, followed by ball milling for 1 hour at 80% of the maximum speed of the ball mill apparatus.

To oxidize the PTMPT, 20 g of the polymer-carbon mixture were dispersed in methanol (technical grade, VWR) within a 1000 ml round bottom glass reactor. Stirring the mixture with a magnetic bar, $0.2729 \cdot (20-x)$ g of sodium tungstate (Na_2WO_4 99%, Sigma Aldrich), $0.1765 \cdot (20-x)$ g of ethylenediaminetetraacetic sodium salt (EDTA 98.5%, Sigma Aldrich), and $2 \cdot (20-x)$ ml of a 30% aqueous solution of hydrogen peroxide (H_2O_2, Sigma Aldrich) were added. The reaction took place for 48 hours in a stirred oil bath at 60°C, accompanied by an air-cooled reflux condenser. The resulting mixture was filtered several times under vacuum using a 1:1 volume ratio solution of water and methanol until the washing solution became colorless. The obtained mixture was dried in a vacuum oven (Binder) at 60°C overnight and further ball-milled for 1 hour at 80% of the maximum speed of the ball mill apparatus.

The synthesized samples had the following theoretical compositions (in weight fractions):

- **PTMA-GN15**: 85% PTMA, 15% graphene nanoplatelets (2-10 nm, Thermo Scientific)
- **PTMA-SP15**: 85% PTMA, 15% carbon black (Super P, Timcal)
- **PTMA-MW15**: 85% PTMA, 15% multi-walled carbon nanotubes (NC7000, Nanocyl)
- **PTMA-MW10**: 90% PTMA, 10% multi-walled carbon nanotubes
- **PTMA-MW5**: 95% PTMA, 5% multi-walled carbon nanotubes
- **PTMA-MW2.5**: 97.5% PTMA, 2.5% multi-walled carbon nanotubes

5.2.2. Electrode preparation

To obtain the PTMA-based cathodes used in the electrochemical characterization tests, a water-based method was employed. In a typical preparation, the following components were combined: 900 mg of the polymer-carbon mixture, 50 mg of conductive carbon (Super C45, IMERYS), 30 mg of carboxymethyl cellulose from a 3% weight aqueous solution (CMC, Walocel CRT 2000 PPA 12), 20 mg of styrene-butadiene rubber from a 40% latex solution (SBR, Zeon BM451-B), and 500 mg of deionized water (solid/solvent weight ratio: 40/60). To ensure thorough mixing, the components were blended in a planetary centrifugal mixer (ARE-250, THINKY) at 2000 rpm for 10 minutes. The weight ratio of the electrode components was maintained at 90:5:3:2 (PTMA/MWCNT:C45:CMC:SBR). Subsequently, the mixture was coated onto a carbon-coated aluminum foil (Wellcos) with a wet thickness of 120 µm, for the low mass loading electrodes, or 300 µm, for the high mass loading ones. The slurry-coated foil was then dried overnight in a dry room with a dew point below -70°C. Electrodes with a diameter of 12 mm (or 18 mm, for the impedance tests) were cut and pressed with a force of 1 ton. These electrodes were further dried at 80°C for 12 hours in a Büchi oven connected to a vacuum pump, maintaining a pressure below $1 \cdot 10^{-3}$ mbar. Finally, the dried electrodes were transferred to an argon-filled glove box (MB200B ECO, MBraun) with an oxygen concentration and water content below 0.1 ppm, where the cells were assembled.

5.3. Modeling tools

5.3.1. Macroscale physical model of the battery

The physical model, derived and presented in Section 4.6, is composed of the equations summarized in **Table 6.3**. The model simulates the behavior of a dual-ion battery, i.e., a battery with a cathode where anions partake in the redox process and an anode where cations are instead involved, with a modified version of the pseudo-2D Doyle-Fuller-Newman model for the macroscale physical simulation of lithium-ion batteries. The cathode is a porous electrode, while the anode is modelled as a metal surface, and the electrodes are separated by a porous separator. The model is implemented in COMSOL Multiphysics®, in the version 6.0, using the Battery Design Module. The EIS is simulated with COMSOL Multiphysics® by linearizing the model around the chosen open-circuit potential and performing the Laplace transform.[234]

5.3.2. Cost and performance analysis model

An analysis of the energy density and cost was conducted using a modified version of the freely available software BatPaC 5.0, which is described in detail in a report published by the Argonne National Laboratory.[75] This software model is specifically designed to simulate battery packs with predetermined energy and power ratings. It takes into account the costs associated with various components, such as active materials, conductive carbon, binders, separators, electrolytes, current collectors, casings, pack current collectors, cooling systems, labor, and overhead expenses. Furthermore, it considers investment costs related to the production site.

More details about the parameters used in the model and on the types of simulated battery packs are given in the Appendix of the Sections where BatPac 5.0 is employed.

6. Results and discussion

The results and related discussions presented in this section and its subsections have been reported in the following scholarly journal articles, which have already been published, submitted for publication, or are currently undergoing peer-review.

Section 6.1:

- Zuo W.*, **Innocenti A.***, Zarrabeitia M., Bresser D., Yang Y., Passerini S., Layered Oxide Cathodes for Sodium-Ion Batteries: Storage Mechanism, Electrochemistry, and Techno-economics. *Accounts of Chemical Research* **2023**, 56, 3, 284-296

- **Innocenti A.***, Beringer S.*, Passerini S., Cost and Performance Analysis as a Valuable Tool for Battery Material Research. *Nature Reviews Materials* **2024**, 9, 347-357

Section 6.2:

- **Innocenti A.**, Adenusi H., Passerini S., Assessing N-Type Organic Materials for Lithium Batteries: A Techno-Economic Review. *InfoMat* **2023**, 5, 11, e12480

Section 6.3:

- **Innocenti A.**, Álvarez Moisés I., Gohy J.-F., Passerini S., A Modified Doyle-Fuller-Newman Model Enables the Macroscale Physical Simulation of Dual-ion Batteries. **2023**, 580, 233429

Section 6.4:

- **Innocenti A.**, Álvarez Moisés I., Lužanin O., Dominko R., Bitenc J., Gohy J.-F., Passerini S., Practical cell design for PTMA-based organic batteries: an experimental and modeling study. **2023**, *https://doi.org/10.1021/acsami.3c11838*

*: Co-first authors

6.1. Cost and energy density analysis as valuable tool for battery material research

The analysis of cost and performance is a crucial aspect of battery research, since it provides provide insights and guidance for researchers and industry professionals on the current state and the possible future of electrochemical energy storage[13,235–238]. Typically, the cost and performance analysis has been employed with a high-level approach, which addresses the directions that battery technology should take to achieve specific targets of energy density and price, without focusing on specific materials and/or using actual experimental data, but making assumptions on the properties that batteries have (or should have)[239]

Instead, an accurate low-level approach that focuses on the implementation of cost and performance analysis in the material discovery phase is seldom seen[240,241]. Even when the cost and energy density estimations for new materials are given, very simplistic calculations and assumptions are often done. For example, estimating the energy density of a new cathode material multiplying the maximum obtainable specific capacity with the average voltage value gives only a partial and often very optimistic picture of the true energy density that can be achieved by a battery cell with such a cathode in realistic conditions. Or assuming that a cathode material whose precursors have a low price translates automatically in an inexpensive battery pack, without considering how the conditions for a scale up to a commercial solution influence the final cost, or the actual share of the cathode cost in the whole system[242]. If properly applied, the cost and performance analysis can actually well support the research of new energy storage materials, since currently a variety of new chemistries are explored as complementary solutions or substitutes to lithium-ion batteries.

In this Section, we will present both examples of high-level and low-level approach, applying the cost and performance analysis for two research problems: understanding the different impact of raw material price increases on the cost of LIBs and SIBs (high-level approach) and selecting the best performing sodium-ion cathodes for the implementation in battery packs according to the shape of their voltage curve (low level approach).

6.1.1. Impact of raw material price increases on LIBs and SIBs

One relevant example of a high level approach was given in Vaalma et al.[13], which compared the cost and energy density of lithium- and sodium-ion batteries, using and evaluating the impact of possible improvements in the sodium-ion technology. Compared to LIBs, the absence of cost-sensitive elements like Li and Co in sodium-ion cathodes and the use of aluminum current collector for the anode should have led to a much lower cost for SIBs.[243] However, the results of Vaalma et al. opposed this assumption, due to the lower energy density that the SIBs materials could ensure.

In a more recent work from our group, where an account on layered oxide sodium cathodes was presented,[56] we proposed a similar analysis, focusing on the latter class of materials and taking into account price fluctuations of the raw materials for LIBs and SIBs. In fact, the price of the main raw materials for LIBs rose drastically due to the pandemic crisis and geopolitical instabilities, while the main raw materials for SIBs have experienced a smaller price increment. For instance, the price of lithium carbonate (Li_2CO_3) passed from 7.20 \$ kg^{-1} in January 2020 to 78.00 \$ kg^{-1} in April 2022, whereas sodium carbonate (Na_2CO_3) costed 0.25 \$ kg^{-1} and 0.40 \$ kg^{-1} on the same dates, respectively. Therefore, it is expected that the costs of current LIBs and SIBs would differ substantially from those of 2 years ago. We estimated the cost of selected lithium- and sodium-ion cathode materials by modelling their synthesis process (more information about raw material prices and the synthesis models are found in **Appendix 1** in **Table A1.2**).

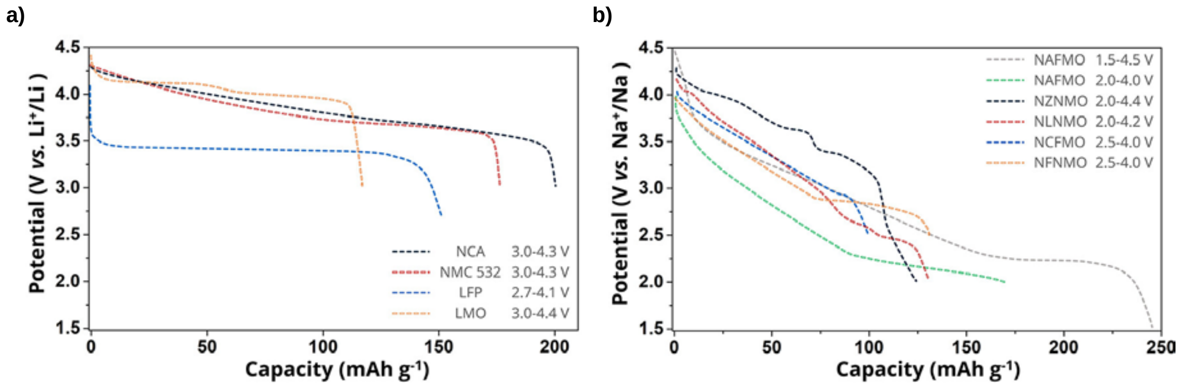

Figure 6.1 *- Discharge curves of the selected (a) lithium cathodes and (b) sodium cathodes from the respective references. Reproduced from permission from Zuo et al., CC BY 4.0 2023, ACS Publications*[56]

The modelled LIBs are $Li[Ni_{0.5}Mn_{0.3}Co_{0.2}]O_2$ (NMC 532), $Li[Ni_{0.8}Co_{0.15}Al_{0.05}]O_2$ (NCA), $LiFePO_4$ (LFP) and $LiMn_2O_4$ (LMO) coupled with graphite as anode, whose cost has been recalculated with the same scheme used for the sodium-ion cathodes (**Figure 6.1.a**). The modelled SIBs cathode are chosen among the most advanced and promising layered oxides present in literature: $Na_{0.66}[Al_{0.1}Fe_{0.05}Mn_{0.85}]O_2$ (NAFMO),[244] $Na_{0.66}[Ni_{0.26}Fn_{0.06}Mn_{0.67}]O_2$ (NZNMO),[245,246] $Na[Li_{0.10}Ni_{0.35}Mn_{0.55}]O_2$ (NLNMO),[247] $Na_{0,9}[Cu_{0.22}Fe_{0.30}Mn_{0.48}]O_2$ (NCFMO),[248,249] and $Na[Fe_{0.40}Ni_{0.30}Mn_{0.30}]O_2$ (NAFMO),[250]each coupled with a biomass-derived hard carbon as anode (**Figure 6.1.b**).[251] The data required for the simulations of these materials were obtained from the publications that described their synthesis and performances. The NAFMO is simulated in its fully sodiated phase ($Na[Al_{0.1}Fe_{0.05}Mn_{0.85}]O_2$), considering the addition of a stoichiometric amount of $Na_2C_2O_4$ as sacrificial salt in the cathode.[252]

The software BatPac 5.0 was used to simulate different commercial battery packs with several lithium- and sodium-ion cathodes, to compare the gravimetric and volumetric energy density of the different solutions, as well as the cost of the packs considering the different prices of raw materials in January 2020 and April 2022.[75] The data required for the simulation of the selected lithium-ion batteries were already present in the BatPac 5.0 database. The simulated battery packs are the ones of a small domestic energy storage system of 7 kW and 11.5 kWh, a plug-in hybrid electric vehicle (pHEV) of 110 kW and 15 kWh, and a high-end full electric vehicle (EV) of 150 kW and 100 kWh (see **Table A1.3** of the **Appendix 1**).

Figure 6.2.a and **Figure 6.2.b** show the mass/energy costs of the evaluated cathodes. In 2020, the mass costs of the evaluated Na cathodes follow the order NLNMO (12.48 $\$ kg^{-1}$) > NZNMO > NFNMO > NCFMO > NAFMO (10.22 $\$ kg^{-1}$), which are comparable to those of LFP (12.46 $\$ kg^{-1}$) and LMO (11.16 $\$ kg^{-1}$). Two years after, the cost difference between these cathode materials increased substantially. The costs of Li cathodes increased by at least 143%, while those of NAFMO and NCFMO only increased by 16% and 14%, respectively. The mass cost increment of NLNMO is 62%, which is the highest among the Na cathodes due to the presence of Li. As a result, the mass costs of Li cathodes have become significantly higher than those of Na cathodes. Note that the content of Co of the considered Li cathodes is very low; otherwise, the difference in cost would be greater.

Similar trends are observed in energy cost. In 2020, NAFMO and NLNMO showed the lowest and highest energy costs of 25.34 and 33.76 $\$ kWh^{-1}$ among Na cathodes, respectively, which are higher than those of LFP (24.21 $\$ kWh^{-1}$) and LMO (23.43 $\$ kWh^{-1}$). Two years later, the energy costs of the five Na cathodes follow the order NLNMO (54.56 \$ kWh^{-1}) > NZNMO (41.11 \$ kWh^{-1}) > NFNMO (40.42 \$ kWh^{-1}) > NCFMO (39.77 \$ kWh^{-1}) > NAFMO (29.67 \$ kWh^{-1}), which are lower than those of LFP (58.91 \$ kWh^{-1}) and LMO (59.94 \$ kWh^{-1}), demonstrating that the current layered oxide sodium cathodes have a substantial cost advantage over lithium cathodes.

Figure 6.2.c presents the costs of 36 different battery packs based on the price of raw materials in January 2020 and April 2022. LFP-/LMO-based packs show the lowest costs, followed by NMC-/NCA-based batteries. With increased pack energy, the energy cost of LIBs decreases due to economy of scale effects and the lower impact of the hardware costs (casings, battery management system, and cooling system). The energy costs of all SIBs are higher than those of LIBs. NZNMO-/NFNMO-based battery packs for grid storage show the lowest energy cost among the SIB packs, but it is still 33% higher than that of LFP-/LMO-based grid storage packs. NAFMO has the lowest mass and energy cost among the considered Na cathodes. However, the pack costs of NAFMO-based SIBs are much higher than those of NZNMO, NCFMO, and NFNMO because of a lower working potential and increased positive electrode porosity due to the presence of the sacrificial salt.

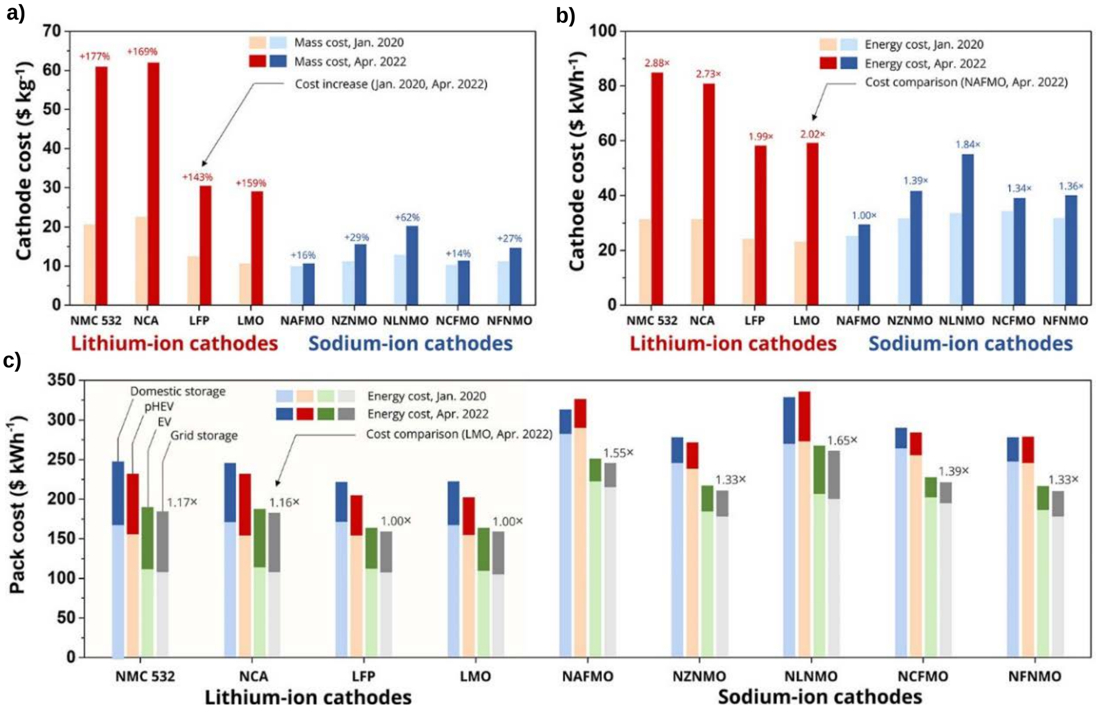

Figure 6.2 – Comparison of (a) cost per unit mass and (b) cost per unit energy between lithium-ion and sodium-ion cathodes. (c) Costs of battery packs based on various lithium- and sodium-cathode materials. Reproduced from permission from Zuo et al., CC BY 4.0 2023, ACS Publications[56]

NLNMO has the highest cost among the Na cathodes, and NLNMO-based batteries show the highest pack costs, demonstrating that high ratio of Li, such as 10%, should be avoided in cost-effective Na cathodes.

From these results, we can see how the current raw material costs of Na cathodes are substantially lower than those of Li cathodes. However, the pack costs of SIBs are still higher than those of LIBs To clarify the cost gap between SIBs and LIBs, cost breakdowns of grid-storage packs are analyzed more in detail.

As presented in **Figure 6.3.a**, the positive active materials, negative active materials, electrolyte, pack and module purchased items, and electrode-preparation compounds (carbon + binder + solvent) occupy over 90% of the pack cost. Except for the NLNMO-based battery, the cathode costs of the evaluated SIBs are comparable to or even lower than those of LMO-/LFP-based batteries. However, the negative active material costs much more in SIBs than in LIBs because of the higher average working potential of hard carbon than graphite and the lower working potential of Na cathodes. For example, the hard carbon costs $19,183 in NAFMO-based SIBs, which is 3 times the cost of graphite in LFP-based LIBs. Besides, the lower energy densities of both the cathode and anode for SIBs require higher amounts of electrolyte, electrode-preparation compounds, and the pack + module purchased items, leading to unfavorable pack cost of SIBs. An increase in the electrolyte price is hence more impactful for SIBs than LIBs.

With the higher amount of positive active material, the cost of the SIB packs might be significantly reduced by transitioning from poly(vinylidene difluoride) (PVdF) dissolved in N-methyl-2-pyrrolidone (NMP) to water-soluble binders due to the cost advantages of water over NMP (70–200 times), water-soluble and F-free polymers over PVdF (2–5 times), and the lower energy needed for the electrode drying process.[253,254] The challenge of incorporating water-soluble binders lies in the high reactivity of NaxTMO2 toward moisture.[255,256] Better surface coverage of the active material particles by the binder, suppressing electrolyte decomposition, and enhanced mechanical integrity of such electrodes could be achieved via the interaction with the hydroxyl/carboxyl groups in such water-soluble polymers as well as the reduced swelling with the electrolyte.[257,258]

LFP-based LIBs and NZNMO-based SIBs are further selected to compare the cost proportions of pack components (**Figure 6.3.b**). With the increment in energy of battery packs, the cost proportions of the electrode active materials, electrolyte, and electrode-preparation compounds increase, while the ones of purchased items and hardware decrease. The positive active material occupies a smaller cost proportion in NIBs than in SIBs. On the contrary, the balance of negative active material, electrolyte, and electrode-preparation components is higher than that of LIBs. Moreover, more current collectors and separators are required for SIBs, leading to a higher cost for positive current collectors and separators. The cost proportion of the negative current collector in NIB packs is 2–3% lower than in LIB packs, as the expensive Cu could be replaced by Al.

In summary, the analyzed layered oxide-based SIBs have cost advantages for the positive active material and negative current collector, which are outbalanced by the higher costs of other battery components, due to the lower energy density of the modelled SIBs. Nevertheless, the difference in cost between January 2020 and April 2022 is much more relevant for the LIBs, with a cost increase between +30% for LFP and +45% for NMC 532. Instead, the cost increase is limited between +10% and +23% for the SIBs, confirming their higher resilience to raw material price increases.

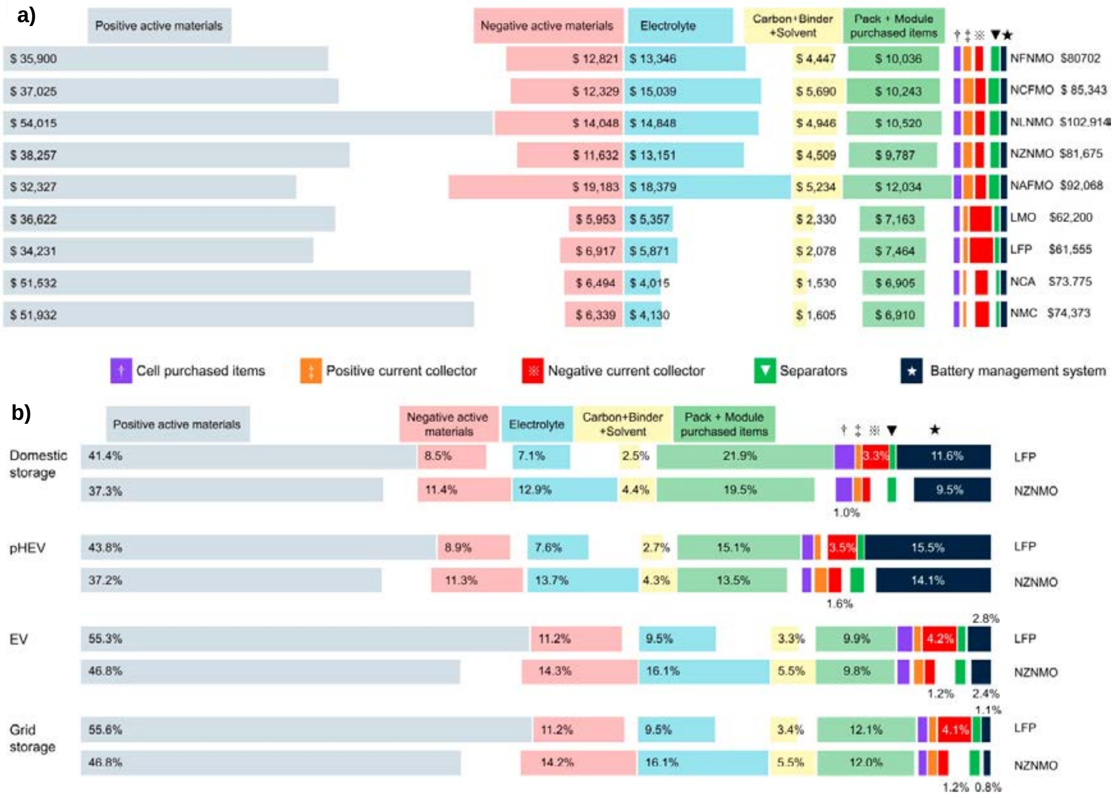

Figure 6.3 *– (a) Cost breakdown of various SIBs and LIBs for grid storage. (b) Cost breakdown of LFP-based and NZNMO-based battery packs with the prices of April 2022. Reproduced from permission from Zuo et al., CC BY 4.0 2023, ACS Publications*[56]

6.1.2. Link between voltage profile and performance in sodium-ion battery packs

To illustrate the potentialities of a low-level approach for the cost and performance analysis on battery material research, we will explore some case studies regarding sodium-ion battery packs. Our objective is to illustrate how to select the most promising active materials, or of treatments to improve their performance, for further experiments and investigation. We do this by quantitatively analyzing the results of these simulations, using the effect of lower cut-off voltage and pre-sodiation strategies as examples, to assess their impact on the cost and energy density of sodium-ion batteries.

Our analysis will draw from published works on sodium-ion batteries, utilizing experimental data retrieved from literature (see **Table A1.4**). Each case study will consider three cathode materials, while the anode material will be the same for all the analyses. Among all the metrics provided as results by the simulations, we will focus on the pack gravimetric energy density (in $Wh\cdot kg^{-1}$), pack volumetric energy density (in $Wh\cdot l^{-1}$), and pack cost per kWh (in $\$\cdot kWh^{-1}$), which are used to assess the size and cost of the resulting battery packs. In **Table 6.1**, all the results of the simulations for the three case studies are reported, and the energy density and cost of all the modelled battery packs are compared between them and with lithium-ion batteries in **Figure A1.3**, **Figure A1.4,** and **Figure A1.5**.

Lower cut-off voltage variation

The key to achieve (sodium-ion) batteries with good energy density and low cost is to develop cathode materials which can combine a high average working voltage with a high specific capacity. Equally important, the voltage should not excessively decrease while discharging the battery, since a battery pack must be designed to provide the required power performance even at low state of charge. If the voltage sinks too much, the current has to increase accordingly to keep the electric power (i.e., the voltage by current product) constant in the low state of charge region. All the cables and busbars connected to the current collectors have to be designed bigger and heavier to withstand a higher current without excessive heating and voltage drop, contributing to the energy density decrease of the battery pack. Moreover, there are limits related to the power electronics, too: the USABC recommends that the minimum battery voltage should not be lower than 50-55% of its maximum voltage, to stay within the working range of the power converters.[259,260]

Nevertheless, the sodium-ion battery literature is full of examples of cathode materials with relatively high specific capacity that are cycled in large voltage windows, from about 4 V to well below 2.5 V, and a similar trend can be observed also for many materials that belong to the already mentioned innovative post-lithium-ion chemistries. This is usually the result of voltage profiles with several plateaus and strong gradients. Commercial lithium-ion battery cathodes, instead, have a lower cut-off voltage between 2.5 V and 3.5 V, according to the type of material, and they are characterized by high and gently sloping voltages, as the NMC family or the NCA, or by single or double high-voltage plateaus, like LFP and LMO[6]. These properties help in keeping stable the power provided by the battery even at low state of charge.

Table 6.1 *– Summary of the main results of the simulations for all the case studies*

Lower cut-off voltage variation

Material	**Lower cut-off voltage target**	**Lower cut-off voltage [V]**	**Pack volumetric energy density [Wh·l^{-1}]**	**Pack gravimetric energy density [Wh·kg^{-1}]**	**Pack cost per kWh [\$·kWh^{-1}]**	**Capacity loss after cut [%]**	**Battery average voltage [V]**
$NaFe(PO_4)$	Initial value	0.30	157.0	84.2	156.9	0.84%[a]	2.17
	1.5 V	1.50	141.4	75.7	171.4	26.95%	2.58
	USABC target	2.28	116.3	61.8	205.7	48.53%	2.88
$Na[Ni_{0.3}Fe_{0.4}Mn_{0.3}]O_2$	Initial value	1.30	208.4	108.0	136.9	0.26%[a]	2.77
	1.5 V	1.50	207.0	107.2	137.7	2.02%	2.80
	USABC target	2.09	190.4	98.1	148.6	17.46%	2.97
$Na_3V_2(PO_4)_2F_3$	Initial value	2.30	199.9	106.0	158.9	0.36%[a]	3.61
	1.5 V	-	-	-	-	-	-
	USABC target	2.37	199.3	105.7	159.3	0.99%	3.62

Pre-sodiation for the capacity increase of cathode materials

Material	**Pre-sodiation**	**Lower cut-off voltage [V]**	**Pack volumetric energy density [Wh·l^{-1}]**	**Pack gravimetric energy density [Wh·kg^{-1}]**	**Pack cost per kWh [\$·kWh^{-1}]**	**Capacity gain with p.-s. [%]**	**Battery average voltage [V]**
$Na_3V_2(PO_4)_2FO_2$	No	2.15	203.4	108.4	161.7	0	3.47
	Yes (anode)	0.15	214.3	118.1	142.3	49.6	2.98
	Yes (cathode)	0.15	196.8	110.3	148.0	49.6	2.98
$Na_{0.6}[Ni_{0.22}Al_{0.11}Mn_{0.66}]O_2$	No	1.60	230.6	119.2	126.0	0	3.43
	Yes (anode)	0.50	238.8	129.9	111.9	66.9	2.83
	Yes (cathode)	0.50	209.5	117.3	119.7	66.9	2.83
$Na_{0.6}[Ni_{0.22}Fe_{0.11}Mn_{0.66}]O_2$	No	1.30	211.8	108.5	138.0	0	3.17
	Yes (anode)	0.70	221.7	119.7	120.8	66.4	2.65
	Yes (cathode)	0.70	194.7	108.3	129.1	66.4	2.65

Pre-sodiation for first cycle sodium loss compensation

Material	Pre-sodiation	Lower cut-off voltage [V]	Pack volumetric energy density [$Wh \cdot l^{-1}$]	Pack gravimetric energy density [$Wh \cdot kg^{-1}$]	Pack cost per kWh [$\$ \cdot kWh^{-1}$]	Capacity gain with p.-s. [%]	Battery average voltage [V]
$Na_3Fe_2(PO_4)_3$	No	0.70	147.5	77.1	173.1	0	2.39
	Yes (anode)	0.45	153.3	81.4	163.4	16.8	2.29
	Yes (cathode)	0.45	150.0	79.9	165.5	16.8	2.29
$Na_{0.95}[Ni_{0.32}Mn_{0.32}Mg_{0.16}Ti_{0.21}]O_2$	No	1.30	205.6	104.0	143.9	0	3.00
	Yes (anode)	0.70	211.4	108.6	137.2	15.4	2.88
	Yes (cathode)	0.70	204.2	106.0	138.9	15.4	2.88
$Na_2Mn[Fe(CN)_6]$	No	1.95	159.3	99.3	130.3	0	3.11
	Yes (anode)	0.70	168.4	105.2	121.9	14.4	3.05
	Yes (cathode)	0.70	165.7	103.6	123.2	14.4	3.05

[a] The capacity loss at the initial value of cut-off voltage is higher than 0 because this initial cut-off voltage was slightly adjusted to obtain a round number.

Moreover, the anode materials of choice for sodium-ion batteries are hard carbons, i.e., disordered carbonaceous materials where sodium ions can be reversibly de-/intercalated in their closed nanoporosity and graphitic domains[261]. Hard carbons anodes are characterized by a voltage profile that combines a plateau region around 0.1 V and a sloping region where the voltage rises gradually to about 1.5 V [251]. When a sodium-ion cathode and anode are combined in a full cell, the anode sloping voltage region causes a gradual drop of the battery voltage from the mid to low state of charge of the battery, regardless of the voltage profile of the cathode. This effect is not present in commercial lithium-ion full cells, where the graphite anode voltage rises steeply only for extremely low states of charge[262]. Hence, sodium-ion batteries are even more affected than lithium-ion batteries by a drop in the voltage towards the end of discharge. A strongly sloping voltage can be found also in other classes of negative electrodes still in research phase, such as conversion-alloying materials[45] and organic anodes[172].

The voltage window in which a sodium-ion battery is cycled is then a fundamental parameter not only for what concerns the stability of the electrodes and the capacity retention[263], but also for the design of the battery pack. By increasing the lower cut-off voltage of the battery, its average voltage is increased and there are benefits related to the battery pack architecture, but this comes at the expense of a part of the available capacity. A material with a higher specific capacity that is delivered mostly at low voltage could have then the same or even worse overall performance in battery packs of a material with a lower capacity which lies entirely at a higher, more stable voltage.

To study the effect of this variable, the lower cut-off voltage of the batteries obtained by coupling the cathode materials with the hard carbon anode is varied and the cost and energy density simulations are carried out. We will consider as cut-off voltage targets both 55% of the maximum cell voltage (as of USABC specifications) and 1.5 V, which was reported as typical minimum cell voltage in recent publications and datasheets on commercial sodium-ion batteries.[264] The materials subjects of this analysis are the maricite-phase $NaFe(PO_4)$ (NFP),[265] $Na[Ni_{0.3}Fe_{0.4}Mn_{0.3}]O_2$, an O3-phase layered oxide (NNFMO),[250] and $Na_3V_2(PO_4)_2F_3$, a vanadium-based polyanionic compound (NVPF).[266]

Looking at **Figure 6.4**, we can observe how the three materials are affected in a remarkably different way from this cut, according to the shape of the cathode voltage. The higher its slope, the larger the capacity that has to be removed to achieve the target cut-off voltages, a fact that is detrimental for the performance of the pack. The removal of this capacity comes however with an increase of the average operation voltage, which is instead beneficial for the energy density. The relative impact of these two effects depends on the shape of the voltage curve. For instance, the average voltage of the NFP battery increases from 2.17 V to 2.58 V (+19%) when moving the cut-off to 1.5 V, and to 2.88 V (+33%) when the 55% maximum voltage criterion is used. However, the stronger effect among the two is the capacity drop: in fact, there is a 10% decrease in pack gravimetric energy density and a 9.2% pack cost increase for the 1.5 V cut-off, and the values rise respectively to 26.6% and 31.1% for the higher cut-off voltage. The NNFMO battery has already an initial cut-off voltage of 1.3 V, so raising it to 1.5 V does not cause a relevant drop the pack metrics (ca. 2% capacity loss). With 55% of the maximum voltage, i.e., 2.09 V, the capacity instead decreases more than 17%, while the average voltage increases of only 7%, resulting in a decrease of pack energy density and increase of cost respectively of -9.1% and +8.6%. The NVPF battery shows instead already an initial lower-cut-off voltage very near to the USABC target (2.30 vs. 2.37), and its increase to this value causes virtually no detrimental effect on the battery pack performance.

We can then recognize that, in the case of the cathode materials with strongly sloping voltage profiles, there are limitations in terms of available capacity when considering practical cut-off voltage restrictions, which need to be applied to limit the voltage drop during discharge. However, many (sodium-ion) battery cathode materials are still cycled within a very wide voltage range. In light of this, we recommend calculating the actual battery voltage curve after coupling with a suitable anode material. Then, when reporting the capacity and energy density achievable with a specific cathode material, it is crucial to take into account the aforementioned cut-off voltage limitations.

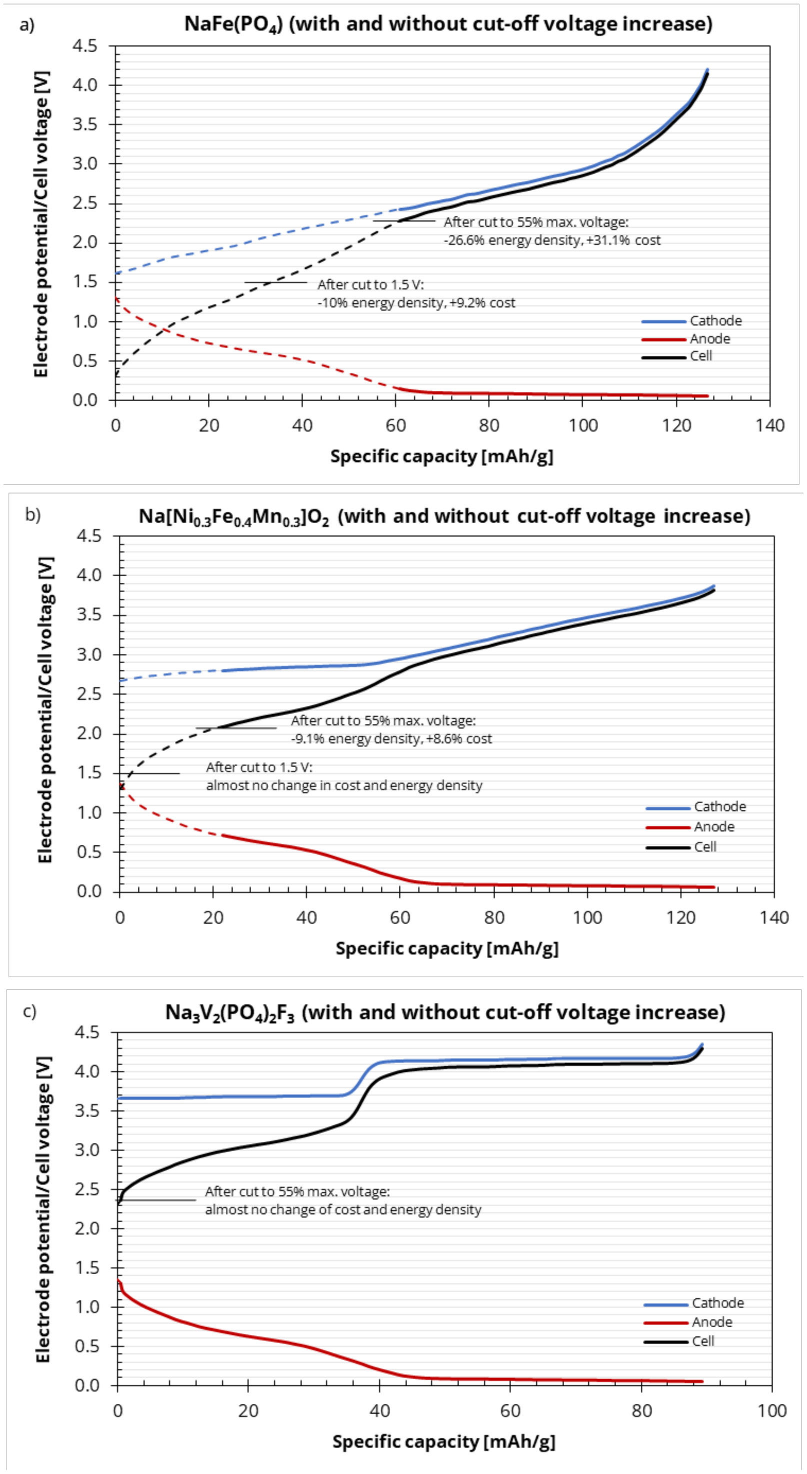

Figure 6.4 *– Electrode potentials of cathode and anode and resulting cell voltages of the materials analyzed in the lower cut-off voltage study. a) NFP; b) NNFMO; c) NVPF. The dashed line represents the part of battery voltage and capacity that are removed after the increase of the lower cut-off voltage to the USABC target of 55% of the maximum voltage.*

This approach ensures that the performance of the materials aligns more closely with what is achieved in realistic applications, and it is helpful to select among novel materials the ones that meet the operative voltage window requirements for the implementation in battery packs. The decrease in performance due to a higher cut-off voltage, if reasonably limited, may be regarded as acceptable if this strongly benefits the pack architecture, as if in the 1.5 V cut-off case for NFP and the 2.09 V cut-off case for NNMFO, where the relevant metrics suffer a change lower than 10%.

Pre-sodiation for the capacity increase of cathode materials

Some sodium-ion cathode materials are synthesized with a less than stoichiometric sodium content. This holds true, for instance, with materials in the P2-phase layered oxide class[267] and certain polyanionic compounds.[266] Consequently, their complete capacity cannot be harvested without the addition of sodium to their structure. However, in a standard battery, the source of cations is the cathode, with the anode being in its discharged form when the battery is manufactured. Pre-sodiation is a treatment applied to the anode or cathode material, providing additional sodium ions to facilitate the utilization of the cathode's full capacity.[268]

The electrochemical pre-sodiation of anodes and cathodes with sodium metal can be applied at laboratory scale, but it is not regarded as a scalable and industrially viable pathway. Solutions that can be easily implemented in the roll-to-roll production process, such as chemical treatments in baths that were by now reported for only lithium-based systems, are interesting for the anode side.[269–271] The pre-sodiation of cathodes with sacrificial salts can be another viable approach: during the first charge of the battery, the electrochemical decomposition of the sacrificial salt, assumed here to be sodium oxalate, results in sodium ions and gases as products, hence providing cations that can be used for full sodiation of the cathode structure.[252,272–274] This comes at the expense of the porosity of the positive electrode, whose value rises due to the void space left behind by the decomposition of the sacrificial salt. Salts that are compatible with the solvents used during the electrode processing can be employed, and the gasses generated by the reaction are then evacuated from the cell after the battery formation cycles.

However, it is important to note that the capacity unlocked by pre-sodiation in these partially sodiated cathode materials primarily resides at low potentials, typically below 2.5 V. Therefore, the energy that can be extracted from this additional capacity is lower than that which is already present in the as-synthesized cathode material. An assessment of the energy density and cost of the battery, both with and without the pre-sodiation treatment, is essential to determine the utility of this strategy to increase the cathode capacity.

We will simulate two scenarios: one with sacrificial salt addition in the cathode, which increases the porosity of the positive electrode, and another with an ideal pre-sodiation of the anode. The latter method does not induce detrimental porosity increases and is assumed to be inexpensive, imagining an optimized pre-sodiation implemented in the roll-to-roll process of the negative electrode. These two simulation scenarios represent the best and worst-case scenarios for assessing the impact on the energy density and cost of battery packs resulting from this treatment. The cathode materials chosen for the study are $Na_3V_2(PO_4)_2FO_2$ (NVPFO), an oxygen-substituted NVPF,[266] $Na_{0.6}[Ni_{0.22}Al_{0.11}Mn_{0.66}]O_2$ (NNAMO),[275] and $Na_{0.6}[Ni_{0.22}Fe_{0.11}Mn_{0.66}]O_2$ (NNFMO),[276] two P2-phase layered oxides, all requiring additional sodium to fully exploit their capacity. The description of the calculations regarding the pre-sodiation with sacrificial salt are reported in the Supporting Information.

The results of the simulation demonstrate that, in the best-case scenario, the battery performance is improved, with an increase in volumetric energy density of at least 3.5%, in gravimetric energy density of minimum 9%, and a decrease in the cost per kWh of the battery pack of at least 11%. This improvement holds true for pre-sodiation of the anode, under the most optimistic hypothesis. However, with the use of sacrificial salt in the cathode, the energy densities decrease below the non-pre-sodiated case. The increase in capacity, which is almost 50% for NVPFO and more than 60% for the two-layered oxides, is not sufficient to counteract the increase in porosity caused by the presence of sacrificial salt. An increase of porosity results in more void space in the battery that has to be filled with electrolyte, decreasing the compactness of the battery and increasing the weight (and the cost) caused by inactive components (current collectors, separator, electrolyte, hardware).[56] Nevertheless, the cost of the pack is still lower than the base case, since the quantity of (expensive) active materials required to achieve the target pack energy reduces thanks to the higher capacity.

Moreover, we observe that for all materials, the average battery voltage substantially decreases after both types of pre-sodiation. For instance, in the case of NVPFO, it drops from 3.47 to 2.98, a 14% decrease. This is also evident in **Figure 6.5**, where the capacity added by the pre-sodiation of the cathode is highlighted in light blue. For NVPFO, the added capacity consists mostly of a plateau at around 1.5 V, which, after the subtraction of the anode voltage, falls well below 1 V. In the case of the two-layered oxides, the capacity unlocked by pre-sodiation lies between 2.5 and 2 volts, resulting in a sharply sloping profile of the battery voltage that ends with a cut-off below 1 V.

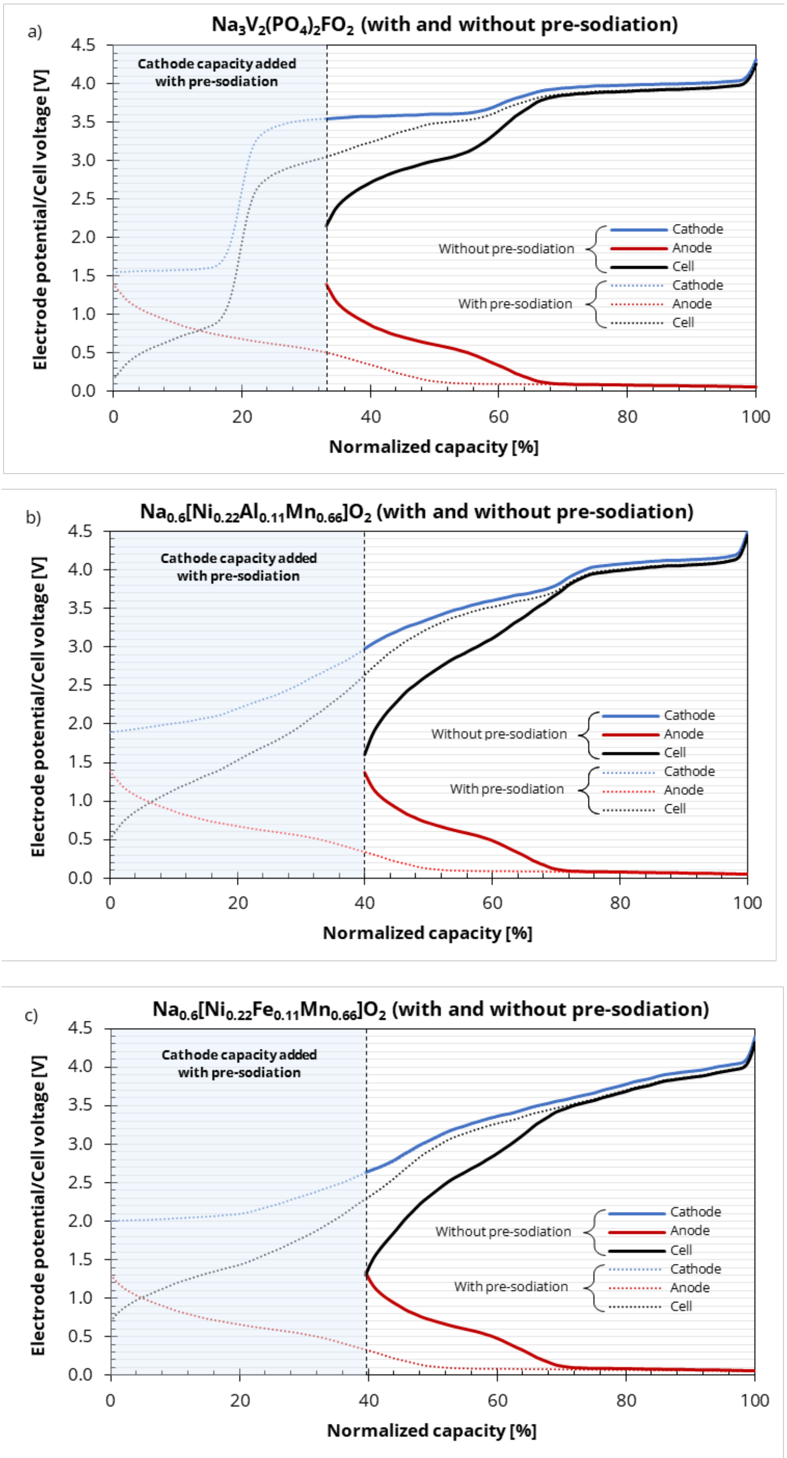

Figure 6.5 *– Electrode potentials of cathode and anode and resulting cell voltages of the materials analyzed in the pre-sodiation for the capacity increase of cathode materials study. a) NVPFO; b) NNAMO; c) NNFMO. The light blue part represents the part of cathode capacity that is added with the pre-sodiation. The capacity is normalized by dividing for the specific capacity with pre-sodiation of the cathode material.*

As a result, after integrating the area below the curve and dividing by the capacity of the battery, the average voltage decreases significantly, which is detrimental to the energy and cost of the battery. Lastly, it is important to note that the cut-off voltage after pre-sodiation is much lower than both the 1.5 V and 55% of the maximum voltage targets discussed in Section 2.1. Therefore, when considering cut-off voltage limits, it becomes questionable whether all or part of this additional capacity can actually be utilized.

In summary, based on the results of this case study, we recommend a critical discussion of the voltage at which the capacity obtained from pre-sodiation (or, more broadly, from the addition of cations to enhance the capacity of active materials) is situated. Modeling the impact of the cathode capacity increase with a cost and performance model can provide valuable support for studies aimed at quantitatively assessing the improvements resulting from such treatments.

Pre-sodiation for the first cycle sodium loss compensation

Pre-sodiation strategies can be used to overcome the loss of sodium during the first cycle of the battery, too. Hard carbon anodes tend to have a significantly lower initial coulombic efficiency than graphite anodes (typically <80% vs. >90%) due to their higher surface area that leads to increased SEI formation. Such a low initial coulombic efficiency causes the loss of a considerable part of the available battery capacity, since the cathode is the source of sodium in the cell and it has to provide the necessary cations to form the SEI on the hard carbon.

It is then interesting to examine the impact of compensating for the initial cycle sodium loss using the cost and energy density analysis, evaluating the effect on battery pack performance resulting from the improvement in the initial coulombic efficiency with pre-sodiation, a technique that, as described in Section 2.2, entail several complications in the battery production.

For this case study, we selected three additional cathode materials from different classes, each characterized by distinct physical and electrochemical properties: $Na_3Fe_2(PO_4)_3$, an iron-based polyanionic compound (NFPO),[277] $Na_{0.95}[Ni_{0.32}Mn_{0.32}Mg_{0.16}Ti_{0.21}]O_2$, an O3-phase layered oxide (NNMMTO),[69] and $Na_2Mn[Fe(CN)_6]$, a Prussian blue analogue (NMFCN).[278] The detailed methodology for the implementation of the initial coulombic efficiency of both anode and cathode in the simulations is provided in the Supporting Information.

Based on the results of the simulations, it is evident that the battery performance is consistently improved with the compensation for the first cycle sodium loss. This improvement holds true for all cases in the anode pre-sodiation hypothesis. In the case of sacrificial salt addition in the cathode, a decrease in pack energy densities is observed, but it only applies to NNMMTO.

In the best-case scenario, there is a minimum increase of 4% and 4.4% percent in volumetric and gravimetric energy density, respectively, while the cost per pack decreases by at least 5%. Since the added capacity with the pre-sodiation in this case is notably lower than the capacity increase observed in the previous study (Section 2.2), the improvements in relevant metrics are comparatively limited. Nevertheless, the average voltage decreases only slightly in this case, especially for NMFCN, which features a high voltage plateau. With NMFCN, the capacity recovered with the sodium compensation lies at a relatively high voltage compared to the other two materials (see **Figure 6.6**). Consequently, it experiences a relatively greater improvement due to the shape of its voltage profile.

NMFCN is also minimally affected by the use of sacrificial salt as a pre-sodiation additive and is only marginally penalized compared to the best-case scenario provided by anode pre-sodiation. This may be attributed to the inherently low density of this Prussian Blue Analogue, around 1.8 $g \cdot cm^{-3}$, which is even lower than the density of the sacrificial salt used in this work (sodium oxalate, which has a density of 2.34 $g \cdot cm^{-3}$). As a result, the space occupied in the positive electrode by the sacrificial salt is limited compared to the space occupied by the active material itself. The pre-sodiation with sacrificial salt is only beneficial for the battery pack performance for NFPO too, which has also a rather low density (3.4 $g \cdot cm^{-3}$). Instead, in the case of NNMMTO, characterized by a density of 4.4 $g \cdot cm^{-3}$, the increase in porosity caused by the salt inclusion in the cathode coating outweighs the gains in terms of capacity.

In synthesis, the simulation of cost and energy density has provided valuable insights into the effectiveness of compensating for the initial sodium loss through pre-sodiation. Such an analysis can be applied to determine whether it's worthwhile to conduct pre-sodiation studies on a specific active material and to quantify the actual improvements in the metrics of the final battery. If the capacity that is recovered is situated at a high voltage, the capacity increase is indeed beneficial for the final battery pack performance. The use of sacrificial salts may be more appropriate for active materials that are already characterized by low density since, in this case, the impact of porosity increase is limited compared to the benefits of capacity recovery.

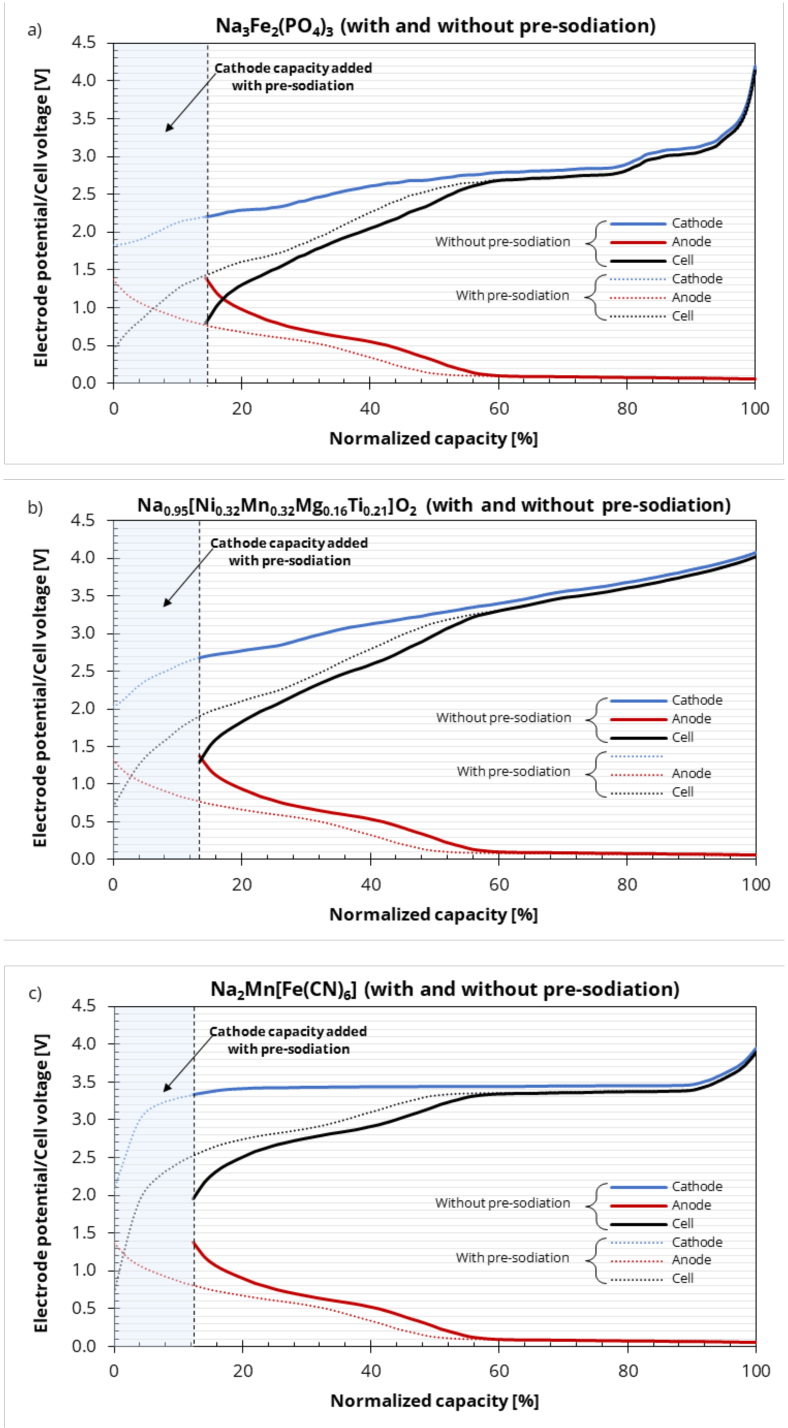

Figure 6.6 *– Electrode potentials of cathode and anode and resulting cell voltages of the materials analyzed in the pre-sodiation for the first cycle sodium loss compensation study. a) NFPO; b) NNMMTO; c) NMFCN. The light blue part represents the part of cathode capacity that is added with the pre-sodiation. The capacity is normalized by dividing for the specific capacity with pre-sodiation of the cathode material.*

6.2. Assessing N-Type Organic Materials for Lithium-Batteries

Herein, we present the most extensively studied, relevant n-type cathode and anode materials for organic batteries, a detailed cost and performance analysis battery packs performed with the software BatPaC 5.0.[75] We also discuss the implications of design choices of the organic electrodes on the energy density and cost of battery packs, focusing on the influence of the conductive carbon content, the active material mass loading, and the electrode density.

Organic materials are typically classified and discussed based on these different constituent elements and functional groups. Here, we categorize these materials based on a practical criterion: whether or not they require a lithium-metal anode. This classification separates the materials into two categories, i.e., lithium-deficient and lithium-sufficient organic materials. Most n-type cathodes require a lithium-metal anode to function in a battery, although lithium metal batteries face challenges regarding the production and handling of thin reactive anode foils and cycle life.[20,52,279] Recent works have explored organic cathodes that contain enough lithium and are stable towards oxygen and moisture, similar to commercial inorganic cathodes.[158] These organic cathodes, synthesized in their discharged form, can be used with a conventional graphite anode or other organic anode materials, resulting in organic battery production that is potentially analogue to inorganic lithium-ion battery production. As a result, a material's lithium deficiency or sufficiency affects the production process from synthesis to assembly, as well as the performance and stability of the battery during operation. Lithium-sufficient organic materials can simplify the battery production process and eliminate the need for a lithium-metal anode; such batteries are easier to manufacture and handle. This criterion of lithium deficiency or sufficiency is a crucial factor in evaluating the practicality and potential of n-type organic materials for battery applications.

Until now, organic battery materials were not the focus of thorough techno-economic assessments, despite their cost being one of the main arguments commonly used as an advantage for this type of chemistry. The widespread availability of organic molecules as potential economical precursors to electrode materials is mainly due to the petrochemical industry, and in minor part to bio-derived resources.[66] Although, this does not translate so easily to an inexpensive battery, for two main reasons.

Firstly, the synthesis process of the actual cathode or anode from the precursors can have a very low yield, require expensive catalysts, and/or are not scalable to an industrial production process. For instance, PTO can be theoretically obtained from the oxidation of pyrene, a sub-product of the production of coal.[280] However, the oxidation of the specific sites of the pyrene molecule to obtain the ketone oxygens in the right positions is not easily achievable, and a synthesis route with expensive catalysts and low yield has to be utilized.[281] Li et al. listed the projected cost of a variety of organic cathode materials using the data from the reactions found in literature, and no material had a cost lower than 400 $\$\cdot kg^{-1}$.[156] It should be remarked that the current cost of lithium-ion battery active materials is in the 10-60 $\$\cdot kg^{-1}$ range, depending on the raw material prices and the market conditions.[56,282] Currently, only a handful of n-type materials are available in large quantities and relatively low price (e.g., benzoquinone, AQ, PTCDA), being already used in other industries. This class of materials is still in its infancy; thus, it is understandable that the focus is not yet on the development of large-scale and cost-effective syntheses. Very promising materials can be discovered utilizing lab-scale synthesis methods and their production process optimized to fit an industrial environment.

Secondly, the cathode or anode cost per unit mass has an influence on the total battery cost, but the specific capacity and the average voltage of the materials are also fundamental to understand how much material is needed to satisfy the energy and power requirements of the battery pack. A battery built with an organic cathode material with an extremely low cost per unit mass but very poor energy density will require a much higher quantity of active material than in a normal lithium-ion battery. Hence, multiplying necessary mass to specific cost, the final actual cost of the organic cathode can be higher than the inorganic cathode case. Moreover, lower energy density at the electrode level means that larger batteries have to be built, and costs that scale with the area (e.g., separators, current collectors) and the volume (e.g., electrolyte, casings) of the battery pack will also have a greater impact.

Hence, understanding the actual gravimetric and volumetric energy density that can be obtained in a full-scale battery with n-type organic materials such as cathodes or anodes is fundamental to assess their cost-effectiveness. Thus far, the most detailed energy density assessment of organic batteries was made by Judez et al., where cells were simulated with an in-house algorithm and the influence of binder content, carbon content, electrolyte quantity, N/P ratio, and areal capacity was studied.[283] They used four model organic materials belonging to different chemistries with the specific capacity, one average discharge voltage value, and the density as material properties. They identified the electrolyte/active material ratio as the most important parameter to achieve high energy density organic batteries, but they did not discuss the projected cost of such batteries. A recent review on organic materials from Kim et al. recognized how the potential practical application of such materials should be the main priority.[89]

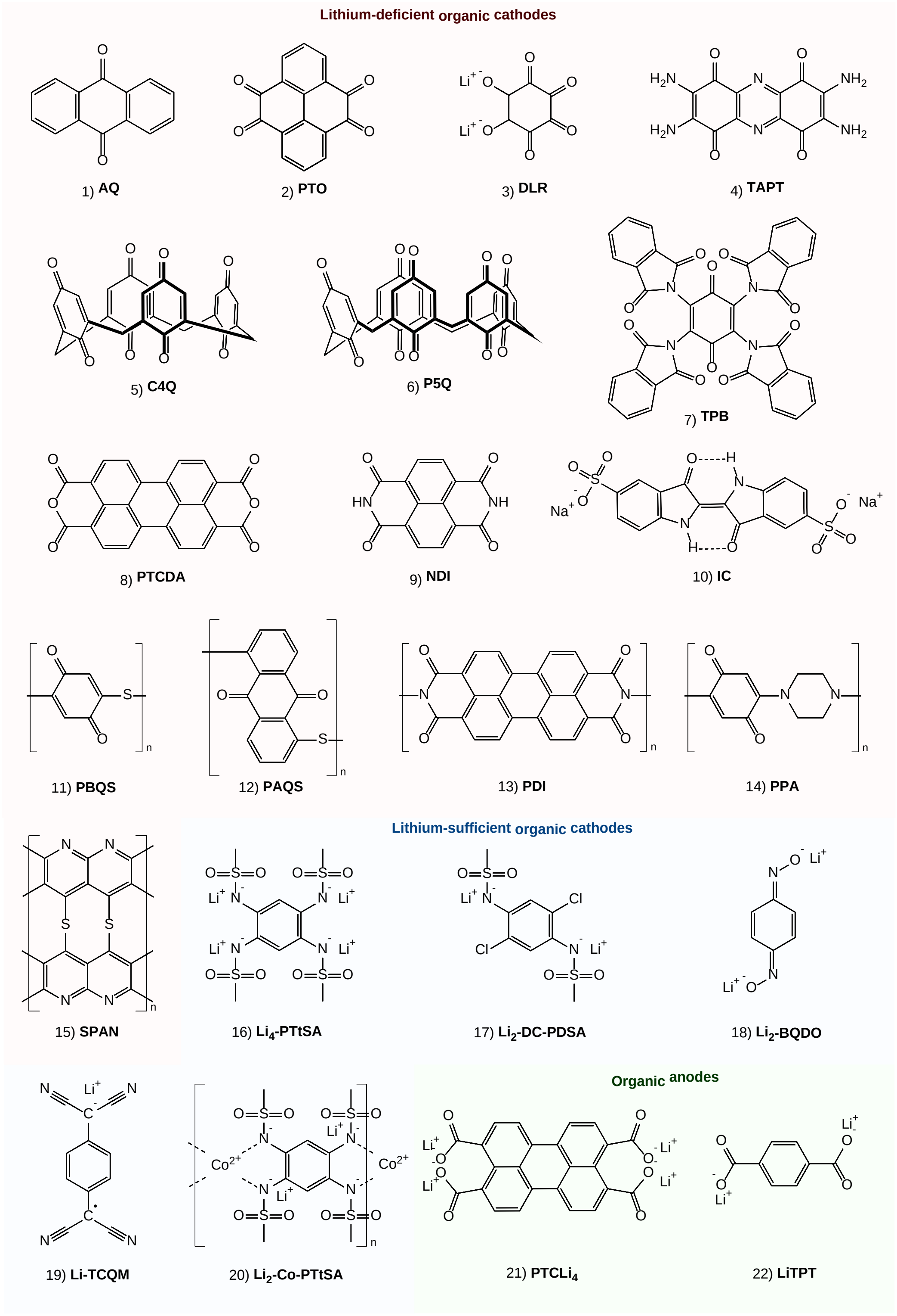

Figure 6.7 *– Representation of the organic materials included in the cost and performance analysis; categorized as lithium-deficient cathodes (red), lithium-sufficient cathodes (blue), and organic anode (green).*

Hence, they reported the electrochemical performances of organic batteries found in literature referring to the whole electrode composition and the related experimental data, and not theoretical values or material-level quantities. Another review from Lu & Chen included a small analysis of the energy density and cost of a 100 kWh, 150 kW battery pack with benzoquinone and dilithium rhodizonate (material 3) as cathodes and lithium metal as anode, as well as with dilithium terephthalate (material 22) and a polydopamine-derived polymer as anodes for NMC 622 batteries.[67]

It was found that the polymer-based anode materials have the poorest performance compared to graphite with NMC 622 as cathode, in terms of both the energy density and the cost. Alternatively, comparing a NMC 622-Li battery with benzoquinone and dilithium rhodizonate lithium metal batteries, the former would still be advantageous from every aspect except the cathode active material cost, even when considering the theoretical capacity values for the small organic molecules. The analysis performed in this work uses the BatPaC model software, but it considered only four materials, no lithium-sufficient cathodes, and it did not study the influence of the electrode design on the final results.

We now present a detailed cost and energy density analysis of battery packs built with the 22 molecules and polymers represented in **Figure 6.7**, dividing between lithium-deficient and lithium-sufficient cathodes. Lithium-deficient cathodes will be simulated with lithium metal as anode and compared to lithium metal batteries with NMC 622 and LFP as cathode. For the organic molecules, the N/P ratio is set to 1.1, while for the inorganic cathodes the same parameter has a value of 0.3. Lithium-sufficient materials will be coupled to graphite, DLT, and $PTCLi_4$ as anodes and compared to lithium-ion batteries with NMC 622 and LFP as cathode and graphite as anode. All the organic batteries will be simulated with two configurations, one with high active material mass loading (96%), similar to the loading of commercial lithium-ion batteries, and one with a lower active material loading (65%), to represent a typical loading of lab-scale studies where a large amount of conductive carbon is usually added. The specific capacity and the voltage profile were obtained from experimental data in relevant publications, while the density values were estimated.

Moreover, in the cost analysis, two additional scenarios will be considered, i.e., low and high cost of lithium, to compare the resulting batteries both with the current prices of raw materials and with pre-2022 ones. The cost associated with all the lithium-deficient cathode materials is assumed to be 10 $\$\cdot kg^{-1}$, while the one for the lithium-sufficient cathode materials and the lithium-containing anodes is 10 $\$\cdot kg^{-1}$ in the low lithium cost scenario, and 20 $\$\cdot kg^{-1}$ in the high lithium cost scenario. Making estimates based on lab-scale synthesis yields and prices for reactants would not be representative of an industrial production scenario for these materials.[114] Hence, we decided to assume a standard, low cost for all the organic materials, slightly lower than the one of LFP pre-2022.

A brief overview of the properties of all the active materials is reported in **Table 6.2**. The summary of the simulation conditions can be found in **Table A2.1** of the **Appendix 2**.

We would like to remark that we are using the most optimistic conditions to simulate the organic battery packs, as we assume that the n-type cathodes and anodes would be able to work in the same conditions of commercial lithium-ion batteries (e.g., electrolyte type and quantity, cathode thickness, active material loading, separator type and thickness, pulse resistance). Hence, the following analysis should be interpreted as a best-case scenario for the implementation of such materials in actual battery packs.

***Table 6.2** – List of the organic and inorganic materials included in the cost and energy density analysis*

Type of material	Material code	Classification	Specific capacity [mAh·g]	True density [g·cm^{-3}]	Average potential [V vs Li/Li^{+}]	Reference(s)
Organic materials	**AQ**	Lithium-deficient	250	1.31	2.26	141
	PTO	Lithium-deficient	362	1.67	2.55	113
	DLR	Lithium-deficient	503	1.80	2.18	93
	TAPT	Lithium-deficient	306	1.60	2.43	122
	C4Q	Lithium-deficient	442	1.30	2.59	124
	P5Q	Lithium-deficient	418	1.30	2.60	125
	TPB	Lithium-deficient	231	1.60	2.28	128
	PTCDA	Lithium-deficient	134	1.71	2.43	130
	NDI	Lithium-deficient	167	1.55	2.29	131
	IC	Lithium-deficient	97	1.78	2.19	134,139
	PBQS	Lithium-deficient	274	1.20	2.68	152
	PAQS	Lithium-deficient	199	1.20	2.19	141
	PDI	Lithium-deficient	127	1.20	2.46	155
	PPA	Lithium-deficient	232	1.20	2.58	156
	SPAN	Lithium-deficient	580	1.20	1.78	157
	Li$_4$-PTtSA	Lithium-sufficient	111	1.60	2.69	164
	Li$_2$-DC-PDSA	Lithium-sufficient	155	1.60	3.24	164
	Li$_2$-BQDO	Lithium-sufficient	335	1.30	2.80	169
	Li-TCQN	Lithium-sufficient	126	1.60	3.13	171
	Li$_2$-Co-PTtSA	Lithium-sufficient	93	1.50	3.09	166
	PTCLi$_4$	Anode	108	1.70	1.20	183
	LiTPT	Anode	276	1.55	0.96	94,284
Inorganic materials	**NMC 622**	Lithium-sufficient	187	4.65	3.82	75
	LFP	Lithium-sufficient	157	3.45	3.40	75
	Graphite	Anode	360	2.27	0.14	75

6.2.1. Analysis of lithium-deficient organic materials

The summary of the simulation results on the lithium-deficient cathode materials is shown in **Figure 6.8**, where the NMC and LFP batteries are indicated in red, and the organic materials in shades of blue. The darker blue shows the low active material content case, while the lighter blue indicates the high active material content case.

The volumetric energy density (**Figure 6.8.a**) is notably low for all the organic batteries, mostly owing to the low density of the cathode materials (between 1.2 and 1.78 g·cm^{-3}), especially when compared with the ones of NMC 622 (4.65 g·cm^{-3}) and LFP (3.45 g·cm^{-3}). Comparing IC and PDI, despite IC having lower electrochemical performances than PDI in terms of specific capacity and voltage profile, the former's higher density (1.78 g·cm^{-3} vs. 1.2 g·cm^{-3}) makes it possible to obtain a pack volumetric energy density of 119 Wh·l^{-1} in the high active material content case, while PDI achieves only 111 Wh·l^{-1}.

Moreover, the lithium-deficient organic materials require an amount of lithium equal to 110% of the cathode capacity (N/P=1.1), the latter being completely delithiated. Instead, NMC 622 and LFP already have lithium inside the crystal structure, hence the lithium anode is set to only 30% of the capacity (N/P=0.3), to act as reserve in case of irreversible lithium loss. Hence, the thick, low density lithium anode required by the organic cathodes further decreases the volumetric energy density.

The gravimetric energy density of the n-type organic batteries is nearer to the inorganic battery performances (**Figure 6.8.b**), and some small molecules like DLR (185 Wh·kg^{-1}) and P5Q (186 Wh·kg^{-1}) are almost at the level of an LFP lithium metal battery (192 Wh·kg^{-1}). Small molecules with lower capacity and/or lower voltage perform poorly, as well as the majority of the polymers, since polymerization of the redox-active monomers usually results in more inactive mass and a decrease of the redox potential. Only the SPAN manages to achieve a relatively high gravimetric energy density (160 Wh·kg^{-1}) thanks to the very high specific capacity provided by the reaction between lithium and sulfur. However, when considering a lower, standard active material content in the electrode, these values decrease between 19% and 28%, according to the specific organic compound. Therefore, achieving the highest possible amount of active material in the electrode is crucial to maximize energy density and remain competitive with inorganic systems.

This latter statement can be confirmed when looking at the cost comparison. The same small molecules cited above have the potential of reaching an equal or lower cost than inorganic lithium metal batteries in the low lithium cost scenario and with high active material content, especially considering that their actual cost could be even lower than the 10 $\$\cdot kg^{-1}$ assumed here (**Figure 6.8.c**). Nevertheless, such small molecules are also the ones that suffer the most from dissolution problems in common electrolytes, and their number of cycles before the end-of-life is two-three orders of magnitude lower than NMC 622 and LFP. A scenario with high lithium cost (**Figure 6.8.d**) seems to impact organic and inorganic batteries with the same magnitude (+35% for NMC 622, +42% for LFP, between 25% and 50% for the organic materials). Despite not containing any lithium in the cathode, and hence not incurring cost increases for the positive electrode, the organic batteries contain more lithium metal in the anode, due to their higher N/P ratio, hence they can be severely affected by a lithium price hike.

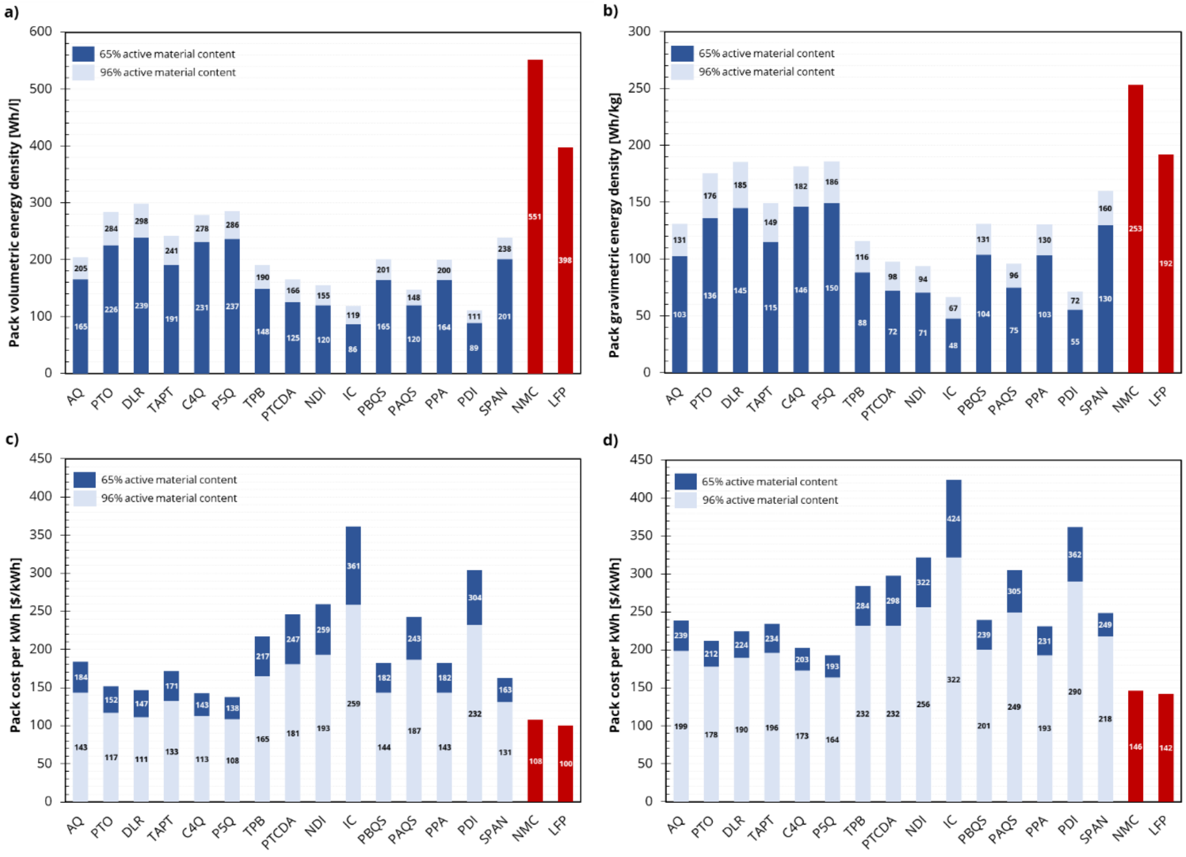

Figure 6.8 *– Comparison of the a) pack volumetric energy density, b) pack gravimetric energy density and pack cost per kWh in the c) low lithium cost scenario and d) high lithium cost scenario for the lithium-deficient organic cathode materials (in shades of blue) and inorganic cathodes (in red), both with lithium metal anode.*

6.2.2. Analysis of lithium-sufficient organic materials

The simulation results for the lithium-sufficient organic cathode batteries are reported in **Figure 6.9**, with the NMC and LFP batteries in red. The organic batteries with $PTCLi_4$ as anode are indicated in shades of blue, the ones with LiTPT as anode in shades of yellow, and the ones with graphite as anode in shades of green. The lighter colours represent the high active material content case, while the darker ones indicate the low active material content case.

The first comparison can be done between the performance of the different anodes. In all the cases, $PTCLi_4$ displays the poorest performance, LiTPT lies in between and graphite is the superior material. The most straightforward reason can be found in the relatively high average potential of $PTCLi_4$ (1.20 V vs. Li/Li^+) and of LiTPT (0.96 V vs. Li/Li^+) when compared to the one of graphite (0.14 V vs. Li/Li^+). A higher anode potential results in a lower full cell voltage, hence requiring more cathode and anode active material to achieve the same stored energy of a cell with a higher voltage. Moreover, both organic materials show a lower specific capacity than graphite (360 $mAh \cdot g^{-1}$ vs. 108 $mAh \cdot g^{-1}$ for $PTCLi_4$ and 276 $mAh \cdot g^{-1}$ for LiTPT), another factor that increases the mass of anode needed for the final battery to balance the cathode capacity. Finally, the density of graphite is 50% higher than that of $PTCLi_4$ and 50% higher than LiTPT, which has an influence on the final volumetric energy density and on the cost and weight of the casing required by cells, modules, and pack. The cost of the battery pack is in the first approximation inversely related with the energy density of the pack, evidenced in **Figure 6.9.c** and **Figure 6.9.d**.

Focusing on the performance of the lithium-sufficient cathodes, we can rank the analyzed materials as Li_2-BQDO > Li_2-DC-PDSA > Li-TCQN > Li_4-PTtSA > Li_2-Co-PTtSA. Similar to the lithium-deficient materials analysis, the volumetric energy density of the organic batteries is much inferior compared to those of the inorganic batteries (**Figure 6.9.a**), due to the low density of the organic materials.

Li_2-BQDO possesses a very high specific capacity (335 $mAh \cdot g^{-1}$) and a good average voltage when discharging (2.80 V vs. Li/Li^+, thus achieving 114 $Wh \cdot kg^{-1}$ when coupled with graphite, which is still much lower than NMC 622 (177 $Wh \cdot kg^{-1}$) or even LFP (143 $Wh \cdot kg^{-1}$) (**Figure 6.9.b**). Remarkably, the projected cost per kWh of a Li_2-BQDO/graphite battery in the high active material content case and in the high lithium cost scenario is lower than the cost of both NMC 622 and LFP batteries (139 $\$ \cdot kWh^{-1}$ vs. 144 $\$ \cdot kWh^{-1}$ for NMC 622 and 141 $\$ \cdot kWh^{-1}$ for LFP). Also, in the low lithium cost scenario, the cost of the organic battery is similar to the inorganic ones. These numbers should not be interpreted as a unequivocal superiority of this material over commercial lithium-ion batteries, but as an indication that Li_2-BQDO (or a material with similar/superior properties) could be a promising candidate for a cost-effective organic battery, especially in situations of lithium price hike.

Li_2-Co-PTtSA displays the highest cycling stability among the lithium-sufficient ones, possesses the lowest energy density and cost per kWh in all the scenarios and configurations. Nevertheless, its performances are only slightly inferior than the corresponding monomer Li_4-PTtSA.

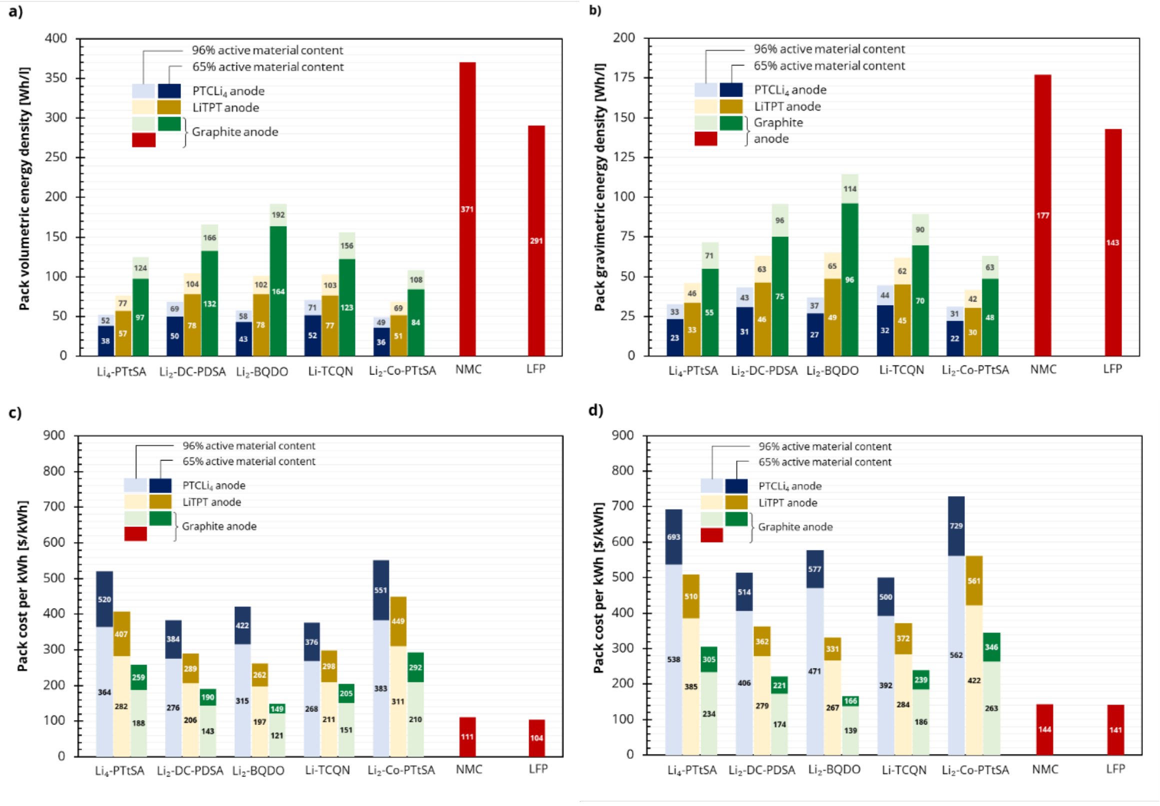

Figure 6.9 *– Comparison of the a) pack volumetric energy density, b) pack gravimetric energy density and pack cost per kWh in the c) low lithium cost scenario and d) high lithium cost scenario for the lithium-sufficient organic cathode materials (in shades of blue, yellow and green) and inorganic cathodes (in red), with different anode materials.*

To study the influence of specific electrode design parameters in relation to the results of the energy density and cost modelling, we simulated with BatPaC four organic battery configurations: one lithium-deficient cathode (P5Q) with lithium metal anode and one lithium-sufficient cathode (Li_2-BQDO) with three anode materials (graphite, LiTPT, and $PTCLi_4$). The simulations were made by varying three design parameters, i.e., the amount of conductive additive, the active material mass loading, and the electrode density.

6.2.3. Influence of the carbon content

As demonstrated in the results reported in **Figure 6.8** and **Figure 6.9**, maximizing the weight fraction of active material in the positive electrode is fundamental to achieve the highest energy density and lowest cost for the organic battery packs, in order to be competitive with lithium metal and lithium-ion batteries based on inorganic cathodes. However, since organic materials are usually poor electronic conductors, a high amount of conductive carbon is usually added to the electrode to obtain a working electrode.[285]

Lu & Chen reported the electronic conductivity of a variety of organic materials, which was found to vary widely between 10^{-15} and 10^{-3} $S\cdot cm^{-1}$, but the vast majority of the analyzed n-type materials had a conductivity in the 10^{-11}-10^{-7} $S\cdot cm^{-1}$ range.[67] Lithium metal oxides usually display an electronic conductivity $>10^{-6}$ $S\cdot cm^{-1}$, and a small amount of carbon is normally necessary to ensure good performances (2-4% of the weight of the electrode). Some inorganic lithium compounds are characterized by much lower conductivities, such as lithium titanium oxide (10^{-13} $S\cdot cm^{-1}$) or lithium iron phosphate (10^{-9} $S\cdot cm^{-1}$), but strategies such as carbon coating and nanosizing of the electrode particles enable these materials to be viable for commercial applications with the same amount of carbon as the other metal oxides.[5,286]

For organic materials, using conductive additives with high aspect ratios such as carbon nanotubes or high surface area such as graphene, graphene oxide and reduced graphene oxide has been reported to be an effective strategy to decrease the amount of necessary carbon in the electrode.[145,206,287,288] The optimization of the electrode preparation, often overlooked in fundamental studies on new materials, was also beneficial.[139,183,289]

From the results of the simulations (**Figure 6.10**), we observe that, in all the battery configurations, as the amount of conductive additive in the organic electrodes increases, the decrease in gravimetric and volumetric energy density, as well as the increase in pack cost, become more pronounced. Keeping the fraction of binder constant, when the conductive additive fraction increases, the active material fraction decreases, and with a fixed thickness of the electrode, this results in a decrease of the active material loading. Hence, the areas of the electrodes must increase to achieve the design capacity, and all the costs directly related to the area of the battery (separators, current collectors) will also rise. The electrode preparation becomes more expensive too, since a bigger area has to be coated, and the costs for binders, conductive additives and solvent for the slurry will have a greater impact. For the P5Q/Li metal battery and the Li_2-BQDO/graphite battery (**Figure 6.10.a** and **6.10.b**), an increase of 5% of the weight fraction of carbon in the cathode corresponds to an average increase of cost of about 4%, and an average decrease of volumetric and gravimetric energy density respectively of about 3.5% and 3%.

We identify how the fully organic batteries, i.e., Li_2-BQDO/LiTPT and Li_2-BQDO/PTCLi$_4$, are greatly affected by a higher amount of conductive additive in the electrodes (**Figure 6.10.c** and **6.10.d**). For these two configurations, we considered that both anode and cathode are affected by the carbon addition. For a full organic cell, the average cost increment for each 5% step increase of conductive additive is ≈6%, and the volumetric and gravimetric energy decreases are ≈4.5% and ≈4%, respectively.

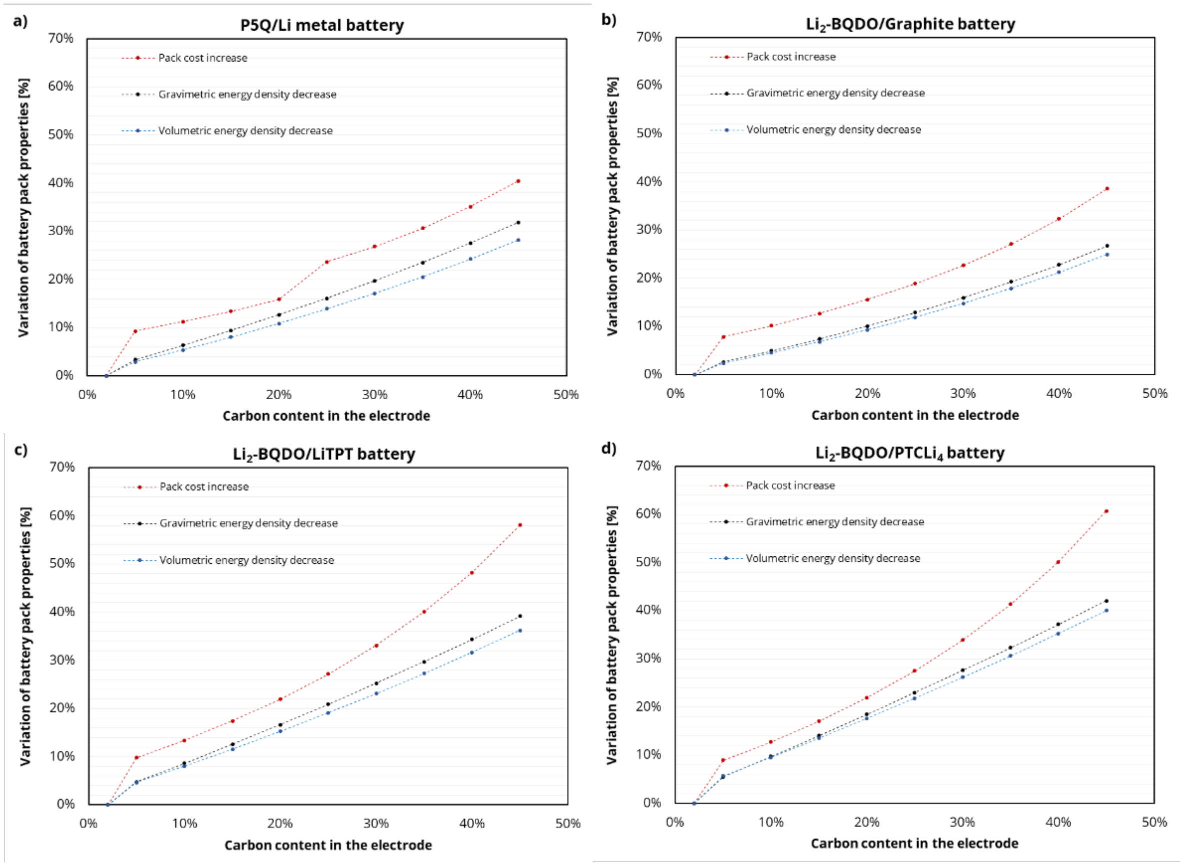

__Figure 6.10__ – The influence of the carbon content in the electrode(s) on the battery pack properties for a) a P5Q/Li metal battery, b) a Li_2-BQDO/Graphite battery, c) a Li_2-BQDO/LiTPT battery, and d) a Li_2-BQDO/PTCLi$_4$ battery. The percentage variations of the battery pack properties refer to the case with the lowest amount of carbon. For the Li_2-BQDO/LiTPT battery and the Li_2-BQDO/PTCLi$_4$ battery, the carbon content is also increased in the negative electrode.

6.2.4. Influence of the active material content

Maximizing the weight fraction of active material in the electrode is not the only means to obtain practical batteries, since a high active material mass loading is also necessary to optimize the utilization of the available space in the battery pack. Electrodes with a thickness between 30 and 90 µm are standard for commercial lithium ion batteries, according to the application and the specific material, corresponding to mass loadings between 5 and 20 mg·cm^{-2}.[290,291]

For organic battery materials, active material mass loadings found in literature are often below 1 mg·cm^{-2}, but to achieve high energy densities, the target should be higher than 10 mg·cm^{-2}, to achieve areal capacities similar to those of inorganic materials. However, due to the low density of organic materials, such a mass loading results in a relatively high electrode thickness. For example, in the four battery configurations shown in **Figure 6.11**, the highest mass loading is 11.37 mg·cm^{-2}, corresponding to a cathode thickness of 120 µm, yet such thick electrodes incur problems related to the severely increased mass transport resistance in the porous electrode.[292]

The importance of the mass loading, and hence of the areal capacity, to compete with commercial technologies was recognized by Molina et al., which developed a conjugated microporous n-type polymer as cathode for lithium batteries and engineered the cathode to achieve mass loadings between 9 and 60 mg·cm^{-2}, using single walled carbon nanotubes and reduced graphene oxide as conductive additives.[145] Iordache et al. studied PTCLi$_4$ and reported electrodes with an active material mass loading up to 12 mg·cm^{-2}, obtained by minimizing the quantity of multiwalled carbon nanotubes used as electronically conducting agent.[183] Also, the works from the Vlad group on lithium-sufficient organic materials showed the possibility of constructing batteries with mass loadings up to 50 mg·cm^{-2}.[164,166]

By decreasing the maximum cathode thickness, we simulated the decrease of the active material mass loading in the four organic battery configurations, and the effect that this design parameter has on the energy density and on the cost of the battery pack (**Figure 6.11**). For all cases, the result is an overall worsening of the battery pack properties, which becomes more intense when the mass loading decreases further. The cause of the decrease of volumetric and gravimetric energy density and of the rise in cost are similar to the one of the carbon content in the electrode, i.e., the electrode surface needs to increase to meet the design requirements due to the lower capacity per unit area.

The Li$_2$-BQDO/PTCLi$_4$ battery suffers the mildest consequences from the decrease of the active material mass loading of the cathode (**Figure 6.11.d**). At the lowest simulated mass loading (1.90

mg·cm^{-2}), the cost of the battery pack increases only 33% compared to the base case at 11.37 mg·cm^{-2}, compared to the +91% of the P5Q/Li metal battery, +84% of the Li$_2$-BQDO/graphite battery, and +82% of the Li$_2$-BQDO/LiTPT battery (**Figure 6.11.b**, **6.11.c**, and **6.11.d,** respectively). The reason for the relatively small cost increase (and energy density decrease) for the Li$_2$-BQDO/PTCLi$_4$ battery is that together with the cathode, the anode thickness also decreases, due to the lower capacity that must be balanced. Since the low-density PTCLi$_4$ anode has a modest specific capacity compared to the other anodes and to Li$_2$-BQDO (**Table 6.2**), its thickness decreases far more than the cathode, partially offsetting the detrimental effects of the cathode active material loading reduction.

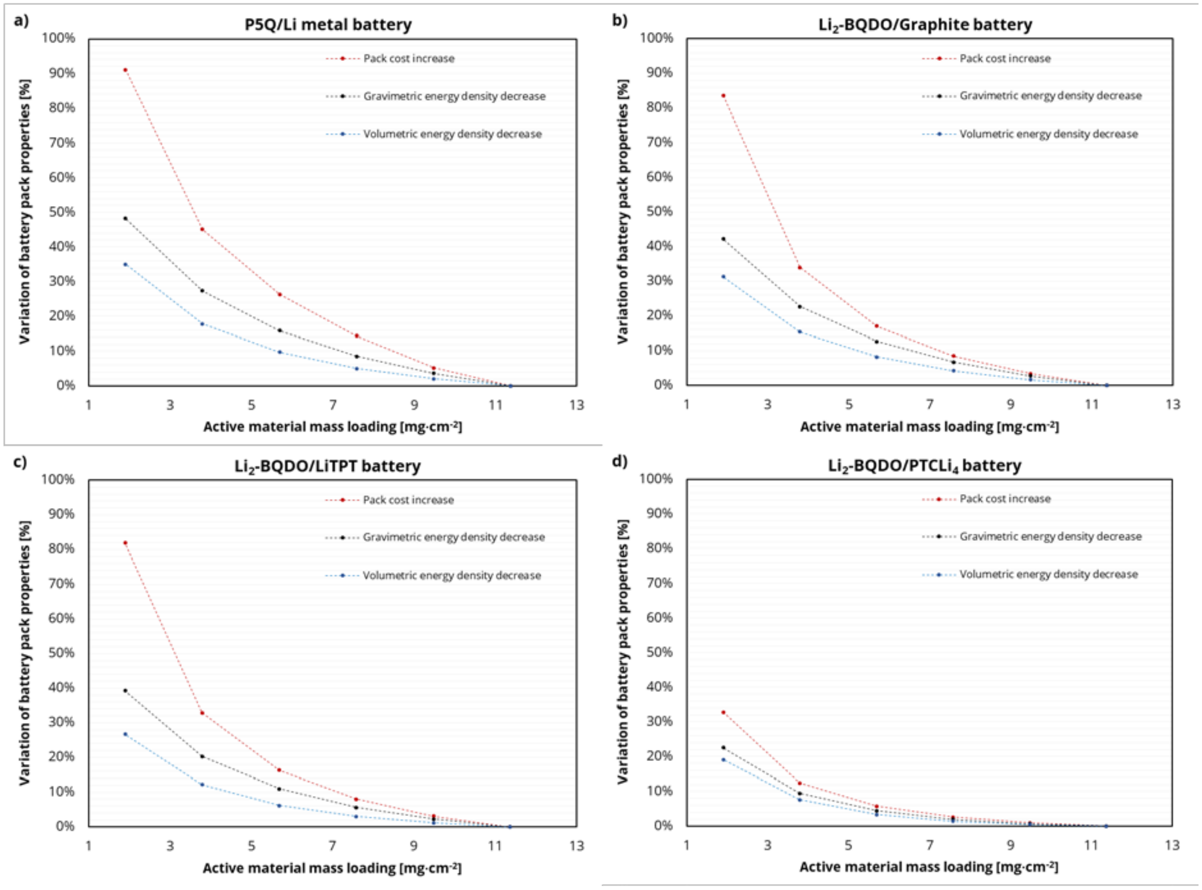

__Figure 6.11__ – The influence of the active material mass loading of the cathode on the battery pack properties for a) a P5Q/Li metal battery, b) a Li$_2$-BQDO/Graphite battery, c) a Li$_2$-BQDO/LiTPT battery, and d) a Li$_2$-BQDO/PTCLi$_4$ battery. The percentage variations of the battery pack properties refer to the case with the highest active material mass loading.

6.2.5. Influence of the electrode density

Finally, the density of the organic electrodes plays a pivotal role in the optimization of the energy density and cost of the battery. Organic materials tend to have intrinsically lower density than inorganic ones, [67] due to the light elements they are composed of, thus placing them at a disadvantage when considering the size of the battery pack. The density of the final electrode obtained from the organic active material also takes into account the densities of the conductive carbon and binder, as well as the porosity of the electrode. This last parameter is fundamental to achieve the best performances of the final battery: the porosity is the necessary empty space required to hold the electrolyte in the electrode, a space that could theoretically be filled with active material, thereby increasing the energy stored in the same volume of electrode. Hence, a high porosity results in a overall lower energy density of the cell, but it assures a good wetting of the electrode with the electrolyte. A low porosity is good to maximize the energy density and to improve the electronic conductivity, but it can affect the rate performance in case of insufficient electrolyte quantity.[293]

For instance, in the study from Molina et al. the density of the organic cathode obtained with the buckypaper technique was estimated to be 0.2 $g\cdot cm^{-3}$, resulting in electrodes thicker than 3 mm and with a porosity of ~70% to achieve 60 $mg\cdot cm^{-2}$ active material loading.[145] However, commercial lithium-ion battery cathodes are usually limited to max. 120 µm of thickness for high-energy configurations,[75] to avoid an excessive increase of the mass transport resistance and the cracking of the electrode after coating and drying, and the porosity is usually in the 20-30% range. High thickness and porosity could cause manufacturing problems and the need for an excessive quantity of electrolyte to fill the electrode void space. Lombardo et al. studied the influence of the electrode porosity for disodium biphenyl-4,4'-dicarboxylate, a n-type organic anode for sodium-ion batteries, by varying the compression ratio of the electrode after calendering.[294] They found that the higher the compression ratio (i.e., the lower the porosity), the higher the specific capacity at all current rates, which they interpreted as a result of the improvement of the electronic conductivity of the electrode.

To understand the impact of the electrode density on the cost and energy density results, the same four organic batteries were simulated increasing the cathode porosity while keeping the same active material loading, hence increasing the thickness of the positive electrode (**Figure 6.12**). In this case the volumetric energy density is the parameter most affected by a decrease of the electrode density, followed closely by the gravimetric energy density. The evident effect of a lower electrode density is to increase the volume of the whole battery pack, jeopardizing the volumetric energy density. The gravimetric energy density decreases too, because of the increased weight caused by the additional electrolyte required to fill the porosity of the cathode and from the bigger metal casings of cells, modules, and pack.

The cost per kWh increases the least in the P5Q/Li metal battery, but this configuration also experiences the largest decrease of both energy densities (**Figure 6.12.a**). Since the lithium metal anode is a thin and compact layer, if the density of the cathode decreases, the overall energy density will be more affected than the other organic batteries (**Figure 6.12.b**, **6.12.c**, and **6.12.d**), where the contribution to the size and the mass of the cells is shared equally between the two porous electrodes.

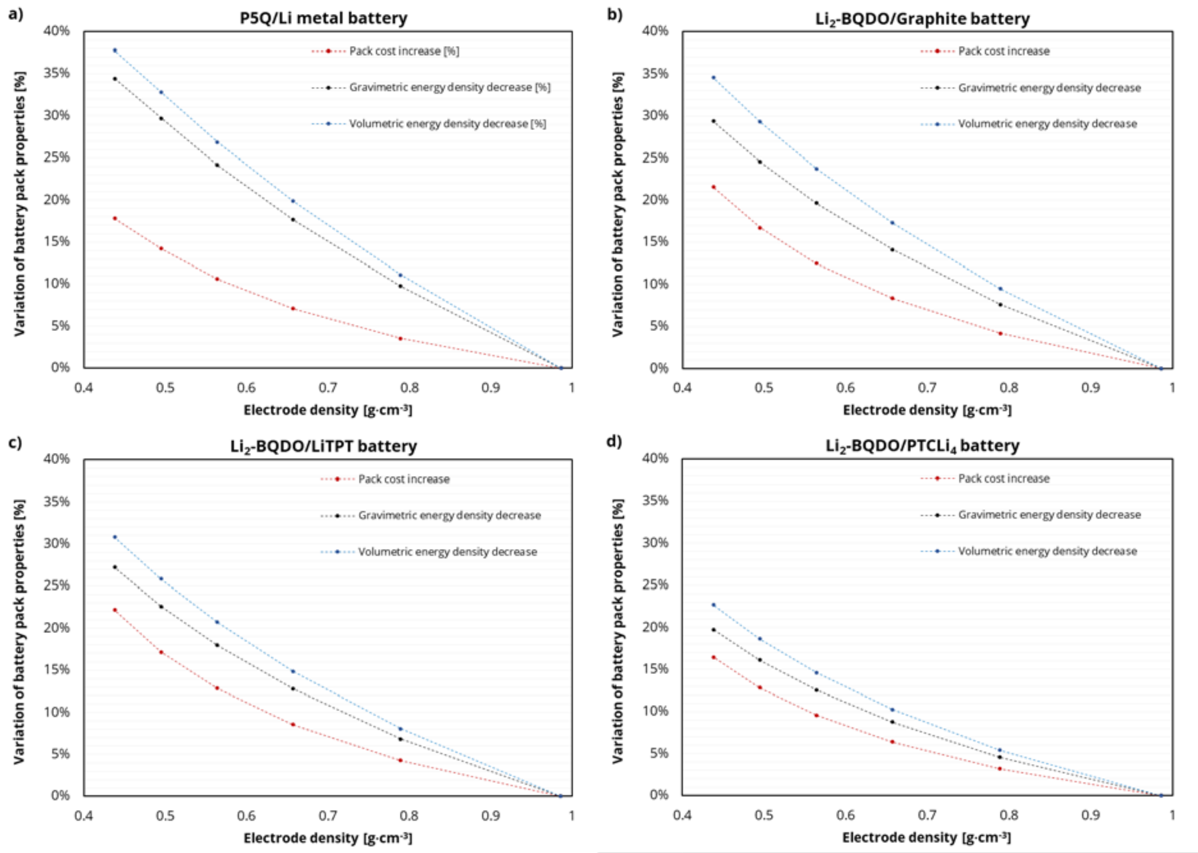

__Figure 6.12__ – The influence of the cathode density on the battery pack properties for a) a P5Q/Li metal battery, b) a Li_2-BQDO/Graphite battery, c) a Li_2-BQDO/LiTPT battery, and d) a Li_2-BQDO/PTCLi$_4$ battery. The percentage variations of the battery pack properties refer to the case with the highest cathode density.

6.2.6. Conclusion

In conclusion, the best performing materials were found to be small molecules, that usually exhibit the lowest capacity retention, highlighting the need for further research efforts in terms of the stabilization during the cycling of such molecules in batteries, through molecular engineering and/or electrolyte formulation. Air-stable, lithium-sufficient materials, despite being inferior from the energy density point of view, could become cost-effective materials competing with inorganic chemistries.

Overall, while n-type organic materials have potential as a low-cost and sustainable solution for energy storage, further research is necessary to optimize the synthesis process and the electrode design, and to improve their energy density and stability during operation. We recommend implementing the evaluation of the practicality and cost-effectiveness of organic materials in full-scale battery packs using detailed energy density and cost simulations, with optimistic assumptions for their potential scale-up in a commercial setup. This practice can provide pivotal insights into the viability of organic materials for future battery technologies

6.3. A modified Doyle-Fuller-Newman model for the simulation of dual-ion batteries

So far, p-type organic materials, which store charge through the interaction with anions, were not the subject of the cost and performance analysis. We already mentioned how with such materials, whose potential lies in the 3.5-4.5 V range, it is convenient to use with alkali metal anodes or carbonaceous anode materials to obtain high-voltage batteries. As a consequence, these batteries function in a dual-ion arrangement, wherein the anode and cathode interact respectively with cations and anions. The electrolyte plays a crucial role in this system, serving as the sole source of both anions and cations for the proper functioning of the dual-ion battery.[295]

The working principle of dual-ion batteries represents also their main drawback. The participation of the anions in the redox reaction means that there has always has to be enough salt in the electrolyte to allow the electrochemical reaction at the cathode to reach its full extent.[295] During the charge of the dual-ion battery, the salt concentration in the electrolyte decreases, due to the insertion of anions and cations respectively in the cathode and the anode. Vice versa, during discharge, the salt concentration increases due to the reversible de-insertion of the ions (**Figure 6.13**). This cyclic behavior of the salt concentration during charge and discharge can be also found in lead-acid batteries, which are based on the reaction between negatively charged sulfate ions and lead/lead oxide electrodes.[296] In fact, the energy density of lead-acid batteries is mainly limited by the large amount of the concentrated sulfuric acid solution needed to avoid the salt depletion during the discharge of the battery.

The same line of reasoning applies then to dual-ion batteries, and their design has hence to consider a thick enough separation region between the electrodes and/or a highly concentrated electrolyte to assure the presence of ions for the electrochemical reactions, both factors that decrease the energy density and increase the cost of a battery.[97,297] This is an additional limiting factor when compared for instance to lithium-ion batteries, where the salt concentration has local variations and gradients but then retains the same average value during operation.[298] In fact, in lithium-ion batteries, during charge lithium-ions are de-inserted at the cathode and inserted in the anode, and vice versa during discharge (**Figure 6.13**). Hence, the electrolyte is only a medium for the ions to travel between the electrodes, and a salt concentration of 1M (1000 mol$\cdot$m^{-3}) is sufficient to ensure good ionic conductivity and to avoid local ion depletion at the electrode/electrolyte interface.

In order to properly design batteries based on p-type materials, which normally operate in a dual-ion configuration, there is the need for a physics-based model that can accurately describe and simulate the behavior of this novel system in practically relevant configurations. Such a model would provide a deeper understanding of the electrochemical processes involving the variation of the salt concentration in the electrolyte and assist in the proper design of dual-ion batteries. So far, dual-ion batteries have been the focus of only mechanistic computational studies, involving Density Functional Theory (DFT) and Molecular Dynamics (MD), which investigated the interaction between anions and host structures in terms of electrochemical stability, potential of the electrochemical reaction, or reversibility of the insertion process.[299–302] However, the size and timescale of these models does not allow the simulation of entire batteries for full charge and discharge cycles or other types of characterization tests such as electrochemical impedance spectroscopy (EIS). A class of models that is suited for this objective are macroscale physic-based models, based on partial differential equations that aim to reproduce the physical processes involved in the battery operation. As far as the author knows, only one work in literature employed such a model in a system that included an anion-adsorbing cathode material, which was however mixed with a lithium-ion cathode material, and no experimental data were presented to validate the results of the simulations.[303]

In this Section, we propose a modified version of the standard pseudo-2D Doyle-Fuller-Newman (DFN) model, a widely used macroscale physical model originally developed for lithium-ion batteries,[298] to account for the different redox reactions that occur at the cathode and anode of dual-ion batteries. The model can simulate the variation of salt concentration in the electrolyte during charge and discharge of the dual-ion battery, including the concentration gradients that form along the battery thickness. It has been validated against cycling and impedance experimental data from dual-ion batteries with a mixture of poly(2,2,6,6-tetramethyl-1-piperidinyloxy methacrylate) (PTMA), belonging to the anion-interacting p-type class of organic materials, and multi-walled carbon nanotubes as cathode electrode material, a thick glass fiber separator, a lithium metal anode, and 1M $LiPF_6$ in EC:DEC 1:1 as the electrolyte in a lab-scale three-electrode cell setup. We will show how the model can serve as a valuable tool for supporting the design of dual-ion batteries, which entails a delicate balance between separator thickness, salt concentration, porosity and amount of cathode active material. This model will be then applied in the next section to support both experimental results on p-type organic materials and the related cost and performance analysis.

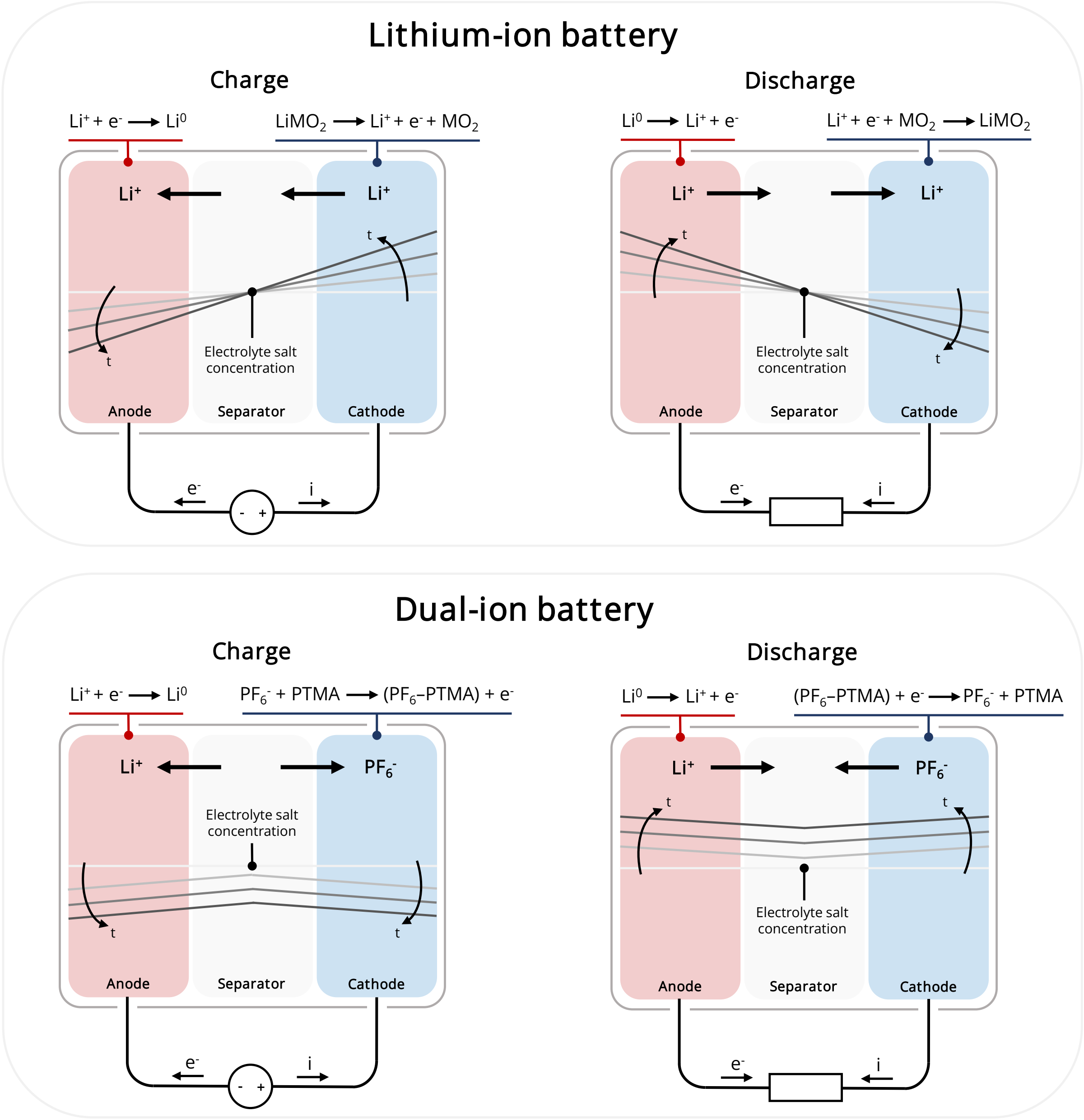

Figure 6.13 *– Schematic depiction of the charge and discharge processes of a lithium-ion battery (top) and a dual-ion battery (bottom), with the expected trend of the electrolyte salt concentration.*

6.3.1. Physical model

In this section, we report the developed physical model for dual-ion batteries, with the objective to show the key differences with the classic DFN model for lithium-ion batteries.

The 1D domain of the model is represented in **Figure 6.14**, composed by a dimensionless point representing the lithium metal anode for the cation redox reaction ($x = 0$), a porous separator (from $x = 0$ to $x = L_{sep}$), and a porous cathode for the anion redox reaction (from $x = L_{sep}$ to $x = L_{sep} + L_{pos}$). In each node of the cathode domain, analogously with the standard DFN model, a particle with radius r is present, to simulate the distribution of the anion concentration in the cathode material.

The model's equations are presented in **Table 6.3**, together with the boundary conditions of the partial differential equations (PDEs), while the step-by-step derivation of the model was already presented in Section 4.6. The meaning of all the used symbols is in **Table A3.1**. Being a 1D model, the gradients written in the following equations have to be intended as the derivative along the x-axis (or the r-axis, for the conservation of mass in the solid electrode).

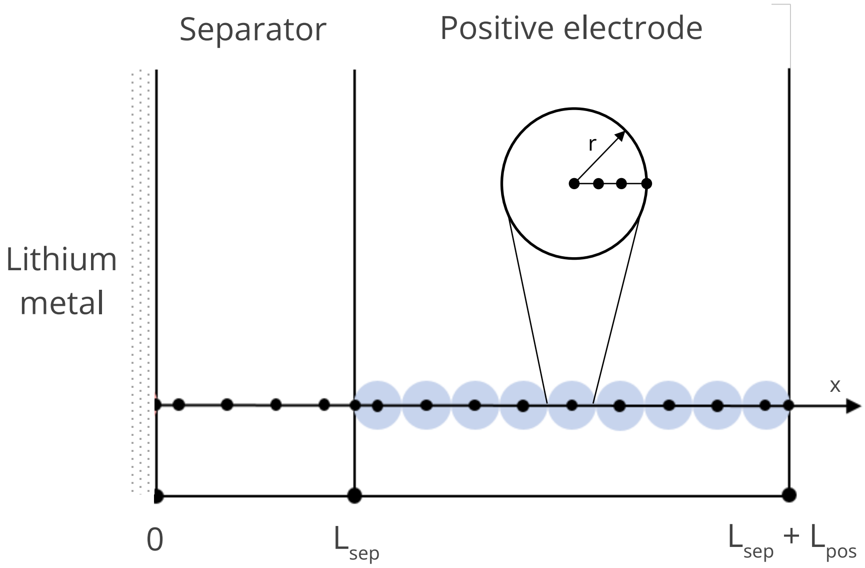

Figure 6.14 *– Representation of the model domain*

Table 6.3 *– Equations and boundary conditions of the dual-ion battery model*

Conservation of charge in the solid electrode

$$\nabla \cdot \left(-\sigma_{eff} \nabla \overline{\phi_s}\right) = a_s \bar{j} F + a_s C_{dl} \nabla\left(\overline{\phi_s} - \overline{\phi_e}\right) \tag{6.1}$$

$$\begin{cases} \nabla \overline{\phi_s}\big|_{x=L_{sep}+L_{pos}} = -\dfrac{i}{\sigma_{eff}} \\ \nabla \overline{\phi_s}\big|_{x=L_{sep}} = 0 \\ \overline{\phi_s}\big|_{x=0} = 0 \end{cases} \tag{6.2}$$

Conservation of charge in the liquid electrolyte

$$\nabla \cdot \left(-\kappa_{eff} \nabla \overline{\phi_e} - \frac{2\kappa_{eff} RT}{F} (t_+^0 - 1) \left(1 + \frac{\partial f_\pm}{\partial \ln c_e}\right) \nabla \ln \overline{c_e}\right) = -a_s \bar{j} F - a_s C_{dl} \nabla\left(\overline{\phi_s} - \overline{\phi_e}\right) \tag{6.3}$$

$$\begin{cases} -\kappa_{eff} \nabla \overline{\phi_e} - \dfrac{2\kappa_{eff} RT}{F} (t_+^0 - 1) \left(1 + \dfrac{\partial f_\pm}{\partial \ln c_e}\right) \nabla \ln \overline{c_e}\Big|_{x=L_{sep}+L_{pos}} = 0 \\ -\kappa_{eff} \nabla \overline{\phi_e} - \dfrac{2\kappa_{eff} RT}{F} (t_+^0 - 1) \left(1 + \dfrac{\partial f_\pm}{\partial \ln c_e}\right) \nabla \ln \overline{c_e}\Big|_{x=0} = i \end{cases} \tag{6.4}$$

Conservation of mass in the solid electrode

$$\frac{\partial c_s}{\partial t} = \frac{1}{r^2} \frac{\partial}{\partial r}\left(D_s r^2 \frac{\partial c_s}{\partial r}\right) \tag{6.5}$$

$$\begin{cases} \nabla c_s|_{r=0} = 0 \\ \nabla c_s|_{r=R_p} = -\bar{j} \end{cases} \tag{6.6}$$

Conservation of mass in the liquid electrolyte

$$\varepsilon_e \frac{\partial \overline{c_e}}{\partial t} = \nabla \cdot \left(D_{e,eff} \nabla \overline{c_e}\right) + a_s\, t_+^0\, \bar{j} \tag{6.7}$$

$$\begin{cases} \nabla \overline{c_e}|_{x=L_{sep}+L_{pos}} = 0 \\ D_{e,eff} \nabla \overline{c_e}|_{x=0} = (1 - t_+^0)\, \bar{j} \end{cases} \tag{6.8}$$

Electrochemical reaction (Butler-Volmer equation)

$$i = i_0 \left(\exp\left\{\frac{(1-\alpha) n F \eta}{RT}\right\} - \exp\left\{-\frac{\alpha n F \eta}{RT}\right\}\right) \tag{6.9}$$

$$\begin{cases} i|_{x=0} = \bar{j} F \\ i|_{x=L_{sep}+L_{pos}} = -\bar{j} F \end{cases} \tag{6.10}$$

Other definitions

$$V = \overline{\phi_s}\big|_{x=L_{sep}+L_{pos}} - \overline{\phi_s}\big|_{x=0} + R_{ext}\, i \tag{6.11}$$

$$\eta = \overline{\phi_s} - \overline{\phi_e} - E_{ocp} \tag{6.12}$$

$$Q = A\, \varepsilon_{s,pos}\, L_{pos}\, c_{max,pos}\, F\, (SOC_{max,pos} - SOC_{min,pos}) \tag{6.13}$$

$$c_{s,0,pos} = c_{s,max,pos}\left[SOC\left(SOC_{max,pos} - SOC_{min,pos}\right) + SOC_{min,pos}\right] \tag{6.14}$$

$$c_{e,0} = c_{e,ref}\left(1 - \frac{SOC\,\frac{Q}{F}}{c_{l,ref}\, A\left(\varepsilon_{e,sep}\, L_{sep} + \varepsilon_{e,pos}\, L_{pos}\right)}\right) \tag{6.15}$$

In the separator domain we have $\bar{j} = 0$, since there is no electrochemical reaction, while the lithium metal anode is modelled as an electrode surface, which becomes a dimensionless point in the 1D model, and a flux of ions is used as boundary condition for the conservation of mass in the liquid electrode in $x = 0$ (eq. 6.16). The potential $\overline{\phi_s}$ is set to 0 V in correspondence of the anode, and the lithium metal overpotential is calculated from the Butler-Volmer equation related to lithium-ion batteries. For the lithium metal anode, $E_{ocp} = 0$, while for the cathode the open circuit potential is taken from experimental data, function of the concentration of anions in the material, and inserted in the model as lookup table (**Figure A3.1**). The exchange current density i_0 in the Butler-Volmer equation is assumed to be a constant both for the cathode and for the anode side. The properties of the electrolyte are modelled according to the empirical equations given in Landesfeind & Gasteiger,[233] where the ionic conductivity, the salt diffusion coefficient, the activity coefficient and the transference number of $LiPF_6$ in EC:DEC 1:1 are measured in a wide range of salt concentrations and temperatures (see eq. (4.74) - (4.77)). Compared to the formal derivation, which focuses on the basic model, here in the main text we added the contribution of the double layer capacitance in the charge conservation equations in the electrode (eq. (6.1)) and the electrolyte (eq. (6.2)).[304]

The current applied to the battery is calculated according to the capacity Q and the desired C-rate. The initial state of charge (SOC) is inserted as a parameter and the initial concentration of anions in the cathode particles and the initial salt concentration in the electrolyte are calculated respectively with eq. (6.17) and (6.18). The galvanostatic cycling is simulated in the 3-4 V range, while the EIS is modelled at different SOCs in open circuit voltage conditions, as in the respective experiments. A contact resistance R_{ext} is added to the model to take into account the eventual impact of the cables resistance in the experimental results.

The main differences between the DFN model for dual-ion batteries and lithium-ion batteries are summarized in the following points:

- Since the redox reaction at the dual-ion battery cathode involves the consumption of anions during charge and their generation during, when the current density applied to the battery i is positive, the flux of anions j is negative, being j by convention positive when exiting the cathode material. However, i is by convention positive when the battery is charged, i.e., when the electrons flow from the cathode to the anode. Hence, the two quantities have opposite signs in a dual-ion battery, while for the same line of reasoning, it is the opposite in a lithium-ion battery (**Figure 6.13**).

- This affects the formulation of the conservation of charge in the solid electrode and the liquid electrolyte, where the sign of the right-hand terms of the two equations is the opposite of the corresponding ones of a lithium-ion battery model (see eq. (4.44) and (4.61)).

- The mass conservation in the liquid electrolyte is affected too. In this case, the transference number multiplied by the ion flux in the right-hand side of eq. (6.7) is t_+^0, the one associated to the cations. Instead, in the standard DFN model for lithium-ion batteries, this term is multiplied by t_-^0, the anion transference number (see eq. (4.52)). This arises from the fact that $a_s\bar{j}$ anions are generated in the volume during the electrochemical reaction and $a_s t_-^0 \bar{j}$ are transported out of the volume due the electrical current. Since the sum of the anion and cation transference numbers is equal to 1, the number of anions that stays in the volume is $a_s t_+^0 \bar{j}$. The same line of reasoning applies for the lithium-ion battery case, with inverted transference numbers.

- Finally, the initial electrolyte salt concentration $c_{e,0}$ is a function of the SOC of the cell. In fact, according to the SOC, a fraction of the anions present in the electrolyte will be stored in the cathode as a consequence of the electrochemical reaction, and the salt present in the electrolyte has to be consumed to provide anions for such a reaction. The higher the SOC, the higher the amount of anions in the cathode, and hence the lower $c_{e,0}$. The fraction of eq. (6.15) represents the ratio between the moles of anions present in the cathode and the maximum amount of moles of anions available in the electrolyte. In the lithium-ion battery model, $c_{e,0}$ is a constant, since its average value does not change during the operation of the battery.

6.3.2. Comparison of model results and experimental data

In **Table 6.4**, we report the value of the parameters used for the simulation of the dual-ion battery. The proposed parameter set has been derived by measuring, estimating, and assuming the numerical values, and it can be refined with further measurements on the studied system in future works. However, we do not aim to find the definitive parameter set that can describe univocally the system, but to show that the capability of the model to reproduce galvanostatic charge/discharge and EIS experimental results obtained with a laboratory-scale PTMA/Li metal battery.

***Table 6.4** – Values of the model parameters for the simulation of a PTMA|Li metal cell*

Parameter	Unit of measurement	Anode	Separator/Electrolyte/Cell	Cathode	Reference
α	$[-]$	0.5	-	0.5	Assumed
a_s	$[m^{-1}]$	-	-	$1{\cdot}10^5$	Assumed
A	$[m^2]$	-	$2.545{\cdot}10^{-4}$	-	Measured
bg	$[-]$	-	1.5	1.5	Assumed
$c_{e,ref}$	$[mol \cdot m^{-3}]$	-	1000	-	Measured
$c_{s,max}$	$[mol{\cdot}m^{-3}]$	-	-	4375	Estimated
C_{dl}	$[F \cdot m^{-2}]$	-	-	0.01	Assumed
D_s	$[m^2 \cdot s^{-1}]$	-	-	$2.5{\cdot}10^{-13}$	Assumed
ε_e	$[-]$	-	0.9	0.374	Estimated
ε_s	$[-]$	-	-	0.505	Estimated
i_0	$[A \cdot m^{-2}]$	5	-	2.7	Assumed
L	$[m]$	-	$260{\cdot}10^{-6}$	$62.6{\cdot}10^{-6}$	Measured
R_{ext}	$[\Omega \cdot m^2]$	-	$2.5{\cdot}10^{-4}$	-	Estimated
R_p	$[m]$	-	-	$10{\cdot}10^{-6}$	Assumed
σ	$[S \cdot m^{-1}]$	-	-	$2.0{\cdot}10^{-2}$	Assumed
SOC_{min}	[%]	-	-	0	Assumed
SOC_{max}	[%]	-	-	100	Assumed
T_0	$[K]$	293.15	293.15	293.15	Measured

7.

The variation of the electrolyte salt concentration during the operation of the dual-ion battery is shown in **Figure 6.15.c** and **Figure 6.15.d**, obtained by simulating a 10C charge and discharge cycle in galvanostatic mode in the model (**Figure 6.15.a**). Upon charge (**Figure 6.15c**), the average concentration of the salt decreases, since the electrochemical reactions at the anode and the cathode that are both consuming the electrolyte ions, while during the subsequent discharge (**Figure 6.15.d**) the ions are released by the electrodes and the initial average salt concentration is restored. The gradient of concentration along the thickness of the cell is due to mass transport limitations in the electrolyte due to the high employed current (10C).

In lithium-ion battery simulations with an analogous model, the salt concentration usually develops a gradient along the thickness of the battery, especially when high currents are used, but the average value remains always constant, since the same number of lithium ions is consumed in one electrode and generated in the other.[298]

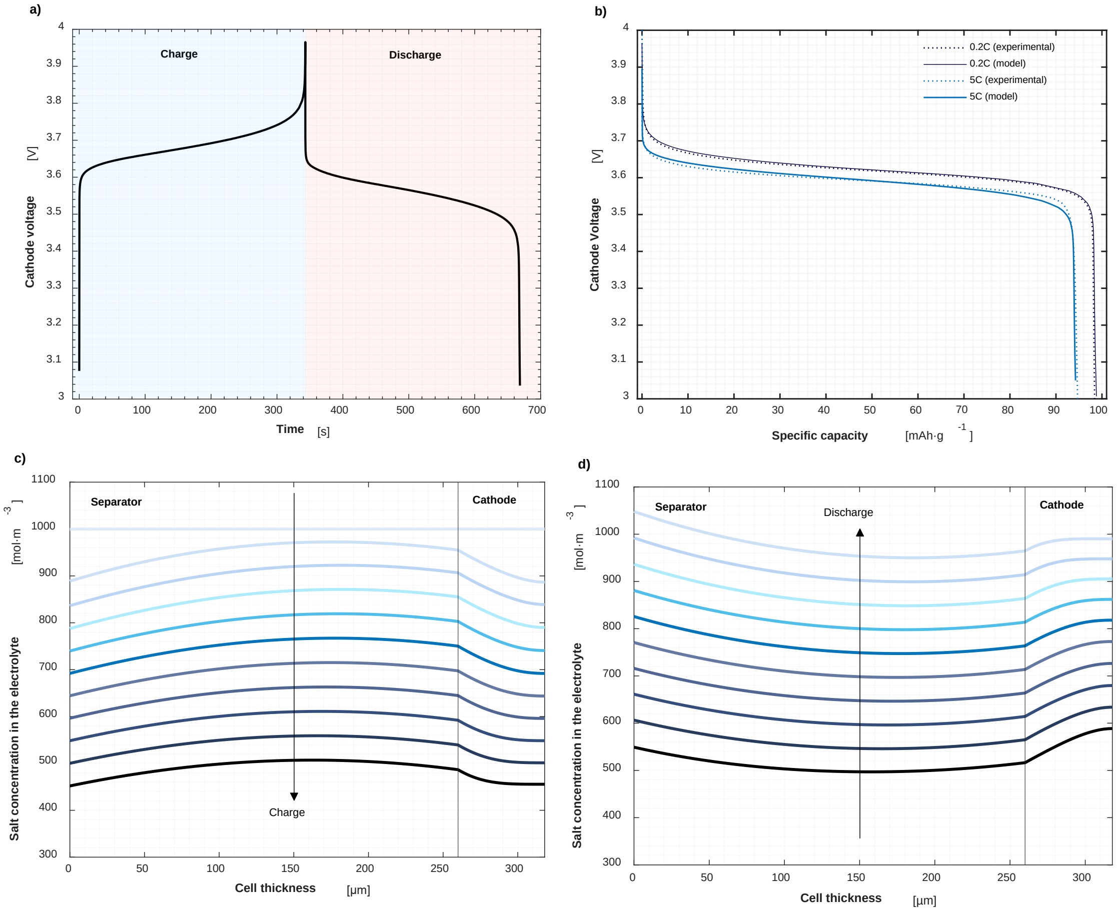

Figure 6.15 *– a) Voltage vs. time during a simulated galvanostatic charge and discharge cycle at 10C of the PTMA/Li metal cell, b) Comparison between the voltage vs. specific capacity characteristics of the model results (solid line) and the experimental data (dotted line) at 0.2C and 5C, c) Selected electrolyte salt concentration profiles at different time steps during the simulated 10C charge of the of the PTMA/Li metal cell, d) Selected electrolyte salt concentration profiles at different time steps during the simulated 10C discharge of the of the PTMA/Li metal cell*

In case of poorly conductive electrolytes and/or large C-rates applied for long time, the salt concentration can locally approach zero in lithium-ion batteries, but as soon as the load is disconnected, the diffusion processes starts to equilibrate the salt concentration and to restore its initial value.

Instead, the electrolyte salt can potentially get completely depleted in the dual-ion case: in the results of **Figure 6.15.c**, at the end of the discharge the average salt concentration value is ≈ 450 mol·m^{-3}. With a thicker cathode, where more active material has to be charged, or with a thinner or less porous separator, where less electrolyte and hence less salt is available, the salt concentration can reach zero before the charge process is fully complete, curtailing the energy that is possible to store in the dual-ion battery. This interplay between the size and porosity of the electrodes and separator and salt concentration in the electrolyte is then crucial to the design of this class of batteries.

Two experimental discharge curves at 0.2C and 5C are compared with model results at the same C-rates in **Figure 6.15.b**. The data were obtained by measuring the PTMA cathode potential against a pseudo-reference lithium metal electrode in a three-electrode configuration, to eliminate the influence of the lithium metal counter electrode. Therefore, in the simulations the cathode voltage (and the cathode impedance spectra shown in the next paragraphs) are measured against a modelled reference electrode placed in the separator next to the cathode. The model is able to well reproduce the experimental voltage-specific capacity relationship both at low and high current, with discrepancies in the voltage at low state of charge in the latter case, probably due to the solid diffusion modelling.

The only other work which proposed a macroscale physical modelling of a PTMA-based electrode did not consider the influence of diffusion of anions in the active material, since they assumed that the PTMA was forming a gel with the electrolyte and that no solid diffusion was taking place.[303] In our simulations, it was necessary to include the spherical particle modelling of the anion particles to reproduce the variation of specific capacity experimentally measured at different current rates. The anion diffusion coefficient in the solid D_S was set to a value of $2.5 \cdot 10^{-13}$ m^2·s^{-1}, a relatively high value when compared to typical lithium diffusion coefficients in inorganic cathode materials.[286] Nevertheless, the influence of the solid diffusion on the results of the simulations is determined by the radius of the particles, too. Herein, it was assumed to be 10 µm, but SEM images of both the PTMA powder (**Figure A3.2.a**) and the PTMA electrodes (**Figure A3.2.b**) did not show a clear particle size or shape, rather indicating an amorphous morphology. Hence, this parameter could be subject of refinement in future works, possibly considering the modelling of a particle size distribution instead of a single particle size as in this model.[305]

The comparison between the impedance spectrum between 100 kHz and 100 mHz at 53.4% SOC obtained in the model and the experimental one at the same SOC can be found in **Figure 6.16.a**. The two spectra agree very well in the high-mid frequency range, where the charge transfer resistance of the electrochemical reaction is usually identified. The short low frequency impedance tail, associated to diffusion phenomena, is well reproduced, too. The main discrepancy between the two spectra is the second, small semicircle between 4.5 and 5 Ω in the real axis, which could be associated to an additional interfacial phenomenon, such a cathode electrolyte interphase, which is not considered in the model's equations.[234] Hence, with the current state of the model, no combination of parameters could reproduce this two-semicircle spectrum that is experimentally measured.

By comparing the simulated and the experimental spectra in the whole SOC range in **Figure 6.16.b**, we see how the trend of the model results follows the one of the EIS data, with a decrease of the low frequency diffusion resistance when going towards the mid SOC region, a sharp increase of the same resistance at very low and very high SOCs, and a fairly constant value of the semicircle(s) in the high and medium frequency range. The lower slope of the model low frequency impedance at 99.8% and 0.3% SOC compared to the corresponding ones in the experimental data suggests that the for the model a semi-infinite diffusion approximation is still valid in the chosen frequency range, while the shape of the experimental data resembles the one of a limited diffusion case.[306] Hence, as suggested above in the discussion of the galvanostatic cycling data, an improvement of the modelling of the solid diffusion in the electrode particles may be necessary to well reproduce also this frequency range at extreme SOCs.

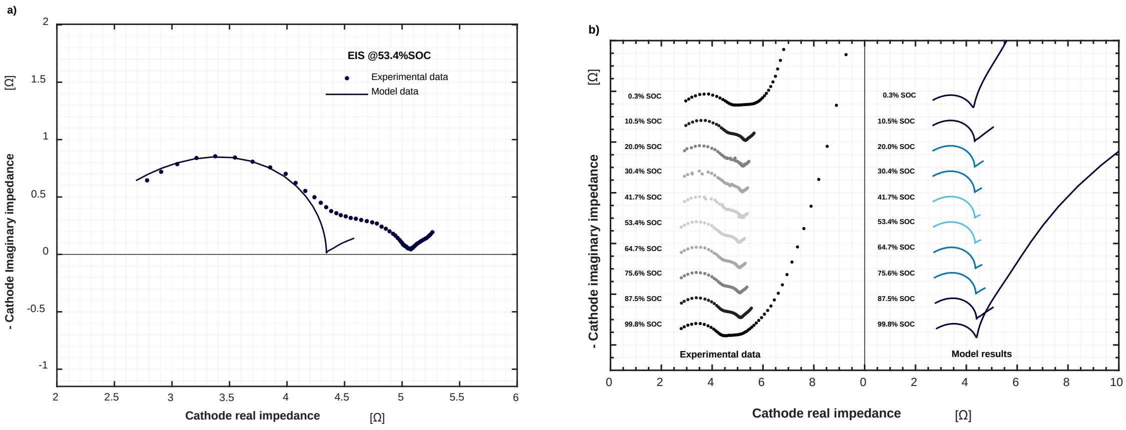

Figure 6.16 *– a) Comparison between the experimental (dotted) and the modelled (line) impedance spectrum at 53.4% SOC, b) Comparison between the experimental (grey scale, dotted) and the modelled (blue scale, line) impedance spectra at all the measured SOCs*

6.3.3 Application of the model for the design of dual-ion batteries

Despite the discussed limitations, the experimental data agrees with the model results, and the simulated trend of the electrolyte salt concentration during battery charge and discharge follows the theoretical one. These findings indicate that the model can successfully simulate the dual-ion battery operation.

Other than obtaining a deeper mechanistic understanding of the studied system, this model can well support the design of dual-ion batteries that respect the constraints imposed by the anion-involving redox reaction at the cathode, while optimizing key design parameters such as separator porosity and thickness, cathode porosity and thickness, and electrolyte salt concentration.

To give an example which uses the starting electrolyte salt concentration as design parameter, we simulate the dual-ion battery with the values reported in **Table 6.4**, except for a decrease of the separator thickness and porosity ($L_{sep} = 75\ \mu m$, $\varepsilon_{e,sep} = 0.5$). The resulting lower separator volume an accommodate only about one sixth of the electrolyte quantity that can occupy the volume calculated with the separator geometry of **Table 6.4**. Hence, the availability of anions for the electrochemical reaction decreases, and in fact the maximum specific capacity reached by the dual-ion battery during charge with this configuration is about 42 mAh·g^{-1}, with the salt electrolyte concentration that approaches zero at the cathode-current collector interface (**Figure 6.17.a**). By increasing the starting salt concentration in the electrolyte to 2000 mol·m^{-3} (2M), the reached specific capacity in charge doubles, reaching 86 mAh·g^{-1}, but only with a 3000 mol·m^{-3} (3M) starting concentration the full specific capacity is restored, and the salt concentration is still 970 mol·m^{-3} at the end of the charge. From **Figure 6.17.b**, we can see how the average electrolyte ionic conductivity in the battery varies sensibly along the three cases. For the 1M electrolyte, the conductivity decreases almost monotonically, while with the 2M and 3M electrolyte an increase is also observed, due to the lower conductivity of the solution at high concentrations.[233,307] This has an impact on the voltage profile during charge, and it is especially evident in the 3M case, where the overpotential at low SOC is stronger than in the other two simulated curves.

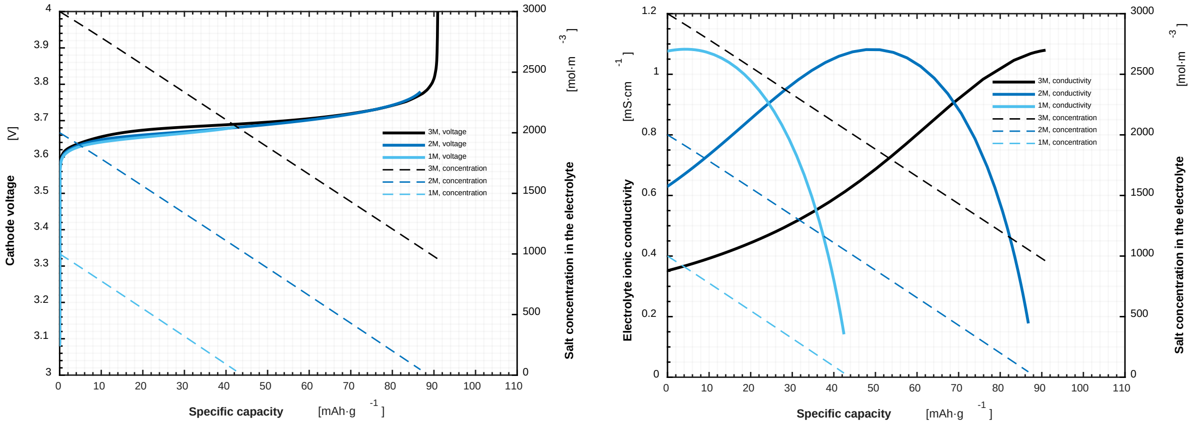

Figure 6.17 *– a) Comparison between the experimental (dotted) and the modelled (line) impedance spectrum at 53.4% SOC, b) Comparison between the experimental (grey scale, dotted) and the modelled (blue scale, line) impedance spectra at all the measured SOCs*

6.3.4 Conclusions

In conclusion, we propose a modified version of the Doyle-Fuller-Newman model to simulate the operation of dual-ion batteries, which involve both cations and anions in the redox reactions respectively at the anode and the cathode. The developed model successfully accounts for the variation of the average salt concentration in the electrolyte during the charge and discharge of the battery. The model is validated against experimental data from dual-ion batteries with PTMA, demonstrating its ability to well simulate the operation of these batteries.

This model has important implications for the design of dual-ion batteries, which require careful consideration of the electrolyte's salt concentration due to the involvement of anions in the redox reaction. By using the developed model, it is possible to optimize key design parameters such as separator porosity and thickness, cathode porosity and thickness, and electrolyte salt concentration to improve the performance of dual-ion batteries and obtain practical solutions.

This section, having introduced a macroscopic physical modelling of a dual-ion battery, can also serve as a starting point for an accurate mechanistic description of this peculiar class of batteries, with the objective of overcoming the discussed limitations. The proposed model can also be readily adapted to other anion-hosting materials, such as graphite or other p-type organic electrode materials.

6.4. Practical cell design for PTMA-based organic batteries

In this Section, we present a comprehensive study on PTMA-based batteries that covers various aspects, including optimizing the type and quantity of carbon additive in the electrode and maximizing the active mass loading at a lab-scale, simulating the behavior of PTMA-Li metal batteries based on the experimental results through physical modeling to evaluate the influence of design parameters, and conducting a detailed cost and energy analysis for these batteries. In general, by proposing this systematic methodology, we want to shed light on the challenges of transferring good results obtained in the typical laboratory conditions in battery material research to a more practical configuration.

6.4.1 Experimental results

Increasing the active material mass loading and accordingly the usable areal capacity entails having the smallest possible amount of conductive carbon in the final electrode. Hence, choosing an additive that can ensure good electrochemical performances when combined with PTMA while keeping its amount as low as possible is a crucial step in the electrode optimization. We synthesized then three batches with different conductive carbons added during the synthesis process, i.e., multi-walled carbon nanotubes (PTMA-MW15), graphene nanoplatelets (PTMA-GN15), and carbon black (PTMA-SP15). The weight fraction of additive with respect to the precursor was fixed to 15% for all the three batches. The results of the physicochemical characterization of these samples are reported in **Table 6.5**.

The synthesized batches were analysed with TGA, with a two-step procedure: a pyrolysis in inert gas (N_2) up to 800°C followed a cooldown period and an oxidation in 5% O_2 and 95% N_2 up to 800°C, for the sample with multi-walled carbon nanotubes, or 1000°C, for the other samples. The pyrolysis step induces the decomposition of the polymeric part, as evident from the sharp decline in the sample mass observed in **Figure 6.18.a** at around the 40-minute mark (220°C) for all the samples. Most of the decomposition products are gases which leave the crucible, but a minor fraction of the polymer decomposes into pyrolysis soot, i.e., carbonaceous particles.[308] Hence, the mass loss during the pyrolysis is not equal to the polymer weight fraction, since a small but relevant part remains as a solid product. Therefore, the oxidation step is required to burn off the carbon species remaining in the sample, which will be a mixture of pyrolysis soot and conductive carbon additive.

The TGA confirmed the presence of two distinct polymer and conductive carbon phases, in a relative weight ratio comparable to the one set during synthesis (**Figure 6.18.b**). In fact, we can see how the derivative of the mass loss (DTG) during the oxidation phase shows two peaks for all the studied samples (**Figure A4.2.a**, **Figure A4.2.b** and **Figure A4.2.c**). The peak at lower temperature can be associated to the oxidation of the pyrolytic soot formed by the polymer pyrolysis during the first phase of the TGA test in inert atmosphere,[308] while the second peak can be assigned to the combustion of the conductive additive. In fact, when performing the same TGA test on the sole conductive carbon additives, the oxidation DTG peaks of multi-walled carbon nanotubes and graphene nanoplatelets correspond with the second DTG peak of the respective polymer-carbon mixtures. The carbon black oxidation peak has the same shape of the second DTG peak of PTMA-SP15, but shifted of ≈80°C, as the heat released by the preceding oxidation of the pyrolysis soot may decrease the activation energy of the carbon black oxidation. By measuring the mass loss of each sample up to the point where the DTG has a maximum between the two peaks, it is possible to estimate the amount of polymer present in the mixture, by summing the mass loss due to the pyrolysis and the one due to the oxidation of the pyrolytic soot derived from the polymer. Moreover, the residual mass at the end of the oxidation indicates the amount of non-volatile impurities that are present in the samples due to the synthesis process, hence giving a more accurate representation of the composition of the mixture. The weight fraction of PTMA resulting from the TGA curves is about 1.5-2.5% lower than the theoretical one, probably due to a small fraction of non-polymerized monomer after the first synthesis step which was washed away.

The true density of the samples was measured with helium pycnometry, and the results were 1.266 $g\cdot cm^{-3}$ for PTMA-MW15, 1.262 $g\cdot cm^{-3}$ for PTMA-GN15, and 1.238 $g\cdot cm^{-3}$ for PTMA-SP15. The lower value for the latter sample can be associated to the low true density of carbon black (1.83 $g\cdot cm^{-3}$) when compared to graphene nanoplatelets (2.26 $g\cdot cm^{-3}$).[309] Despite having PTMA-MW15 the largest true density value, the true density of the multi-walled carbon nanotubes is actually assumed to be even slightly lower than the other additives (1.75 $g\cdot cm^{-3}$).[309] However, the lower amount of carbon and higher amount of high-density metal oxide impurities in PTMA-MW15 than the other two samples explain this discrepancy. It is worth to note that the density of these active materials is around one third of lithium iron phosphate (3.45 $g\cdot cm^{-3}$) and one fourth of lithium layered oxides (>4.5 $g\cdot cm^{-3}$),[75] due to the light organic elements of which they are made of, and this comes as a disadvantage for the volumetric capacity of PTMA-based batteries.

The electronic conductivity of the powders, measured through impedance spectroscopy, reveal that how PTMA-MW15 is the most conductive sample, with a value of $5.1\cdot 10^{-2}$ $S\cdot cm^{-1}$. The multi-walled carbon nanotubes are known to form good percolation networks the electron conduction thanks to their high aspect ratio (≈ 160) and specific surface area (250-300 $m^2 \cdot g^{-1}$),[310] leading to a relatively high value for the electronic conductivity. Note that the solid-state electronic conductivity of PTMA is estimated to be in the 10^{-11} $S \cdot cm^{-1}$ order of magnitude,[311] with only very pure nanometer-thick PTMA films that reach 10^{-5} $S \cdot cm^{-1}$.[312] The benefits of using high aspect ratio conductive additives for radical polymer batteries was also confirmed by studies that employed vapor-grown carbon fibers (VGCF) during the electrode preparation.[207,209,313] The graphite nanoplatelets offer only one order of magnitude less specific surface areas (20-40 $m^2 \cdot g^{-1}$), and the aspect ratio lies in the 10-100 range even in the same sample, due to agglomeration and stacking of the nanoplatelets,[314] therefore a lower value of $4.8 \cdot 10^{-3}$ $S \cdot cm^{-1}$ is measured. The carbon black has a lower surface area (≈ 60 $m^2 \cdot g^{-1}$) too, while the aspect ratio has a value close to unity due to its quasi-spherical shape. Hence, the formation of a percolation network with this additive is severely hindered, achieving only a limited electronic conductivity of $1.5 \cdot 10^{-7}$.[315]

SEM images on the powders and on the electrodes are in accordance with the electronic conductivity measurements. In fact, in the images of PTMA-SP15 powder and electrode, charging effects are noticeable in several parts of the samples, an indicator of the presence of isolated non-conductive polymer agglomerates in the analyzed materials (**Figure A4.3**). In the PTMA-GN15 electrode images, some insulating polymer particles can be also individuated, but not in the powder sample (**Figure A4.4**). Such features are not seen in images of the PTMA-MW15 samples (**Figure A4.5**).

The composition, mass loading, density and porosity of the electrodes are reported in **Table 6.6**. The obtained active material mass loadings are >4 $mg \cdot cm^{-2}$, and the electrode density of PTMA-GN15 and PTMA-MW15 is almost equal (respectively, 0.788 and 0.787 $g \cdot cm^{-3}$), while the one of PTMA-SP15 is significantly lower (0.689 $g \cdot cm^{-3}$). This results in a porosity of around 38% for the first two samples and around 45% for the latter (see the Supporting Information for the details about the calculations). The values are relatively high for battery electrodes, which usually lie in the 20-30% range,[291] but since PTMA-based cathodes require a high amount of electrolyte due to the involvement of anions in the electrochemical reaction, larger and more numerous pores can be beneficial for a properly working electrode.

The electrochemical performances of the three samples in galvanostatic charge and discharge tests in coin cells with a lithium metal anode are reported in **Table 6.7**, and shown in **Figure 6.18.c** and **6.18.d**. The PTMA-MW15 sample has the highest specific capacity and the lowest overpotential at every current rate, as it can be seen from the specific capacity trend and the voltage-capacity curves.

At 1C, the specific capacity of PTMA-MW15 is 99.7 mAh·g^{-1}, against 57.1 mAh·g^{-1} for PTMA-SP15 and 50.8 mAh·g^{-1} of PTMA-GN15. The capacity of the latter materials drops to about 23 mAh·g^{-1} at 5C, while PTMA-MW15 retains 92.4 mAh·g^{-1} (**Figure A4.9.a**). The worse performance of PTMA-SP15 and PTMA-GN15 could be explained by their lower electronic conductivity and homogeneity of the sample, which hinders the access to the full capacity of the material. Instead, PTMA-MW15 achieves at 1C about 90% of the theoretical specific capacity (111 mAh·g^{-1}), with the remaining 10% of unused capacity which can be explained by the slightly lower weight fraction of PTMA in the cathode than the theoretical one, and by the incomplete oxidation of the polymer during the synthesis process.

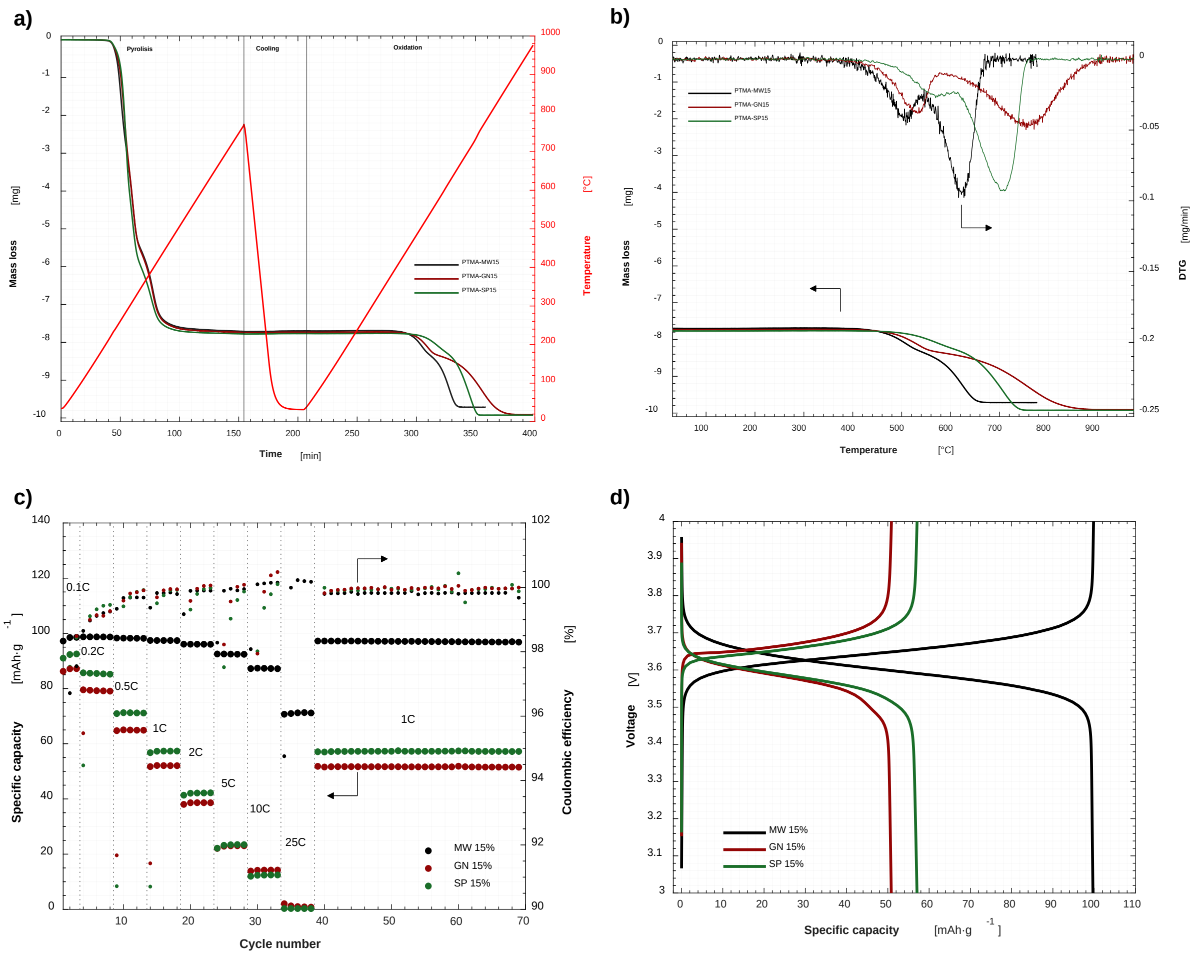

***Figure 6.18** – a) TGA results of the PTMA-MW15, PTMA-GN15, and PTMA-SP15 samples, b) Detail on the oxidation part of the TGA results on the three samples, with the respective DTG curves; c) Specific capacity and coulombic efficiency vs. cycle number for the rate performance test of the three samples in coin cells with a lithium metal anode at 20°C; d) Related voltage vs. specific capacity charge and discharge curves of the three samples at 1C (cycle n° 50 of **Figure 6.18.c**)*

The PTMA-MW15 sample was able to cycle satisfactorily with sodium metal as anode too,[316,317] hence using sodium ions as cations in the dual-ion battery configuration, albeit with worse rate performance and cycling stability than the lithium-based system probably due to the lower ionic conductivity of the 1M $NaPF_6$ in EC:PC 3:7 when compared to 1M $LiPF_6$ in EC:DMC 1:1, and to the higher instability of sodium metal (**Figure A4.10**).[82,318]

***Table 6.5** – Results of the physicochemical characterization of the polymer-carbon powder samples*

Sample	**Additive**	**Theoretical powder composition [a]**	**Actual powder composition [b]**	**Powder true density [g·cm^{-3}]**	**Powder electronic conductivity [S·cm^{-1}]**
PTMA-GN15	Graphene nanoplatelets	85/15	83.57/15.42/1.01	1.2616 ± 0.0001	(4.8 ± 0.2)·10^{-3}
PTMA-SP15	Carbon black	85/15	82.72/16.54/0.74	1.2383 ± 0.0001	(1.5 ± 0.3)·10^{-7}
PTMA-MW15	Multi-walled carbon nanotubes	85/15	83.45/13.56/2.99	1.2660 ± 0.0002	(5.1 ± 0.5)·10^{-2}
PTMA-MW10	Multi-walled carbon nanotubes	90/10	87.60/10.10/2.30	1.2265 ± 0.0004	(7.1 ± 0.8)·10^{-3}
PTMA-MW5	Multi-walled carbon nanotubes	95/5	92.63/5.38/1.99 [c]	1.1930 ± 0.0001	(5.8 ± 0.6)·10^{-7}
PTMA-MW2.5	Multi-walled carbon nanotubes	97.5/2.5	95.06/2.94/2.00 [c]	1.1794 ± 0.0001	-

[a] Polymer/conductive additive weight ratio [b] Polymer/conductive additive/impurities weight ratio

***Table 6.6** – Results of the physicochemical characterization of the electrodes*

Sample	**Theoretical electrode composition [a]**	**Actual electrode composition [b]**	**Electrode mass loading [mg·cm^{-2}]**	**Electrode density [g·cm^{-3}] [c]**	**Electrode porosity [%] [c]**
PTMA-GN15	76.5/13.5/5/5	75.2/13.9/5/5/0.9	4.44 ± 0.21	0.788 ± 0.025	38.66 ± 1.35
PTMA-SP15	76.5/13.5/5/5	74.4/14.9/5/5/0.7	4.06 ± 0.21	0.689 ± 0.007	45.46 ± 1.35
PTMA-MW15	76.5/13.5/5/5	75.1/12.2/5/5/2.7	4.09 ± 0.22	0.787 ± 0.017	37.91 ± 1.35
			8.40 ± 0.32[d]	-	-
			9.01 ± 0.53[e]	-	-
PTMA-MW10	81/9/5/5	78.9/9.1/5/5/2.0	3.79 ± 0.07	0.727 ± 0.015	41.62 ± 1.18
PTMA-MW5	85.5/4.5/5/5	83.4/4.8/5/5/1.8	4.12 ± 0.05	0.746 ± 0.017	39.10 ± 1.37
PTMA-MW2.5	87.75/2.25/5/5	85.6/2.6/5/5/1.8	4.28 ± 0.12	0.738 ± 0.004	39.28 ± 0.35

[a] Polymer/conductive additive/C45/binder weight ratio, [b] Polymer/conductive additive/C45/binder/impurities weight ratio, [c] The density and porosity measurements were done on other electrodes than the ones used for the electrochemical characterization, prepared in the same conditions and with the same parameters, [d] Mass loading of electrodes obtained increasing the coating wet thickness from 120 µm to 300 µm, [e] Mass loading of electrodes obtained increasing the coating wet thickness from 120 µm to 300 µm and the solid weight fraction in the slurry from 40% to 45%

Table 6.7 *- Results of the electrochemical characterization of selected electrodes*

Sample	Active material mass loading	Theoretical Specific capacity/ Areal capacity/ Volumetric capacity	Specific capacity/ Areal capacity/ Volumetric capacity @0.2C (Discharge)	Specific capacity/ Areal capacity/ Volumetric capacity @1C (Discharge)	Specific capacity/ Areal capacity/ Volumetric capacity @5C (Discharge)
PTMA-GN15	4.38 mg·cm^{-2}	111 mAh·g^{-1}/ 0.486 mAh·cm^{-2}/ 66.9 mAh·cm^{-3}/	79.2 mAh·g^{-1}/ 0.347 mAh·cm^{-2}/ 47.7 mAh·cm^{-3}/	52.1 mAh·g^{-1}/ 0.228 mAh·cm^{-2}/ 31.4 mAh·cm^{-3}/	23.3 mAh·g^{-1}/ 0.102 mAh·cm^{-2}/ 14.1 mAh·cm^{-3}/
PTMA-SP15	4.20 mg·cm^{-2}	111 mAh·g^{-1}/ 0.466 mAh·cm^{-2}/ 58.5 mAh·cm^{-3}/	85.3 mAh·g^{-1}/ 0.358 mAh·cm^{-2}/ 45.0 mAh·cm^{-3}/	57.4 mAh·g^{-1}/ 0.241 mAh·cm^{-2}/ 30.3 mAh·cm^{-3}/	23.4 mAh·g^{-1}/ 0.098 mAh·cm^{-2}/ 12.3 mAh·cm^{-3}/
PTMA-MW15	4.11 mg·cm^{-2}	111 mAh·g^{-1}/ 0.456 mAh·cm^{-2}/ 66.8 mAh·cm^{-3}/	99.8 mAh·g^{-1}/ 0.410 mAh·cm^{-2}/ 60.1 mAh·cm^{-3}/	98.1 mAh·g^{-1}/ 0.403 mAh·cm^{-2}/ 59.1 mAh·cm^{-3}/	91.2 mAh·g^{-1}/ 0.375 mAh·cm^{-2}/ 54.9 mAh·cm^{-3}/
	9.65 mg·cm^{-2}	111 mAh·g^{-1}/ 1.07 mAh·cm^{-2}/ 66.8 mAh·cm^{-3}/	100.2 mAh·g^{-1}/ 0.967 mAh·cm^{-2}/ 60.3 mAh·cm^{-3}/	91.3 mAh·g^{-1}/ 0.881 mAh·cm^{-2}/ 55.0 mAh·cm^{-3}/	66.0 mAh·g^{-1}/ 0.637 mAh·cm^{-2}/ 39.7 mAh·cm^{-3}/
PTMA-MW10	3.92 mg·cm^{-2}	111 mAh·g^{-1}/ 0.435 mAh·cm^{-2}/ 61.7 mAh·cm^{-3}/	97.0 mAh·g^{-1}/ 0.380 mAh·cm^{-2}/ 53.9 mAh·cm^{-3}/	92.6 mAh·g^{-1}/ 0.363 mAh·cm^{-2}/ 51.5 mAh·cm^{-3}/	76.8 mAh·g^{-1}/ 0.301 mAh·cm^{-2}/ 42.7 mAh·cm^{-3}/
PTMA-MW5	4.23 mg·cm^{-2}	111 mAh·g^{-1}/ 0.469 mAh·cm^{-2}/ 63.3 mAh·cm^{-3}/	97.1 mAh·g^{-1}/ 0.410 mAh·cm^{-2}/ 55.4 mAh·cm^{-3}/	83.1 mAh·g^{-1}/ 0.351 mAh·cm^{-2}/ 47.4 mAh·cm^{-3}/	56.2 mAh·g^{-1}/ 0.237 mAh·cm^{-2}/ 32.1 mAh·cm^{-3}/
PTMA-MW2.5	4.15 mg·cm^{-2}	111 mAh·g^{-1}/ 0.461 mAh·cm^{-2}/ 62.7 mAh·cm^{-3}/	93.2 mAh·g^{-1}/ 0.387 mAh·cm^{-2}/ 52.6 mAh·cm^{-3}/	75.8 mAh·g^{-1}/ 0.315 mAh·cm^{-2}/ 42.8 mAh·cm^{-3}/	35.6 mAh·g^{-1}/ 0.148 mAh·cm^{-2}/ 20.1 mAh·cm^{-3}/

Due to the good performances shown by multi-walled carbon nanotubes as conductive additives for the synthesis of PTMA, we tried to lower the amount added in the polymerization reaction, to obtain active materials with higher content of redox polymer and to maximize the areal capacity of the resulting cathodes. Therefore, we prepared three additional batches, PTMA-MW10, PTMA-MW5, PTMA-MW2.5, respectively with 10%, 5% and 2.5% weight fraction of multi-walled carbon nanotubes added during synthesis with respect to the monomer precursor.

The same characterization steps were repeated (**Table 6.5**), and the TGA curves of **Figure 6.19.a** show how the mass loss during the pyrolysis phase, i.e., the one associated with the polymer decomposition, increases with the PTMA fraction in the sample. The DTG curves of the oxidation phase are quite different among the four samples (**Figure 6.19.b**). PTMA-MW10 still shows two peaks, with the first one corresponding to the one at lower temperature of the PTMA-MW15, hence to the pyrolytic soot oxidation. The second peak is situated 40°C lower than the peak of the carbon additive oxidation (**Figure A4.2.d**), probably due to the heat released by the combustion of the pyrolytic soot. PTMA-MW5 and PTMA-MW2.5 are characterized by only one DTG peak, hence it is not possible to distinguish between the mass loss due to the pyrolytic soot and the multi-walled carbon nanotubes (**Figure A4.2.e** and **Figure A4.2.f**). The amount of polymer in these two samples was hence estimated by assuming that they have the same percentage difference between the actual and theoretical weight fractions of PTMA of the average of PTMA-MW15 and PTMA-MW10. Overall, the actual PTMA fraction in the powders of the analysed samples is about 2.5% lower than the desired value.

The true density of the powders was found to be 1.227 g·cm^{-3} for PTMA-MW10, 1.193 g·cm^{-3} for PTMA-MW5, and 1.179 g·cm^{-3} for PTMA-MW2.5, with an expected decreasing trend of the density with the increase of the polymer fraction. From these measurements, it is estimated that the PTMA polymer has a true density of 1.17 g·cm^{-3}.

By measuring the electronic conductivity of the powders, a clear trend with the carbon fraction is evident. PTMA-MW10 manages to achieve a value of $7.1\cdot10^{-3}$ S·cm^{-1}, PTMA-MW5 of $8.5\cdot10^{-7}$ S·cm^{-1}, while it was not possible to measure the conductivity of PTMA-MW2.5, being probably too insulating for such a characterization. Decreasing the quantity of multi-walled carbon nanotubes brings, as expected, a decrease in the electronic conductivity. The SEM images reflect these findings: the PTMA-MW10 powder already shows plenty of non-conductive regions, evidenced by the white parts in the image caused by the electrostatic charging of the polymer particles (**Figure A4.6**), and the images of PTMA-MW5 and -MW2.5 powders are blurred because of this effect, which is even stronger in the latter samples because of the lower carbon content and the very low electronic conductivity (**Figure A4.7** and **Figure A4.8**). Isolated, non-conductive particles can be seen in the images of surfaces of the electrodes made with the active materials, with the number of these particles increasing as the additive fraction decreases.

The average active material mass loading of the electrodes made with these samples is higher than the PTMA-MW15 sample (4.09 mg·cm^{-2}) only for PTMA-MW5 and PTMA-MW2.5 (4.12 mg·cm^{-2} and 4.28 mg·cm^{-2}, respectively), with comparable porosities and slightly lower electrode densities due to the larger polymer fraction. Instead, electrodes made with PTMA-MW10 consistently and unexpectedly show lower mass loading (3.79 mg·cm^{-2}) and higher electrode porosity (>41%).

The electrochemical performances of the four samples, compared in **Figure 6.19.c** and reported in **Table 6.7**, show how the carbon fraction in the material strongly affects the performance at mid-high current rates. In fact, at 0.2C the materials have a rather comparable specific capacity, while the difference becomes much more relevant at 1C and 5C. As seen in **Figure 6.19**, where the voltage-specific capacity curves at 1C are compared, the samples with lower amount of carbon suffer from both an overpotential caused by a higher resistance of the electrode and from a lower final capacity that seems to be caused by diffusion limitations. In fact, EIS measurements made with a three-electrode setup on these four PTMA-based cathodes revealed that PTMA-MW5 (**Figure A4.11.c**) and PTMA-MW2.5 (**Figure A4.11.d**) have a much larger low-frequency impedance than PTMA-MW15 (**Figure A4.11.a**), for the whole state of charge range.

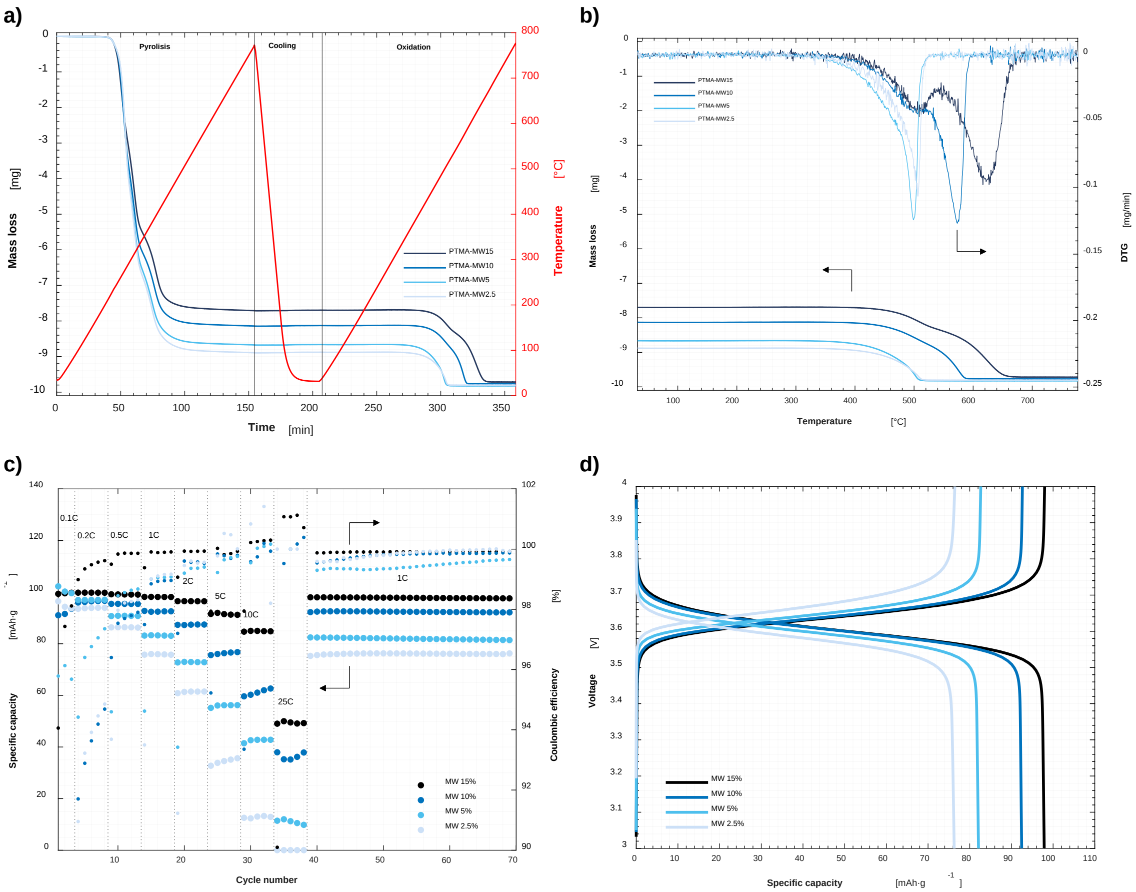

Figure 6.19 – a) TGA results of the PTMA-MW15, PTMA-MW10, PTMA-MW5, and PTMA-MW2.5 samples, b) Detail on the oxidation part of the TGA results on the four samples, with the respective DTG curves; c) Specific capacity and coulombic efficiency vs. cycle number for the rate performance test of the four samples in coin cells with a lithium metal anode at 20°C; d) Related voltage vs. specific capacity charge and discharge curves of the four samples at 1C (cycle n° 50 of ***Figure 6.19.c****)*

The impedance at low-frequency is commonly associated to the diffusion of ions in the electrolyte and in the electrode, and a high impedance in this region is connected to a “cut” in the available capacity at moderate and high current rates.[22,306] However, the impedance of the PTMA-MW10 cell is lower than the one of all the other samples (**Figure A4.11.b**), which is apparently in contrast with the results in galvanostatic cycling, which show that the capacity is inferior than PTMA-MW15 at all the current rates. The smaller impedance may be explained by the slightly lower mass loading and higher porosity that characterize this sample.

The performance of two cells made with such electrodes are shown in **Figure 6.20.a** and **Figure 6.20.b** (Cell 1: 9.65 mg·cm^{-2}, Cell 2: 9.39 mg·cm^{-2}). The increase in mass loading did not affect the specific capacity at low rates, but the polarization at currents equal or higher than 1C is evident. The loss of capacity and the increased overpotential when compared to the performance at low loading are probably caused by the higher resistance of the thicker electrodes, and to enhanced mass transport losses because of the larger distance the ions have to travel. The higher currents cause also higher overpotentials on the lithium metal side, which contribute significantly to the loss of capacity (**Figure A4.12**). It has to be remarked that the PTMA cathodes show good cycling stability even at such high mass loadings and that most of the degradation seems to come from the effect of the lithium metal anode. While with 1M $LiPF_6$ in EC:DMC 1:1 the degradation is evident and dendrite formation as well as capacity fading are observed (**Figure A4.13.a**), with a modified electrolyte (1M LiFSI in EC:DMC 1:1) the cells are able to cycle at moderate rates for hundreds of cycles. It is know that LiFSI can form more stable interfaces on the lithium metal anode than $LiPF_6$,[319,320] and electrodes with mass loading >8 mg·cm^{-2} were tested with the latter electrolyte and they achieved 700 cycles, the most of which at 0.9C, with low capacity fading, thanks to the crosslinking of the PTMA polymer[147,206] and the higher stability of the lithium metal anode (**Figure A4.13.b**).

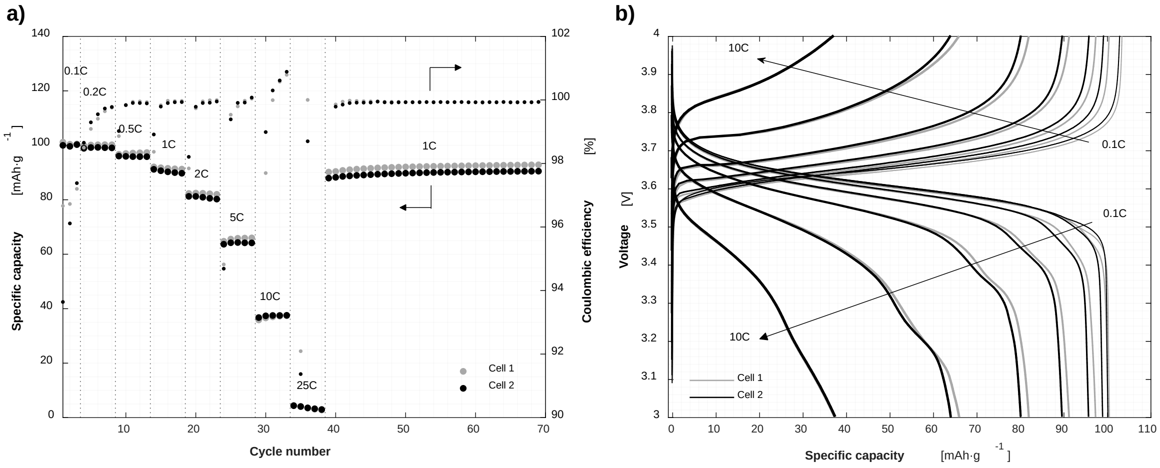

Figure 6.20 - *a) Specific capacity and coulombic efficiency vs. cycle number for the rate performance test of the PTMA-MW15 high mass loading electrodes in coin cells with a lithium metal anode at 20°C; b) Related voltage vs. specific capacity charge and discharge curves of the two samples at several current rates*

6.4.2 Design of a PTMA battery: physical simulations

The experimental results obtained in coin cells with the PTMA cathodes should be then put into perspective, to understand how such a high mass loading organic battery could be implemented in a realistic battery design. In fact, by using thick and very porous glass fiber separators and adding plenty of electrolyte in the cells, the involvement of the anions in the PTMA redox process is not a limiting factor. When the quantity of electrolyte is limited, such as the very thin commercial plastic separators with relatively low porosity, the electrochemical performances are severely limited if a 1M electrolyte is used. This can be seen in the charge/discharge curves shown in **Figure A4.14**, where both low and high mass loading electrodes were tested in lithium metal coin cells with a 10 µm polyolefin separator with a minimal amount of electrolyte to wet the separator and the cathode. Only 12 mAh·g^{-1} are available at 1C for a 4.73 mg·cm^{-2} cathode, and 8 mAh·g^{-1} for a 9.10 mg·cm^{-2} one with such a separator and electrolyte quantity, because the quantity of anions present in the battery is not sufficient to fully charge the PTMA cathode.

We introduce then a dimensionless design parameter that can be used to understand whether the quantity of anions present in the electrolyte is enough to exploit the whole capacity of the PTMA cathode (and, in general, every dual-ion battery cathode). The parameter, indicated as K, is calculated as

$$K = \frac{(c_{e,ref} - c_{e,min})}{c_{s,max,pos}} \cdot \left(\frac{L_{sep}\varepsilon_{l,sep}}{L_{pos}\varepsilon_{s,pos}} + \frac{\varepsilon_{l,pos}}{\varepsilon_{s,pos}} \right) \tag{6.19}$$

where $c_{e,ref}$ is the salt molar concentration in the electrolyte that is present when the battery is fully discharged, $c_{e,min}$ is the minimum salt molar concentration in the electrolyte that should not be exceeded when charging the battery, because of the excessive decrease of the ionic conductivity or of the electrochemical stability of the electrolyte, $c_{s,max,pos}$ is the molar concentration of active sites in the PTMA, L_{sep} and L_{pos} are respectively the thickness of the separator and cathode, and $\varepsilon_{l,pos}$, $\varepsilon_{l,sep}$, and $\varepsilon_{s,pos}$ are respectively the volume fraction of electrolyte in the cathode (i.e., the cathode porosity), of electrolyte in the separator (i.e., the separator porosity), and of active material in the cathode. We consider a metal foil as anode, such as lithium or sodium metal, and not a porous anode as a graphite electrode, and hence we do not include the volume of the anode in the formula.

If K is higher than 1, the number of anions in the electrolyte are sufficient to compensate the positive charges generated in the cathode during the charge of the PTMA battery. On the contrary, with K lower than 1, the active material in the cathode requires more anions than the ones that are available in the electrolyte. This dimensionless parameter is directly proportional to the initial electrolyte salt concentration and to the size and porosity of the separator, and it is inversely proportional to the concentration of active sites in the cathode, as well as on its size and solid fraction. The derivation of K can be found in the Supporting Information.

Through this parameter, we can investigate which combinations of design parameters allow the proper functioning of a PTMA battery, i.e., that provides enough anions to fully charge the cathode and does not deplete excessively the salt concentration in the electrolyte. In **Figure 6.21**, the trend of K with some design parameters is shown. For all the figures, the value of $c_{s,max,pos}$ used to calculate K is 4375 mol·m^{-3}, which corresponds to a practical specific capacity of 100.2 mAh·g^{-1} if a density the PTMA polymer of 1.17 g·cm^{-3} is assumed.

In **Figure 6.21.a**, the parameters corresponding to a low mass loading electrode and 1M electrolyte are used for the calculations, and the separator thickness and porosity are varied. All the configurations below the solid black like at $K = 1$ would not charge completely the battery, while the ones over the line would allow the use of the full capacity of the cathode. We can see how even the electrodes with the lower loading could not be fully charged without very thick and porous separator, like the glass fiber ones used in the experiments in coin cells, which are only used in research scale batteries. A commercial style separator, with thickness lower than 20 µm and electrolyte volume fraction lower than 50%, would charge only around 20% of the battery ($K \approx 0.2$).

By increasing the electrode thickness to the values of the high mass loading cathodes developed in this work and keeping the same electrolyte concentration and volume fractions, **Figure 6.21.b** shows that no configuration up to 300 µm of separator thickness could allow the PTMA battery to fully charge, since K is always lower than 1. This could come as a contradiction to our experimental results with the high mass loading electrodes, which, despite being done with a 260 µm separator with around 90% electrolyte volume fraction, achieved the full capacity at low current rates. However, in these calculations of K we assume that the electrode and the separator have the same area, while in our coin cell setup the separator had a 16 mm diameter and the cathode 12 mm diameter, hence the separator could accommodate around the double of electrolyte than if it had the same size of the cathode.

Hence, to obtain a viable battery with such a high mass loading electrode while using a thin commercial separator, assumed to have a thickness of 16 µm and a pore fraction of 37%, it is necessary to increase the concentration of the salt in the electrolyte. In **Figure 6.21.c**, the thickness and porosity of the cathode are varied, assuming a salt concentration of 3000 mol·m^{-3} (3M), near the solubility limit of $LiPF_6$ in EC:DMC 1:1 at ambient temperature. By varying the cathode parameters, two contrasting effects happen: increasing the thickness of the cathode means of course having a larger amount of active material that needs to be charged, but it also means that there is more porosity in the electrode that can be exploited to accommodate electrolyte, providing additional anions for the redox process. The latter effect is more pronounced the higher the pore fraction of the cathode, vice versa for the former. With these parameters, the high mass loading cathode obtained experimentally, which has a pore fraction of around 39%, could not be fully charged. Only by increasing the cathode porosity to values higher than 50% a proper design is achieved. However, this modification decreases the active material mass loading of the electrode if the thickness is kept constant, because there is less space available for the active material, hence the resulting mass loading and the areal capacity would be inferior to the ones of our experimental results.

Therefore, to try to keep the same cathode parameters of the ≈10 mg·cm^{2} PTMA electrodes, we can assume the use of a hypothetical superconcentrated electrolyte, based on the 20M LiTFSI-LiFSI in a water and acetonitrile mixture electrolyte reported in a work of Yang et al.[321] The starting concentration would be then in this case 20000 mol·m^{-3}, but a lower limit for the minimum concentration is set to 14000 mol·m^{-3}, since an excessive decrease of the salt concentration in a superconcentrated electrolyte would lead to extensive decomposition of the solvent due to restriction of the electrochemical stability window.[321] This configuration allows to fully charge the high mass loading cathode with a thickness of 163.2 µm and a porosity of 38% with a thin commercial separator, since K is higher than 1 in the plot region corresponding to this parameter combination (**Figure 6.21.d**).

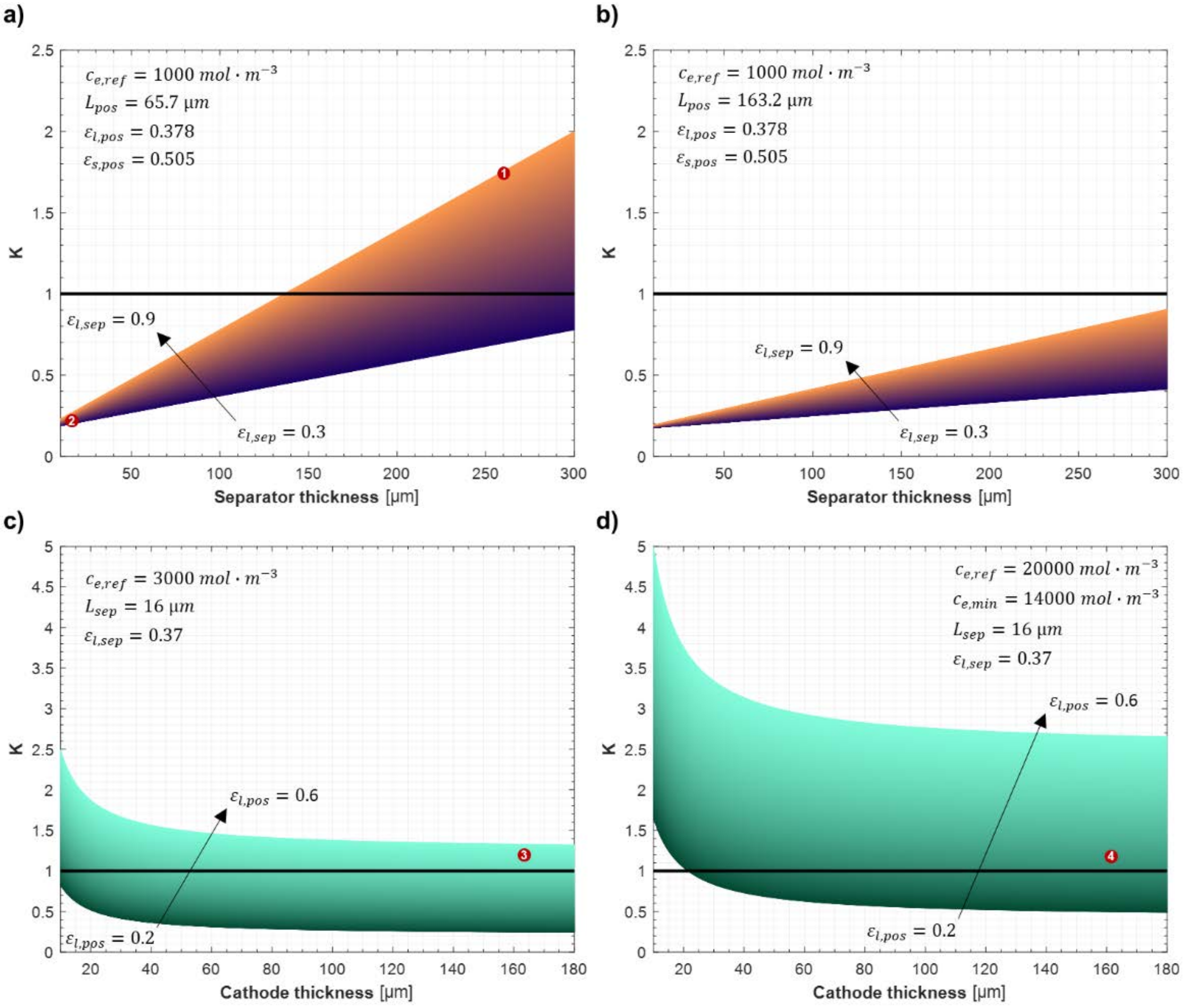

Figure 6.21 – *Study of the trend of the parameter K with a) the separator thickness and porosity, with a lean electrolyte and a low mass loading electrode, b) the separator thickness and porosity, with a lean electrolyte and a high mass loading electrode, c) the cathode thickness and porosity, with a concentrated electrolyte and a thin commercial separator, and d) the cathode thickness and porosity, with a superconcentrated electrolyte and a thin commercial separator. The red dots with the numbers inside indicate the cases that are simulated with the physical model*

Through the use of the physical model for dual-ion batteries, already presented and applied in Section 6.3, we simulated several cases with different design parameters combinations of the PTMA batteries, to validate the empirical trends of K delineated in the previous paragraphs with more rigorous physics-based simulations. The four cases are indicated in **Figure 6.21** with red dots in the region of the graphs corresponding to the chosen values of cathode and separator geometry and electrolyte concentrations. All the values of the model's parameters can be found in **Table A4.1** and **Table A4.2**, and the model domains in the four different simulated cases is illustrated in **Figure A4.15**.

For case 1, where a thin, low mass loading electrode 65.6 µm thick and with 38% porosity is coupled with a 260 µm thick, very porous (90%) glass fiber separator[322] with a 1M electrolyte, the battery can be fully charged up to the maximum available specific capacity, and the salt concentration in the electrolyte (measured by the model at the cathode-current collector interface) decreases down to 440 mol·m^{-3} (**Figure 6.22.a**). Due to the dependence of the electrolyte ionic conductivity with the concentration of the salt, the conductivity will drop from to 10.7 mS·cm^{-1} at the beginning of the charge to 8.9 mS·cm^{-1} towards its end, hence hindering the ionic transport at high SOC. When the separator is switched to a thin commercial separator 16 µm thick and with 37% porosity,[323] keeping the same cathode and electrolyte (case 2), only 21 mAh·g^{-1} are achieved before the salt concentration drops to values near zero, with a consequent severe drop of the electrolyte ionic conductivity (**Figure 6.22.b**).

For case 3 the concentration of the lithium salt in the electrolyte is increased up to 3000 mol·m^{-3}, the cathode thickness and porosity are set respectively to 162.3 µm and 54%, while keeping the same separator. With this configuration, the PTMA battery can be fully charged, but the salt concentration drops to around 120 mol·m^{-3} (**Figure 6.22.c**). The ionic conductivity initially raises from 3.5 mS·cm^{-1} to the maximum of 10.7 mS·cm^{-1} around 70% SOC, since at very high concentrations the conductivity is lower than at the optimum around 1000 mol·m^{-3}, but then it sharply decreases to 4.4 mS·cm^{-1} at the end of the charge.

Finally, in case 4 the use of a 20M superconcentrated electrolyte is simulated, assuming a constant ionic conductivity of 5 mS·cm^{-1}, a transference number of 0.5, a diffusion coefficient of 7.5·10^{-11} m^{2}·s^{-1}, and an activity coefficient of 1, due to the lack of data on the transport properties of such an electrolyte. By using the same electrode thickness of case 3 but decreasing the porosity to 38%, we obtain the same high mass loading cathode presented in the experimental section, which can be charged to its full capacity without exceeding the lower limit of salt concentration (14000 mol·m^{-3}) (**Figure 6.22.d**).

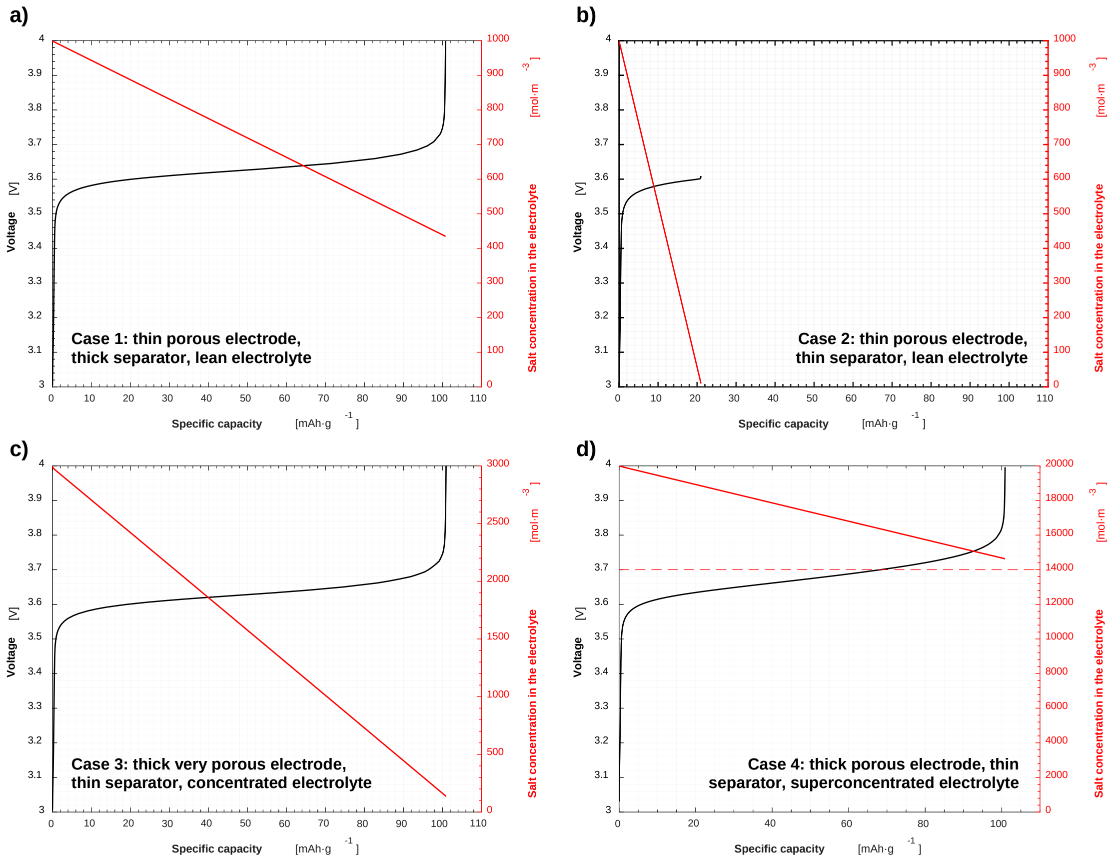

Figure 6.22 *- Voltage and electrolyte salt concentration vs. specific capacity for the four simulated cases during a 0.1C charge. a) Case 1, b) Case 2, c) Case 3, d) Case 4*

6.4.3 Design of a PTMA battery: cost and energy density analysis

The PTMA batteries of these four cases are further analysed from a techno-economic point of view, i.e., modeling their potential cost and energy density for a domestic energy storage battery of 11.5 kWh by using the comprehensive software BatPac 5.0. The sets of parameters used in the model are reported in **Table A4.3**, while the main results of the simulations are reported in **Table A4.4** and shown in **Figure 6.23**. Together with the organic batteries, results obtained by simulating lithium iron phosphate (LFP) and nickel-manganese-cobalt oxide (NMC 622) lithium metal batteries are also reported as comparison, since the PTMA is coupled with a lithium metal anode and putting them side by side with inorganic cathode chemistries together with a graphite anode would be unfair for the latter battery class. We assumed a relatively low cost for the PTMA active material, equal to 10 \$·kg^{-1}, slightly inferior to the one of LFP pre-2022.[75,324]

Case 1 achieves only 26 Wh·kg^{-1} and 25 Wh·l^{-1} at the cell level, for a cost of 287 \$·kWh^{-1}, due to the very thick separator that adds inactive weight and volume to the battery and whose pores requires a high amount of (expensive and heavy) electrolyte to be filled.

In case 2, where the separator is commercial but the specific capacity of the cathode is only one fifth of the regular one, the price rises to 829 \$·kWh^{-1}, with a decrease in both gravimetric and volumetric energy density of the cell when compared to case 1. Despite the thin separator and the much lower quantity of electrolyte in the cell, the insufficient capacity of the positive electrode causes a severe increase of the area required to obtain the nominal energy throughput, hence increasing the costs mostly for active materials, separators and current collectors.

With case 3, where a 3M electrolyte is used together with a thicker and more porous PTMA electrode and a commercial separator, we observe a great improvement of both the gravimetric and volumetric energy density, that reach respectively 79 Wh·kg^{-1} and 106 Wh·l^{-1}, for a cost of 201 \$·kWh^{-1}. The cost per liter and density of the electrolyte increase with respect the previous two cases (4.8 \$·l^{-1} and 1.2 g·cm^{-3} vs. 14.1 \$·l^{-1} and 1.4 g·cm^{-3}), due to the three times higher amount of lithium salt dissolved in the solvent, but the benefits brought by the higher areal capacity of the cathode offset this effect.

Finally, we simulate case 4, with the strong assumption that a lithium metal anode could be use with such a semi-aqueous superconcentrated electrolyte,[325] and using 20 \$·l^{-1} and 1.7 g·cm^{-3} as values for the cost and the density of the electrolyte. Compared to the previous case, the further increase of the electrode mass loading by setting the cathode porosity to 38% brings an improvement in the cell level energy densities (100 Wh·kg^{-1} and 139 Wh·l^{-1}) as well as the cell cost (175 \$·kWh^{-1}). Hence, the strategy of using highly concentrated electrolytes is confirmed to be beneficial to achieve more competitive PTMA batteries, despite the higher cost and weight of the electrolyte.

Nevertheless, comparing the results of these cases with the inorganic cathodes, the commercial chemistries have 3-4 times more gravimetric energy density and 4-6 times more volumetric energy density than the best performing organic battery, for a cost that is 35-40% lower. The volumetric energy density is particularly penalized because of the much lower density of PTMA (1.17 g·cm^{-3}) than NMC 622 (4.65 g·cm^{-3}) and LFP (3.45 g·cm^{-3}).

Looking at the cost breakdown (**Figure 6.23.b**), we can observe how the electrolyte is the major cost contributor in the simulated cases with organic batteries, except case 2 where the very high area required by the battery makes the costs for current collectors increase substantially. The cost for the materials required for the electrode preparation has also a large impact, because of the high weight fraction of carbon and binder in the organic electrodes. Instead, in the inorganic cathode batteries, the active material cost is the most relevant contribution by far, due to the high cost per unit mass of NMC 622 and LFP set in the simulations (respectively, 40 \$·kg^{-1} and 25 \$·kg^{-1}) and for the lower relative impact of the other voices of cost in the total amount. The electrolyte represents a mere 1-2% cost fraction in the inorganic cathode batteries, while it is between 8% and 40% for the redox polymer batteries.

In synthesis, the energy density of inorganic cathodes seems out of reach for PTMA batteries, due to the low density of the active material, the inferior specific capacity and the high impact of the electrolyte mass and cost. Nevertheless, we see that the two classes of energy storage devices are nearer in terms of cost per kWh. With the further optimization of the electrode composition to maximize the areal capacity and with a reduction of electrolyte-related costs, a PTMA battery could have potentially a lower cost than a NMC or LFP lithium metal battery. Moreover, these simulations do not consider niche high power-to-energy ratio applications, which may be more suited for such a material.

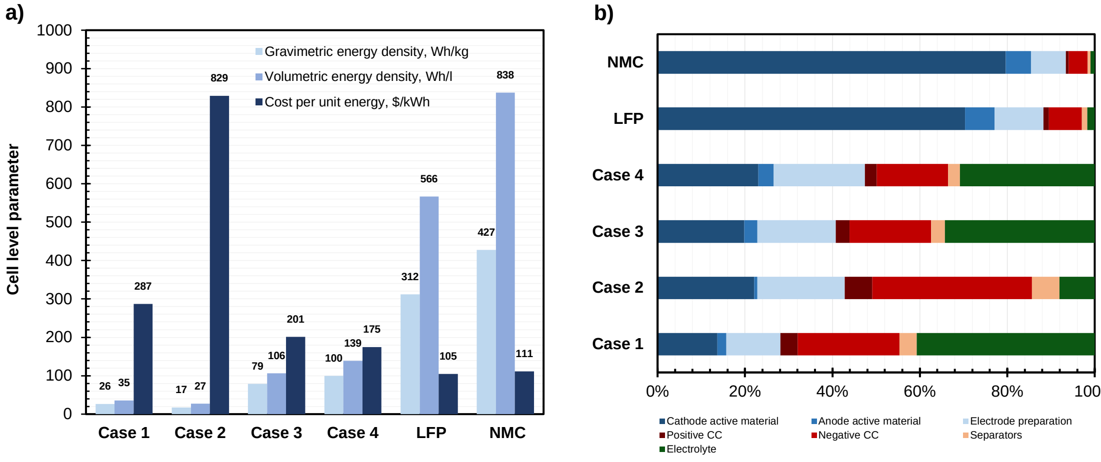

Figure 6.23 *– a) Comparison of the gravimetric energy density, volumetric energy density, and cost per unit energy at the cell level of the simulated battery packs, b) Cost breakdown of the materials required for the cell assembly in the simulated battery packs*

6.4.4 Conclusions

In conclusion, the study focused on the performance and feasibility of high mass loading electrodes using a mixture of PTMA and carbon additives as the cathode material. The results showed that an 85% PTMA – 15% multi-walled carbon nanotubes mixture exhibited excellent performance at both low and high current rates, making it a suitable choice for high mass loading electrodes. The adjustment of the aqueous coating process allowed for viable electrodes with up to 9.65 mg·cm^{-2} of active material loading and a theoretical areal capacity >1 mAh·cm^{-2}. The electrodes kept good rate performance and cycling stability despite the large thickness.

To assess the practical implementation of high mass loading organic batteries, simulations were conducted using different design parameters using a physical model for dual-ion batteries. It was observed that the choice of separator, electrolyte concentration, and electrode geometry significantly influenced the battery's performance. For instance, a porous glass fiber separator enabled the battery to reach its maximum specific capacity even with a 1M electrolyte, but when a thin commercial separator was used, the battery's performance was severely limited, highlighting the benefits of highly concentrated electrolytes for this class of batteries.

The study also examined the techno-economic aspects of PTMA batteries for small battery packs. Modeling their potential cost and performance showed that while the energy density of PTMA batteries may not match that of inorganic cathodes, their cost per kWh could potentially be lower with further optimization of electrode composition, increase of the areal capacity, and reduction in electrolyte-related costs.

In general, in order to provide valuable insights to researchers working on new battery materials, this paper not only emphasizes the importance of considering a broader perspective beyond laboratory-scale batteries but also sheds light on the challenges associated with transferring successful results obtained under typical laboratory conditions to more realistic configurations.

7. Summary and conclusions

In conclusion, this dissertation aimed to propose a way to understand, starting from experimental data retrieved at a laboratory scale, how novel battery materials could be implemented in a real scenario and to compete with the current commercial technology, particularly in the realm of organic batteries, and in general of post-lithium-ion solutions.

The case study on sodium-ion batteries demonstrated the importance of well-performed simulations in identifying suitable materials for real-world applications. By consistently implementing this approach in lab-scale research, efforts can be concentrated on the most promising options among the vast landscape of potential battery materials, ultimately leading to practical solutions for future energy storage needs.

Regarding the analysis on n-type organic materials, small molecules were identified as the best performing, although they normally exhibit low capacity retention. Further research is necessary to stabilize these molecules during battery cycling through molecular engineering and electrolyte formulation. Air-stable, lithium-sufficient materials, while having lower energy density, could become cost-effective alternatives to inorganic chemistries, thanks to their similarity to the current battery technology. To fully evaluate the practicality and cost-effectiveness of organic materials, it is recommended to conduct detailed energy density and cost simulations in full-scale battery packs when presenting experimental results on new materials, considering optimistic assumptions for potential scale-up in commercial setups.

For what concerns p-type organic materials, a modified version of the Doyle-Fuller-Newman model was proposed for simulating the dual-ion battery configuration, which involve both cations and anions in redox reactions. The model successfully accounted for the variation of salt concentration in the electrolyte during charge and discharge. It has significant implications for optimizing the design parameters of dual-ion batteries, such as separator porosity and thickness, cathode porosity and thickness, and electrolyte salt concentration. This model can serve as a starting point for a detailed mechanistic description of dual-ion batteries and can be adapted to other anion-hosting materials.

Finally, we applied the proposed methodology in an experimental work on PTMA, a p-type organic cathode material. Our study demonstrated the excellent performance of PTMA and carbon nanotube mixtures as cathode materials. Adjustments to the aqueous coating process allowed for viable electrodes with high active material loading and theoretical areal capacity (≈10 $mg \cdot cm^{-2}$, >1 $mAh \cdot cm^{-2}$).By studying the results of the physical simulation, we understood how the choice of separator, electrolyte concentration, and electrode geometry can significantly influence the battery's performance. The cost and performance analysis highlighted the benefits of highly concentrated electrolytes and provided insights into the techno-economic aspects of PTMA batteries.

Overall, we emphasize the importance of considering a broader perspective beyond laboratory-scale batteries and address the challenges associated with transferring successful experimental results to more realistic configurations. Thanks to a methodology that can be flexibly applied in the battery material research field in future investigations, we anticipate the development of practical and cost-effective post-lithium-ion battery technologies.

Appendix 1: Supporting information for Section 6.1

The prices of the raw materials in January 2020 and April 2022 for the analysis of **Section 6.1.1** were obtained by comparing various sources (academic papers, databases for price of metals and chemical compounds, bulk chemical vendors), as seen in **Table A1.2**. The analysis considered the change in prices of the organic electrolyte, the separator and the aluminum and copper current collectors, too. As conservative hypothesis, the price of the organic electrolyte for LIBs and SIBs has been considered equal, both in January 2020 and April 2022. As a matter of fact, the substitution of $LiPF_6$ with $NaPF_6$ in the organic electrolyte is assumed to not significantly change the cost of the electrolyte, as evidenced by other works, since the cost of the cation in the salt is just a minimal fraction of the cost of the salt itself.[13,326]Moreover, the rise in price of battery electrolytes between January 2020 and April 2022 can be mostly explained as a result of a generalized shortage of $LiPF_6$ if compared to the high demand, which made the price of the salt rise considerably with only a weak correlation to the lithium precursor prices.[327]

The prices of the materials that are considered in the January 2020 case are the ones on the 01.01.2020, while the prices of the April 2022 case are the 01.04.2022 ones. **Table A1.1** collects the conversion factors used in the conversion between different currencies and the US dollar, as well as the actualization factor to convert 2020 US dollar prices to the same scale of the 2022 US dollar prices to take under account inflation.

Table A1.1 *- Currency exchange rates and actualization factor for US$ in Section 6.1.1*

Currency	Exchange rate with 2020$	Exchange rate with 2022$
US dollar ($)	1.110	1.000
Euro (€)	1.117	1.105
Chinese yuan (¥)	0.144	0.157
Indian rupee (₹)	0.014	0.013

Appendix 1: Supporting information for Section 6.1

Table A1.2 *– Prices of precursors and raw materials for lithium- and sodium-ion batteries in Section 6.1.1*

Material	**Price, Jan 2020 [\$/kg]**	**Price, Apr 2022 [\$/kg]**	**Change [%]**	**Reference(s)**
Lithium carbonate	7.20	78.00	983%	https://tradingeconomics.com/commodity/lithium https://www.metal.com/Chemical-Compound/201102250059
Sodium carbonate	0.25	0.40	60%	https://tradingeconomics.com/commodity/soda-ash
Nickel sulfate hexahydrate	3.85	7.30	90%	https://www.metal.com/Nickel/201908270001 https://tradingeconomics.com/commodity/nickel
Cobalt sulfate heptahydrate	8.20	18.60	127%	https://www.metal.com/Chemical-Compound/201102250381 https://tradingeconomics.com/commodity/cobalt
Manganese sulfate monohydrate	0.85	1.70	100%	https://www.metal.com/Manganese/201805300001 https://tradingeconomics.com/commodity/manganese
Aluminum nitrate nonahydrate	0.45	0.80	78%	https://www.made-in-china.com/products-search/hot-china-products/Aluminum_Nitrate_Price.html https://tradingeconomics.com/commodity/aluminum
Zinc sulfate monohydrate	0.60	1.00	67%	https://tradingeconomics.com/commodity/zinc https://dir.indiamart.com/impcat/zinc-sulphate-monohydrate.html
Copper sulfate pentahydrate	1.96	3.00	53%	https://www.chemanalyst.com/Pricing-data/copper-sulphate-1163 https://tradingeconomics.com/commodity/copper
Iron sulfate heptahydrate	0.10	0.15	50%	https://www.made-in-china.com/price/iron-sulfate-price.html https://tradingeconomics.com/commodity/ironore62
Manganese dioxide	1.50	3.12	108%	https://www.metal.com/Manganese/202105130001 https://tradingeconomics.com/commodity/manganese
Iron phosphate	2.67	4.00	50%	https://tradingeconomics.com/commodity/ironore62 https://www.metal.com/Ternary-precursor-material/202111010002
Glucose	0.70	0.60	-14%	https://www.selinawamucii.com/insights/prices/united-states-of-america/glucose/ https://www.alibaba.com/showroom/glucose-price-per-ton.html
Sodium oxalate	1.00	1.60	60%	https://dir.indiamart.com/impcat/sodium-oxalate.html

Material	**Price, Jan 2020 [\$/m^2]**	**Price, Apr 2022 [\$/m^2]**	**Change [%]**	**Reference(s)**
Copper foil (8 µm)	0.90	1.13	26%	https://tradingeconomics.com/commodity/copper; https://www.metal.com/Copper
Aluminum foil (15 µm)	0.20	0.25	25%	https://tradingeconomics.com/commodity/aluminum; https://www.metal.com/Aluminum
Separator (15 µm)	0.16	0.14	-13%	https://www.metal.com/Ternary-precursor-material

Material	**Price, Jan 2020 [\$/l]**	**Price, Apr 2022 [\$/l]**	**Change [%]**	**Reference(s)**
Organic electrolyte	12.9	24.7	91%	https://www.metal.com/Ternary-precursor-material

The following assumptions were made in the modeling of the synthesis processes:

- The modeled reactions are 1) for multi-transition metal layered oxides, the co-precipitation of the transition metal sources with sodium carbonate in water in a stirred reactor and the calcination of the precipitate mixture with sodium/lithium carbonate, and 2) for LFP and LMO, a solid-state reaction, i.e., the calcination of the milled precursors mixture.[328–330]

- The transition metal sources for the production of layered oxides are the hydrated sulfate salts, except for aluminum, for which the hydrated nitrate salt was employed. The LFP uses lithium carbonate, iron phosphate and glucose (for the carbon coating) as precursors, while LMO has lithium carbonate and electrolytic manganese dioxide.

- A fixed cost of 17 M$/year has been assumed for every production process, which is added to the costs of the raw materials to obtain the final cost of the cathode. With an assumed output of the plant of 6500 kg/day and 320 days of operation per year, this results in an additional 8 $/kg in the final cost of the cathode other than the raw material costs. This figure was estimated after the comparison of different references about the quantification of fixed and operative costs for cathode production plants of sizes similar to the one modeled in this work.[76,330,331]

The price of the graphite (for LIBs) and hard carbon (for SIBs) anodes have been set respectively to 12.50 $/kg (the standard BatPac 5.0 value) and 10$/kg for both January 2020 and April 2022. The price for hard carbon has been estimated considering studies on production of activated carbons from biomass precursors.[332]

The characteristics of the four types of battery packs considered in the simulations are summarized in **Table A1.3**.

Table A1.3 *– Characteristics of the simulated battery packs in Section 6.1.1*

Parameter	**Domestic storage battery**	**Grid storage battery**	**pHEV battery**	**EV battery**
Number of cells per module (total)	36	4	20	20
Number of cells in parallel group in module	1	1	1	4
Number of modules in row	2	42	2	5
Number of rows of modules per pack	1	7	1	4
Number of modules in parallel	1	7	1	1
Number of packs manufactured per year	500,000	500,000	500,000	500,000
Pack energy, kWh	11.5	500	15	100
Target battery pack power at 20% SOC, kW	7	250	110	150
Power-to-energy ratio	0.61	0.5	7.3	1.50

The specific capacity, the voltage range, and the initial coulombic efficiency (ICE) of the cathode materials were retrieved (when possible) from the respective publications indicated as references in **Table A1.4**. Their density was assumed to be 4.4 g·cm^{-3} for O3-phase layered oxides, 4.2 g·cm^{-3} for P2-phase layered oxides, 3.4 g·cm^{-3} for polyanionic compounds, and 1.8 g·cm^{-3} for Prussian blue analogues. The cost of the materials was modelled according to the methodology described in Baumann et al.,[29] where a part of the final material price is related to the cost of production and the rest is a weighted average of the elements' prices, with the weight corresponding to the mass fraction of the element in the compound. For all the cathode materials, the cost of production was assumed to be 9.5 $\$\cdot\mathrm{kg}^{-1}$.

Table A1.4 *- Details on the analysed cathode materials from literature in section 6.1.2*

Material	Class	Code	Specific capacity (w/o pre-sodiation) [mAh·g^{-1}]	Voltage range (w/o pre-sodation) [V vs. Na/Na^{+}]	Initial coulombic efficiency [%]	Density [g·cm^{-3}]	Material cost $[\$\cdot\mathrm{kg}^{-1}]$	Ref.
$NaFe(PO_4)$	Polyanionic compound	**1**	138	1.51 – 4.21	87.5	3.4	10	265
$Na[Ni_{0.3}Fe_{0.4}Mn_{0.3}]O_2$	Layered metal oxide (O3)	**2**	132	2,52 – 3,87	84%	4.4	13	250
$Na_3V_2(PO_4)_2F_3$	Polyanionic compound	**3**	109	2.21 – 4.36	98%[a]	3.4	18	266
$Na_3V_2(PO_4)_2FO_2$	Polyanionic compound	**4**	178 (119)	1.13 - 4.32 (2.14 – 4.32)	98%[a]	3.4	18	266
$Na_{0.6}[Ni_{0.22}Al_{0.11}Mn_{0.66}]O_2$	Layered metal oxide (P2)	**5**	217 (130)	1.56 - 4.50 (2.51 – 4.50)	95%[a]	4.2	13	275
$Na_{0.6}[Ni_{0.22}Fe_{0.11}Mn_{0.66}]O_2$	Layered metal oxide (P2)	**6**	206 (124)	1.51 – 4.38 (2.31 – 4.38)	95%[a]	4.2	13	276
$Na_3Fe_2(PO_4)_3$	Polyanionic compound	**7**	110	1.82 – 4.20	95%	3.4	10	277
$Na_{0.95}[Ni_{0.32}Mn_{0.32}Mg_{0.16}Ti_{0.21}]O_2$	Layered metal oxide (O3)	**8**	121	2.01 – 4.08	94%	4.4	13.5	69
$Na_2Mn[Fe(CN)_6]$	Prussian blue analogue	**9**	149	2.00 – 3.95	92.5%	1.8	10.5	278

[a] Assumed

The cost and energy density simulations are performed with a modified version of the open-access software BatPac 5.0. The simulated battery pack is a grid-scale energy storage battery with 500 kWh of rated energy and 250 kW of rated power[333], composed of a series of 4 cells in every module. The modules are 294, arranged in 7 parallels of 42 modules in series. In total, 1,176 cells are considered. The yearly production of this battery pack is set to 100,000 packs per year, obtaining a capacity of the production site of 50 $GWh \cdot y^{-1}$.

The cathode materials considered in the analyses are listed in **Table A1.4**, together with their properties that are needed for the simulations and a numerical code that refers to each of them. The density is assumed taking reasonable values according to the specific material and to its class (layered oxide, polyanionic compound, or Prussian blue analogue)[56,334] All the voltage profiles of the cathode materials and the respective battery voltages before and after the increase of the lower cut-off voltage to the USABC target are reported in **Figure A1.6-Figure A1.20**.

All the analyzed cathodes from literature are coupled with the same commercial hard carbon anode, characterized by a specific capacity of 298 $mAh \cdot g^{-1}$, a density of 1.5 $g \cdot cm^{-3}$ and a cost of 7 $\$ \cdot kg^{-1}$ [251]. The composition of the cathode electrodes was set to 94:3:3 weight ratio between active material, conductive carbon, and binder, while the one for the anode was set to 95:2:3. The cost of the aluminum foil, used for both anode and cathode, was set to 0.21 $\$/m^2$, while the one of the separators to 0.12 $\$/m^2$.

The battery voltage profiles are obtained after considering 82.5% as the initial coulombic efficiency of the anode, the initial coulombic efficiency of the cathode according to Table **S1**, and a N/P ratio after formation equal to 1.1 (see Section 3.1 of these Supporting Information for details about how the initial coulombic efficiencies and the N/P ratio were implemented in the simulations).

The average voltage (ratio between battery energy and battery capacity) is calculated for every voltage curve and given as input to the software as voltage value to design the battery pack. BatPac uses by default the 50% SOC as design voltage, but this may be inaccurate for profiles with plateaus at different voltages (e.g., $Na_3V_2(PO_4)_2FO_2$ with pre-sodiation, **Figure 6.5.a** in the main text). All the other parameters required by BatPac which are not mentioned in the main text or in the Supporting Information have been left to the default value of the version 5.0.

The initial coulombic efficiencies of anode and cathode were considered in these cost and energy density simulations by rescaling the potential of the anode and/or cathode and reducing the specific capacity of the cathode accordingly.

We define the N/P ratio $\frac{N}{P}$, the initial coulombic efficiency of the anode ICE_a and the initial coulombic efficiency of the cathode ICE_c as

$$\left(\frac{N}{P}\right) = \frac{C_a}{C_c} \tag{A1}$$

$$ICE_a = \frac{C_a}{C'_a} \tag{A2}$$

$$ICE_c = \frac{C'_c}{C''_c} \tag{A3}$$

where C_a and C'_a are the capacities of the anode respectively after and before formation, and C'_c and C''_c are the capacities of the cathode respectively after and before formation without considering the decrease of capacity due to the irreversible capacity of the anode.

Hence, we can define the difference of capacity before and after formation of anode ΔC_a and cathode ΔC_c as

$$\Delta C_a = C'_a - C_a = C_a\left(\frac{1}{ICE_a} - 1\right) \tag{A4}$$

$$\Delta C_c = C''_c - C'_c = C'_c\left(\frac{1}{ICE_c} - 1\right) \tag{A5}$$

The anode potential is shifted and rescaled according to the value of the N/P ratio, calculating the new maximum state of charge of the anode $SOC'_{max,a}$ as

$$SOC'_{max,a} = \frac{1}{\left(\frac{N}{P}\right)} \tag{A6}$$

and using the potential at this state of charge as potential at 100% anode state of charge in the rescaled anode potential curve. See **Figure A1.1** for a graphical explanation of the concept.

To find the new minimum state of charge of the cathode $SOC'_{min,c}$ due to the compensation of the irreversible coulombic efficiency of the anode, we write C'_c as the sum of several capacity contributions as

$$C_c' = C_c + \Delta C_a - \Delta C_c \tag{A7}$$

where C_c is the capacity of the cathode after formation and considering the decrease of capacity due to the irreversible capacity of the anode. The irreversible capacity loss of the cathode, i.e., sodium ions that are not able to insert again in the cathode structure after the first cycle due to structural changes and thermodynamic limitations, is used to compensate the irreversible capacity loss of the anode due to SEI formation[335]. The difference between the two irreversible losses is added to C_c, which can be considered as the design cathode capacity, to give the actual amount of cathode capacity C_c' that must be provided by the battery to compensate the anode irreversibility.

Rearranging equation S7 we get

$$C_c' = C_c + C_a\left(\frac{1}{ICE_a} - 1\right) - C_c'\left(\frac{1}{ICE_c} - 1\right) \tag{A8}$$

Dividing by C_c, we can write

$$\frac{C_c'}{C_c} = 1 + \frac{C_a}{C_c}\left(\frac{1}{ICE_a} - 1\right) - \frac{C_c'}{C_c}\left(\frac{1}{ICE_c} - 1\right) \tag{A9}$$

Recognizing that $\frac{C_a}{C_c}$ is the definition of the N/P ratio and rearranging the equation, we obtain

$$\frac{C_c}{C_c'} = \frac{\frac{1}{ICE_c}}{1 + \frac{N}{P}\left(\frac{1}{ICE_a} - 1\right)} \tag{A10}$$

This value is multiplied by the specific capacity of the cathode to take into account that the battery contains additional inactive cathode mass that was used only to compensate the irreversibility of the anode, hence reducing the actual specific capacity of the cathode.

Finally, the new minimum state of charge of the cathode $SOC_{min,c}'$ can be found as

$$SOC_{min,c}' = 1 - \frac{C_c}{C_c'} \tag{A11}$$

and using the potential at this state of charge as potential at 0% cathode state of charge in the rescaled cathode potential curve. See **Figure A1.2** for a graphical explanation of the concept.

Please note that equation (A7) is only valid if ΔC_c is lower of $\Delta C_a \cdot \frac{N}{P}$, i.e., if the irreversibility of the anode cannot be compensated entirely by the irreversibility of the cathode, a condition that is always respected during the simulations.

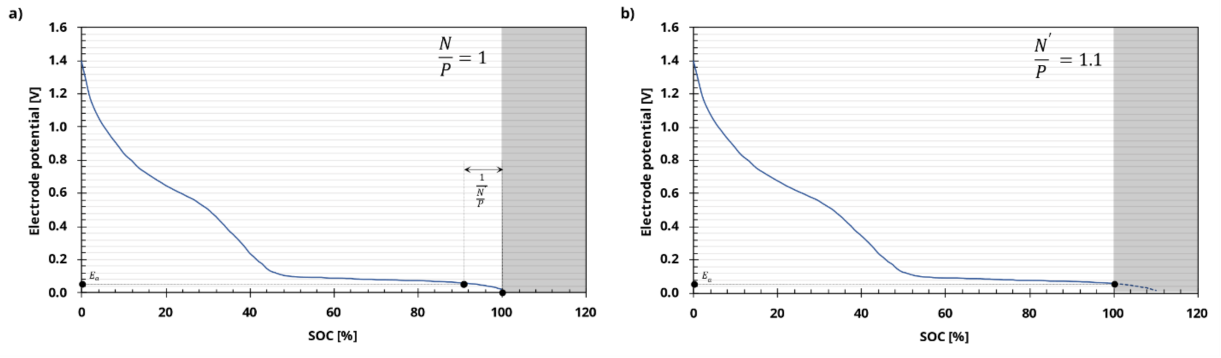

Figure A1.1 – Explanation of the modification made on the anode voltage profile for the implementation of the N/P ratio: a) case with N/P ratio equal to 1, b) case with N/P ratio equal to 1.1. The grey part of the chart and the dashed part of the line is not considered in the final anode voltage.

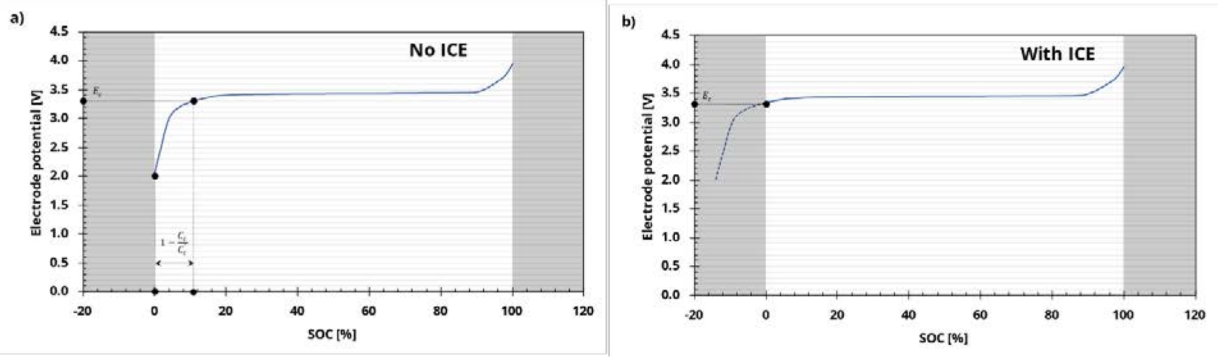

Figure A1.2 – Explanation of the modification made on the cathode voltage profile for the implementation of the initial coulombic efficiency (ICE): a) case without ICE implementation, b) case with ICE implementation. The grey part of the chart and the dashed part of the line is not considered in the final cathode voltage.

All the sodium-ion batteries analysed in this work are compared with lithium-ion batteries with $Li[Ni_{0.8}Mn_{0.1}Co_{0.1}]O_2$ (NMC) and $LiFe(PO_4)$ (LFP) as cathodes and graphite as anode (red in the charts of **Figure A1.3**, **Figure A1.4**, and **Figure A1.5**). The cost used for the lithium-ion cathodes in the simulations is 28.7 $/kg for NMC and 8.7 $/kg for LFP, in line with the current prices for these materials[282]. All the other data required for the lithium-ion battery simulations were taken from the default values for these materials in BatPac 5.0. For the sodium-ion batteries, the best and the worst values of energy densities and cost are reported, considering all the simulated lower voltage cut-offs and types of pre-sodiation.

Appendix 1: Supporting information for Section 6.1

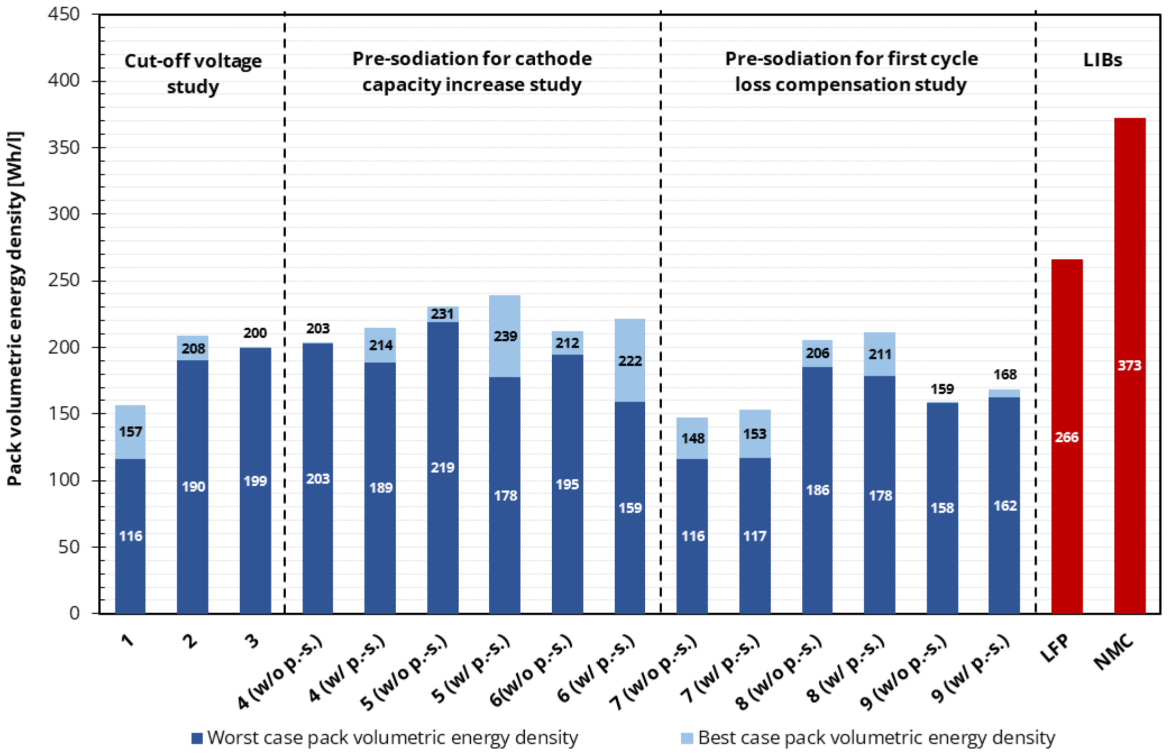

Figure A1.3 *– Comparison of the volumetric energy density of the sodium-ion battery packs simulated with the cathode materials taken from literature and a hard carbon anode. The best and the worst values of volumetric energy density are reported, considering all the simulated lower voltage cut-offs and types of pre-sodiation. In red, two examples of lithium-ion battery packs are shown as comparison.*

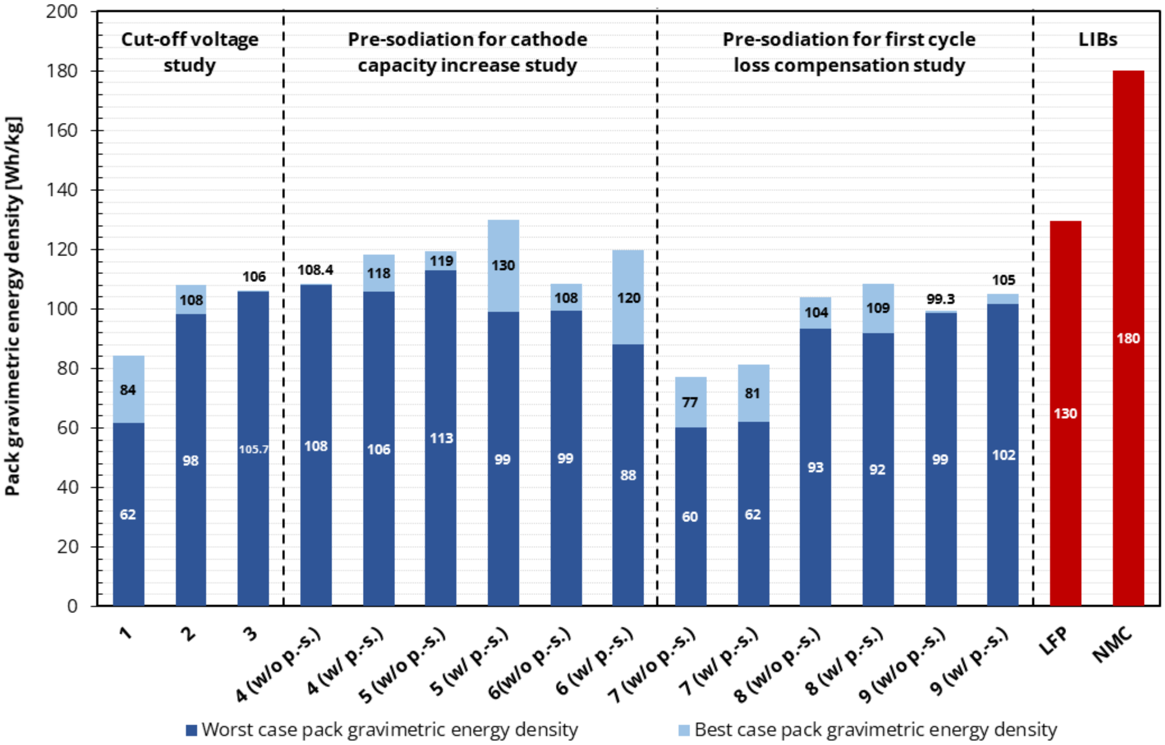

***Figure A1.4** – Comparison of the gravimetric energy density of the sodium-ion battery packs simulated with the cathode materials taken from literature and a hard carbon anode. The best and the worst values of gravimetric energy density are reported, considering all the simulated lower voltage cut-offs and types of pre-sodiation. In red, two examples of lithium-ion battery packs are shown as comparison.*

Appendix 1: Supporting information for Section 6.1

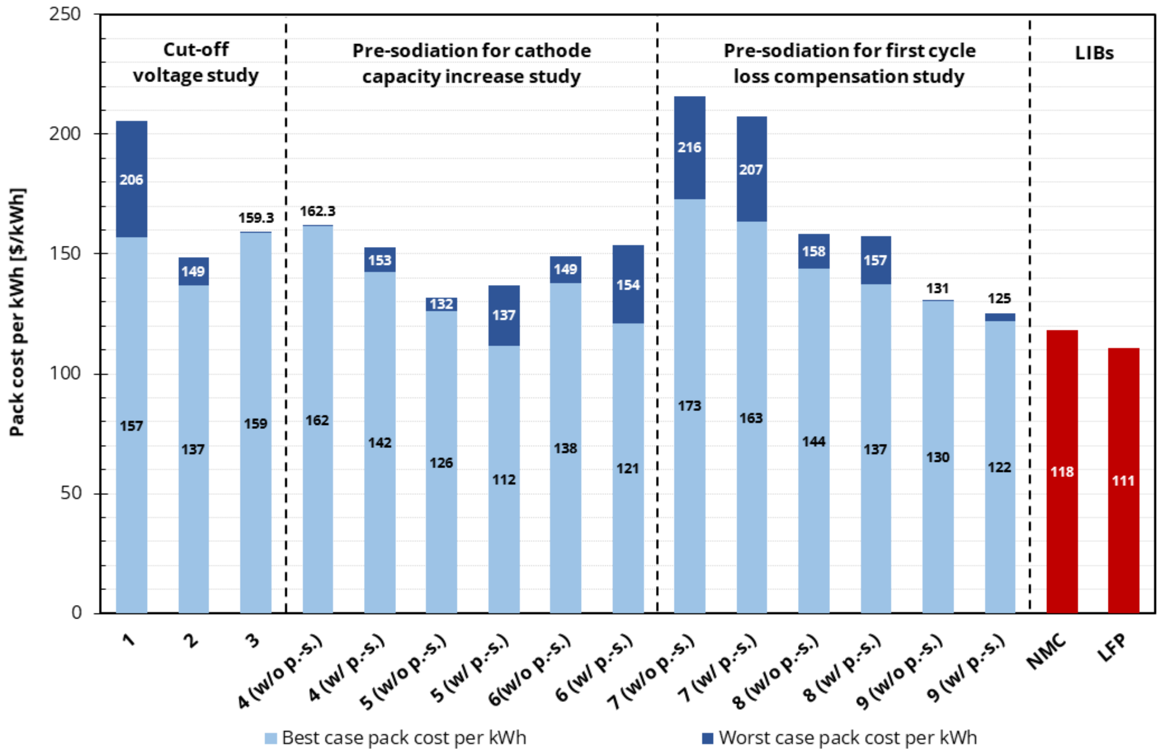

Figure A1.5 *– Comparison of the gravimetric energy density of the sodium-ion battery packs simulated with the cathode materials taken from literature and a hard carbon anode. The best and the worst values of gravimetric energy density are reported, considering all the simulated lower voltage cut-offs and types of pre-sodiation. In red, two examples of lithium-ion battery packs are shown as comparison.*

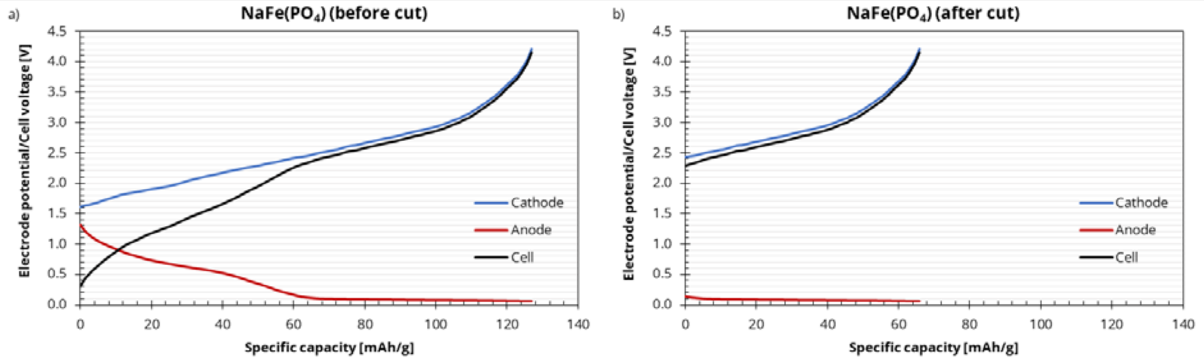

Figure A1.6 *– Electrode potentials and voltage profile of a NaFe(PO$_4$)/hard carbon sodium-ion battery a) at the initial lower cut-off voltage and b) with the increase of the lower cut-off voltage to the 55% of the maximum battery voltage. The specific capacity refers to the cathode mass.*

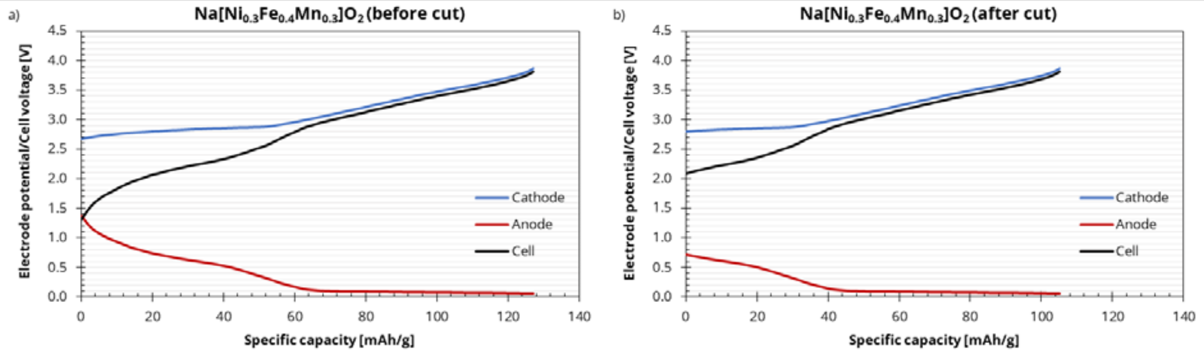

Figure A1.7 *– Electrode potentials and voltage profile of a Na[Ni$_{0.3}$Fe$_{0.4}$Mn$_{0.3}$]O$_2$/hard carbon sodium-ion battery a) at the initial lower cut-off voltage and b) with the increase of the lower cut-off voltage to the 55% of the maximum battery voltage. The specific capacity refers to the cathode mass.*

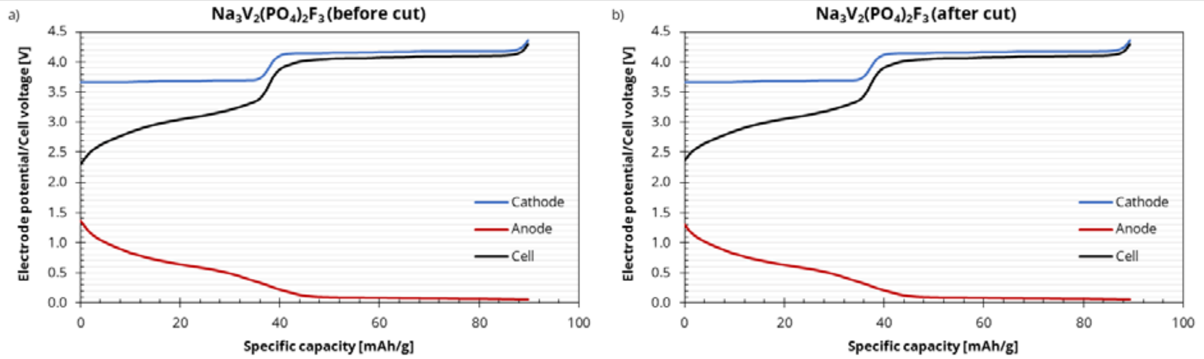

Figure A1.8 *– Electrode potentials and voltage profile of a Na$_3$V$_2$(PO$_4$)F$_3$/hard carbon sodium-ion battery a) at the initial lower cut-off voltage and b) with the increase of the lower cut-off voltage to the 55% of the maximum battery voltage. The specific capacity refers to the cathode mass.*

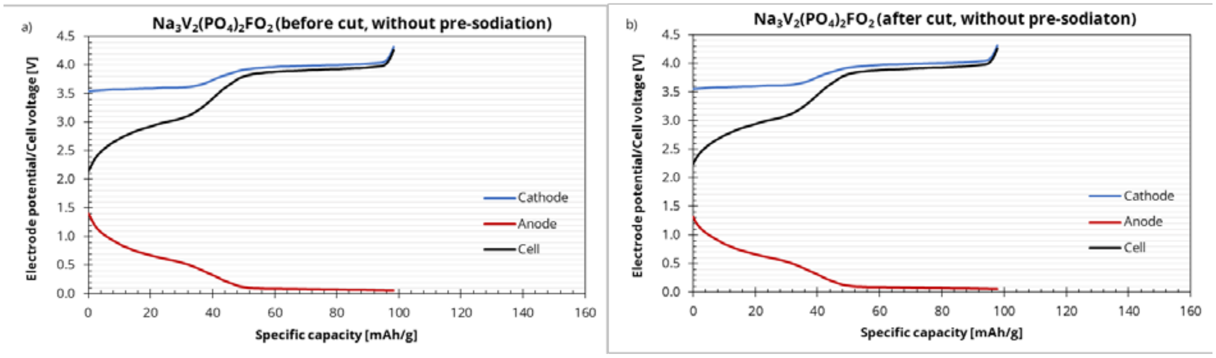

__Figure A1.9__ – Electrode potentials and voltage profile of a $Na_3V_2(PO_4)FO_2$/hard carbon sodium-ion battery (without pre-sodiation for the addition of sodium to the non-stoichiometric cathode) a) at the initial lower cut-off voltage and b) with the increase of the lower cut-off voltage to the 55% of the maximum battery voltage. The specific capacity refers to the cathode mass.

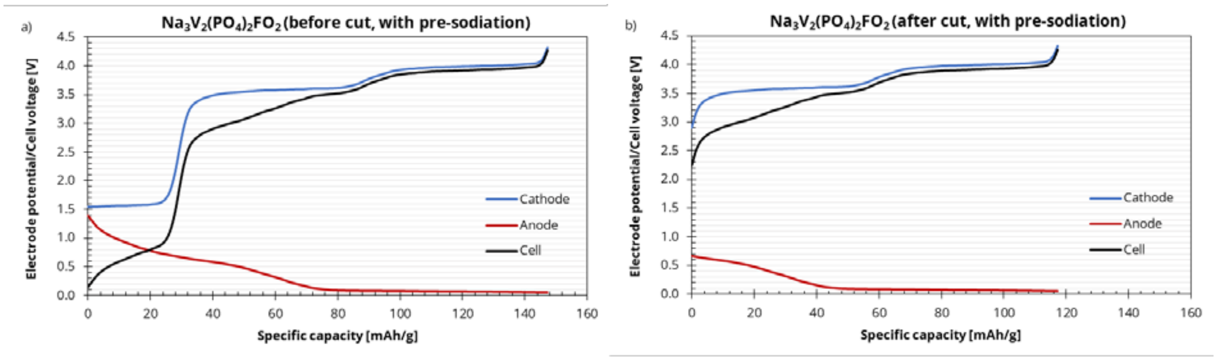

__Figure A1.10__ – Electrode potentials and voltage profile of a $Na_3V_2(PO_4)FO_2$/hard carbon sodium-ion battery (with pre-sodiation for the addition of sodium to the non-stoichiometric cathode) a) at the initial lower cut-off voltage and b) with the increase of the lower cut-off voltage to the 55% of the maximum battery voltage. The specific capacity refers to the cathode mass.

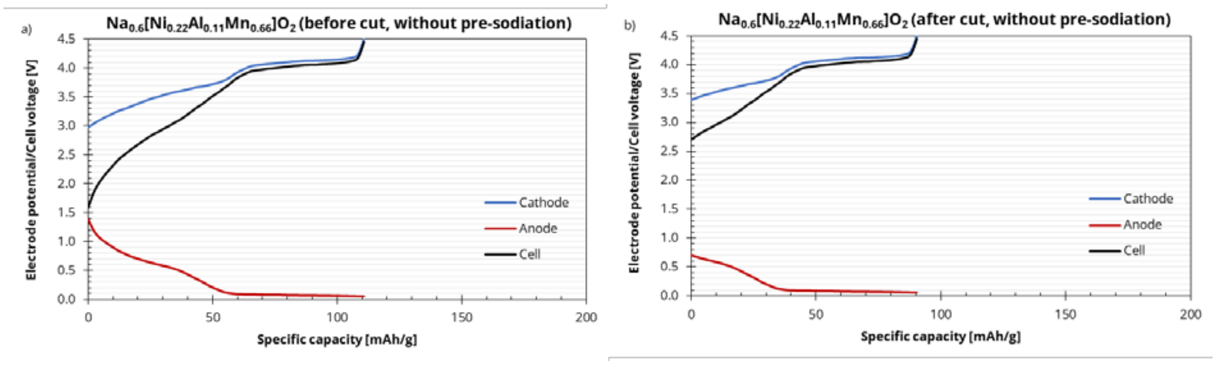

__Figure A1.11__ – Electrode potentials and voltage profile of a $Na_{0.6}[Ni_{0.22}Al_{0.11}Mn_{0.66}]O_2$/hard carbon sodium-ion battery (without pre-sodiation for the addition of sodium to the non-stoichiometric cathode) a) at the initial lower cut-off voltage and b) with the increase of the lower cut-off voltage to the 55% of the maximum battery voltage. This specific capacity refers to the cathode mass.

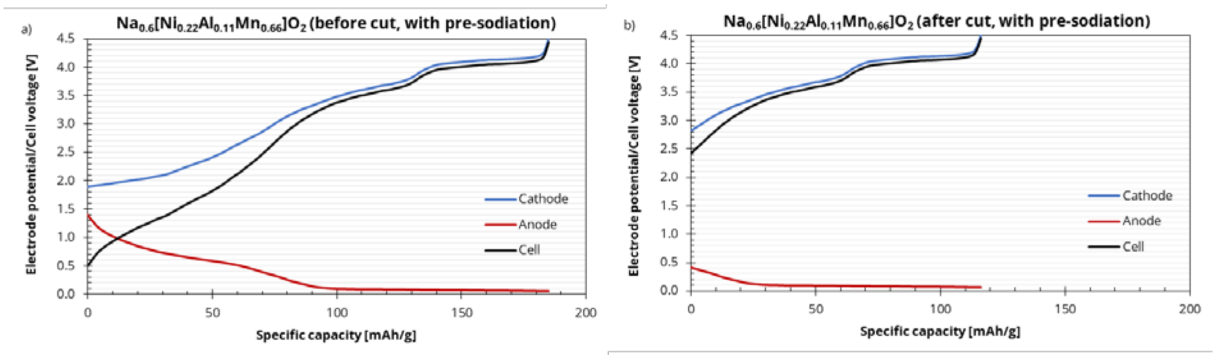

Figure A1.12 – *Electrode potentials and voltage profile of a $Na_{0.6}[Ni_{0.22}Al_{0.11}Mn_{0.66}]O_2$/hard carbon sodium-ion battery (with pre-sodiation for the addition of sodium to the non-stoichiometric cathode) a) at the initial lower cut-off voltage and b) with the increase of the lower cut-off voltage to the 55% of the maximum battery voltage. The specific capacity refers to the cathode mass.*

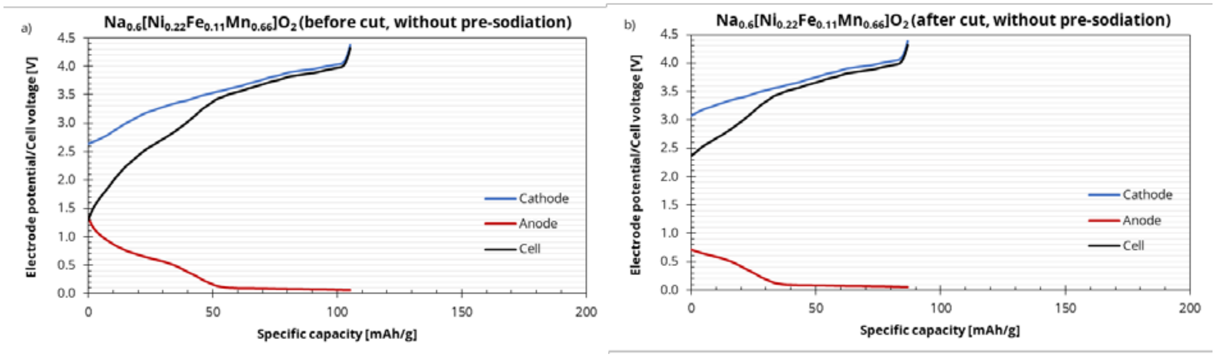

Figure A1.13 – *Electrode potentials and voltage profile of a $Na_{0.6}[Ni_{0.22}Fe_{0.11}Mn_{0.66}]O_2$/hard carbon sodium-ion battery (without pre-sodiation for the addition of sodium to the non-stoichiometric cathode) a) at the initial lower cut-off voltage and b) with the increase of the lower cut-off voltage to the 55% of the maximum battery voltage. The specific capacity refers to the cathode mass.*

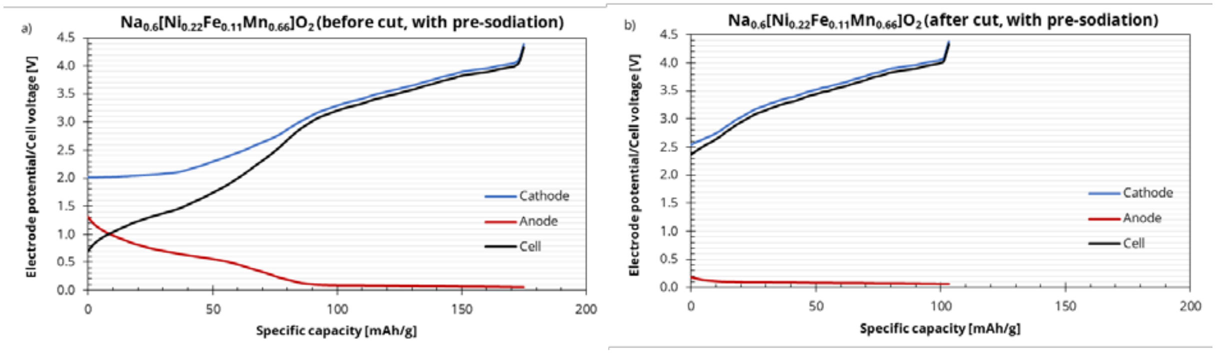

Figure A1.14 – *Electrode potentials and voltage profile of a $Na_{0.6}[Ni_{0.22}Fe_{0.11}Mn_{0.66}]O_2$/hard carbon sodium-ion battery (with pre-sodiation for the addition of sodium to the non-stoichiometric cathode) a) at the initial lower cut-off voltage and b) with the increase of the lower cut-off voltage to the 55% of the maximum battery voltage. The specific capacity refers to the cathode mass.*

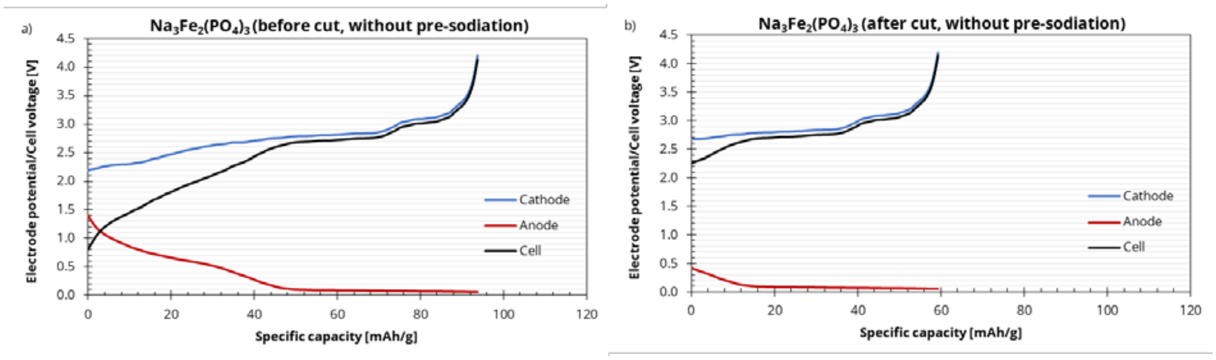

Figure A1.15 *– Electrode potentials and voltage profile of a* $Na_3Fe_2(PO_4)_3$*/hard carbon sodium-ion battery (without pre-sodiation for the compensation of the first cycle sodium loss) a) at the initial lower cut-off voltage and b) with the increase of the lower cut-off voltage to the 55% of the maximum battery voltage. The specific capacity refers to the cathode mass.*

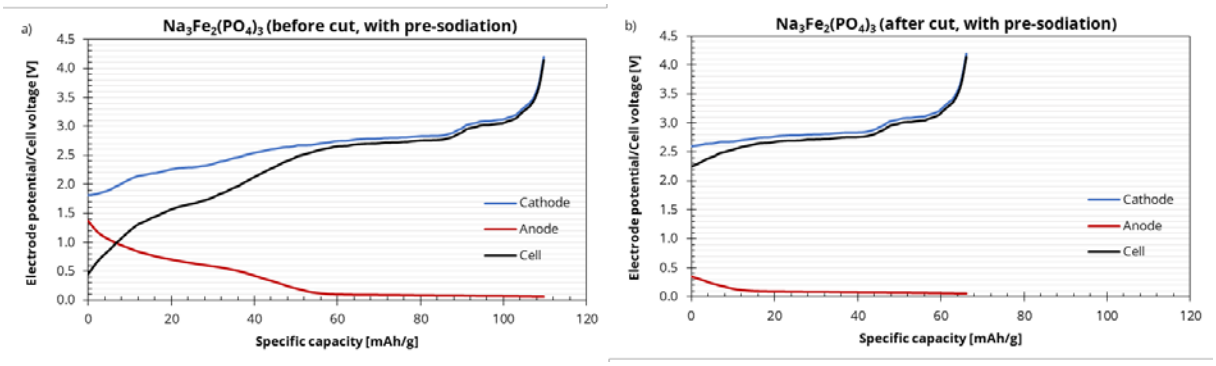

Figure A1.16 *– Electrode potentials and voltage profile of a* $Na_3Fe_2(PO_4)_3$*/hard carbon sodium-ion battery (with pre-sodiation for the compensation of the first cycle sodium loss) a) at the initial lower cut-off voltage and b) with the increase of the lower cut-off voltage to the 55% of the maximum battery voltage. The specific capacity refers to the cathode mass.*

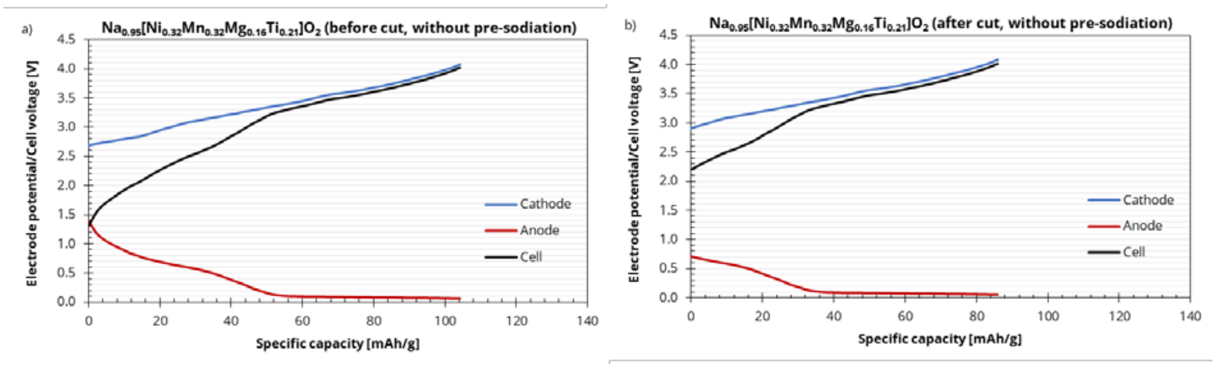

Figure A1.17 *– Electrode potentials and voltage profile of a* $Na_{0.95}[Ni_{0.32}Mn_{0.32}Mg_{0.16}Ti_{0.21}]O_2$*/hard carbon sodium-ion battery (without pre-sodiation for the compensation of the first cycle sodium loss) a) at the initial lower cut-off voltage and b) with the increase of the lower cut-off voltage to the 55% of the maximum battery voltage. The specific capacity refers to the cathode mass.*

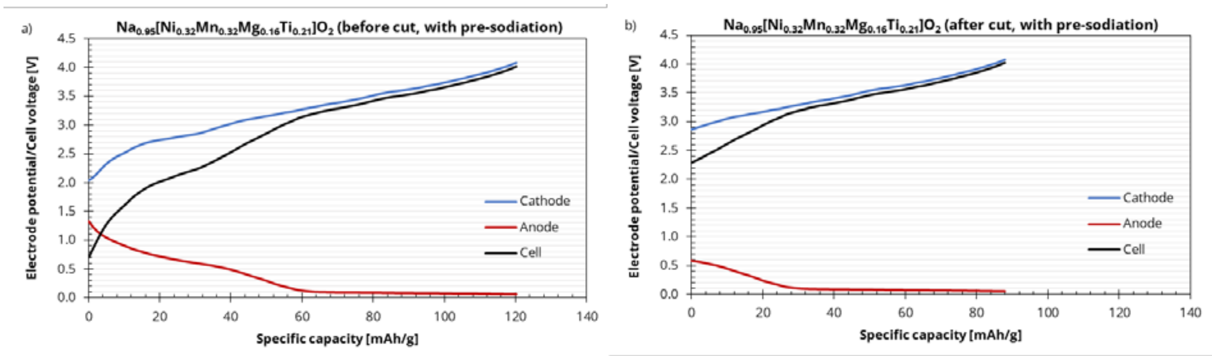

Figure A1.18 – *Electrode potentials and voltage profile of a $Na_{0.95}[Ni_{0.32}Mn_{0.32}Mg_{0.16}Ti_{0.21}]O_2$/hard carbon sodium-ion battery (with pre-sodiation for the compensation of the first cycle sodium loss) a) at the initial lower cut-off voltage and b) with the increase of the lower cut-off voltage to the 55% of the maximum battery voltage. the specific capacity refers to the cathode mass.*

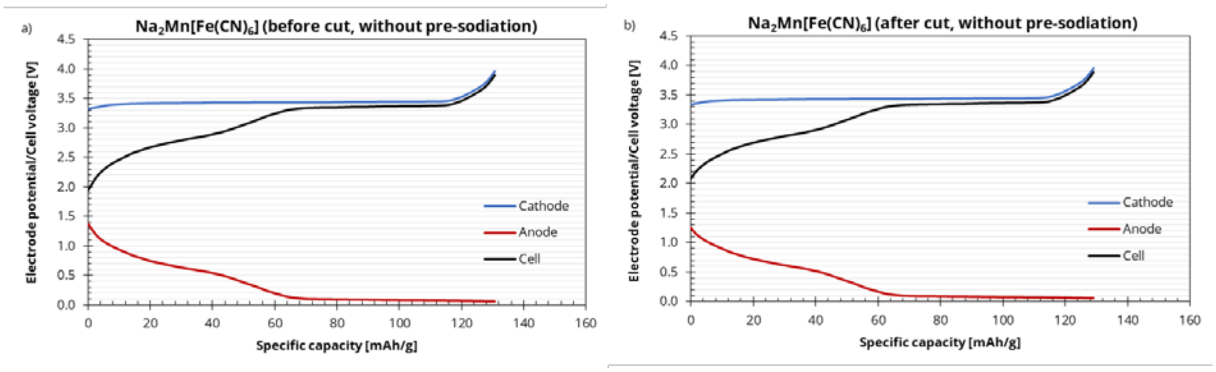

Figure A1.19 – *Electrode potentials and voltage profile of a $Na_2Mn[Fe(CN)_6]O_2$/hard carbon sodium-ion battery (without pre-sodiation for the compensation of the first cycle sodium loss) a) at the initial lower cut-off voltage and b) with the increase of the lower cut-off voltage to the 55% of the maximum battery voltage. The specific capacity refers to the cathode mass.*

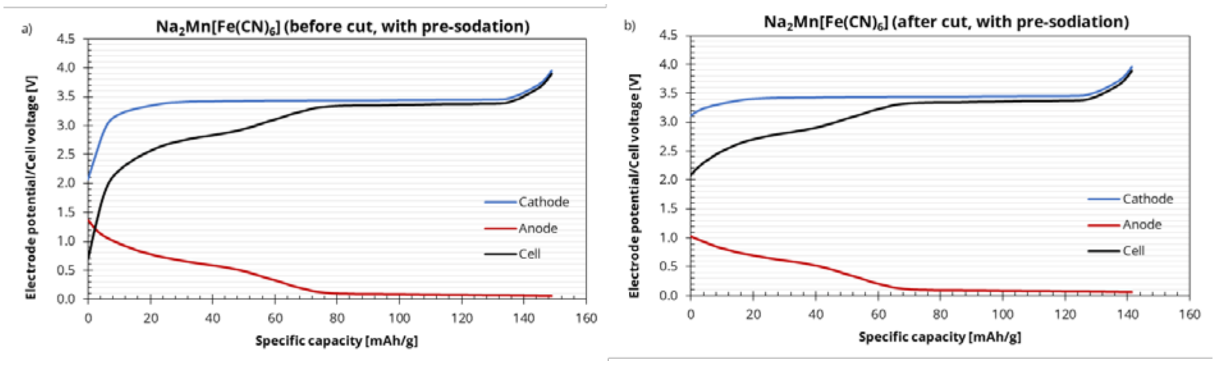

Figure A1.20 – *Electrode potentials and voltage profile of a $Na_2Mn[Fe(CN)_6]O_2$/hard carbon sodium-ion battery (with pre-sodiation for the compensation of the first cycle sodium loss) a) at the initial lower cut-off voltage and b) with the increase of the lower cut-off voltage to the 55% of the maximum battery voltage. The specific capacity refers to the cathode mass.*

Appendix 2: Supporting information for Section 6.2

The simulated battery pack is intended for use in grid-scale energy storage and has a power rating of 250 kW and an energy rating of 500 kWh. It comprises four cells in each module, with a total of 294 modules arranged in seven parallels of 42 modules in series. In total, the battery pack includes 1,176 cells. The production volume is set at 100,000 packs per year, which translates to a production capacity of 50 GWh per year.[333]

The material densities were obtained from relevant publications or estimated using reasonable values. The positive and negative electrode compositions (except for the lithium metal anode) are 96:2:2 (active material:conductive carbon:binder weight ratio) for the high active material content case and 65:30:5 for the low active material content case. For the inorganic battery simulations, the electrode compositions are always in the high active material content case.

In an optimistic scenario, it is assumed that the common liquid electrolyte used for lithium-ion batteries (LP30, 1M $LiPF_6$ in EC:DMC 1:1 vol/vol) can be used with the organic electrode materials and the lithium metal anode.

The lithium metal anode cost is a function of the thickness of the anode itself. Since the processing of thin lithium metal anodes becomes increasingly expensive as the thickness is reduced, this relationship is modelled through an empirical relationship obtained from a study on the cost modelling of future high-energy batteries. The authors of the work assumed a cost of the extrusion process of 11.1 $\$\cdot kg^{-1}$, and a calendering step cost that reduces the thickness to a maximum of 5 µm of 16.9 $\$\cdot kg^{-1}$. The range of thicknesses considered in the article is between 20 µm and 50 µm, but some of the resulting lithium metal anode thicknesses in the simulations are lower than 20 µm. Hence, we extended the aforementioned range, assuming every calendering step of 5 µm below 20 µm would cost 33.8 $\$\cdot kg^{-1}$. We assumed an increased cost of processing in this thickness range because the production of lithium metal foil below 20 µm does not have an established manufacturing technique due to the difficulties of fabricating and handling such thin lithium foils.[279]

Hence, the final formula for the cost of the lithium anode is:

$$Lithium\ anode\ cost = Lithium\ metal\ cost + 11.1\ \$ \cdot kg^{-1} + 16.9\ \$ \cdot kg^{-1} \cdot n + 33.8\ \$ \cdot kg^{-1} \cdot m$$

The parameter n is equal to 1 when the lithium foil thickness is higher than 50 µm, and it increases one unit each time the lithium foil thickness becomes 5 µm less thick than 50 µm, up to a maximum of 7. The parameter m is equal to 0 when the lithium foil thickness is higher than 20 µm, and it increases one unit each time the lithium foil thickness becomes 5 µm less thick than 20 µm, up to a maximum of 4.

Table A2.1 *- Summary of the different simulation parameters for the low and high cost lithium scenario*

	Low active material loading case	**High active material loading case**
Low cost lithium scenario	**Lithium-deficient materials**: 10 $·kg^{-1}, 65% AM content **Lithium-sufficient materials**: 10 $·kg^{-1}, 65% AM content **Organic anodes**: 10 $·kg^{-1}, 65% AM content **NMC 622 cost**: 22 $·kg^{-1} **LFP cost**: 12.5 $·kg^{-1} **Lithium metal cost**: 50 $·kg^{-1}	**Lithium-deficient materials**: 10 $·kg^{-1}, 96% AM content **Lithium-sufficient materials**: 10 $·kg^{-1}, 96% AM content **Organic anodes**: 10 $·kg^{-1}, 96% AM content **NMC 622 cost**: 22 $·kg^{-1} **LFP cost**: 12.5 $·kg^{-1} **Lithium metal cost**: 50 $·kg^{-1}
High cost lithium scenario	**Lithium-deficient materials**: 10 $·kg^{-1}, 65% AM content **Lithium-sufficient materials**: 20 $·kg^{-1}, 65% AM content **Organic anodes**: 20 $·kg^{-1}, 65% AM content **NMC 622 cost**: 40 $·kg^{-1} **LFP cost**: 25 $·kg^{-1} **Lithium metal cost**: 400 $·kg^{-1}	**Lithium-deficient materials**: 10 $·kg^{-1}, 96% AM content **Lithium-sufficient materials**: 20 $·kg^{-1}, 96% AM content **Organic anodes**: 20 $·kg^{-1}, 96% AM content **NMC 622 cost**: 40 $·kg^{-1} **LFP cost**: 25 $·kg^{-1} **Lithium metal cost**: 400 $·kg^{-1}

Appendix 3: Supporting information for Section 6.3

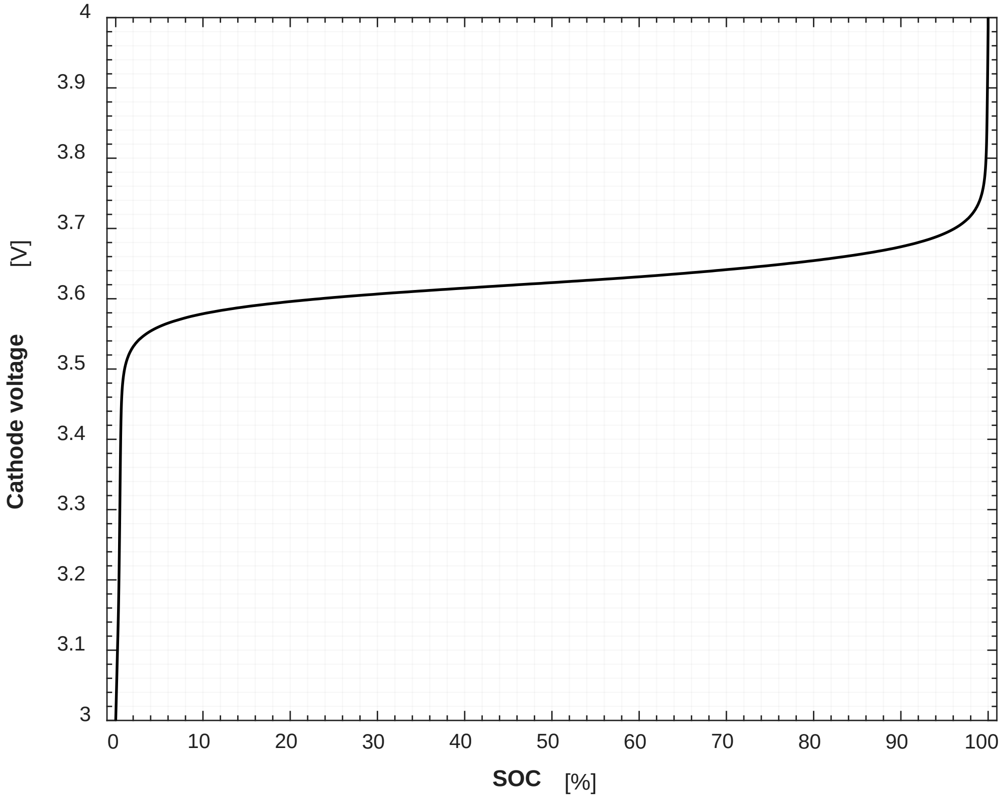

Figure A3.1 *– Open circuit potential vs. state of charge characteristic of the PTMA-based cathode used as an input for the model. The curve is derived from a 0.1C discharge curve at 20°C obtained with the same experimental setup described in the main text*

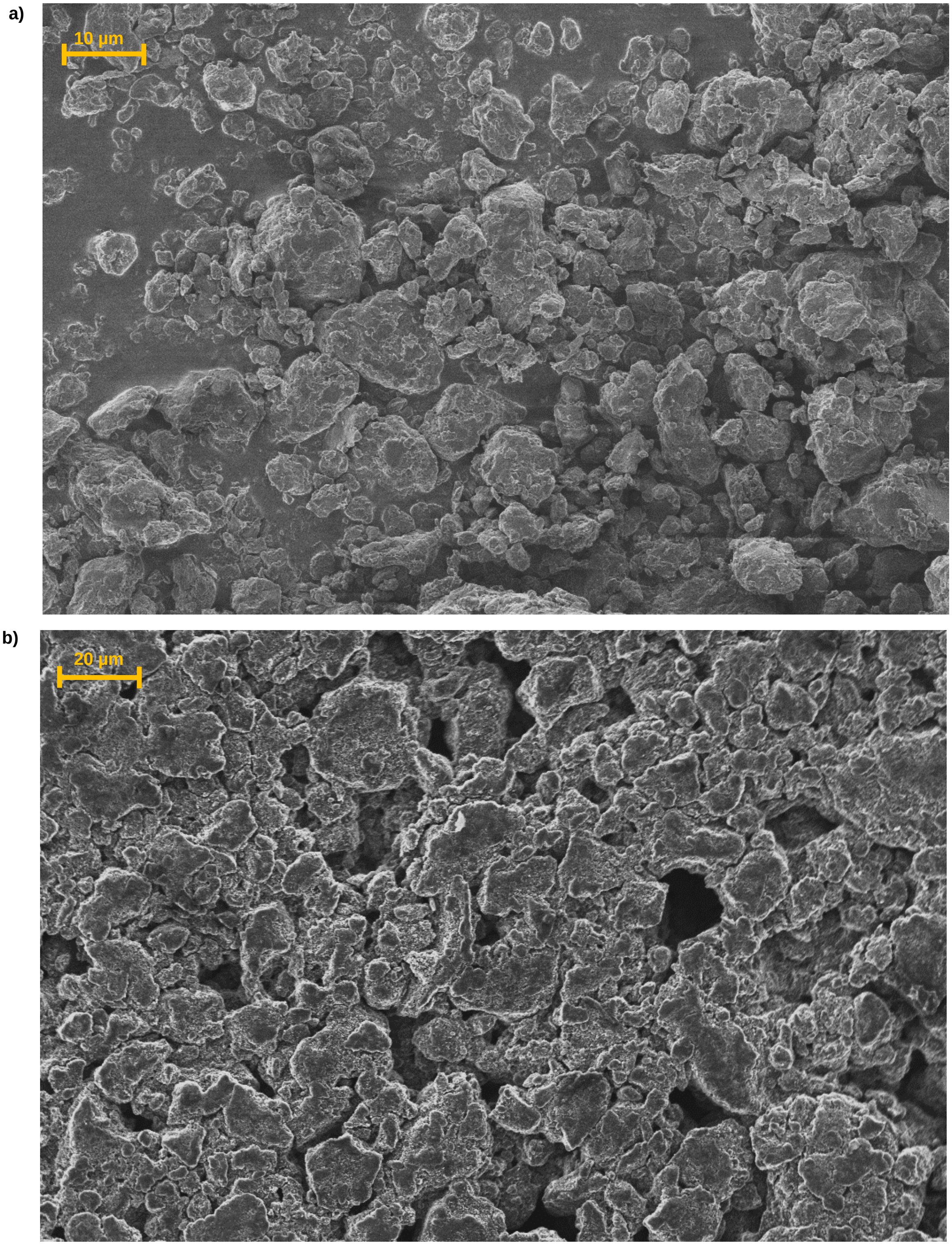

Figure A3.2 *– Scanning electron microscopy image of a) the PTMA/MWCNT active material powder and b) a PTMA/MWCNT-based electrode analogue to the one used in the electrochemical tests described in Section 5.1.2*

Appendix 3: Supporting information for Section 6.3

Table A3.1 *– Table of symbols used in the model definition*

Symbol	Unit of measurement	Description	Symbol	Unit of measurement	Description
Latin			**Greek**		
a	$[m^{-1}]$	Specific active area	α	$[-]$	Transfer coefficient
A	$[m^2]$	Electrode area	ε	$[-]$	Volume fraction
c	$[mol{\cdot}m^{-3}]$	Lithium concentration	η	$[V]$	Overpotential
C_{dl}	$[F{\cdot}m^{-2}]$	Double layer capacitance	κ	$[S{\cdot}m^{-1}]$	Ionic conductivity
D	$[m^2{\cdot}s]$	Diffusion coefficient	ϕ	$[V]$	Electric potential
E_{ocp}	$[V]$	Open circuit potential	σ	$[S{\cdot}m^{-1}]$	Electronic conductivity
F	$[A{\cdot}s{\cdot}mol^{-1}]$	Faraday constant	**Subscript**		
$\left(1+\frac{\partial f_{\pm}}{\partial \ln c_e}\right)$	$[-]$	Activity coefficient	$\boldsymbol{0}$		initial
i	$[A{\cdot}m^{-2}]$	Current density	$\boldsymbol{e}$		electrolyte
i_0	$[A{\cdot}m^{-2}]$	Exchange current density	$\boldsymbol{eff}$		effective
j	$[mol{\cdot}m^{-2}{\cdot}s^{-1}]$	Lithium molar flux	$\boldsymbol{max}$		maximum
L	$[m]$	Cell component length	$\boldsymbol{min}$		minimum
Q	$[mAh]$	Capacity	$\boldsymbol{pos}$		positive
R	$[J{\cdot}mol^{-1}{\cdot}K^{-1}]$	Universal gas constant	$\boldsymbol{ref}$		reference
R_{ext}	$[\Omega{\cdot}m^2]$	External resistance	$\boldsymbol{s}$		solid
R_p	$[m]$	Particle radius	$\boldsymbol{sep}$		separator
SOC	$[-]$	State of charge	**Superscript**		
t_0^+	$[-]$	Cation transference number	$\boldsymbol{bg}$		Bruggeman coefficient
T	$[K]$	Temperature	**Coordinate**		
V	$[V]$	Cell voltage	x		Linear coordinate
			r		Radial coordinate
			t		Time

Appendix 4: Supporting information for Section 6.4

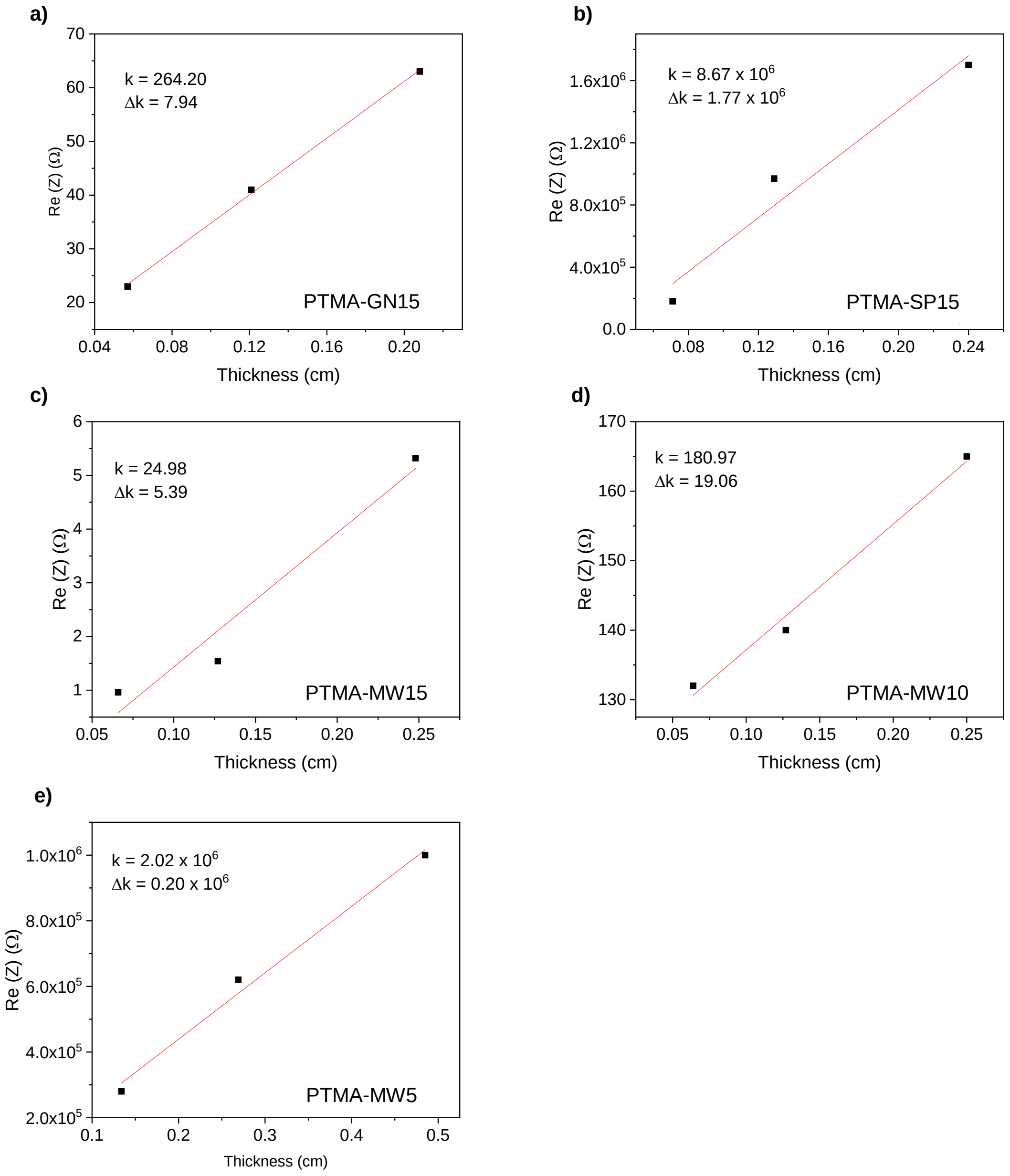

Figure A4.1 *– Results of the resistance measurements on the pellets of the samples a) PTMA-GN15, b) PTMA-SP15, c) PTMA-MW15, d) PTMA-MW10, e) PTMA-MW5.*

Appendix 4: Supporting information for Section 6.4

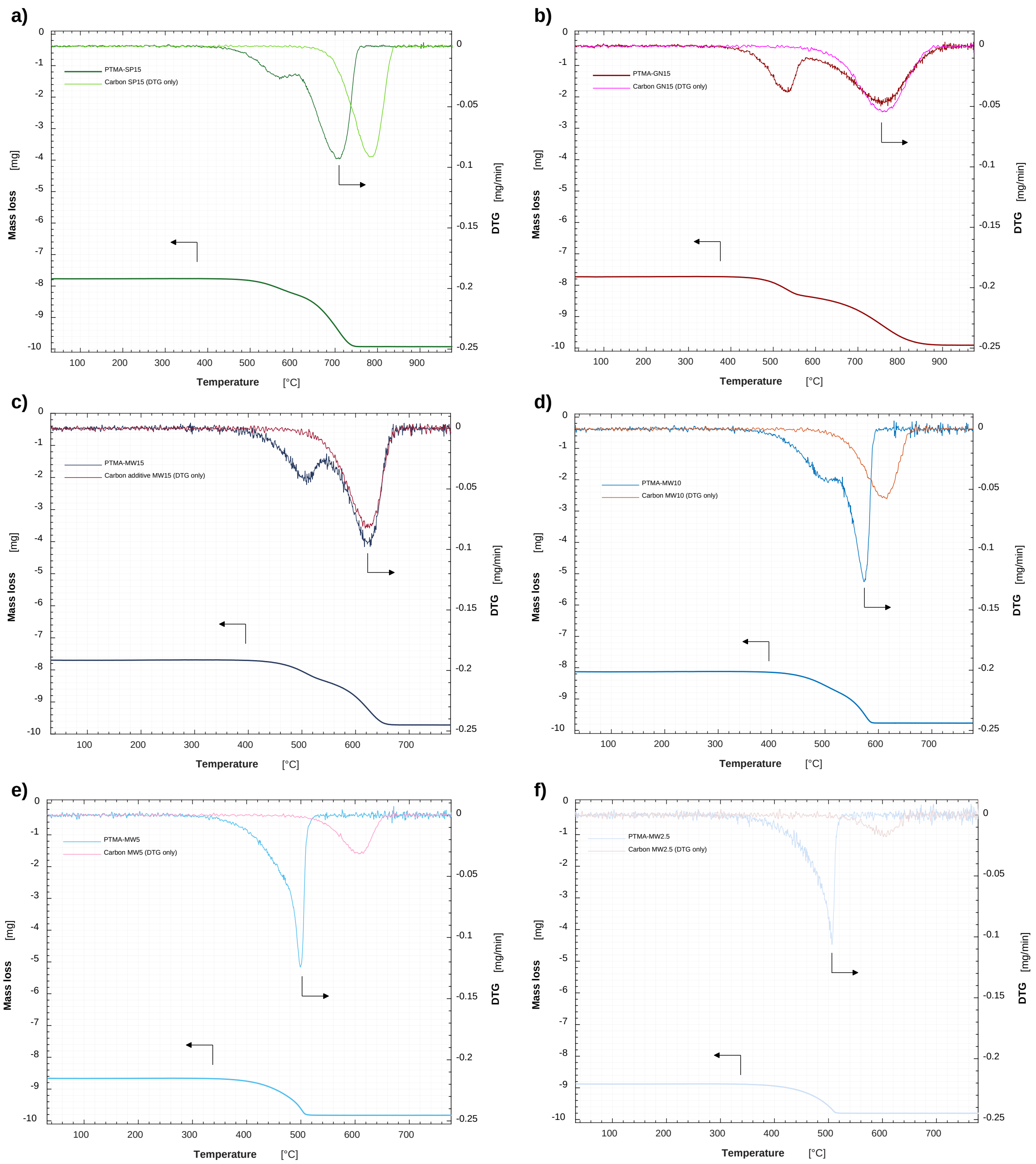

***Figure A4.2** – TGA curves during oxidation of the polymer-carbon mixtures together with the DTG curve of the oxidation of only the carbon additive. a) PTMA-SP15, b) PTMA-GN15, c) PTMA-MW15, d) PTMA-MW10, e) PTMA-MW5, f) PTMA-MW2.5*

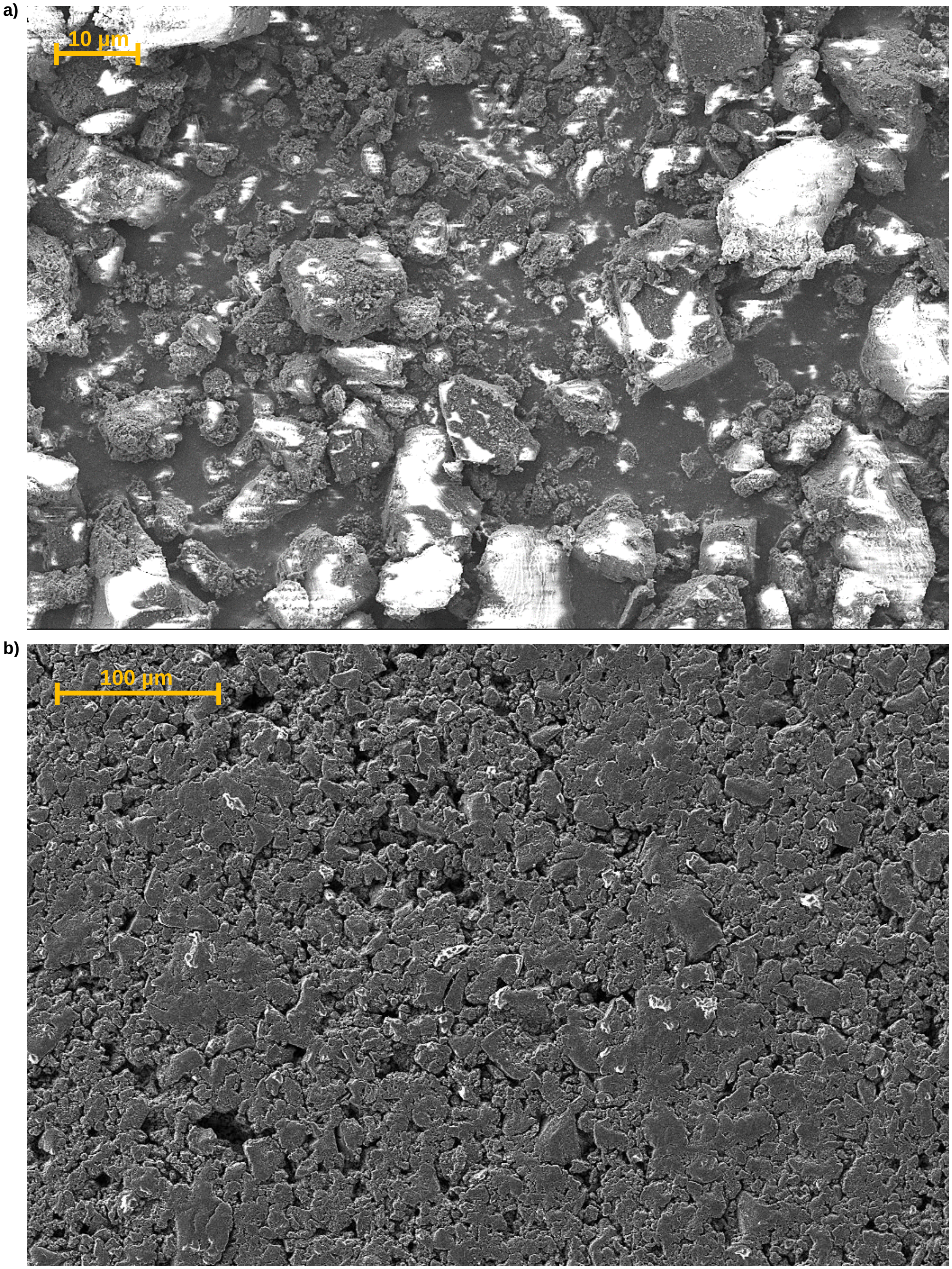

Figure A4.3 *- SEM images of the PTMA-SP15 sample a) as powder and b) the related electrode surface*

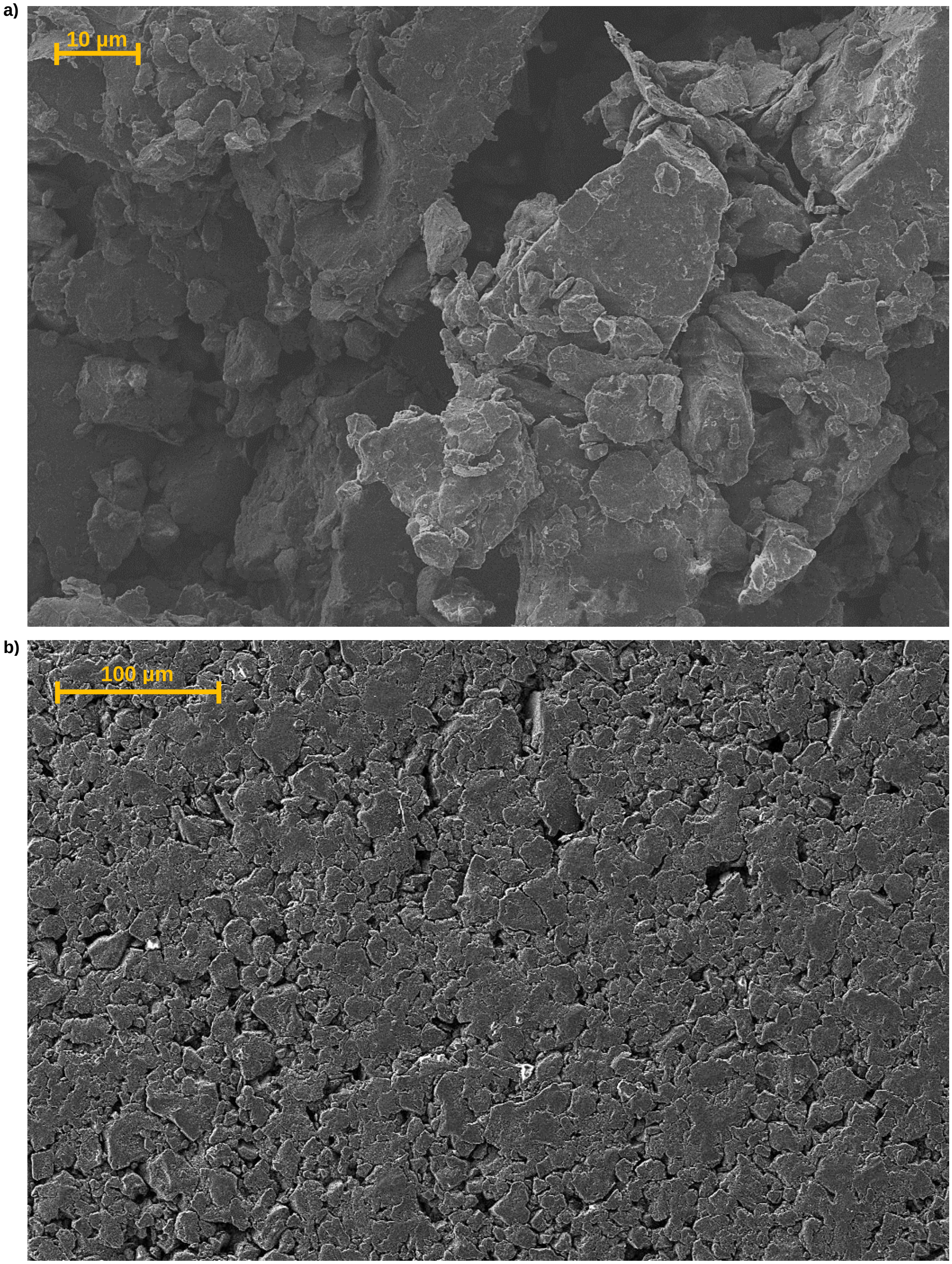

***Figure A4.4** – SEM images of the PTMA-GN15 sample a) as powder and b) the related electrode surface*

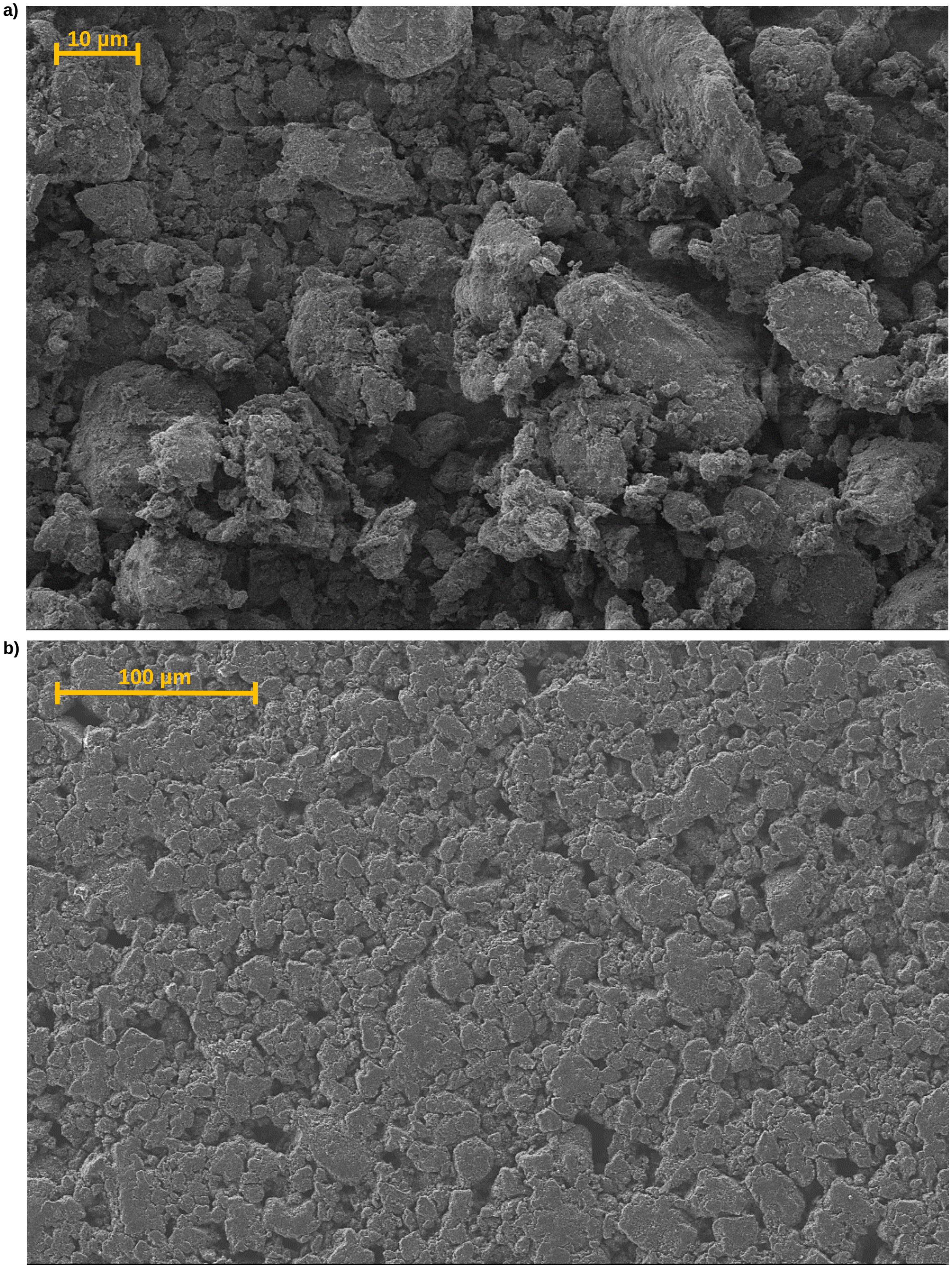

Figure A4.5 *– SEM images of the PTMA-MW15 sample a) as powder and b) the related electrode surface*

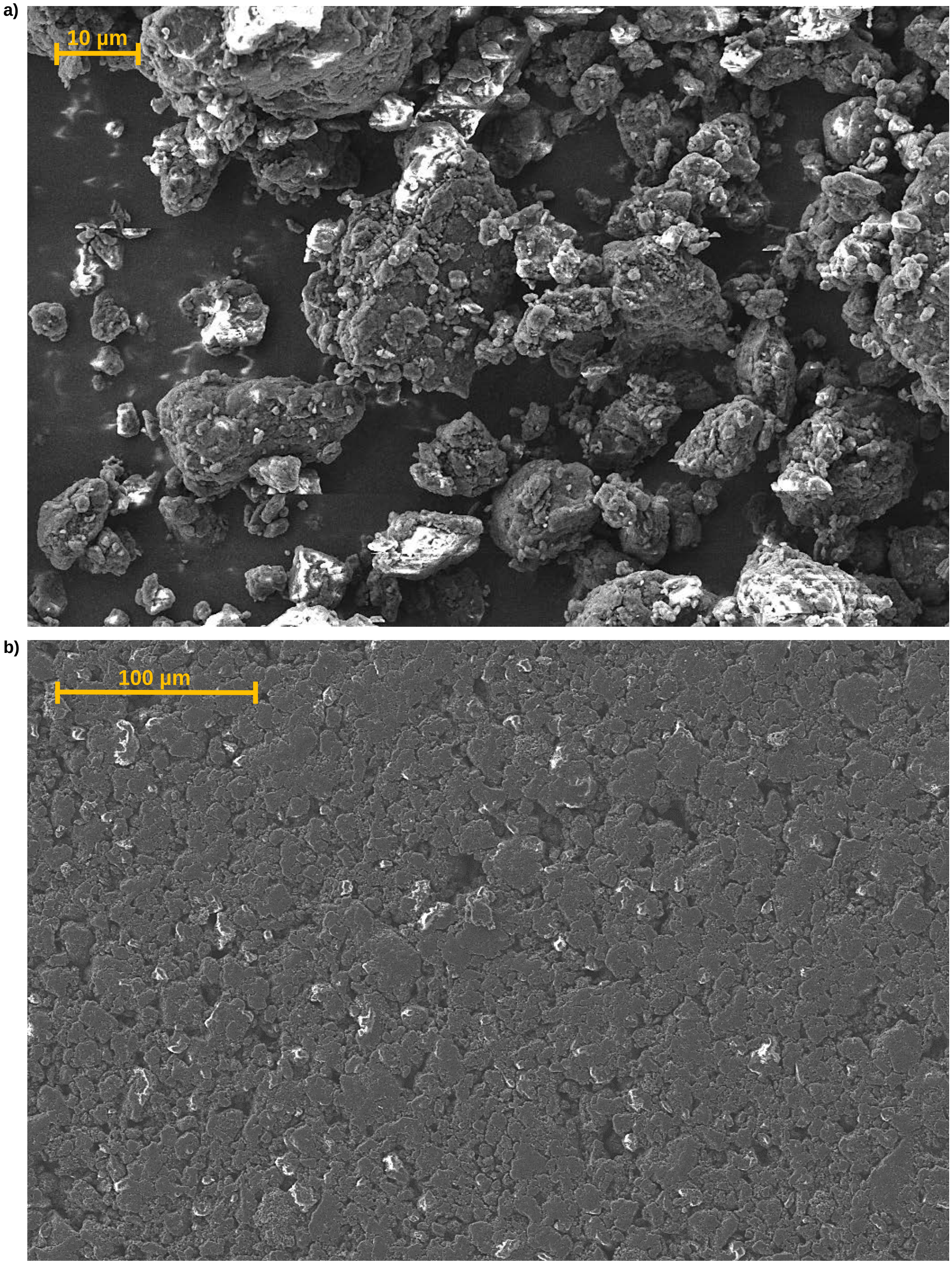

Figure A4.6 *– SEM images of the PTMA-MW10 sample a) as powder and b) the related electrode surface*

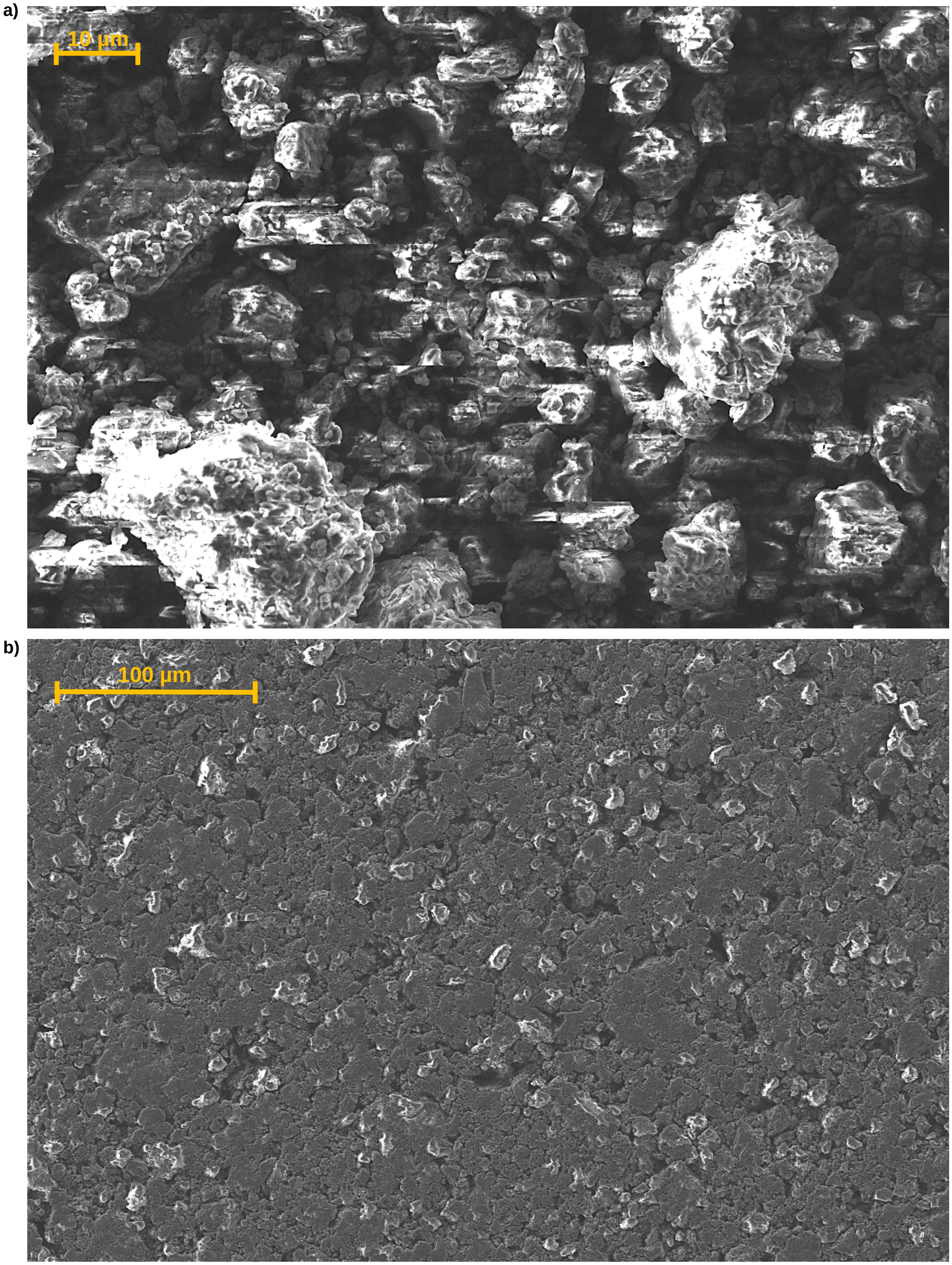

Figure A4.7 *– SEM images of the PTMA-MW5 sample a) as powder and b) the related electrode surface*

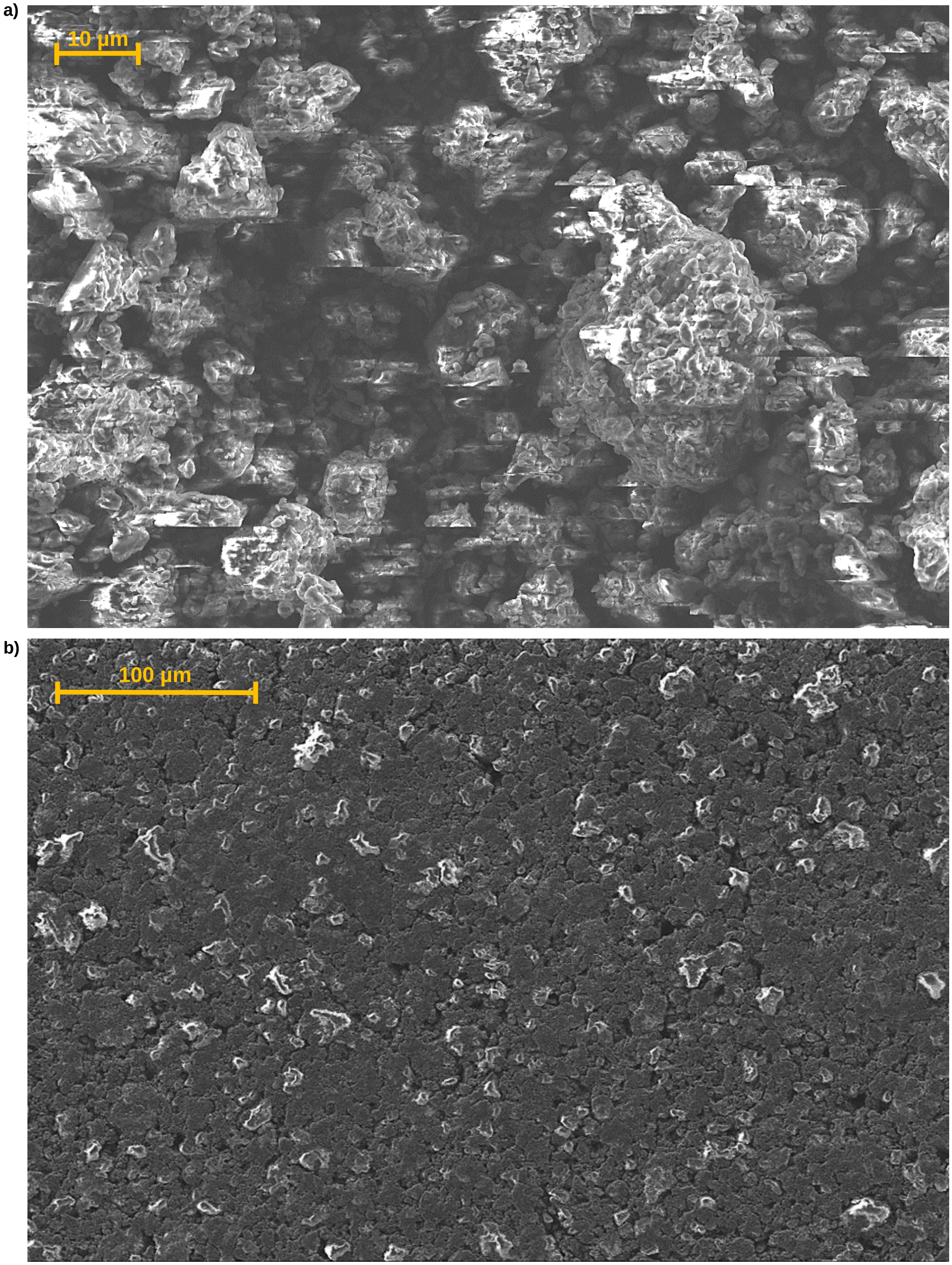

Figure A4.8 *– SEM images of the PTMA-MW2.5 sample a) as powder and b) the related electrode surface*

The porosity of the electrodes θ was calculated as

$$\theta = \frac{\rho_{el,app}}{\rho_{el}} \tag{A12}$$

where $\rho_{el,app}$ is the apparent density of the electrodes, and ρ_{el} is the true density of the electrodes. The apparent density was calculated by measuring the thickness of the electrodes, calculating the volume and dividing the mass of the coating by the obtained value.

The true density was obtained by estimating the density of each of the electrode components, i.e., for the PTMA polymer 1.17 g·cm^{-3}, for the multi-walled carbon nanotubes 1.75 g·cm^{-3}, for the graphene nanoplatelets 2.26 g·cm^{-3}, for the Super P and the C45 1.83 g·cm^{-3}, for the binder mixture 1.1 g·cm^{-3}, and for the inorganic impurities 5 g·cm^{-3}. Then, the following formula was applied

$$\rho_{el} = \frac{1}{\left(\frac{w_p}{\rho_p} + \frac{w_{cp}}{\rho_{cp}} + \frac{w_{ce}}{\rho_{ce}} + \frac{w_b}{\rho_b} + \frac{w_i}{\rho_i}\right)} \tag{A13}$$

where w_p and ρ_p are the weight fraction and density of the PTMA polymer, w_{cp} and ρ_{cp} are the weight fraction and density of the conductive carbon additive in the polymer, w_{ce} and ρ_{ce} are the weight fraction and density of the conductive carbon additive in the electrode, w_b and ρ_b are the weight fraction and density of the binder mixture, and w_i and ρ_i are the weight fraction and density of inorganic impurities.

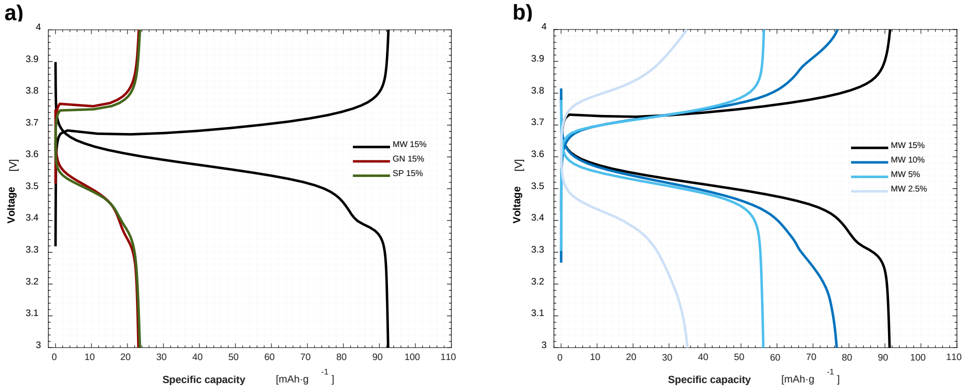

Figure A4.9 *– a) Voltage vs. specific capacity charge and discharge curves of PTMA-MW15, PTMA-GN15, and PTMA-SP15 at 5C (cycle n° 27 of Figure 1.c of the main text), b) Voltage vs. specific capacity charge and discharge curves of PTMA-MW15, PTMA-MW10, PTMA-MW5, and PTMA-MW2.5 at 5C (cycle n° 27 of* ***Figure 2.c*** *of the main text)*

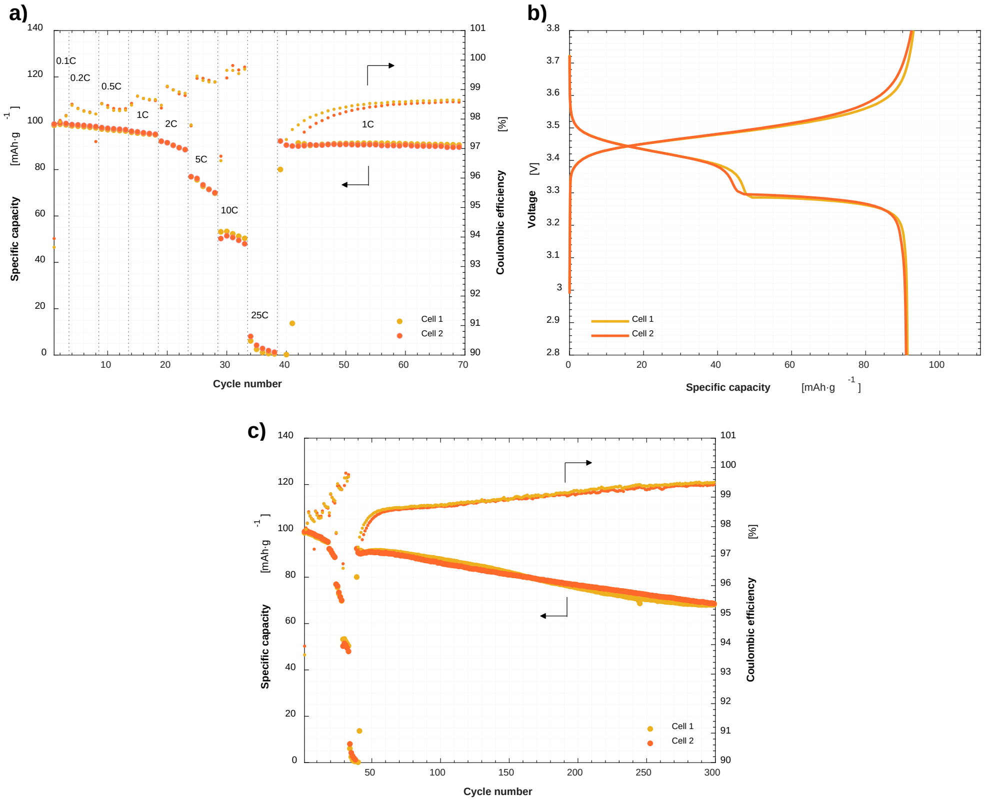

Figure A4.10 *– a) Specific capacity and coulombic efficiency vs. cycle number for the rate performance test of the PTMA-MW15 sample in two coin cells with a sodium metal anode at 20°C (zoom on rate performance) b) Voltage vs. specific capacity charge and discharge curves of PTMA-MW15, 1C (cycle n° 50 of* ***Figure A4.10.a****), c) Specific capacity and coulombic efficiency vs. cycle number for the rate performance test of the PTMA-MW15 sample in two coin cells with a sodium metal anode at 20°C (whole test). The voltage step during discharge in the PTMA-Na cell, not present in the lithium-based cells, may be due to an overpotential caused by the interaction between the sodium metal anode and the EC:PC solvent* [336]

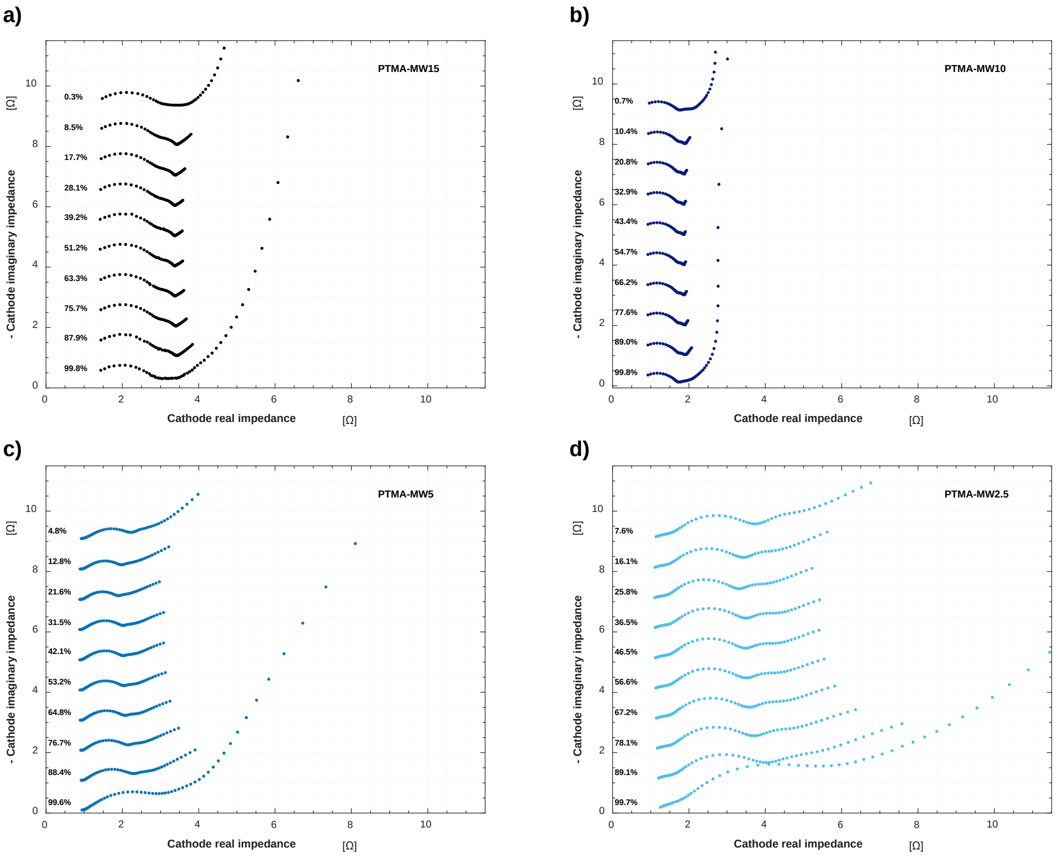

Figure A4.11 *– Cathode impedance spectra at different SOCs (indicated by the percentage next to the spectra) of a) PTMA-MW15, b) PTMA-MW10, c) PTMA-MW5, and d) PTMA-MW2.5 in a three-electrode configuration*

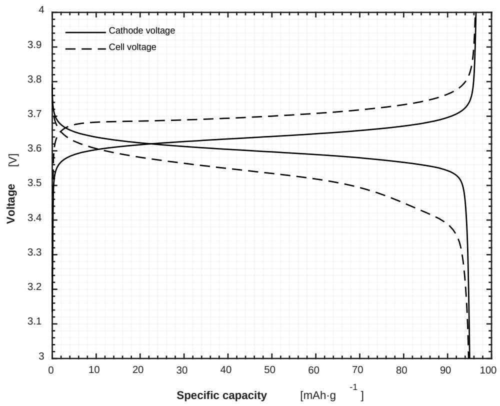

Figure A4.12 *– Cathode voltage vs. lithium metal reference electrode (solid line) and vs. lithium metal anode (dashed line) in a 5C galvanostatic discharge using the three-electrode EL-Cell setup and a 3.88 mg·cm*$^{-2}$ *PTMA-MW15-based electrode. Note the overpotential caused by the lithium metal anode.*

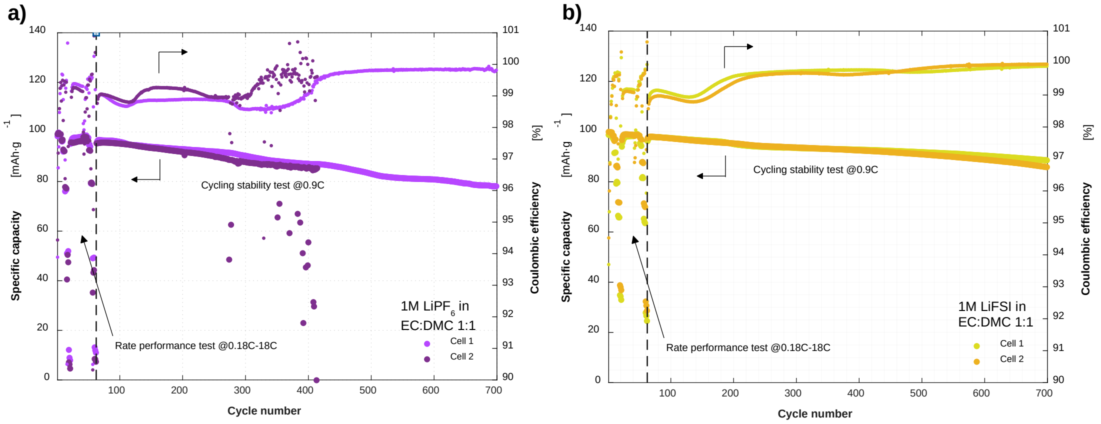

Figure A4.13 *- Specific capacity and coulombic efficiency vs. cycle number for galvanostatic charge/discharge test of the PTMA-MW15 sample in coin cell with lithium metal anode at 20°C with a) 1M LiPF6 in EC:DMC 1:1 (Cell 1: 8.65 mg·cm-2, Cell 2: 8.34 mg·cm*$^{-2}$*) and b) 1M LiFSI in EC:DMC 1:1 (Cell 1: 8.56 mg·cm*$^{-2}$*, Cell 2: 8.18 mg·cm*$^{-2}$*)*

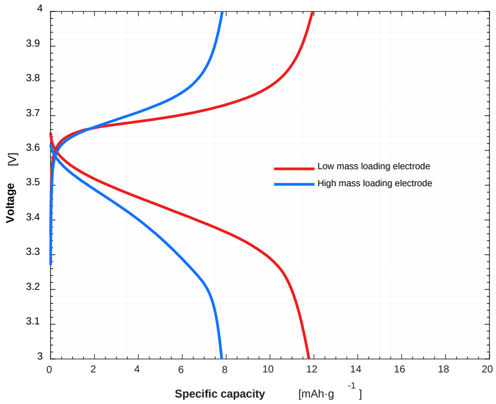

Figure A4.14 *– Voltage vs. specific capacity of PTMA-MW15 cathodes in coin cell with lithium metal anode at 20°C, using 10 µm thick polyolefin separator with a minimal quantity of electrolyte (Low mass loading: 4.78 mg·cm*$^{-2}$*, High mass loading: 9.15 mg·cm*$^{-2}$*)*

The dimensionless parameter K was obtained by relating the quantity of anions that are present in the electrolyte and the quantity that it needed to fully balance the positive charge formed on the PTMA cathode during charge.

We can express the quantity of anions available in the electrolyte Λ_l as

$$\Lambda_l = (c_{e,ref} - c_{e,min}) \cdot A \cdot (L_{sep}\varepsilon_{l,sep} + L_{pos}\varepsilon_{l,pos}) \tag{A14}$$

where the area of the battery A multiplied by the space available in the separator and the cathode gives the volume occupied by the electrolyte, which is then multiplied by the "available" salt concentration in the electrolyte.

Instead, quantity of anions required to charge the PTMA cathode Λ_s is written as

$$\Lambda_s = c_{s,max,pos} \cdot A \cdot (L_{pos}\varepsilon_{s,pos}) \tag{A15}$$

where the area of the battery A multiplied by the space occupied by the active material in the cathode gives the volume occupied by the active material, further multiplied by the concentration of redox-active sites. This latter parameter can be expressed as

$$c_{s,max,pos} = \frac{Q_{th}}{F} \cdot \rho_p \tag{A16}$$

where Q_{th} is the specific capacity of the active material, F is the Faraday constant, and ρ_p is the density of the active material. By assuming Q_{th} equal to 100.2 mAh·g^{-1}, which is the maximum practical specific capacity that was obtained at low current rate, and ρ_p equal to 1.17 g·cm^{-3}, we obtain a value for $c_{s,max,pos}$ of 4375 mol·m^{-3}.

By dividing Λ_l by Λ_s, we obtain the parameter K as

$$\begin{aligned} K = \frac{\Lambda_l}{\Lambda_s} &= \frac{(c_{e,ref} - c_{e,min}) \cdot A \cdot (L_{sep}\varepsilon_{l,sep} + L_{pos}\varepsilon_{l,pos})}{c_{s,max,pos} \cdot A \cdot (L_{pos}\varepsilon_{s,pos})} \\ &= \frac{(c_{e,ref} - c_{e,min})}{c_{s,max,pos}} \cdot \left(\frac{L_{sep}\varepsilon_{l,sep}}{L_{pos}\varepsilon_{s,pos}} + \frac{\varepsilon_{l,pos}}{\varepsilon_{s,pos}}\right) \end{aligned} \tag{A17}$$

Hence, if $K > 1$, $\Lambda_l > \Lambda_s$, meaning that there are more available anions in the electrolyte than the one required to balance the charge of the cathode, and the battery can then be fully charged. Vice versa, when $K < 1$, $\Lambda_l < \Lambda_s$, and the anions in the electrolyte are fully depleted before the PTMA-based battery can fully charge.

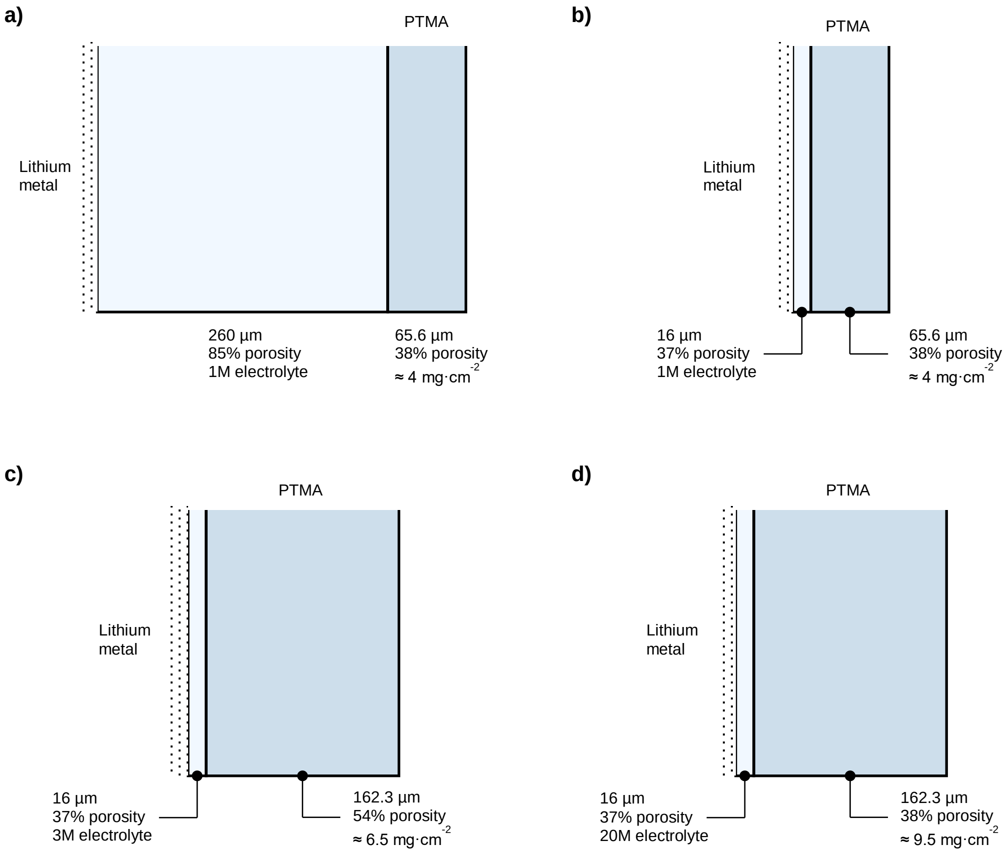

***Figure A4.15** - Model domain in the simulated cases presented in the main text: a) Case 1, b) Case 2, c) Case 3 and d) Case 4*

***Table A4.1** - Values assigned to the model parameters that vary in the simulated cases*

Parameter	Unit of measurement	Case 1	Case 2	Case 3	Case 4
L_{sep}	$[m^{-1}]$	$260 \cdot 10^{-6}$	$16 \cdot 10^{-6}$	$16 \cdot 10^{-6}$	$16 \cdot 10^{-6}$
$\varepsilon_{l,sep}$	$[-]$	0.9	0.37	0.37	0.37
L_{pos}	$[m^{-1}]]$	$65.6 \cdot 10^{-6}$	$65.6 \cdot 10^{-6}$	$162.3 \cdot 10^{-6}$	$162.3 \cdot 10^{-6}$
$\varepsilon_{l,pos}$	$[-]$	0.38	0.38	0.54	0.38
$\varepsilon_{s,sep}$	$[-]$	0.51	0.51	0.37	0.51
$c_{e,ref}$	$[mol \cdot m^{-3}]$	1000	1000	3000	20000

Table A4.2 *– Values assigned to the model parameters that remain constant in all the simulated cases*

Parameter	**Unit of measurement**	**Anode**	**Separator/Electrolyte/Cell**	**Cathode**
α	$[-]$	0.5	-	0.5
a_s	$[m^{-1}]$	-	-	$1 \cdot 10^{5}$
A	$[m^2]$	-	$1.131 \cdot 10^{-4}$	-
^{bg}	$[-]$	-	1.5	1.5
$c_{s,max}$	$[mol \cdot m^{-3}]$	-	-	4375
C_{dl}	$[F \cdot m^{-2}]$	-	-	0.02
D_s	$[m^2 \cdot s^{-1}]$	-	-	$2.5 \cdot 10^{-13}$
i_0	$[A \cdot m^{-2}]$	5	-	3.15
R_{ext}	$[\Omega \cdot m^2]$	-	0	-
R_p	$[m]$	-	-	$10 \cdot 10^{-6}$
σ	$[S \cdot m^{-1}]$	-	-	$2.5 \cdot 10^{-2}$
SOC_{min}	$[\%]$	-	-	0
SOC_{max}	$[\%]$	-	-	100
T_0	$[K]$	293.15	293.15	293.15

Appendix 4: Supporting information for Section 6.4

The parameters which are varied in the model for the simulations of the organic and inorganic lithium metal batteries are reported in **Table A4.3**, and the ones not mentioned in the table are left at the default value of BatPac 5.0.[75] The updated prices for the commercial active materials, electrolyte, current collectors and separators were retrieved from a specialized website.[324] The main results of the simulations are shown in **Table A4.4**.

Table A4.3 *- Modified parameters in the BatPac 5.0 model for the cost and performance analysis*

	Type of battery **Code**	**PTMA - Li** **Case 1**	**PTMA - Li** **Case 2**	**PTMA - Li** **Case 3**	**PTMA - Li** **Case 4**	**LFP - Li** **LFP**	**NMC 622 - Li** **NMC**
	Description	**Thin electrode, thick separator, lean electrolyte**	**Thin electrode, thin separator, lean electrolyte**	**Thick very porous electrode, thin separator, concentrated electrolyte**	**Thick electrode, thin separator, superconcentrated electrolyte**	**LFP lithium metal battery for comparison**	**NMC 622 lithium metal battery for comparison**
Parameters	**Specific capacity, mAh/g**	101	21	101	101	157	187
	Cathode thickness, µm	65.6	65.6	162.3	162.3	120	120
	Cathode porosity, %	38%	38%	54%	38%	25%	25%
	Cathode active material density, g/cm^3	1.17	1.17	1.17	1.17	4.65	3.45
	Cathode composition (AM:CC:B)	76.5:18.5:5	76.5:18.5:5	76.5:18.5:5	76.5:18.5:5	94:03:03	94:03:03
	Slurry solvent	Water	Water	Water	Water	NMP	NMP
	N/P ratio	0.3	0.3	0.3	0.3	0.3	0.3
	Separator thickness, µm	260	16	16	16	16	16
	Separator porosity, %	90%	37%	37%	37%	25%	25%
	Separator density, g/cm^3	0.25	0.60	0.60	0.60	0.60	0.60
	Electrolyte density, g/cm^3	1.2	1.2	1.4	1.7	1.2	1.2
	Electrolyte cost, $/L	4.8	4.8	14.1	20	4.8	4.8
	Cathode active material cost, $/kg	10	10	10	10	25	40
	Cathode conductive carbon cost, $/kg	7	7	7	7	7	7
	Cathode binder cost, $/kg	10	10	10	10	15	15
	Cathode solvent cost, $/kg	0	0	0	0	4.5	4.5
	Anode active material cost, $/kg	200	200	200	200	200	200

Table A4.4 *- Main results of the cost and performance analysis*

	Type of battery **Code**	**PTMA - Li** **Case 1**	**PTMA - Li** **Case 2**	**PTMA - Li** **Case 3**	**PTMA - Li** **Case 4**	**LFP - Li** **LFP**	**NMC 622 - Li** **NMC**
	Description	**Thin electrode, thick separator, lean electrolyte**	**Thin electrode, thin separator, lean electrolyte**	**Thick very porous electrode, thin separator, concentrated electrolyte**	**Thick electrode, thin separator, superconcentrated electrolyte**	**LFP lithium metal battery for comparison**	**NMC 622 lithium metal battery for comparison**
Results	**Positive active material, $/pack**	378.61	1820.93	378.61	378.61	656.85	811.53
	Negative active material, $/pack	56.48	56.40	56.94	57.11	63.15	59.00
	Electrode preparation, $/pack	342.73	1648.36	342.73	342.73	104.48	80.68
	Positive current collector, $/pack	108.21	518.31	60.36	45.16	11.71	7.21
	Negative current collector, $/pack	644.66	3007.98	356.76	267.60	70.71	44.07
	Separators, $/pack	108.23	519.65	59.57	44.36	11.04	6.68
	Electrolyte, $/pack	1126.70	662.41	654.89	506.26	16.11	9.62
	Battery system total energy, kWh	11.48	11.49	11.48	11.47	11.41	11.38
	Battery system rated power, kW	7.00	7.00	7.00	7.00	7.00	7.00
	Battery system capacity, Ah	44.65	44.65	44.65	44.65	48.08	44.33
	Battery system nominal operating voltage, V	257.10	257.32	257.05	256.96	237.41	256.69
	Cell volume, L	4.49	5.93	1.50	1.15	0.28	0.19
	Cell mass, kg	6.02	9.46	2.02	1.59	0.51	0.37
	Cell capacity, Ah	44.65	44.65	44.65	44.65	48.08	44.33
	Cell specific energy, Wh/kg	26	17	79	100	312	427
	Cell energy density, Wh/L	35	27	106	139	566	838
	Cell cost, $/kWh	287	829	201	175	105	111

List of Abbreviations

AQ	anthraquinone
C4Q	calix[4]quinone
DFN	Doyle-Fuller-Newman
DLR	dilithium rhodizonate
DMC	dimethyl carbonate
DME	dimethoxyethane
DOL	dioxolane
DTG	derivative of the thermogravimetric curve
EC	ethylene carbonate
EDX	energy-dispersive X-ray spectroscopy
EIS	electrochemical impedance spectroscopy
EV	electric vehicle
GHG	greenhouse gas
IC	indigo carmine
LFP	lithium iron phospate
Li_2-BQDO	dilithium benzoquinone dioximate
Li_2-Co-PTtSA	dilithium cobalt benzene-1,2,4,5-tetra-methylsulfonamide
Li_2-DC-PDSA	dilithium 2,5-dichloro-1,4-phenylene-bis-methylsulfonylamide
Li_4-PTtSA	tetralithium benzene-1,2,4,5-tetra-methylsulfonamide
LIB	lithium-ion battery
LiFSI	ithium bis(fluorosulfonyl)imide
Li-TCQM	lithium tetracyanoquinodimethane
LiTFSI	lithium bis(trifluorosulfonyl)imide
LiTPT	dilithium terephthalate
LMO	lithium manganese oxide
LP30	1M $LiPF_6$ in EC:DMC 1:1
NAFMO	$Na_{0.66}[Al_{0.1}Fe_{0.05}Mn_{0.85}]O_2$
NAFMO	$Na[Fe_{0.40}Ni_{0.30}Mn_{0.30}]O_2$

NCA	lithium nickel-cobalt-aluminum oxide
NCFMO	$Na_{0.9}[Cu_{0.22}Fe_{0.30}Mn_{0.48}]O_2$
NDI	1,4,5,8-naphthalenediimide
NLNMO	$Na[Li_{0.10}Ni_{0.35}Mn_{0.55}]O_2$
NMC	lithium nickel-manganese-cobalt oxide
NZNMO	$Na_{0.66}[Ni_{0.26}Fn_{0.06}Mn_{0.67}]O_2$
P2D	pseudo-two dimensional
P5Q	pillar[5]quinone
PAQS	polyanthraquinonyl sulphide
PBQS	polybenzoquinonyl sulphide
PDE	partial differential equations
PDI	poly(3,4,9,10-perylenetetracarboxylic dianhydride ethylene diamine)
PPA	poly(piperazine-altbenzoquinone)
PTCDA	perylenetetracarboxylic dianhydride
PTCLi4	tetralithium 3,4,9,10-perylene-tetracarboxylic-dianhydride
PTMA	poly(2,2,6,6-tetramethyl-1-piperidinyloxy methacrylate)
PTO	pyrene-4,5,9,10-tetraone
SEM	scanning electron microscopy
SHE	standard hydrogen electrode
SIB	sodium-ion battery
SOC	state of charge
SPAN	sulfurized polyacrylonitrile
TAPT	2,3,7,8-tetraaminophenazine-1,4,6,9-tetraone
TGA	thermogravimetric analysis
TPB	2,3,5,6-tetraphthalimido-1,4-benzoquinone
VGCF	vapor grown carbon fibers
XRD	x-ray diffraction

List of Tables

Table 6.1 – Summary of the main results of the simulations for all the case studies..........................69

Table 6.2 – List of the organic and inorganic materials included in the cost and energy density analysis 83

Table 6.3 – Equations and boundary conditions of the dual-ion battery model 99

Table 6.4 – Values of the model parameters for the simulation of a PTMA|Li metal cell................102

Table 6.5 – Results of the physicochemical characterization of the polymer-carbon powder samples 112

Table 6.6 – Results of the physicochemical characterization of the electrodes 112

Table 6.7 - Results of the electrochemical characterization of selected electrodes 113

Table A1.1 - Currency exchange rates and actualization factor for US$ in Section 6.1.1 128

Table A1.2 – Prices of precursors and raw materials for lithium- and sodium-ion batteries in Section 6.1.1 129

Table A1.3 – Characteristics of the simulated battery packs in Section 6.1.1 131

Table A1.4 - Details on the analysed cathode materials from literature in section 6.1.2 132

Table A2.1 - Summary of the different simulation parameters for the low and high cost lithium scenario 146

Table A3.1 – Table of symbols used in the model definition 149

Table A4.1 - Values assigned to the model parameters that vary in the simulated cases 163

Table A4.2 – Values assigned to the model parameters that remain constant in all the simulated cases 164

Table A4.3 - Modified parameters in the BatPac 5.0 model for the cost and performance analysis. 165

Table A4.4 - Main results of the cost and performance analysis 165

List of Figures

Figure 1.1 – a) Forecasted yearly GHG emission trends from possible pathways, according to the policies implemented by statesm Copyright © 2022, IPCC [1] b) Breakdown by sector of the global GHG emissions in 2022. CC BY 4.0, 2023 IEA [2] 2

Figure 1.2 – a) Predicted demand of lithium and cobalt for the battery industry between 2016 and 2050; b) Total amount of produced lithium and cobalt with current production rates and with a 2% yearly increase of production between 2016 and 2050. Adapted with permission from Vaalma et al.[13], Copyright © 2018, Springer Nature......3

Figure 2.1 – Scheme of the charge and discharge process of a battery (the reactions refer to a lithium-ion battery)......7

Figure 2.2 – Example of the potential of the electrodes and the resulting cell voltage of a battery vs. the state of charge (SOC). Reproduced with permission from Rabissi et al., Copyright © 2021 Wiley[22] 7

Figure 2.3 - Relationship between Gibbs free energy, chemical potential and open circuit potential in a battery. (a) and (b): single phase solid solution, (c) and (d): two phase solid solution, (e) and (f): two phase solid solution with intermediate phase. Reproduced with permission from Gao et a., Copyright © 2015, IOP Publishing [23] 8

Figure 2.4 – a) Trend of the price per kWh of commercial lithium-ion batteries in the last thirty years, b) Gravimetric vs. Volumetric energy density of commercial lithium-ion batteries. Reproduced with permission from Ziegler and Trancik. CC BY-BC 3.0 2021, RSC Publishing[25]......10

Figure 2.5 – Examples of crystal structures of cathode materials for lithium-ion batteries: (a) Layered oxide: $LiCoO_2$, (b) Spinel: $LiMn_2O_4$, (c) Olivine: $LiFePO_4$. Lithium ions are represented as green spheres, CoO_6 octahedra in blue; MnO_6 octahedra in fuchsia, Fe–O polyhedra in ochre, PO_4 tetrahedra in violet. Reproduced with permission from Islam and Fisher, CC BY 3.0 2014, RSC Publishing[37] ..12

Figure 2.6 – Depiction of lithium intercalation (staging) into graphite, with the related potential curves during charge and discharge of a graphite anode vs. lithium metal. Reproduced with permission from Asenbauer et al., CC BY 3.0 2020, RSC Publishing[40]......14

Figure 2.7 – Price of selected battery raw materials and lithium-ion batteries, 2015-2023. Reproduced with permission, CC BY 4.0, 2023 IEA[11]......17

Figure 2.8 – General electrochemical reactions for n-type (top left) and p-type (bottom left) organic materials and relative examples of reactions with 1,4-benzoquinone and (2,2,6,6-tetramethylpiperidin-1-yl)oxyl (TEMPO). 20

Figure 2.9 – a) Voltage/specific capacity curves of several n-type small molecule organic cathodes, among which AQ and PTO [113], b) Voltage/specific capacity curve of the 1st, 2nd and 10th cycle of a TAPT/Li metal cell in 1M LiTFSI in DOL/DME [122], c) Voltage/specific capacity curve of the 1st, 20th and 50th cycle of a P5Q/Li metal cell in a poly(methacrylate)/poly(ethylene glycol)-based gel polymer electrolyte [125], d) Specific capacity vs. cycle number for three small imide molecules as cathodes for lithium metal batteries, including NDI [131], e) Reaction scheme for the synthesis of PPA from vanillin and piperazine [156], f) Voltage/specific capacity curve of a SPAN/Li metal cell in an ionic liquid-based electrolyte. All the images are reproduced from permission from the respective publishers. 24

Figure 2.10 – a) Voltage/specific capacity curve for the first cycles of Li_4-PTtSA and b) the related specific capacity vs. cycle number chart [164], c) Comparison between the voltage and specific capacity of LFP and Li_2-DC-PDSA [164], d) First two cycles of Li_2-BQDO, with a depiction of the charged and discharged forms of the molecule [169], e) Voltage/specific capacity curve for the first cycles of Li-TCQM and f) the related specific capacity vs. cycle number chart at different current rates [171], g) Voltage/specific capacity curve at different active material mass loadings of Li_2-Co-PTtSA and h) the related specific capacity vs. cycle number chart at different current rates [166] All the images are reproduced from permission from the respective publishers. 26

Figure 2.11 – a) Voltage/specific capacity curve of a Super P blank electrode in 1M $LiPF_6$ in EC/DEC[174], b) Voltage/specific capacity curve of selected cycles of a maleic acid-based organic anode[181], c) Voltage/specific capacity and d) cycling stability of a 12.0 mg·cm^{-2} $PTCLi_4$ electrode in 1M $LiPF_6$ in a 1:1:1 volume mixture of EC, DMC and EMC[183], e) Voltage/specific capacity curve and f) cycling stability of a LiTPT electrode in 1M $LiPF_6$ in EC/DMC[94]. All the images are reproduced from permission from the respective publishers. 28

Figure 2.12 – a) Charge/discharge curve of a polyacetylene-lithium metal battery[185], b) Voltage vs. specific capacity for a triphenylamine-based microporous polymer battery vs. lithium metal at different current rates[186], c) Voltage vs. specific capacity curves of a dibenzo-1,4-dioxine-TCNQ charge-transfer complex cathode vs. lithium metal at different weight ratios of active material in the positive electrode[190], d) Voltage vs. specific capacity curves at the 100th, 1000th, 5000th, and 10000th cycle at 10C of a poly(3-vinyl-N-methylphenothiazine)-based battery vs. lithium metal [187], e) Voltage vs. specific capacity curves at 1C and 1/4C for a N,N-diphenyl-5,10-phenazine-based battery vs. lithium metal[188], f) Capacity vs. current rate plot for a PTMA-based battery vs. lithiated graphite, using 1M and 1.5M LiFSI in EC:DMC 4:6[209]. All the images are reproduced from permission from the respective publishers. 31

Figure 4.1 – Different types of chronopotentiometric techniques, according to the value and the direction of the current pulse: a) Constant current chronopotentiometry, b) Chronopotentiometry with linearly rising current, c) Current reversal chronopotentiometry, d) Cyclic chronopotentiometry (galvanostatic cycling). Reproduced with permission from Pyun et al., Copyright © 2012 Springer Nature[210]..35

Figure 4.2 – Example of an impedance spectra obtained by physical simulations of a commercial lithium-ion battery, with highlighted the frequency ranges and the associated different resistance sources (HFR=high frequency resistance, R_{CT}: charge transfer resistance, R_{diff}: diffusion resistance). Reproduced with permission from Rabissi et al., Copyright © 2021 Wiley [22]....................................38

Figure 4.3 – a) Scheme of a scanning electron microscope; b) Different signals generated during SEM measurements and their penetration depth. Reproduced with permission from T. Schmid[221].............39

Figure 4.4 – a) Depiction of the main parts of a TGA instrument; b) Mass loss vs. temperature in a TGA measurement on calcium oxalate monohydrate, at 10 and 200 $K \cdot min^{-1}$. Reproduced with permission from NETZSCH GmbH[224]...40

Figure 4.5 – a) Difference between bulk density and true density. Adapted from 3P Instruments [229] b) Scheme of the main components and volumes of a gas pycnometer. Reproduced with permission from Pharmacopeia[230] 41

Figure 6.1 - Discharge curves of the selected (a) lithium cathodes and (b) sodium cathodes from the respective references. Reproduced from permission from Zuo et al., CC BY 4.0 2023, ACS Publications[56] 63

Figure 6.2 – Comparison of (a) cost per unit mass and (b) cost per unit energy between lithium-ion and sodium-ion cathodes. (c) Costs of battery packs based on various lithium- and sodium-cathode materials. Reproduced from permission from Zuo et al., CC BY 4.0 2023, ACS Publications[56].........65

Figure 6.3 – (a) Cost breakdown of various SIBs and LIBs for grid storage. (b) Cost breakdown of LFP-based and NZNMO-based battery packs with the prices of April 2022. Reproduced from permission from Zuo et al., CC BY 4.0 2023, ACS Publications[56] 67

Figure 6.4 – Electrode potentials of cathode and anode and resulting cell voltages of the materials analyzed in the lower cut-off voltage study. a) NFP; b) NNFMO; c) NVPF. The dashed line represents the part of battery voltage and capacity that are removed after the increase of the lower cut-off voltage to the USABC target of 55% of the maximum voltage. 72

Figure 6.5 – Electrode potentials of cathode and anode and resulting cell voltages of the materials analyzed in the pre-sodiation for the capacity increase of cathode materials study. a) NVPFO; b) NNAMO; c) NNFMO. The light blue part represents the part of cathode capacity that is added with the pre-sodiation. The capacity is normalized by dividing for the specific capacity with pre-sodiation of the cathode material........ 75

Figure 6.6 – Electrode potentials of cathode and anode and resulting cell voltages of the materials analyzed in the pre-sodiation for the first cycle sodium loss compensation study. a) NFPO; b) NNMMTO; c) NMFCN. The light blue part represents the part of cathode capacity that is added with the pre-sodiation. The capacity is normalized by dividing for the specific capacity with pre-sodiation of the cathode material. 78

Figure 6.7 – Representation of the organic materials included in the cost and performance analysis; categorized as lithium-deficient cathodes (red), lithium-sufficient cathodes (blue), and organic anode (green). 81

Figure 6.8 – Comparison of the a) pack volumetric energy density, b) pack gravimetric energy density and pack cost per kWh in the c) low lithium cost scenario and d) high lithium cost scenario for the lithium-deficient organic cathode materials (in shades of blue) and inorganic cathodes (in red), both with lithium metal anode. 85

Figure 6.9 – Comparison of the a) pack volumetric energy density, b) pack gravimetric energy density and pack cost per kWh in the c) low lithium cost scenario and d) high lithium cost scenario for the lithium-sufficient organic cathode materials (in shades of blue, yellow and green) and inorganic cathodes (in red), with different anode materials. 87

Figure 6.10 – The influence of the carbon content in the electrode(s) on the battery pack properties for a) a P5Q/Li metal battery, b) a Li_2-BQDO/Graphite battery, c) a Li_2-BQDO/LiTPT battery, and d) a Li_2-BQDO/$PTCLi_4$ battery. The percentage variations of the battery pack properties refer to the case with the lowest amount of carbon. For the Li_2-BQDO/LiTPT battery and the Li_2-BQDO/$PTCLi_4$ battery, the carbon content is also increased in the negative electrode. 89

Figure 6.11 – The influence of the active material mass loading of the cathode on the battery pack properties for a) a P5Q/Li metal battery, b) a Li_2-BQDO/Graphite battery, c) a Li_2-BQDO/LiTPT battery, and d) a Li_2-BQDO/$PTCLi_4$ battery. The percentage variations of the battery pack properties refer to the case with the highest active material mass loading........ 91

Figure 6.12 – The influence of the cathode density on the battery pack properties for a) a P5Q/Li metal battery, b) a Li_2-BQDO/Graphite battery, c) a Li_2-BQDO/LiTPT battery, and d) a Li_2-BQDO/$PTCLi_4$

battery. The percentage variations of the battery pack properties refer to the case with the highest cathode density...93

Figure 6.13 – Schematic depiction of the charge and discharge processes of a lithium-ion battery (top) and a dual-ion battery (bottom), with the expected trend of the electrolyte salt concentration. 97

Figure 6.14 – Representation of the model domain 98

Figure 6.15 – a) Voltage vs. time during a simulated galvanostatic charge and discharge cycle at 10C of the PTMA/Li metal cell, b) Comparison between the voltage vs. specific capacity characteristics of the model results (solid line) and the experimental data (dotted line) at 0.2C and 5C, c) Selected electrolyte salt concentration profiles at different time steps during the simulated 10C charge of the of the PTMA/Li metal cell, d) Selected electrolyte salt concentration profiles at different time steps during the simulated 10C discharge of the of the PTMA/Li metal cell 103

Figure 6.16 – a) Comparison between the experimental (dotted) and the modelled (line) impedance spectrum at 53.4% SOC, b) Comparison between the experimental (grey scale, dotted) and the modelled (blue scale, line) impedance spectra at all the measured SOCs 105

Figure 6.17 – a) Comparison between the experimental (dotted) and the modelled (line) impedance spectrum at 53.4% SOC, b) Comparison between the experimental (grey scale, dotted) and the modelled (blue scale, line) impedance spectra at all the measured SOCs 107

Figure 6.18 – a) TGA results of the PTMA-MW15, PTMA-GN15, and PTMA-SP15 samples, b) Detail on the oxidation part of the TGA results on the three samples, with the respective DTG curves; c) Specific capacity and coulombic efficiency vs. cycle number for the rate performance test of the three samples in coin cells with a lithium metal anode at 20°C; d) Related voltage vs. specific capacity charge and discharge curves of the three samples at 1C (cycle n° 50 of **Figure 6.18.c**)...............................111

Figure 6.19 – a) TGA results of the PTMA-MW15, PTMA-MW10, PTMA-MW5, and PTMA-MW2.5 samples, b) Detail on the oxidation part of the TGA results on the four samples, with the respective DTG curves; c) Specific capacity and coulombic efficiency vs. cycle number for the rate performance test of the four samples in coin cells with a lithium metal anode at 20°C; d) Related voltage vs. specific capacity charge and discharge curves of the four samples at 1C (cycle n° 50 of **Figure 6.19.c**).......115

Figure 6.20 - a) Specific capacity and coulombic efficiency vs. cycle number for the rate performance test of the PTMA-MW15 high mass loading electrodes in coin cells with a lithium metal anode at 20°C; b) Related voltage vs. specific capacity charge and discharge curves of the two samples at several current rates...117

Figure 6.21 – Study of the trend of the parameter K with a) the separator thickness and porosity, with a lean electrolyte and a low mass loading electrode, b) the separator thickness and porosity, with a lean electrolyte and a high mass loading electrode, c) the cathode thickness and porosity, with a concentrated electrolyte and a thin commercial separator, and d) the cathode thickness and porosity, with a superconcentrated electrolyte and a thin commercial separator. The red dots with the numbers inside indicate the cases that are simulated with the physical model.. 120

Figure 6.22 - Voltage and electrolyte salt concentration vs. specific capacity for the four simulated cases during a 0.1C charge. a) Case 1, b) Case 2, c) Case 3, d) Case 4 122

Figure 6.23 – a) Comparison of the gravimetric energy density, volumetric energy density, and cost per unit energy at the cell level of the simulated battery packs, b) Cost breakdown of the materials required for the cell assembly in the simulated battery packs.. 124

Figure A1.1 – Explanation of the modification made on the anode voltage profile for the implementation of the N/P ratio: a) case with N/P ratio equal to 1, b) case with N/P ratio equal to 1.1. The grey part of the chart and the dashed part of the line is not considered in the final anode voltage. 136

Figure A1.2 – Explanation of the modification made on the cathode voltage profile for the implementation of the initial coulombic efficiency (ICE): a) case without ICE implementation, b) case with ICE implementation. The grey part of the chart and the dashed part of the line is not considered in the final cathode voltage.. 136

Figure A1.3 – Comparison of the volumetric energy density of the sodium-ion battery packs simulated with the cathode materials taken from literature and a hard carbon anode. The best and the worst values of volumetric energy density are reported, considering all the simulated lower voltage cut-offs and types of pre-sodiation. In red, two examples of lithium-ion battery packs are shown as comparison......... 137

Figure A1.4 – Comparison of the gravimetric energy density of the sodium-ion battery packs simulated with the cathode materials taken from literature and a hard carbon anode. The best and the worst values of gravimetric energy density are reported, considering all the simulated lower voltage cut-offs and types of pre-sodiation. In red, two examples of lithium-ion battery packs are shown as comparison. 138

Figure A1.5 – Comparison of the gravimetric energy density of the sodium-ion battery packs simulated with the cathode materials taken from literature and a hard carbon anode. The best and the worst values of gravimetric energy density are reported, considering all the simulated lower voltage cut-offs and types of pre-sodiation. In red, two examples of lithium-ion battery packs are shown as comparison. 139

Figure A1.6 – Electrode potentials and voltage profile of a $NaFe(PO_4)$/hard carbon sodium-ion battery a) at the initial lower cut-off voltage and b) with the increase of the lower cut-off voltage to the 55% of the maximum battery voltage. The specific capacity refers to the cathode mass. 140

Figure A1.7 – Electrode potentials and voltage profile of a $Na[Ni_{0.3}Fe_{0.4}Mn_{0.3}]O_2$/hard carbon sodium-ion battery a) at the initial lower cut-off voltage and b) with the increase of the lower cut-off voltage to the 55% of the maximum battery voltage. The specific capacity refers to the cathode mass. 140

Figure A1.8 – Electrode potentials and voltage profile of a $Na_3V_2(PO_4)F_3$/hard carbon sodium-ion battery a) at the initial lower cut-off voltage and b) with the increase of the lower cut-off voltage to the 55% of the maximum battery voltage. The specific capacity refers to the cathode mass. 140

Figure A1.9 – Electrode potentials and voltage profile of a $Na_3V_2(PO_4)FO_2$/hard carbon sodium-ion battery (without pre-sodiation for the addition of sodium to the non-stoichiometric cathode) a) at the initial lower cut-off voltage and b) with the increase of the lower cut-off voltage to the 55% of the maximum battery voltage. The specific capacity refers to the cathode mass. 141

Figure A1.10 – Electrode potentials and voltage profile of a $Na_3V_2(PO_4)FO_2$/hard carbon sodium-ion battery (with pre-sodiation for the addition of sodium to the non-stoichiometric cathode) a) at the initial lower cut-off voltage and b) with the increase of the lower cut-off voltage to the 55% of the maximum battery voltage. The specific capacity refers to the cathode mass. 141

Figure A1.11 – Electrode potentials and voltage profile of a $Na_{0.6}[Ni_{0.22}Al_{0.11}Mn_{0.66}]O_2$/hard carbon sodium-ion battery (without pre-sodiation for the addition of sodium to the non-stoichiometric cathode) a) at the initial lower cut-off voltage and b) with the increase of the lower cut-off voltage to the 55% of the maximum battery voltage. This specific capacity refers to the cathode mass..............................141

Figure A1.12 – Electrode potentials and voltage profile of a $Na_{0.6}[Ni_{0.22}Al_{0.11}Mn_{0.66}]O_2$/hard carbon sodium-ion battery (with pre-sodiation for the addition of sodium to the non-stoichiometric cathode) a) at the initial lower cut-off voltage and b) with the increase of the lower cut-off voltage to the 55% of the maximum battery voltage. The specific capacity refers to the cathode mass. 142

Figure A1.13 – Electrode potentials and voltage profile of a $Na_{0.6}[Ni_{0.22}Fe_{0.11}Mn_{0.66}]O_2$/hard carbon sodium-ion battery (without pre-sodiation for the addition of sodium to the non-stoichiometric cathode) a) at the initial lower cut-off voltage and b) with the increase of the lower cut-off voltage to the 55% of the maximum battery voltage. The specific capacity refers to the cathode mass. 142

Figure A1.14 – Electrode potentials and voltage profile of a $Na_{0.6}[Ni_{0.22}Fe_{0.11}Mn_{0.66}]O_2$/hard carbon sodium-ion battery (with pre-sodiation for the addition of sodium to the non-stoichiometric cathode) a) at the initial lower cut-off voltage and b) with the increase of the lower cut-off voltage to the 55% of the maximum battery voltage. The specific capacity refers to the cathode mass. 142

Figure A1.15 – Electrode potentials and voltage profile of a $Na_3Fe_2(PO_4)_3$/hard carbon sodium-ion battery (without pre-sodiation for the compensation of the first cycle sodium loss) a) at the initial lower cut-off voltage and b) with the increase of the lower cut-off voltage to the 55% of the maximum battery voltage. The specific capacity refers to the cathode mass. 143

Figure A1.16 – Electrode potentials and voltage profile of a $Na_3Fe_2(PO_4)_3$/hard carbon sodium-ion battery (with pre-sodiation for the compensation of the first cycle sodium loss) a) at the initial lower cut-off voltage and b) with the increase of the lower cut-off voltage to the 55% of the maximum battery voltage. The specific capacity refers to the cathode mass. 143

Figure A1.17 – Electrode potentials and voltage profile of a $Na_{0.95}[Ni_{0.32}Mn_{0.32}Mg_{0.16}Ti_{0.21}]O_2$/hard carbon sodium-ion battery (without pre-sodiation for the compensation of the first cycle sodium loss) a) at the initial lower cut-off voltage and b) with the increase of the lower cut-off voltage to the 55% of the maximum battery voltage. The specific capacity refers to the cathode mass. 143

Figure A1.18 – Electrode potentials and voltage profile of a $Na_{0.95}[Ni_{0.32}Mn_{0.32}Mg_{0.16}Ti_{0.21}]O_2$/hard carbon sodium-ion battery (with pre-sodiation for the compensation of the first cycle sodium loss) a) at the initial lower cut-off voltage and b) with the increase of the lower cut-off voltage to the 55% of the maximum battery voltage. the specific capacity refers to the cathode mass. 144

Figure A1.19 – Electrode potentials and voltage profile of a $Na_2Mn[Fe(CN)_6]O_2$/hard carbon sodium-ion battery (without pre-sodiation for the compensation of the first cycle sodium loss) a) at the initial lower cut-off voltage and b) with the increase of the lower cut-off voltage to the 55% of the maximum battery voltage. The specific capacity refers to the cathode mass. 144

Figure A1.20 – Electrode potentials and voltage profile of a $Na_2Mn[Fe(CN)_6]O_2$/hard carbon sodium-ion battery (with pre-sodiation for the compensation of the first cycle sodium loss) a) at the initial lower cut-off voltage and b) with the increase of the lower cut-off voltage to the 55% of the maximum battery voltage. The specific capacity refers to the cathode mass. 144

Figure A3.1 – Open circuit potential vs. state of charge characteristic of the PTMA-based cathode used as an input for the model. The curve is derived from a 0.1C discharge curve at 20°C obtained with the same experimental setup described in the main text 147

Figure A3.2 – Scanning electron microscopy image of a) the PTMA/MWCNT active material powder and b) a PTMA/MWCNT-based electrode analogue to the one used in the electrochemical tests described in Section 5.1.2 148

Figure A4.1 – Results of the resistance measurements on the pellets of the samples a) PTMA-GN15, b) PTMA-SP15, c) PTMA-MW15, d) PTMA-MW10, e) PTMA-MW5..150

Figure A4.2 – TGA curves during oxidation of the polymer-carbon mixtures together with the DTG curve of the oxidation of only the carbon additive. a) PTMA-SP15, b) PTMA-GN15, c) PTMA-MW15, d) PTMA-MW10, e) PTMA-MW5, f) PTMA-MW2.5 151

Figure A4.3 - SEM images of the PTMA-SP15 sample a) as powder and b) the related electrode surface 152

Figure A4.4 – SEM images of the PTMA-GN15 sample a) as powder and b) the related electrode surface..153

Figure A4.5 – SEM images of the PTMA-MW15 sample a) as powder and b) the related electrode surface..154

Figure A4.6 – SEM images of the PTMA-MW10 sample a) as powder and b) the related electrode surface..155

Figure A4.7 – SEM images of the PTMA-MW5 sample a) as powder and b) the related electrode surface..156

Figure A4.8 – SEM images of the PTMA-MW2.5 sample a) as powder and b) the related electrode surface..157

Figure A4.9 – a) Voltage vs. specific capacity charge and discharge curves of PTMA-MW15, PTMA-GN15, and PTMA-SP15 at 5C (cycle n° 27 of Figure 1.c of the main text), b) Voltage vs. specific capacity charge and discharge curves of PTMA-MW15, PTMA-MW10, PTMA-MW5, and PTMA-MW2.5 at 5C (cycle n° 27 of **Figure 2.c** of the main text)...159

Figure A4.10 – a) Specific capacity and coulombic efficiency vs. cycle number for the rate performance test of the PTMA-MW15 sample in two coin cells with a sodium metal anode at 20°C (zoom on rate performance) b) Voltage vs. specific capacity charge and discharge curves of PTMA-MW15, 1C (cycle n° 50 of **Figure A4.10.a**), c) Specific capacity and coulombic efficiency vs. cycle number for the rate performance test of the PTMA-MW15 sample in two coin cells with a sodium metal anode at 20°C (whole test). The voltage step during discharge in the PTMA-Na cell, not present in the lithium-based cells, may be due to an overpotential caused by the interaction between the sodium metal anode and the EC:PC solvent [336]..159

Figure A4.11 – Cathode impedance spectra at different SOCs (indicated by the percentage next to the spectra) of a) PTMA-MW15, b) PTMA-MW10, c) PTMA-MW5, and d) PTMA-MW2.5 in a three-electrode configuration........160

Figure A4.12 – Cathode voltage vs. lithium metal reference electrode (solid line) and vs. lithium metal anode (dashed line) in a 5C galvanostatic discharge using the three-electrode EL-Cell setup and a 3.88 mg·cm^{-2} PTMA-MW15-based electrode. Note the overpotential caused by the lithium metal anode. 160

Figure A4.13 - Specific capacity and coulombic efficiency vs. cycle number for galvanostatic charge/discharge test of the PTMA-MW15 sample in coin cell with lithium metal anode at 20°C with a) 1M LiPF6 in EC:DMC 1:1 (Cell 1: 8.65 mg·cm-2, Cell 2: 8.34 mg·cm^{-2}) and b) 1M LiFSI in EC:DMC 1:1 (Cell 1: 8.56 mg·cm^{-2}, Cell 2: 8.18 mg·cm^{-2})........161

Figure A4.14 – Voltage vs. specific capacity of PTMA-MW15 cathodes in coin cell with lithium metal anode at 20°C, using 10 µm thick polyolefin separator with a minimal quantity of electrolyte (Low mass loading: 4.78 mg·cm^{-2}, High mass loading: 9.15 mg·cm^{-2})........161

Figure A4.15 - Model domain in the simulated cases presented in the main text: a) Case 1, b) Case 2, c) Case 3 and d) Case 4........163

References

1. IPCC, Synthesis Report of the IPCC Sixth Assessment Report (AR6) - Longer Report. IPCC, Cambridge (2023)

2. IEA, Global energy-related CO_2 emissions by sector. IEA, Paris (2023). Retrieved from https://www.iea.org/data-and-statistics/charts/global-energy-related-co2-emissions-by-sector.

3. IEA, Global EV Outlook 2023. IEA, Paris (2023). Retrieved from: https://www.iea.org/reports/global-ev-outlook-2023/policy-developments.

4. Knobloch, F. *et al.* Net emission reductions from electric cars and heat pumps in 59 world regions over time. *Nat. Sustain.* **3**, 437–447 (2020).

5. Nitta, N., Wu, F., Lee, J. T. & Yushin, G. Li-ion battery materials: present and future. *Mater. Today* **18**, 252–264 (2015).

6. Manthiram, A. A reflection on lithium-ion battery cathode chemistry. *Nat. Commun.* **11**, 1550 (2020).

7. Liu, J. *et al*. The TWh challenge: Next generation batteries for energy storage and electric vehicles. *Next Energy* **1**, 100015 (2023).

8. IEA, Grid-Scale Storage. IEA, Paris (2022). Retrieved from: https://www.iea.org/reports/grid-scale-storage.

9. OSTI, Energy storage technology and cost characterization report. OSTI, Oak Ridge (2019). Retrieved from: https://energystorage.pnnl.gov/pdf/PNNL-28866.pdf

10. Passerini, S. (Europe Section Alessandro Volta Award) From the oil barrel to reactive metals: An approach to the energy transition. *Meet. Abstr.* **MA2022-02**, 2411–2411 (2022).

11. IEA, Global EV Outlook 2023. IEA, Paris (2023). Retrieved from: https://www.iea.org/reports/global-ev-outlook-2023.

12. Munoz, J. F. Tesla Model Y was the world's best-selling car in Q1 2023. Motor1.com (2023). Retrieved from: https://www.motor1.com/news/669135/tesla-model-y-worlds-best-selling-car-q1-2023/

13. Vaalma, C., Buchholz, D., Weil, M. & Passerini, S. A cost and resource analysis of sodium-ion batteries. *Nat. Rev. Mater.* **3**, 18013 (2018).

14. Greim, P., Solomon, A. A. & Breyer, C. Assessment of lithium criticality in the global energy transition and addressing policy gaps in transportation. *Nat. Commun.* **11**, 4570 (2020).

15. Greenwood, M., Wentker, M. & Leker, J. A region-specific raw material and lithium-ion battery criticality methodology with an assessment of NMC cathode technology. *Appl. Energy* **302**, 117512 (2021).

16. Yang, Y. *et al.* On the sustainability of lithium ion battery industry – A review and perspective. *Energy Storage Mater.* **36**, 186–212 (2021).

17. Huang, Y.H. et al. Advancing the Sustainability of Batteries, A Tongji University/Nature Sustainability Expert Panel Report, Shanghai and London, Tongji University and Springer Nature, (2022)

18. Choi, J. W. & Aurbach, D. Promise and reality of post-lithium-ion batteries with high energy densities. *Nat. Rev. Mater.* **1**, 1–16 (2016).

19. Walter, M., Kovalenko, M. V. & Kravchyk, K. V. Challenges and benefits of post-lithium-ion batteries. *New J Chem* **44**, 1677–1683 (2020).

20. Duffner, F. *et al.* Post-lithium-ion battery cell production and its compatibility with lithium-ion cell production infrastructure. *Nature Energy* **6**, 123–134 (2021).

21. Passerini, S., Bresser, D., Moretti, A. & Varzi, A. *Batteries: Present and future energy storage challenges*. (Wiley-VCH, 2020).

22. Rabissi, C., Innocenti, A., Sordi, G. & Casalegno, A. A Comprehensive Physical-Based Sensitivity Analysis of the Electrochemical Impedance Response of Lithium-Ion Batteries. *Energy Technology* 2000986 (2021).

23. Gao, J., Shi, S. Q. & Li, H. Brief overview of electrochemical potential in lithium ion batteries. *Chin. Physics B* (2015).

24. Winter, M., Barnett, B. & Xu, K. Before Li Ion Batteries. *Chem. Rev.* **118**, 11433–11456 (2018).

25. Ziegler, M. S. & Trancik, J. E. Re-examining rates of lithium-ion battery technology improvement and cost decline. *Energy Environ. Sci.* **14**, 1635–1651 (2021).

26. FOTW #1272, January 9, 2023: Electric vehicle battery pack costs in 2022 are nearly 90% lower than in 2008, according to DOE estimates. Retrieved from: *Energy.gov* https://www.energy.gov/eere/vehicles/articles/fotw-1272-january-9-2023-electric-vehicle-battery-pack-costs-2022-are-nearly.

27. Kosfeld, M., Westphal, B. & Kwade, A. Moisture behavior of lithium-ion battery components along the production process. *J. Energy Storage* **57**, 106174 (2023).

28. Schuer, A. R. *et al.* Diagnosis tools for humidity-born surface contaminants on $Li[Ni_{0.8}Mn_{0.1}Co_{0.1}]O_2$ cathode materials for lithium batteries. *J. Power Sources* **525**, 231111 (2022).

29. Winter, M., Moeller, K.-C. & Besenhard, J. O. Carbonaceous and Graphitic Anodes. in *Lithium Batteries* 145–194 (Springer US, 2009).

30. Mizushima, K., Jones, P. C., Wiseman, P. J. & Goodenough, J. B. Li_xCoO_2 (0<x<-1): A new cathode material for batteries of high energy density. *Materials Research Bulletin* vol. 15 783–789 (1980).

31. Tarascon, J. M. *et al.* Synthesis conditions and oxygen stoichiometry effects on Li insertion into the spinel $LiMn_2O_4$. *J. Electrochem. Soc.* **141**, 1421–1431 (1994).

32. Ma, Z. F., Yang, X. Q., Liao, X. Z., Sun, X. & McBreen, J. Electrochemical evaluation of composite cathodes base on blends of $LiMn_2O_4$ and $LiNi_{0.8}Co_{0.2}O_2$. *Electrochem. Commun.* **3**, 425–428 (2001).

33. Zhong, Q., Bonakdarpour, A., Zhang, M., Gao, Y. & Dahn, J. R. Synthesis and Electrochemistry of $LiNi_xMn_{2-x}O_4$. *J. Electrochem. Soc.* **144**, 205–213 (1997).

34. Kuenzel, M. *et al.* Complementary strategies toward the aqueous processing of high-voltage $LiNi_{0.5}Mn_{1.5}O_4$ lithium-ion cathodes. *ChemSusChem* **11**, 562–573 (2018).

35. Li, J. & Ma, Z.-F. Past and present of $LiFePO_4$: From fundamental research to industrial applications. *Chem* **5**, 3–6 (2019).

36. Frith, J. T., Lacey, M. J. & Ulissi, U. A non-academic perspective on the future of lithium-based batteries. *Nat. Commun.* **14**, 420 (2023).

37. Islam, M. S. & Fisher, C. A. J. Lithium and sodium battery cathode materials: computational insights into voltage, diffusion and nanostructural properties. *Chem. Soc. Rev.* **43**, 185–204 (2014).

38. Xu, W. *et al.* Lithium metal anodes for rechargeable batteries. *Energy Environ. Sci.* **7**, 513–537 (2014).

39. Wang, Q. *et al.* Confronting the challenges in lithium anodes for lithium metal batteries. *Adv. Sci. (Weinh.)* **8**, e2101111 (2021).

40. Asenbauer, J. *et al.* The success story of graphite as a lithium-ion anode material – fundamentals, remaining challenges, and recent developments including silicon (oxide) composites. *Sustain. Energy Fuels* **4**, 5387–5416 (2020).

41. Mundszinger, M. *et al.* Morphology and texture of spheroidized natural and synthetic graphites. *Carbon N. Y.* **111**, 764–773 (2017).

42. Dahn, J. R. Phase diagram of Li_xC_6. *Phys. Rev. B Condens. Matter* **44**, 9170–9177 (1991).

43. Winter, M., Besenhard, J. O., Spahr, M. E. & Novak, P. Insertion electrode materials for rechargeable lithium batteries. *Adv. Mater.* **10**, 725–763 (1998).

44. Zuo, X., Zhu, J., Müller-Buschbaum, P. & Cheng, Y.-J. Silicon based lithium-ion battery anodes: A chronicle perspective review. *Nano Energy* **31**, 113–143 (2017).

45. Fang, S., Bresser, D. & Passerini, S. Transition metal oxide anodes for electrochemical energy storage in lithium- and sodium-ion batteries. *Adv. Energy Mater.* **10**, 1902485 (2020).

46. C P, S., Bibin, J. & C, G. Lithium titanate as anode material for lithium-ion cells: a review. *Ionics (Kiel)* **20**, 601–620 (2014).

47. Xu, K. Electrolytes and interphases in Li-ion batteries and beyond. *Chem. Rev.* **114**, 11503–11618 (2014).

48. Kalhoff, J., Eshetu, G. G., Bresser, D. & Passerini, S. Safer Electrolytes for Lithium-Ion Batteries: State of the Art and Perspectives. *ChemSusChem* **8**, 2154–2175 (2015).

49. Tan, S., Ji, Y. J., Zhang, Z. R. & Yang, Y. Recent progress in research on high-voltage electrolytes for lithium-ion batteries. *Chemphyschem* **15**, 1956–1969 (2014).

50. Zhang, S. S. A review on the separators of liquid electrolyte Li-ion batteries. *J. Power Sources* **164**, 351–364 (2007).

51. Lee, H., Yanilmaz, M., Toprakci, O., Fu, K. & Zhang, X. A review of recent developments in membrane separators for rechargeable lithium-ion batteries. *Energy Environ. Sci.* **7**, 3857–3886 (2014).

52. Schmuch, R., Wagner, R., Hörpel, G., Placke, T. & Winter, M. Performance and cost of materials for lithium-based rechargeable automotive batteries. *Nature Energy* **3**, 267–278 (2018).

53. Janek, J. & Zeier, W. G. A solid future for battery development. *Nature Energy* **1**, 16141 (2016).

54. Keller, M., Varzi, A. & Passerini, S. Hybrid electrolytes for lithium metal batteries. *J. Power Sources* **392**, 206–225 (2018).

55. Ma, M. *et al.* A review of all-solid-state electrolytes for lithium batteries: high-voltage cathode materials, solid-state electrolytes and electrode–electrolyte interfaces. *Mater. Chem. Front.* **7**, 1268–1297 (2023).

56. Zuo, W. *et al.* Layered oxide cathodes for sodium-ion batteries: Storage mechanism, electrochemistry, and techno-economics. *Acc. Chem. Res.* **56**, 284–296 (2023).

57. Tian, Y. *et al.* Promises and Challenges of Next-Generation “Beyond Li-ion” Batteries for Electric Vehicles and Grid Decarbonization. *Chem. Rev.* **121**, 1623–1669 (2021).

58. Roberts, S. & Kendrick, E. The re-emergence of sodium ion batteries: testing, processing, and manufacturability. *Nanotechnol. Sci. Appl.* **11**, 23–33 (2018).

59. Tapia-Ruiz, N. *et al.* 2021 roadmap for sodium-ion batteries. *J. Phys. Energy* **3**, 031503 (2021).

60. Manthiram, A., Fu, Y., Chung, S.-H., Zu, C. & Su, Y.-S. Rechargeable Lithium–Sulfur Batteries. *Chem. Rev.* **114**, 11751–11787 (2014).

61. Zhu, K. *et al.* How Far Away Are Lithium-Sulfur Batteries From Commercialization? *Frontiers in Energy Research* **7**, (2019).

62. Maroni, F., Dongmo, S., Gauckler, C., Marinaro, M. & Wohlfahrt-Mehrens, M. Through the maze of multivalent-ion batteries: A critical review on the status of the research on cathode materials for Mg^{2+} and Ca^{2+} ions insertion. *Batter. supercaps* **4**, 1221–1251 (2021).

63. Elia, G. A. *et al.* An overview and prospective on Al and Al-ion battery technologies. *J. Power Sources* **481**, 228870 (2021).

64. Zhang, L., Wang, H., Zhang, X. & Tang, Y. A review of emerging dual-ion batteries: Fundamentals and recent advances. *Adv. Funct. Mater.* **31**, 2010958 (2021).

65. Zhao, X., Zhao-Karger, Z., Fichtner, M. & Shen, X. Halide-based materials and chemistry for rechargeable batteries. *Angew. Chem. Int. Ed Engl.* **59**, 5902–5949 (2020).

66. Liang, Y. & Yao, Y. Positioning Organic Electrode Materials in the Battery Landscape. *Joule* **2**, 1690–1706 (2018).

67. Lu, Y. & Chen, J. Prospects of organic electrode materials for practical lithium batteries. *Nature Reviews Chemistry* **4**, 127–142 (2020).

68. Esser, B. *et al.* A perspective on organic electrode materials and technologies for next generation batteries. *J. Power Sources* **482**, 228814 (2021).

69. Rudola, A. *et al.* Commercialisation of high energy density sodium-ion batteries: Faradion's journey and outlook. *J. Mater. Chem. A Mater. Energy Sustain.* **9**, 8279–8302 (2021).

70. CATL, "CATL Unveils Its Latest Breakthrough Technology by ReleasingIts First Generation of Sodium-ion Batteries," Retrieved from: https://www.catl.com/en/news/665.html (2019).

71. Sapunkov, O., Pande, V., Khetan, A., Choomwattana, C. & Viswanathan, V. Quantifying the promise of 'beyond' Li–ion batteries. *Transl. Mater. Res.* **2**, 045002 (2015).

72. Grande, L. *et al*. The lithium/air battery: still an emerging system or a practical reality? *Adv. Mater.* **27**, 784–800 (2015).

73. Raccichini, R., Varzi, A., Wei, D. & Passerini, S. Critical insight into the relentless progression toward graphene and graphene-containing materials for lithium-ion battery anodes. *Adv. Mater.* **29**, (2017).

74. Parker, J. F., Ko, J. S., Rolison, D. R. & Long, J. W. Translating materials-level performance into device-relevant metrics for zinc-based batteries. *Joule* **2**, 2519–2527 (2018).

75. Nelson, P. A., Ahmed, S., Gallagher, K. G. & Dees, D. W. *Modeling the performance and cost of lithium-ion batteries for electric-drive vehicles, third edition*. Available at: https://www.osti.gov/biblio/1503280 (2019).

76. Wentker, M., Greenwood, M. & Leker, J. A Bottom-Up Approach to Lithium-Ion Battery Cost Modeling with a Focus on Cathode Active Materials. *Energies* **12**, 504 (2019).

77. Li, L. *et al.* Recent progress on sodium ion batteries: potential high-performance anodes. *Energy Environ. Sci.* **11**, 2310-2340 (2018).

78. Abraham, K. M. How comparable are sodium-ion batteries to lithium-ion counterparts? *ACS Energy Lett.* **5**, 3544–3547 (2020).

79. Broux, T. *et al.* High rate performance for carbon-coated $Na_3V_2(PO_4)_2F_3$ in Na-ion batteries. *Small Methods* **3**, 1800215 (2019).

80. Bauer, A. *et al.* The scale-up and commercialization of nonaqueous Na-ion battery technologies. *Adv. Energy Mater.* **8**, 1702869 (2018).

81. Rong, X. *et al.* Robust 3.7 V-$Na_{2/3}[Cu_{1/3}Mn_{2/3}]O_2$ cathode for Na-ion batteries. arXiv, Preprint at: doi:10.48550/ARXIV.2303.15713. (2023)

82. Morales, D. *et al.* Transport studies of $NaPF_6$ carbonate solvents-based sodium ion electrolytes. *Electrochim. Acta* **377**, 138062 (2021).

83. Gonzalo, E., Zarrabeitia, M., Drewett, N. E., López del Amo, J. M. & Rojo, T. Sodium manganese-rich layered oxides: Potential candidates as positive electrode for Sodium-ion batteries. *Energy Storage Mater.* **34**, 682–707 (2021).

84. Moriwake, H., Kuwabara, A., Fisher, C. A. J. & Ikuhara, Y. Why is sodium-intercalated graphite unstable? *RSC Adv.* **7**, 36550–36554 (2017).

85. Jache, B., Binder, J. O., Abe, T. & Adelhelm, P. A comparative study on the impact of different glymes and their derivatives as electrolyte solvents for graphite co-intercalation electrodes in lithium-ion and sodium-ion batteries. *Phys. Chem. Chem. Phys.* **18**, 14299–14316 (2016).

86. Li, X. *et al.* Review on comprehending and enhancing the initial Coulombic efficiency of anode materials in lithium-ion/sodium-ion batteries. *Nano Energy* **77**, 105143 (2020).

87. Shellikeri, A. *et al.* Investigation of Pre-lithiation in Graphite and Hard-Carbon Anodes Using Different Lithium Source Structures. *J. Electrochem. Soc.* **164**, A3914 (2017).

88. Muench, S. *et al.* Polymer-Based Organic Batteries. *Chem. Rev.* **116**, 9438–9484 (2016).

89. Kim, J. *et al.* Organic batteries for a greener rechargeable world. *Nat. Rev. Mater.* **8**, 54–70 (2022).

90. Miller, J. S. Conducting polymers: materials of commerce (Part 1). *Adv. Mater.* **5**, 587–589 (1993).

91. Miller, J. S. Conducting polymers: materials of commerce (Part 2). *Adv. Mater.* **5**, 671–676 (1993).

92. Nakahara, K. *et al.* Rechargeable batteries with organic radical cathodes. *Chem. Phys. Lett.* **359**, 351–354 (2002).

93. Chen, H. & Tarascon, J.-M. From Biomass to a Renewable $Li_xC_6O_6$ Organic Electrode for Sustainable Li-Ion Batteries. *ChemSusChem* **1**, 348–355 (2008).

94. Armand, M. *et al.* Conjugated dicarboxylate anodes for Li-ion batteries. *Nat. Mater.* **8**, 120–125 (2009).

95. Goujon, N., Casado, N., Patil, N., Marcilla, R. & Mecerreyes, D. Organic batteries based on just redox polymers. *Prog. Polym. Sci.* **122**, 101449 (2021).

96. Kye, H., Kang, Y., Jang, D., Kwon, J. E. & Kim, B.-G. P-type redox-active organic electrode materials for next-generation rechargeable batteries. *Adv. Energy Sustain. Res.* **3**, 2200030 (2022).

97. Placke, T. *et al.* Perspective on performance, cost, and technical challenges for practical dual-ion batteries. *Joule* **2**, 2528–2550 (2018).

98. Poizot, P. *et al.* Opportunities and challenges for organic electrodes in electrochemical energy storage. *Chem. Rev.* **120**, 6490–6557 (2020).

99. Han, C. *et al.* Organic quinones towards advanced electrochemical energy storage: recent advances and challenges. *J. Mater. Chem. A Mater. Energy Sustain.* **7**, 23378–23415 (2019).

100. Yang, H. *et al.* Molecular engineering of carbonyl organic electrodes for rechargeable metal-ion batteries: fundamentals, recent advances, and challenges. *Energy Environ. Sci.* **14**, 4228–4267 (2021).

101. Zhang, Z. *et al.* Oxocarbons electrode materials for alkali ion batteries: Challenges, strategies and development. *Batter. supercaps* **4**, 1791 (2021).

102. Esser, B. Redox Polymers as Electrode-Active Materials for Batteries. *Organic Materials* **01**, 063–070 (2019).

103. Dai, G., Wu, T., Chen, H. & Zhao, Y. Quaternary nitrogen redox centers for battery materials. *Curr. Opin. Electrochem.* **29**, 100745 (2021).

104. Banerjee, A., Khossossi, N., Luo, W. & Ahuja, R. Promise and reality of organic electrodes from materials design and charge storage perspective. *J. Mater. Chem. A Mater. Energy Sustain.* **10**, 15215–15234 (2022).

105. Wang, D.-Y., Guo, W. & Fu, Y. Organosulfides: An Emerging Class of Cathode Materials for Rechargeable Lithium Batteries. *Acc. Chem. Res.* **52**, 2290–2300 (2019).

106. Shadike, Z. *et al.* Review on organosulfur materials for rechargeable lithium batteries. *Mater Horiz* **8**, 471–500 (2021).

107. Zhang, B. *et al.* Isometric thionated naphthalene diimides as organic cathodes for high capacity lithium batteries. *Chem. Mater.* **32**, 10575–10583 (2020).

108. Zhang, B. *et al.* Thionated benzo[c]thiophen-1(3H)-one as an organic cathode with high capacity for sulfur-rich all organic lithium-ion batteries. *J. Mater. Chem. A Mater. Energy Sustain.* **9**, 14444–14450 (2021).

109. Kahsay, B. A. *et al.* Investigating an all-organic battery using polyisothianaphthene as a redox-active bipolar electrode material. *J. Power Sources* **428**, 115–123 (2019).

110. Kim, J.-K. Single- and double-redox reaction of poly(2,2,6,6-tetramethylpiperidinyloxy-4-vinylmethacrylate)/ordered mesoporous carbon composite nitroxide radical polymer battery. *J. Power Sources* **477**, 228670 (2020).

111. Feng, X. *et al.* A bipolar organic molecule toward a universal pseudocapacitive cathode for stable dual ion charge storage. *Energy Storage Mater.* **42**, 454–463 (2021).

112. Song, Z. *et al.* A quinone-based oligomeric lithium salt for superior Li–organic batteries. *Energy Environ. Sci.* **7**, 4077–4086 (2014).

113. Liang, Y., Zhang, P. & Chen, J. Function-oriented design of conjugated carbonyl compound electrodes for high energy lithium batteries. *Chem. Sci.* **4**, 1330–1337 (2013).

114. Dieterich, V. *et al.* Estimating the cost of organic battery active materials: a case study on anthraquinone disulfonic acid. *Transl. Mater. Res.* **5**, 034001 (2018).

115. Gregory, T. D., Perry, M. L. & Albertus, P. Cost and price projections of synthetic active materials for redox flow batteries. *J. Power Sources* **499**, 229965 (2021).

116. Cui, H., Hu, P., Zhang, Y., Huang, W. & Li, A. Research progress of high-performance organic material pyrene-4,5,9,10-tetraone in secondary batteries. *ChemElectroChem* **8**, 352–359 (2021).

117. Yokoji, T., Matsubara, H. & Satoh, M. Rechargeable organic lithium-ion batteries using electron-deficient benzoquinones as positive-electrode materials with high discharge voltages. *J. Mater. Chem. A Mater. Energy Sustain.* **2**, 19347–19354 (2014).

118. Ravet, N., Michot, C. & Armand, M., Novel Cathode Materials Based on Organic Couples for Lithium Batteries. *Mat. Res. Soc. Symp. Proc. Vol.* **49**, 60 (1998).

119. Kim, H. *et al.* The Reaction Mechanism and Capacity Degradation Model in Lithium Insertion Organic Cathodes, $Li_2C_6O_6$, Using Combined Experimental and First Principle Studies. *J. Phys. Chem. Lett.* **5**, 3086–3092 (2014).

120. Shimizu, A. *et al.* Introduction of two lithiooxycarbonyl groups enhances cyclability of lithium batteries with organic cathode materials. *J. Power Sources* **260**, 211–217 (2014).

121. Sieuw, L. *et al.* A H-bond stabilized quinone electrode material for Li-organic batteries: the strength of weak bonds. *Chem. Sci.* **10**, 418–426 (2019).

122. Li, Z. *et al.* A small molecular symmetric all-organic lithium-ion battery. *Angew. Chem. Int. Ed Engl.* **61**, e202207221 (2022).

123. Zhang, M., Zhang, Y., Huang, W. & Zhang, Q. Recent Progress in Calix[n]quinone (n =4, 6) and Pillar[5]quinone Electrodes for Secondary Rechargeable Batteries. *Batter. supercaps* **3**, 476–487 (2020).

124. Huang, W. *et al.* Quasi-solid-state rechargeable lithium-ion batteries with a calix[4]quinone cathode and gel polymer electrolyte. *Angew. Chem. Int. Ed Engl.* **52**, 9162–9166 (2013).

125. Zhu, Z. *et al.* All-solid-state lithium organic battery with composite polymer electrolyte and pillar[5]quinone cathode. *J. Am. Chem. Soc.* **136**, 16461–16464 (2014).

126. Sun, H. *et al.* High performance lithium-ion batteries with pillar[5]quinone/ion-liquid system. *Org. Electron.* **83**, 105743 (2020).

127. Sun, H. *et al.* High−Performance organic lithium−ion battery with plastic crystal electrolyte. *Org. Electron.* **87**, 105966 (2020).

128. Luo, Z., Liu, L., Zhao, Q., Li, F. & Chen, J. An Insoluble Benzoquinone-Based Organic Cathode for Use in Rechargeable Lithium-Ion Batteries. *Angew. Chem. Int. Ed Engl.* **56**, 12561–12565 (2017).

129. Yao, M., Sano, H., Ando, H., Kiyobayashi, T. & Takeichi, N. Anthraquinone-based oligomer as a long cycle-life organic electrode material for use in rechargeable batteries. *ChemPhysChem* **20**, 967–971 (2019).

130. Delaporte, N., Lajoie, G., Collin-Martin, S. & Zaghib, K. Toward Low-Cost All-Organic and Biodegradable Li-Ion Batteries. *Sci. Rep.* **10**, 3812 (2020).

131. Chen, J. *et al.* Unraveling the role of aromatic ring size in tuning the electrochemical performance of small-molecule imide cathodes for lithium-ion batteries. *ACS Appl. Mater. Interfaces* **14**, 44330–44337 (2022).

132. Chen, Y. *et al.* Organic electrode for non-aqueous potassium-ion batteries. *Nano Energy* **18**, 205–211 (2015).

133. Rodríguez-Pérez, I. A. *et al.* Mg-ion battery electrode: An organic solid's herringbone structure squeezed upon mg-ion insertion. *J. Am. Chem. Soc.* **139**, 13031–13037 (2017).

134. Yao, M. *et al.* Indigo carmine: An organic crystal as a positive-electrode material for rechargeable sodium batteries. *Sci. Rep.* **4**, 1–6 (2014).

135. Zhang, H., Zhang, R., Ding, F., Shi, C. & Zhao, N. Hydrogen bonding regulation enables indanthrone as a stable and high-rate cathode for lithium-ion batteries. *Energy Storage Mater.* **51**, 172–180 (2022).

136. Shi, T. *et al.* Oxidized indanthrone as a cost-effective and high-performance organic cathode material for rechargeable lithium batteries. *Energy Storage Mater.* **50**, 265–273 (2022).

137. Reddy, A. L. M. *et al.* Lithium storage mechanisms in purpurin based organic lithium ion battery electrodes. *Sci. Rep.* **2**, 1–5 (2012).

138. Kato, M., Sano, H., Kiyobayashi, T., Takeichi, N. & Yao, M. Improvement of the battery performance of indigo, an organic electrode material, using PEDOT/PSS with d-sorbitol. *ACS Omega* **5**, 18565–18572 (2020).

139. Deunf, E., Poizot, P. & Lestriez, B. Aqueous Processing and Formulation of Indigo Carmine Positive Electrode for Lithium Organic Battery. *J. Electrochem. Soc.* **166**, A747 (2019).

140. Rohland, P. *et al.* Redox-active polymers: The magic key towards energy storage – a polymer design guideline progress in polymer science. *Prog. Polym. Sci.* **125**, 101474 (2022).

141. Song, Z. *et al.* Polyanthraquinone as a Reliable Organic Electrode for Stable and Fast Lithium Storage. *Angew. Chem. Int. Ed Engl.* **54**, 13947–13951 (2015).

142. Zhang, K. *et al.* The impact of the molecular weight on the electrochemical properties of poly(TEMPO methacrylate). *Polym. Chem.* **8**, 1815–1823 (2017).

143. Lu, Y., Zhang, Q., Li, L., Niu, Z. & Chen, J. Design Strategies toward Enhancing the Performance of Organic Electrode Materials in Metal-Ion Batteries. *Chem* **4**, 2786–2813 (2018).

144. Janoschka, T. *et al.* Reactive inkjet printing of cathodes for organic radical batteries. *Adv. Energy Mater.* **3**, 1025–1028 (2013).

145. Molina, A. *et al.* Electrode Engineering of Redox-Active Conjugated Microporous Polymers for Ultra-High Areal Capacity Organic Batteries. *ACS Energy Lett.* **5**, 2945–2953 (2020).

146. Molina, A. *et al.* New anthraquinone-based conjugated microporous polymer cathode with ultrahigh specific surface area for high-performance lithium-ion batteries. *Adv. Funct. Mater.* **30**, 1908074 (2020).

147. Wang, S. *et al.* Solution-processable thermally crosslinked organic radical polymer battery cathodes. *ChemSusChem* **13**, 2371–2378 (2020).

148. Song, Z., Zhan, H. & Zhou, Y. Anthraquinone based polymer as high performance cathode material for rechargeable lithium batteries. *Chem. Commun.* 448–450 (2009).

149. Xu, W. *et al.* Factors affecting the battery performance of anthraquinone-based organic cathode materials. *J. Mater. Chem.* **22**, 4032 (2012).

150. Flamme, B., Jismy, B., Abarbri, M. & Anouti, M. Poly-anthraquinone sulfide isomers as electrode materials for extended operating temperature organic batteries. *Mater. Adv.* **2**, 376–383 (2021).

151. Song, Z. *et al.* A quinone-based oligomeric lithium salt for superior Li–organic batteries. *Energy Environ. Sci.* **7**, 4077–4086 (2014).

152. Song, Z., Qian, Y., Zhang, T., Otani, M. & Zhou, H. Poly(benzoquinonyl sulfide) as a High-Energy Organic Cathode for Rechargeable Li and Na Batteries. *Adv. Sci.* **2**, 1500124 (2015).

153. Pirnat, K., Mali, G., Gaberscek, M. & Dominko, R. Quinone-formaldehyde polymer as an active material in Li-ion batteries. *J. Power Sources* **315**, 169–178 (2016).

154. Newkome, G., Schubert, U. & Winter, A. Polyimides and related polymers in battery applications. In An Introduction to Redox Polymers for Energy-Storage Applications, 349–389 (2023).

155. Sharma, P., Damien, D., Nagarajan, K., Shaijumon, M. M. & Hariharan, M. Perylene-polyimide-Based Organic Electrode Materials for Rechargeable Lithium Batteries. *J. Phys. Chem. Lett.* **4**, 3192–3197 (2013).

156. Li, C. *et al.* Low-cost carbonyl polymer design for high-performance lithium-organic battery cathodes. *J. Power Sources* **511**, 230464 (2021).

157. Liu, X. *et al.* Locally concentrated ionic liquid electrolyte with partially solvating diluent for lithium/sulfurized polyacrylonitrile batteries. *Adv. Mater.* **34**, e2207155 (2022).

158. Lu, Y., Zhang, Q., Li, F. & Chen, J. Emerging lithiated organic cathode materials for lithium-ion full batteries. *Angew. Chem. Int. Ed Engl.* **62**, e202216047 (2023).

159. Renault, S. *et al.* A green Li–organic battery working as a fuel cell in case of emergency. *Energy Environ. Sci.* **6**, 2124 (2013).

160. Wang, S. *et al.* Organic $Li_4C_8H_2O_6$ nanosheets for lithium-ion batteries. *Nano Lett.* **13**, 4404–4409 (2013).

161. Hu, Y., Tang, W., Yu, Q., Yang, C. & Fan, C. In situ electrochemical synthesis of novel lithium-rich organic cathodes for all-organic Li-ion full batteries. *ACS Appl. Mater. Interfaces* **11**, 32987–32993 (2019).

---

162. Yu, Q. *et al.* Electrochemically manipulating the redox state of 2,2′,5,5′-tetrahydroxybiphenyl as a new organic Li-rich cathode for Li-ion batteries. *Org. Electron.* **81**, 105661 (2020).

163. Yu, Q. *et al.* Novel low-cost, high-energy-density (>700 Wh·kg^{-1}) Li-rich organic cathodes for Li-ion batteries. *Chem. Eng. J.* **415**, 128509 (2021).

164. Wang, J. *et al.* Conjugated sulfonamides as a class of organic lithium-ion positive electrodes. *Nat. Mater.* **20**, 665-673 (2021).

165. Sieuw, L. *et al.* Through-Space Charge Modulation Overriding Substituent Effect: Rise of the Redox Potential at 3.35 V in a Lithium-Phenolate Stereoelectronic Isomer. *Chem. Mater.* **32**, 9996–10006 (2020).

166. Wang, J. *et al.* High performance Li-, Na-, and K-ion storage in electrically conducting coordination polymers. *Energy & Environmental Science* **15**, 3923-3932 (2022).

167. Wang, J. *et al.* A high-voltage organic framework for high-performance Na- and K-ion batteries. *ACS Energy Lett.* **7**, 668–674 (2022).

168. Zhang, Y. *et al.* Validating the reversible redox of alkali-ion disulfonyl-methanide as organic positive electrode materials. *Mater. Today Chem.* **28**, 101379 (2023).

169. Wang, J. *et al.* . Revealing the reversible solid-state electrochemistry of lithium-containing conjugated oximates for organic batteries. *Sci. Adv.* **9**, eadg6079 (2023).

170. Gupta, D., Gupta, S. J. & Vlad, A. New avenues for organic redox materials as sustainable lithium-ion battery cathodes. *Org. Mater.* **5**, 21–34 (2023).

171. Deng, W. *et al.* A Li-contained air-stable cathode for high-performance all-organic lithium-ion batteries. *Energy Storage Materials* **46**, 535–541 (2022).

172. Lakraychi, A. E., Dolhem, F., Vlad, A. & Becuwe, M. Organic negative electrode materials for metal-ion and molecular-ion batteries: Progress and challenges from a molecular engineering perspective. *Adv. Energy Mater.* **11**, 2101562 (2021).

173. Li, X. *et al.* Electroactive organics as promising anode materials for rechargeable lithium ion and sodium ion batteries. *Energy Mater* **2**, 200014 (2022).

174. Liang, Y. *et al.* Stable long cycling of small molecular organic acid electrode materials enabled by nonflammable eutectic electrolyte. *Small* **18**, e2104538 (2022).

175. Raccichini, R., Varzi, A., Passerini, S. & Scrosati, B. The role of graphene for electrochemical energy storage. *Nat. Mater.* **14**, 271–279 (2015).

176. Li, T., Wang, L. & Li, J. Carbon nanotube enables high-performance thiophene-containing organic anodes for lithium ion batteries. *Electrochim. Acta* **408**, 139947 (2022).

177. Lee, H. H., Park, Y., Shin, K.-H., Lee, K. T. & Hong, S. Y. Abnormal excess capacity of conjugated dicarboxylates in lithium-ion batteries. *ACS Appl. Mater. Interfaces* **6**, 19118–19126 (2014).

178. Renault, S. *et al.* Superlithiation of organic electrode materials: The case of dilithium benzenedipropiolate. *Chem. Mater.* **28**, 1920–1926 (2016).

179. Carvalho, R. P., Marchiori, C. F. N., Brandell, D. & Araujo, C. M. Understanding the lithiation limits of high-capacity organic battery anodes by atomic charge derivative analysis. *J. Chem. Phys.* **157**, 181101 (2022).

180. Lin, Z.-Q. *et al.* Solution-processed nitrogen-rich graphene-like holey conjugated polymer for efficient lithium ion storage. *Nano Energy* **41**, 117–127 (2017).

181. Wang, Y. *et al.* Ultrahigh-capacity organic anode with high-rate capability and long cycle life for lithium-ion batteries. *ACS Energy Lett.* **2**, 2140–2148 (2017).

182. Hu, W., Chen, N., Chen, D. & Tong, B. Conjugated tetrathiafulvalene carboxylates for stable organic lithium batteries. *ChemElectroChem* **9**, (2022).

183. Iordache, A. *et al.* From an enhanced understanding to commercially viable electrodes: The case of PTCLi$_4$ as sustainable organic lithium ion anode material. *Adv. Sustain. Syst.* **1**, 1600032 (2017).

184. Shinozaki, K., Tomizuka, Y. & Nojiri, A. Performance of Lithium/Polyacetylene Cell. *Jpn. J. Appl. Phys. (2008)* **23**, L892 (1984).

185. Naegele, D. Electrically conductive polymers as rechargeable battery electrodes. *Solid State Ion.* **28–30**, 983–989 (1988).

186. Zhang, C. *et al.* Microporous organic polymer-based lithium ion batteries with improved rate performance and energy density. *J. Power Sources* **317**, 49–56 (2016).

187. Kolek, M. *et al.* Ultra-high cycling stability of poly(vinylphenothiazine) as a battery cathode material resulting from π–π interactions. *Energy Environ. Sci.* **10**, 2334–2341 (2017).

188. Dai, G. *et al.* Manipulation of conjugation to stabilize N redox-active centers for the design of high-voltage organic battery cathode. *Energy Storage Mater.* **16**, 236–242 (2019).

189. Rodríguez-Pérez, I. A. *et al.* A hydrocarbon cathode for dual-ion batteries. *ACS Energy Lett.* **1**, 719–723 (2016).

190. Lee, S. *et al.* Charge-transfer complexes for high-power organic rechargeable batteries. *Energy Storage Mater.* **20**, 462–469 (2019).

191. Xie, Y., Zhang, K., Yamauchi, Y., Oyaizu, K. & Jia, Z. Nitroxide radical polymers for emerging plastic energy storage and organic electronics: fundamentals, materials, and applications. *Mater. Horiz.* **8**, 803–829 (2021).

192. Nishide, H. Organic redox polymers as electrochemical energy materials. *Green Chem.* **24**, 4650–4679 (2022).

193. Janoschka, T., Hager, M. D. & Schubert, U. S. Powering up the future: radical polymers for battery applications. *Adv. Mater.* **24**, 6397–6409 (2012).

194. Bobela, D. C. *et al.* Close Packing of Nitroxide Radicals in Stable Organic Radical Polymeric Materials. *J. Phys. Chem. Lett.* **6**, 1414–1419 (2015).

195. Karlsson, C., Suga, T. & Nishide, H. Quantifying TEMPO Redox Polymer Charge Transport toward the Organic Radical Battery. *ACS Appl. Mater. Interfaces* **9**, 10692–10698 (2017).

196. Wang, S., Li, F., Easley, A. D. & Lutkenhaus, J. L. Real-time insight into the doping mechanism of redox-active organic radical polymers. *Nat. Mater.* **18**, 69–75 (2019).

197. Easley, A. D. *et al.* Nitroxide Radical Polymer–Solvent Interactions and Solubility Parameter Determination. *Macromolecules* **53**, 7997–8008 (2020).

198. Kim, J.-K. *et al.* Organic radical battery with PTMA cathode: Effect of PTMA content on electrochemical properties. *J. Ind. Eng. Chem.* **14**, 371–376 (2008).

199. Nakahara, K., Oyaizu, K. & Nishide, H. Electrolyte anion-assisted charge transportation in poly(oxoammonium cation/nitroxyl radical) redox gels. *J. Mater. Chem.* **22**, 13669 (2012).

200. Ernould, B. & Sieuw, L. Negative redox potential shift in fire-retardant electrolytes and consequences for high-energy hybrid batteries. *ACS Applied Energy* (2019).

201. Gerlach, P., Burges, R., Lex-Balducci, A., Schubert, U. S. & Balducci, A. Influence of the salt concentration on the electrochemical performance of electrodes for polymeric batteries. *Electrochim. Acta* **306**, 610–616 (2019).

202. Nakahara, K. *et al.* Al-laminated film packaged organic radical battery for high-power applications. *J. Power Sources* **163**, 1110–1113 (2007).

203. Nakahara, K., Oyaizu, K. & Nishide, H. Organic Radical Battery Approaching Practical Use. *Chem. Lett.* **40**, 222–227 (2011).

204. Muench, S. *et al.* Printable ionic liquid-based gel polymer electrolytes for solid state all-organic batteries. *Energy Storage Materials* **25**, 750–755 (2020).

205. Wild, A. *et al.* Solid electrolyte for organic batteries. *US Patent* (2023).

206. Vlad, A., Rolland, J., Hauffman, G., Ernould, B. & Gohy, J.-F. Melt-polymerization of TEMPO methacrylates with nano carbons enables superior battery materials. *ChemSusChem* **8**, 1692–1696 (2015).

207. Iwasa, S., Nishi, T., Sato, H. & Nakamura, S. Flexibility and high-rate discharge properties of organic radical batteries with gel-state electrodes. *J. Electrochem. Soc.* **164**, A884–A888 (2017).

208. Hatakeyama-Sato, K., Wakamatsu, H., Katagiri, R., Oyaizu, K. & Nishide, H. An ultrahigh output rechargeable electrode of a hydrophilic radical polymer/nanocarbon hybrid with an exceptionally large current density beyond 1 A·cm^{-2}. *Adv. Mater.* **30**, e1800900 (2018).

209. Iwasa, S., Nishi, T. & Nakamura, S. Enhancement of rapid charging capability of organic radical battery using ethylene carbonate-based electrolyte containing LiFSI. *J. Power Sources* **402**, 157–162 (2018).

210. Pyun, S.-I., Shin, H.-C., Lee, J.-W. & Go, J.-Y. Electrochemical Methods. in *Monographs in Electrochemistry* 11–32 (Springer Berlin Heidelberg, 2012).

211. Wang, S. *et al*. Electrochemical impedance spectroscopy. *Nat. Rev. Methods Primers* **1**, (2021).

212. Pastor-Fernández, C., Uddin, K., Chouchelamane, G. H., Dhammika Widanage, W. & Marco, J. A Comparison between Electrochemical Impedance Spectroscopy and Incremental Capacity-Differential Voltage as Li-ion Diagnostic Techniques to Identify and Quantify the Effects of Degradation Modes within Battery Management Systems. *Journal of Power Sources* **360**, 301-318 (2017).

213. Meddings, N. *et al.* Application of electrochemical impedance spectroscopy to commercial Li-ion cells: A review. *J. Power Sources* **480**, 228742 (2020).

214. Vadhva, P. *et al.* Electrochemical impedance spectroscopy for all-solid-state batteries: Theory, methods and future outlook. *ChemElectroChem* **8**, 1930–1947 (2021).

215. Gaberšček, M. Understanding Li-based battery materials via electrochemical impedance spectroscopy. *Nat. Commun.* **12**, 6513 (2021).

216. Nejad, S., Gladwin, D. T. & Stone, D. A. A systematic review of lumped-parameter equivalent circuit models for real-time estimation of lithium-ion battery states. *J. Power Sources* **316**, 183–196 (2016).

217. Devan, S. & Subramanian, V. R. Analytical solution for the impedance of a porous electrode. *J. Electrochem. Soc.* **151**, 6, A905-A913 (2004).

218. Huang, J. & Zhang, J. Theory of Impedance Response of Porous Electrodes: Simplifications, Inhomogeneities, Non-Stationarities and Applications. *J. Electrochem. Soc.* **163**, A1983–A2000 (2016).

219. Vernon-Parry, K. D. Scanning electron microscopy: an introduction. *111-Vs Rev.* **13**, 40–44 (2000).

220. Goldstein, J. I. *et al.* Energy dispersive X-ray spectrometry: Physical principles and user-selected parameters. in *Scanning Electron Microscopy and X-Ray Microanalysis* 209–234 (Springer New York, 2018).

---

221. Scanning-electron microscopy. *Fakultäten an der HU*. Retrieved from: https://fakultaeten.hu-berlin.de/en/mnf/forschung_internationales/grs/salsa/p-a-labs/application-lab/instrumentation/a-labs-sem (2017).

222. Coats, A. W. & Redfern, J. P. Thermogravimetric analysis. A review. *Analyst* **88**, 906 (1963).

223. Ng, H. M. *et al*. Thermogravimetric analysis of polymers. *Encyclopedia of Polymer Science and Technology* 1–29 (2018).

224. NETZSCH GmbH, Thermogravimetric analysis (2022). Retrived from: https://analyzing-testing.netzsch.com/_Resources/Persistent/2/0/b/1/20b16c2dd0761cfeb14330e2bc0b9994d2e3fd19/AN.

225. Characterization of porous solids and powders: surface area, pore size, and density. *Choice (Middletown)* **42**, 42-5288-42–5288 (2005).

226. Nguyen, H. G. T., Horn, J. C., Bleakney, M., Siderius, D. W. & Espinal, L. Understanding material characteristics through signature traits from helium pycnometry. *Langmuir* **35**, 2115–2122 (2019).

227. Westbrook, E. M. Crystal-density measurements. in *International Tables for Crystallography* 152–157 (International Union of Crystallography, 2012).

228. Quantachrome Instruments, Ultrapyc True volume and density analyzer operating Manual. Retrived from: http://eodg.atm.ox.ac.uk/eodg/equipment/Pycnometer_user_manual.pdf (2019).

229. 3P Instruments, Characterization of particles powders pores. Retrieved from: https://www.3p-instruments.com/measurement-methods/gas-pycnometry/ (2019).

230. Pharmacopeial Forum, Density of Solids. Retrieved from: http://www.uspbpep.com/usp32/pub/data/v32270/usp32nf27s0_c699.html (2023).

231. Plett, G. L. *Battery Management Systems, Volume I: Battery Modeling*. (Artech House, 2015).

232. Newman, J. & Thomas-Alyea, K. E. *Electrochemical Systems*. (John Wiley & Sons, 2012).

233. Landesfeind, J. & Gasteiger, H. A. Temperature and concentration dependence of the ionic transport properties of lithium-ion battery electrolytes. *J. Electrochem. Soc.* **166**, A3079–A3097 (2019).

234. Abraham, D. P., Kawauchi, S. & Dees, D. W. Modeling the impedance versus voltage characteristics of $LiNi_{0.8}Co_{0.15}Al_{0.05}O_2$. *Electrochim. Acta* **53**, 2121–2129 (2008).

235. Mauler, L., Duffner, F. & Leker, J. Economies of scale in battery cell manufacturing: The impact of material and process innovations. *Appl. Energy* **286**, 116499 (2021).

236. Duffner, F., Wentker, M., Greenwood, M. & Leker, J. Battery cost modeling: A review and directions for future research. *Renewable Sustainable Energy Rev.* **127**, 109872 (2020).

237. Meister, P. *et al.* Best Practice: Performance and Cost Evaluation of Lithium Ion Battery Active Materials with Special Emphasis on Energy Efficiency. *Chem. Mater.* **28**, 7203–7217 (2016).

238. Greenwood, M., Wentker, M. & Leker, J. A bottom-up performance and cost assessment of lithium-ion battery pouch cells utilizing nickel-rich cathode active materials and silicon-graphite composite anodes. *Journal of Power Sources Advances* **9**, 100055 (2021).

239. Mauler, L., Duffner, F., Zeier, W. G. & Leker, J. Battery cost forecasting: a review of methods and results with an outlook to 2050. *Energy Environ. Sci.* **14**, 4712–4739 (2021).

240. Hagen, M. *et al.* Lithium-sulfur cells: The gap between the state-of-the-art and the requirements for high energy battery cells. *Adv. Energy Mater.* **5**, 1401986 (2015).

241. Moon, H. *et al.* Bio-waste-derived hard carbon anodes through a sustainable and cost-effective synthesis process for sodium-ion batteries. *ChemSusChem* **16**, e202201713 (2023).

242. Johansson, P. *et al.* Ten ways to fool the masses when presenting battery research. *Batter. Supercaps* **4**, 1785–1788 (2021).

243. Wentker, M., Greenwood, M., Asaba, M. C. & Leker, J. A raw material criticality and environmental impact assessment of state-of-the-art and post-lithium-ion cathode technologies. *Journal of Energy Storage* **26**, 101022 (2019).

244. Liu, X. *et al.* Al and Fe-containing Mn-based layered cathode with controlled vacancies for high-rate sodium ion batteries. *Nano Energy* **76**, 104997 (2020).

245. Wu, X. *et al.* P2-type $Na_{0.66}Ni_{0.33-x}Zn_xMn_{0.67}O_2$ as new high-voltage cathode materials for sodium-ion batteries. *J. Power Sources* **281**, 18–26 (2015).

246. Zuo, W. *et al.* Structure-Performance Relationship of Zn^{2+} Substitution in P2–$Na_{0.66}Ni_{0.33}Mn_{0.67}O_2$ with Different Ni/Mn Ratios for High-Energy Sodium-Ion Batteries. *ACS Appl. Energy Mater.* **2**, 4914–4924 (2019).

247. Zheng, S. *et al.* Exploring the working mechanism of Li^+ in O3-type $NaLi_{0.1}Ni_{0.35}Mn_{0.55}O_2$ cathode materials for rechargeable Na-ion batteries. *J. Mater. Chem. A Mater. Energy Sustain.* **4**, 9054–9062 (2016).

248. Mu, L. *et al.* Prototype Sodium-Ion Batteries Using an Air-Stable and Co/Ni-Free O3-Layered Metal Oxide Cathode. *Adv. Mater.* **27**, 6928–6933 (2015).

249. Liu Q., Lin W., Liang C., Guo Y. Positive electrode active material and its preparation method, sodium ion battery and apparatus containing the sodium ion battery. *US Patent* (2021).

250. Kuze, S., Kageura, J., Matsumoto, S., Nakayama, T., Makidera, M., Saka, M., Yamaguchi, T., Yamamoto, T., Nakane, K. *Development of a Sodium Ion Secondary Battery*. (2013).

251. Moon, H. *et al.* Assessing the reactivity of hard carbon anodes: Linking material properties with electrochemical response upon sodium- and lithium-ion storage. *Batter. supercaps* **4**, 960–977 (2021).

252. Niu, Y.-B. *et al.* High-Efficiency Cathode Sodium Compensation for Sodium-Ion Batteries. *Adv. Mater.* **32**, e2001419 (2020).

253. Wood, D. L., III, Li, J. & Daniel, C. Prospects for reducing the processing cost of lithium ion batteries. *J. Power Sources* **275**, 234–242 (2015).

254. Bresser, D., Buchholz, D., Moretti, A., Varzi, A. & Passerini, S. Alternative binders for sustainable electrochemical energy storage – the transition to aqueous electrode processing and bio-derived polymers. *Energy Environ. Sci.* **11**, 3096–3127 (2018).

255. Zuo, W. *et al.* The stability of P2-layered sodium transition metal oxides in ambient atmospheres. *Nat. Commun.* **11**, 3544 (2020).

256. Zuo, W. *et al.* Guidelines for air-stable lithium/sodium layered oxide cathodes. *ACS Mater. Lett.* **4**, 1074–1086 (2022).

257. Yoda, Y., Kubota, K., Isozumi, H., Horiba, T. & Komaba, S. Poly-γ-glutamate binder to enhance electrode performances of P2-$Na_{2/3}Ni_{1/3}Mn_{2/3}O_2$ for Na-ion batteries. *ACS Appl. Mater. Interfaces* **10**, 10986–10997 (2018).

258. Mu, L. *et al.* Water-processable P2-$Na_{0.67}Ni_{0.22}Cu_{0.11}Mn_{0.56}Ti_{0.11}O_2$ cathode material for sodium ion batteries. *J. Electrochem. Soc.* **166**, A251–A257 (2019).

259. Belt, Jeffrey R. *Battery Test Manual For Plug-In Hybrid Electric Vehicles*. United States: N. p., 2010. Web. doi:10.2172/1010675.

260. Christophersen, Jon P. *Battery Test Manual For Electric Vehicles, Revision 3*. United States: N. p., 2015. Web. doi:10.2172/1186745.

261. Xie, F., Xu, Z., Guo, Z. & Titirici, M.-M. Hard carbons for sodium-ion batteries and beyond. *Prog. Energy Combust. Sci.* **2**, 042002 (2020).

262. Asenbauer, J. et al. The success story of graphite as a lithium-ion anode material – fundamentals, remaining challenges, and recent developments including silicon (oxide) composites. *Sustain. Energy Fuels* **4**, 5387–5416 (2020).

263. Zarrabeitia, M. *et al.* Role of the voltage window on the capacity retention of P2-$Na_{2/3}[Fe_{1/2}Mn_{1/2}]O_2$ cathode material for rechargeable sodium-ion batteries. *Communications Chemistry* **5**, 11 (2022).

264. Yadav, P., Shelke, V., Patrike, A. & Shelke, M. Sodium-based batteries: development, commercialization journey and new emerging chemistries. *Oxford Open Materials Science* **3**, itac019 (2023).

265. Kim, J. *et al.* Unexpected discovery of low-cost maricite $NaFePO_4$ as a high-performance electrode for Na-ion batteries. *Energy Environ. Sci.* **8**, 540–545 (2015).

266. Bianchini, M., Xiao, P., Wang, Y. & Ceder, G. Additional sodium insertion into polyanionic cathodes for higher-energy Na-ion batteries. *Adv. Energy Mater.* **7**, 1700514 (2017).

267. Liu, Z. *et al.* Recent progress of P2-type layered transition-metal oxide cathodes for sodium-ion batteries. *Chemistry* **26**, 7747–7766 (2020).

268. Kulkarni, P. *et al.* A comprehensive review of pre-lithiation/sodiation additives for Li-ion and Na-ion batteries. *J. Energy Chem.* **76**, 479–494 (2023).

269. Zou, K. *et al.* Prelithiation/presodiation techniques for advanced electrochemical energy storage systems: Concepts, applications, and perspectives. *Adv. Funct. Mater.* **31**, 2005581 (2021).

270. Huang, Z. *et al.* Progress and challenges of prelithiation technology for lithium-ion battery. *Carbon Energy* **4**, 1107–1132 (2022).

271. Yang, C. *et al.* Roll-to-roll prelithiation of lithium-ion battery anodes by transfer printing. *Nat. Energy* **8**, 703–713 (2023).

272. Sathiya, M. *et al.* Dual Stabilization and Sacrificial Effect of Na_2CO_3 for Increasing Capacities of Na-Ion Cells Based on P2-NaxMO2 Electrodes. *Chem. Mater.* **29**, 5948–5956 (2017).

273. Shanmukaraj, D. *et al.* Highly Efficient, Cost Effective, and Safe Sodiation Agent for High-Performance Sodium-Ion Batteries. *ChemSusChem* **11**, 3286–3291 (2018).

274. Fernández-Ropero, A. J. *et al.* Improved Sodiation Additive and Its Nuances in the Performance Enhancement of Sodium-Ion Batteries. *ACS Appl. Mater. Interfaces* **13**, 11814–11821 (2021).

275. Hasa, I., Passerini, S. & Hassoun, J. Toward high energy density cathode materials for sodium-ion batteries: investigating the beneficial effect of aluminum doping on the P2-type structure. *J. Mater. Chem. A Mater. Energy Sustain.* **5**, 4467–4477 (2017).

276. Hasa, I., Passerini, S. & Hassoun, J. A rechargeable sodium-ion battery using a nanostructured Sb–C anode and P2-type layered $Na_{0.6}Ni_{0.22}Fe_{0.11}Mn_{0.66}O_2$ cathode. *RSC Adv.* **5**, 48928–48934 (2015).

277. Rajagopalan, R. *et al.* Improved Reversibility of Fe^{3+}/Fe^{4+} Redox Couple in Sodium Super Ion Conductor Type $Na_3Fe_2(PO_4)_3$ for Sodium-Ion Batteries. *Adv. Mater.* **29**, (2017).

278. Song, J. *et al.* Removal of interstitial H_2O in hexacyanometallates for a superior cathode of a sodium-ion battery. *J. Am. Chem. Soc.* **137**, 2658–2664 (2015).

279. Schnell, J., Knörzer, H., Imbsweiler, A. J. & Reinhart, G. Solid versus liquid—A bottom-up calculation model to analyze the manufacturing cost of future high-energy batteries. *Energy Technol.* **8**, 1901237 (2020).

280. Figueira-Duarte, T. M. & Müllen, K. Pyrene-based materials for organic electronics. *Chem. Rev.* **111**, 7260–7314 (2011).

281. Hu, J., Zhang, D. & Harris, F. W. Ruthenium(III) chloride catalyzed oxidation of pyrene and 2,7-disubstitued pyrenes: an efficient, one-step synthesis of pyrene-4,5-diones and pyrene-4,5,9,10-tetraones. *J. Org. Chem.* **70**, 707–708 (2005).

282. SMM, Daily Ternary precursor and Material price. Retrieved from: https://www.metal.com/Ternary-precursor-material (2023).

283. Judez, X., Qiao, L., Armand, M. & Zhang, H. Energy Density Assessment of Organic Batteries. *ACS Appl. Energy Mater.* **2**, 4008–4015 (2019).

284. Kaduk, J. A. Terephthalate salts: salts of monopositive cations. *Acta Crystallogr. B* **56 (Pt 3)**, 474–485 (2000).

285. Zhu, Z. & Chen, J. Review—advanced carbon-supported organic electrode materials for lithium (sodium)-ion batteries. *J. Electrochem. Soc.* **162**, A2393–A2405 (2015).

286. Park, M., Zhang, X., Chung, M., Less, G. B. & Sastry, A. M. A review of conduction phenomena in Li-ion batteries. *Journal of Power Sources* **195**, 7904–7929 (2010).

287. Zhao, Q., Wang, J., Chen, C., Ma, T. & Chen, J. Nanostructured organic electrode materials grown on graphene with covalent-bond interaction for high-rate and ultra-long-life lithium-ion batteries. *Nano Res.* **10**, 4245–4255 (2017).

288. Lu, C. *et al.* Achieving high capacity hybrid-cathode $FeF_3@Li_2C_6O_6$/rGO based on morphology control synthesis and interface engineering. *Chem. Commun.* **54**, 3235–3238 (2018).

289. Battaglia, A. M., Pahlavanlu, P., Grignon, E., An, S. Y. & Seferos, D. S. High active material loading in organic electrodes enabled by a multifunctional binder. *ACS Appl. Mater. Interfaces* **14**, 42298–42307 (2022).

290. Lin, Z., Liu, T., Ai, X. & Liang, C. Aligning academia and industry for unified battery performance metrics. *Nat. Commun.* **9**, 5262 (2018).

291. Lain, M. J., Brandon, J. & Kendrick, E. Design Strategies for High Power vs. High Energy Lithium Ion Cells. *Batteries* **5**, 64 (2019).

292. Singh, M., Kaiser, J. & Hahn, H. Thick electrodes for high energy lithium ion batteries. *J. Electrochem. Soc.* **162**, A1196–A1201 (2015).

293. Laue, V., Röder, F. & Krewer, U. Joint structural and electrochemical modeling: Impact of porosity on lithium-ion battery performance. *Electrochim. Acta* **314**, 20–31 (2019).

294. Lombardo, T. *et al.* Experimentally validated three-dimensional modeling of organic-based sodium-ion battery electrode manufacturing. *Batter. Supercaps* **5**, (2022).

295. Jiang, H. *et al.* Rational design of functional electrolytes towards commercial dual-ion batteries. *ChemSusChem* **16**, e202201561 (2023).

296. Cugnet, M. *et al.* A mathematical model for the simulation of new and aged automotive lead-acid batteries. *J. Electrochem. Soc.* **156**, A974 (2009).

297. Dahn, J. R. & Seel, J. A. Energy and capacity projections for practical dual-graphite cells. *J. Electrochem. Soc.* **147**, 899 (2000).

298. Fuller, T. F., Doyle, M. & Newman, J. Simulation and optimization of the dual lithium ion insertion cell. *J. Electrochem. Soc.* **141**, 1–10 (1994).

299. Tasaki, K. Density functional theory study on structural and energetic characteristics of graphite intercalation compounds. *J. Phys. Chem. C Nanomater. Interfaces* **118**, 1443–1450 (2014).

300. Beltrop, K. *et al.* Does size really matter? New insights into the intercalation behavior of anions into a graphite-based positive electrode for dual-ion batteries. *Electrochim. Acta* **209**, 44–55 (2016).

---

301. Vatamanu, J., Borodin, O., Olguin, M., Yushin, G. & Bedrov, D. Charge storage at the nanoscale: understanding the trends from the molecular scale perspective. *J. Mater. Chem. A Mater. Energy Sustain.* **5**, 21049–21076 (2017).

302. Beltrop, K. *et al.* Experimental and computational studies of electrochemical anion intercalation into graphite from target-oriented designed borate-based ionic liquid electrolytes. *J. Power Sources* **469**, 228397 (2020).

303. Thomas-Alyea, K. E. & Aryanpour, M. Design of Composite Electrodes with Anion-Absorbing Active Materials. *J. Electrochem. Soc.* **164**, A6017 (2016).

304. Ong, I. J. Double-Layer Capacitance in a Dual Lithium Ion Insertion Cell. *Journal of The Electrochemical Society* **146,** 4360 (1999).

305. Kirk, T. L., Evans, J., Please, C. P. & Chapman, S. J. Modeling electrode heterogeneity in lithium-ion batteries: Unimodal and bimodal particle-size distributions. *SIAM J. Appl. Math.* **82**, 625–653 (2022).

306. Lasia, A. Impedance of porous electrodes. in *Electrochemical Impedance Spectroscopy and its Applications* 203–250 (Springer New York, 2014).

307. Ravikumar, B., Mynam, M. & Rai, B. Effect of salt concentration on properties of lithium ion battery electrolytes: A molecular dynamics study. *J. Phys. Chem. C Nanomater. Interfaces* **122**, 8173–8181 (2018).

308. ISO, ISO 9924-3:2009. Retrieved from: https://www.iso.org/standard/44151.html (2020).

309. Kim, S. H., Mulholland, G. W. & Zachariah, M. R. Density measurement of size selected multiwalled carbon nanotubes by mobility-mass characterization. *Carbon N. Y.* **47**, 1297–1302 (2009).

310. Bauhofer, W. & Kovacs, J. Z. A review and analysis of electrical percolation in carbon nanotube polymer composites. *Compos. Sci. Technol.* **69**, 1486–1498 (2009).

311. Zhang, Y. *et al.* Impact of the synthesis method on the solid-state charge transport of radical polymers. *J. Mater. Chem. C Mater. Opt. Electron. Devices* **6**, 111–118 (2018).

312. Rostro, L., Wong, S. H. & Boudouris, B. W. Solid state electrical conductivity of radical polymers as a function of pendant group oxidation state. *Macromolecules* **47**, 3713–3719 (2014).

313. Suguro, M., Iwasa, S. & Nakahara, K. Fabrication of a practical and polymer-rich organic radical polymer electrode and its rate dependence. *Macromol. Rapid Commun.* **29**, 1635–1639 (2008).

314. Innes, J. R., Young, R. J. & Papageorgiou, D. G. Graphene nanoplatelets as a replacement for carbon black in rubber compounds. *Polymers (Basel)* **14**, 1204 (2022).

315. Nevers, D. R., Brushett, F. R. & Wheeler, D. R. Engineering radical polymer electrodes for electrochemical energy storage. *J. Power Sources* **352**, 226–244 (2017).

316. Kim, J.-K., Kim, Y., Park, S., Ko, H. & Kim, Y. Encapsulation of organic active materials in carbon nanotubes for application to high-electrochemical-performance sodium batteries. *Energy Environ. Sci.* **9**, 1264–1269 (2016).

317. Hu, Y. *et al.* Molecular-level anchoring of polymer cathodes on carbon nanotubes towards rapid-rate and long-cycle sodium-ion storage. *Mater. Chem. Front.* **2**, 1805-1810 (2018)

318. Iermakova, D. I., Dugas, R., Palacín, M. R. & Ponrouch, A. On the comparative stability of Li and Na metal anode interfaces in conventional alkyl carbonate electrolytes. *J. Electrochem. Soc.* **162**, A7060–A7066 (2015).

319. Qian, J. *et al.* High rate and stable cycling of lithium metal anode. *Nat. Commun.* **6**, 6362 (2015).

---

320. Liu, X. *et al.* Difluorobenzene-based locally concentrated ionic liquid electrolyte enabling stable cycling of lithium metal batteries with nickel-rich cathode. *Adv. Energy Mater.* **12**, 2200862 (2022).

321. Yang, D., Watanabe, M., Takagaki, A. & Ishihara, T. High voltage and capacity dual-ion battery using acetonitrile-aqueous hybrid electrolyte with concentrated LiFSI-LiTFSI. *J. Electrochem. Soc.* **169**, 120516 (2022).

322. Raccichini, R., Furness, L., Dibden, J. W., Owen, J. R. & García-Araez, N. Impedance characterization of the transport properties of electrolytes contained within porous electrodes and separators useful for Li-S batteries. *J. Electrochem. Soc.* **165**, A2741–A2749 (2018).

323. Finegan, D. P. *et al.* Characterising the structural properties of polymer separators for lithium-ion batteries in 3D using phase contrast X-ray microscopy. *J. Power Sources* **333**, 184–192 (2016).

324. SMM. Steel, Aluminum, Nickel, Rare Earth, New Energy, Copper Prices Charts and News. Retrieved from: https://www.metal.com (2023).

325. Yang, C. *et al.* 4.0 V aqueous Li-ion batteries. *Joule* **1**, 122–132 (2017).

326. Susarla, N. & Ahmed, S. Estimating Cost and Energy Demand in Producing Lithium Hexafluorophosphate for Li-Ion Battery Electrolyte. *Ind. Eng. Chem. Res.* **58**, 3754–3766 (2019).

327. SMM. Prices of the Once Extremely Popular Lithium Hexafluorophosphate Lost More than 82% in a Single Month. Retrieved from: https://news.metal.com/newscontent/101819558/prices-of-the-once-extremely-popular-lithium-hexafluorophosphate-lost-more-than-82-in-a-single-month- (2022).

328. Dunn, J. B., Gaines, L., Barnes, M., Wang, M. & Sullivan, J. Material and energy flows in the materials production, assembly, and end-of-life stages of the automotive lithium-ion battery life cycle. Argonne National Lab (US) (2019).

329. Satyavani, T. V. S. L., Srinivas Kumar, A. & Subba Rao, P. S. V. Methods of synthesis and performance improvement of lithium iron phosphate for high rate Li-ion batteries: A review. *Engineering Science and Technology, an International Journal* **19**, 178–188 (2016).

330. Ahmed, S., Nelson, P. A., Gallagher, K. G., Susarla, N. & Dees, D. W. Cost and energy demand of producing nickel manganese cobalt cathode material for lithium ion batteries. *J. Power Sources* **342**, 733–740 (2017).

331. BloombergNEF. Producing battery materials in the DRC could lower supply-chain emissions and add value to the country's cobalt. Retrieved from: https://about.bnef.com/blog/producing-battery-materials-in-the-drc-could-lower-supply-chain-emissions-and-add-value-to-the-countrys-cobalt/ (2021).

332. León, M., Silva, J., Carrasco, S. & Barrientos, N. Design, Cost Estimation and Sensitivity Analysis for a Production Process of Activated Carbon from Waste Nutshells by Physical Activation. *Processes* **8**, 945 (2020).

333. Kubiak, P., Cen, Z., López, C. M. & Belharouak, I. Calendar aging of a 250 kW/500 kWh Li-ion battery deployed for the grid storage application. *J. Power Sources* **372**, 16–23 (2017).

334. Baumann, M. *et al.* Prospective sustainability screening of sodium-ion battery cathode materials. *Adv. Energy Mater.* **12**, 2202636 (2022).

335. Kasnatscheew, J. *et al.* The truth about the 1st cycle Coulombic efficiency of $LiNi_{1/3}Co_{1/3}Mn_{1/3}O_2$ (NCM) cathodes. *Phys. Chem. Chem. Phys.* **18**, 3956–3965 (2016).

336. Rudola, A., Aurbach, D. & Balaya, P. A new phenomenon in sodium batteries: Voltage step due to solvent interaction. *Electrochem. Commun.* **46**, 56–59 (2014).

List of publications

Journal articles

- **Innocenti A.***, Beringer S.*, Passerini S., Cost and Performance Analysis as a Valuable Tool for Battery Material Research. *Nature Reviews Materials* **2024**, 9, 347-357

- **Innocenti A.**, Álvarez Moisés I., Gohy J.-F., Passerini S., A Modified Doyle-Fuller-Newman Model Enables the Macroscale Physical Simulation of Dual-ion Batteries. **2023**, 580, 233429

- **Innocenti A.**, Álvarez Moisés I., Lužanin O., Dominko R., Bitenc J., Gohy J.-F., Passerini S., Practical cell design for PTMA-based organic batteries: an experimental and modeling study. **2023**, *https://doi.org/10.1021/acsami.3c11838*

- **Innocenti A.**, Adenusi H., Passerini S., Assessing N-Type Organic Materials for Lithium Batteries: A Techno-Economic Review. *InfoMat* **2023**, 5, 11, e12480.

- Elmanzalawy M., **Innocenti A.**, Zarrabeitia M., Peter N. J., Passerini S., Augustyn V., Fleischmann S., Mechanistic understanding of microstructure formation during synthesis of metal oxide/carbon nanocomposites. *Journal of Materials Chemistry A* **2023,** 11, 17125-17137

- Álvarez Moisés I., **Innocenti A.**, Notredame B., Passerini S., Gohy J.-F., Liquid crystals as additives in solid polymer electrolytes for lithium metal batteries. *MRS Advances* **2023**, 8, 797–802.

- Zuo W.*, **Innocenti A.***, Zarrabeitia M., Bresser D., Yang Y., Passerini S., Layered Oxide Cathodes for Sodium-Ion Batteries: Storage Mechanism, Electrochemistry, and Techno-economics. *Accounts of Chemical Research* **2023**, 56, 3, 284-296.

- Chen Z., Liang H.-P., Lyu Z., Paul N., Ceccio G., Gilles R., Zarrabeitia M., **Innocenti A.**, Jasarevic M., Kim G.-T., Passerini S., Bresser D., Ultrathin single-ion conducting polymer enabling a stable Li|$Li_{1.3}Al_{0.3}Ti_{1.7}(PO_4)_3$ interface. *Chemical Engineering Journal* **2023**, 467, 143530.

- Rabissi C., Sordi G., **Innocenti A.**, Casalegno A., Fast and reliable calibration of thermal-physical model of lithium-ion battery: a sensitivity-based method. *Journal of Energy Storage* **2023**, 59, 106435.

- Moon H., **Innocenti A.**, Liu H., Zhang H., Weil M., Zarrabeitia M., Passerini S., Bio-Waste-Derived Hard Carbon Anodes Through a Sustainable and Cost-Effective Synthesis Process for Sodium-Ion Batteries. *ChemSusChem* **2023**, 16, e202201713.

- Mariani A., **Innocenti A.**, Varzi A., Passerini S., On the nanoscopic structural heterogeneity of liquid n-alkyl carboxylic acids. *Physical Chemistry Chemical Physics* **2021**, 23, 20282-20287.

- Rabissi C., **Innocenti A.**, Sordi G., Casalegno A., A Comprehensive Physical-Based Sensitivity Analysis of the Electrochemical Impedance Response of Lithium-Ion Batteries. *Energy Technology* **2021**, 9, 2000986.

** = co-first author*

Conference contributions

- Simsek Ö., **Innocenti A.**, Münch S., Passerini S., Schubert U., Novel polymer electrolytes for Li/PTMA batteries. *Organic Battery Days* **2023**, San Sebastian (Spain), poster

- Stepien D., **Innocenti A.**, Lyu Z., Passerini S., Dominic B., Tracking the Li^+ concentration on the surface of lithium metal electrodes upon cycling. *Advanced Battery Power* **2023**, Aachen (Germany) (oral).

- Beringer S., **Innocenti A.**, Passerini S., Cost and performance analysis as a valuable tool for battery research: the case of the optimization of the low cutoff voltage of sodium-ion battery cells. *Advanced Battery Power* **2023**, Aachen (Germany) (poster).

- **Innocenti A.**, Álvarez Moisés I., Gohy F., Passerini S., A modified Doyle-Fuller-Newman model for the physical simulation of dual-ion batteries. *Advanced Battery Power* **2023**, Aachen (Germany) (poster).

- Álvarez Moisés I., **Innocenti A.**, Passerini S., Gohy F., Liquid crystals as additives in solid polymer electrolytes for lithium metal batteries, *MRS Spring* **2023**, San Francisco (United States) (poster)

- **Innocenti A.**, Moon H., Zarrabeitia M., Passerini S., Techno-economic analysis of biowaste-derived hard carbons for sodium-ion batteries, *ABAA13* **2022**, Marrakech (Morocco) (oral)

- **Innocenti A.**, Chen Z., Passerini S., Comparing the cost of lithium- and sodium-ion batteries in view of the recent raw materials price increase, *First Symposium for YouNg Chemists* **2022**, Rome (Italy) (oral)

- **Innocenti A.**, Chen Z., Passerini S., A cost and performance analysis of organic battery materials, *EMRS Spring* **2022**, online conference (oral)

- Passerini S., **Innocenti A.**, A cost and performance analysis of post-lithium-ion batteries, *MRS Fall* **2021**, Boston (United States) (oral)

- Sordi G., Rabissi C., **Innocenti A.**, Casalegno A., Optimizing lithium-ion battery P2D model calibration through sensitivity analysis of physical parameters, *ModVal* **2021**, Sion (Switzerland) (oral)

- **Innocenti A.**, Rabissi C., Sordi G., Casalegno A., A comprehensive physical-based sensitivity analysis of the electrochemical impedance response of lithium-ion batteries, *1st Weinheim Symposium on Energy Technology* **2021**, online conference (oral). **Awarded with the Best Presentation Award.**

Ringraziamenti

Pensare di essere qua a scrivere questi ringraziamenti mi dà una sensazione strana: ho pensato a lungo al momento in cui avrei finito la tesi come così lontano e difficile da raggiungere che non mi sembra vero, adesso, di stare buttando giù queste ultime righe.

Questa idea di irraggiungibilità è stata per molto tempo una costante del mio pensare a questo lavoro, quasi fin da subito dopo aver iniziato il dottorato qui a Ulma. Dopo l'entusiasmo iniziale, la realtà di quanto tutto fosse nuovo, difficile, complesso, incerto, ha colpito molto forte, facendomi sentire quasi insormontabile la sfida di arrivare fino in fondo e di "creare qualcosa di mio". Moltissime volte non è stato facile conviverci, andare avanti, e scendere a patti con tutto ciò.

Se questa sensazione è nel tempo sparita e mi sono sentito sempre più sicuro di me e di quello che potevo riuscire a fare, non è stata solo una presa di coscienza da parte mia: sono stati preziosi e fondamentali l'aiuto e il supporto di tante persone, che qui vorrei ringraziare, in queste poche righe che purtroppo non potranno mai rendere veramente giustizia a quello che vorrei esprimere.

Il primo grazie va a Stefano, che ha creduto in me fin dall'inizio, sin da quando neanche mi aveva incontrato di persona. Ha saputo capire il tipo di lavoro in cui potevo dare il meglio ed indirizzarmi verso un percorso adatto a me e alle mie capacità. Mi ha dato tanta fiducia nel momento in cui io non ne avevo per niente, e di questo gliene sarò sempre grato.

Un grazie speciale anche a Zhen, che è stata la prima persona a insegnarmi da zero, con tanta pazienza, come lavorare davvero bene in laboratorio e sulle batterie. Se sono riuscito a "combinare qualcosa" dal punto di vista sperimentale ed avere la mentalità per questo lavoro, lo devo tanto a lei e alla sua guida.

A tutti i miei colleghi, amici, che ho conosciuto in questi tre anni in HIU e a Ulma: grazie di cuore. Mi sono sentito accolto fin dall'inizio, abbiamo condiviso tanti ricordi indelebili, e sono sempre stato sostenuto nei momenti più complicati. Non voglio scrivere tutto quello che abbiamo passato, servirebbe lo spazio di un'altra tesi, ma tutto resta nelle centinaia di foto insieme, e nel mio cuore. Né voglio scrivere nomi, mi scorderei sicuramente qualcuno e mi porterebbe a fare ingiuste selezioni: ognuno che leggerà saprà benissimo a chi e cosa mi riferisco. Se ho deciso di restare qua a Ulma nel prossimo futuro, lo devo anche a tutti loro.

Grazie tanto anche i miei amici che ho dovuto “lasciare” in Italia. Tante volte ho avuto nostalgia di Pistoia e Milano, ed è stato difficile in certi momenti essere convinti di aver fatto la scelta giusta a venire qua e ricominciare tutto da capo, quando si conoscono delle persone così speciali. Grazie a chi è riuscito a venirmi a trovare e con cui sono stato felicissimo di riuscire a condividere la mia vita qui. Grazie a chi, quando io torno ogni tanto, mi fa sempre sentire come se non fossi mai andato via.

Un grazie enorme alla mia famiglia: Simone, Barbara, Lorenzo, Gianmarco, Emanuele, Cesira, Anna. Per il sostegno costante, per avermi dato così tanto, per avermi insegnato ad essere quello che sono. Da lontano non si riesce mai a trasmettere abbastanza quanto mi manchi essere con loro ogni giorno, e quanto si senta tutta questa (per fortuna, soltanto fisica) distanza. Entrare dalla porta di casa e trovare tutti dentro, che prima era la normalità, è adesso qualcosa di veramente speciale e prezioso per me.

Infine, ma non per importanza, grazie a te, Sophi. Tutte le parole che potrei scrivere qui non riuscirebbero mai descrivere quello che sei riuscita a darmi da quando ci siamo conosciuti. Posso solo ringraziarti per tutto il tuo supporto, che riesci a esprimere in un modo sempre così unico e amorevole. Con te ho quella serenità e tranquillità che cercavo da tanto, e che hanno voluto dire veramente tanto per arrivare alla fine di questo percorso. Non vedo l’ora di passare questa estate (e le prossime) insieme.

Ale

Acknowledgments

Thinking about being here writing these acknowledgments gives me a strange feeling: I've long thought of the moment when I would finish my thesis as something so distant and difficult to achieve that it doesn't feel real now, as I'm jotting down these last lines.

This idea of unattainability has been a constant in my thinking about this work for a long time, almost from the moment I started my doctoral studies here in Ulm. After the initial enthusiasm, the reality of how everything was new, difficult, complex, and uncertain hit me hard, making the challenge of reaching the end and "creating something of my own" seem almost insurmountable. It wasn't always easy to live with it, to move forward, and come to terms with everything.

If this feeling has gradually disappeared over time and I have felt more and more confident in myself and what I could achieve, it wasn't just a self-realization: the help and support of many people have been precious and fundamental, and I would like to thank them here, although these few lines will never truly do justice to what I want to express.

First and foremost, thank you to Stefano, who believed in me from the beginning, even before he had met me in person. He understood the type of work in which I could be good and guided me towards a path that suited me and my capabilities. He gave me so much confidence when I had none, and for that, I will always be grateful.

A special thanks also goes to Zhen, who was the first person to teach me from scratch, with great patience, how to work effectively in the laboratory and with batteries. If I have been able to "accomplish something" from an experimental standpoint and have the right mindset for this work, I owe it to her and her guidance.

To all my colleagues, friends, whom I have met in these three years at HIU and in Ulm: thank you from the bottom of my heart. I felt welcomed from the very beginning, we shared countless unforgettable memories, and I was always supported during the most challenging moments. I don't want to write about everything we went through; it would require the space of another thesis. But everything remains in the hundreds of photos together and in my heart. Nor do I want to mention names; I would surely forget someone and make unfair selections. Every one of them who will read this will know very well to whom and what I am referring. If I have decided to stay here in Ulm in the next future, it's also thanks to all of them.

Thank you so much to my friends whom I had to "leave" in Italy. Many times I have been nostalgic for Pistoia and Milan, and at certain moments, it was difficult to be convinced that I made the right choice to come here and start all over again when you know such special people. Thanks to those who managed to come and visit me, and with whom I was so happy to share my life here. And thanks to those who always make me feel like I never left, whenever I return.

A huge thank you to my family: Simone, Barbara, Lorenzo, Gianmarco, Emanuele, Cesira, Anna. For the constant support, for giving me so much, for teaching me to be who I am. From far away, it's never possible to convey enough how much I miss being with them every day and how much this (fortunately, only physical) distance is felt. Walking through the front door and finding everyone inside, which used to be normality, is now something truly special and precious to me.

Lastly, but not least, thank you, Sophi. All the words I could write here would never be able to fully describe what you have given me since we met. I can just thank you for all your support, which you always express in such a unique and loving way. With you I have the serenity and tranquility that I was since long looking for, and that have meant so much in reaching the end of this journey. I can't wait to spend this summer (and the ones to come) together.

Ale